Computer simulation studies of zeolites and related microporous materials

Tschaufeser, Petra

Award date:
1992

Awarding institution:
University of Bath

COMPUTER SIMULATION STUDIES OF ZEOLITES AND RELATED MICROPOROUS MATERIALS

submitted by Petra Tschaufeser

for the degree of PhD

of the University of Bath

1992

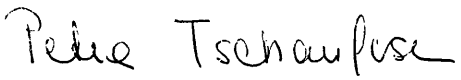

ProQuest LLC
789 East Eisenhower Parkway
P.O. Box 1346
Ann Arbor, MI 48106-1346

ABSTRACT

The aim of this thesis is to apply computer simulation techniques to investigate the structure, properties and stabilities of quartz-polymorphs, zeolites and aluminophosphates at 0 Kelvin, but also at elevated temperatures and pressures.

Chapters 1 and 2 are largely introductory. They review the history, geology, synthesis, properties and structure of zeolites and aluminophosphates. Furthermore the structural techniques that are used to examine zeolite and aluminophosphate structures are discussed and the way these methods complement each other. A major aim was to demonstrate the importance of computer simulation as a further structural technique.

In chapter 3 the static and dynamic simulation methods are discussed in detail with a description of the theoretical background to the techniques. Lattice energy and free energy minimisation are having a substantial impact on studies of the structure and energetics of zeolites, aluminophosphates and quartz-polymorphs. Lattice energy minimisation is a well established technique, having been applied to a wide range of materials. Free energy minimisation represents a new computational development for which an efficient code PARAPOCS is now available.

In chapter 4 the interatomic potential parameters used in this modelling studies are discussed in detail. It describes the various procedures for assigning the potential parameters but also the different potential models which will be tested.

The aim in chapter 5 is to test the validity of the empirical three-body shell model (Sanders, 1984) and a recently derived semi-empirical two-body rigid ion model (Kramer et al, 1991) on quartz polymorphs in order to use them for further simulation studies. This is done by comparing the simulated structural and elastic properties of the quartz-polymorphs with available experimental values at 0 Kelvin and also at elevated temperatures and pressures. In addition, the vibrational spectrum, the thermodynamic properties and the phase transition will be calculated and compared with experimental data.

In the next chapter the validity of the semi-empirical Al-O and P-O potential model is tested on berlinite ($AlPO_4$) in the same fashion as in chapter 5 in order to apply this model for further simulation studies on aluminophosphates.

In chapter 7 lattice energy minimisation is used to calculate the structural and energetic properties of zeolites. The primary aim is to rationalise zeolite stability in terms of structural features. There are some methods described which enable stability to be studied in terms of some structural motif. The ABC-6 family of zeolites is used as a model system, although the approach is quite general.

The aim in chapter 8 is to use lattice energy minimisation to calculate the structural and energetic properties of aluminophosphates in order to gain insight into the factors govern their stability.

The above methods are based on 0 Kelvin lattice energies. To extend them to different temperatures, free energy minimisation studies are in progress.

The aim in chapter 9 and 10 is to apply this technique to zeolites and aluminophosphates. This method is used beside computing the Gibbs free energy also to simulate the thermodynamic (e.g. Cv, Cp, S) and structural (e.g. thermal expansion coefficient) properties of zeolites and aluminophosphates at elevated temperatures. It also provides insight into the factors which govern the energetic and thermodynamic properties and structural changes of these materials.

ACKNOWLEDGEMENTS

I would like to thank my supervisor Dr. S.C. Parker for his help, advice and encouragement throughout the course of this work.

I would also like to thank Dr. A. Wall and Dr. J. O. Titiloye for their many helpful discussions and contributions.

I am also grateful for the support and friendship of all my colleagues at Bath University.

For financial support I am grateful to the "Bundesministerium für Wissenschaft und Forschung" of Austria.

I would especially like to thank Simon Tomlinson for his support and patience throughout the course and the writing of this thesis.

Finally I would like to thank my family for all their encouragement.

Für meine Eltern

CONTENTS

II) STRUCTURE AND PROPERTIES OF ALUMINOPHOSPHATES

III) ATOMISTIC SIMULATION TECHNIQUES

IV) POTENTIAL MODELS

V) APPLICATION OF THE POTENTIAL MODELS TO QUARTZ - POLYMORPHS

VII) STATIC SIMULATION OF ZEOLITES

VIII) STATIC SIMULATION OF ALUMINOPHOSPHATES

IX) LATTICE DYNAMICS OF ZEOLITES

X) LATTICE DYNAMICS OF ALUMINOPHOSPHATES

I. STRUCTURE AND PROPERTIES OF ZEOLITES

1.1. Introduction to zeolite chemistry

Zeolites form a large family of alumosilicates which were first identified in 1756 by the Swedish mineralogist A.F. Cronstedt, who observed that the mineral stilibite visibly lost water when heated in a blowpipe flame. The name comes from Greek *zein,* to boil, and *lithos*, stone.

The zeolites constitute one of the largest groups of minerals known, more than 40 distinct species have been recognized, and about 100 species having no natural counterpart, have been synthesized in the laboratory.

Both synthetic and natural zeolites are widely used in ion-exchange applications. They also offer unique properties as sorbents and molecular sieves and they play a dominant role in heterogeneous catalysis.

The potential application of zeolites stems from their fundamental chemical and physical properties, which in turn are directly related to their chemical compositions and crystal structures.

1.2. Natural occurrence of zeolites

Many zeolites occur naturally. Zeolites are ubiquitous constituents in the vugs and cavities of basic volcanic rocks and other traprock formations. Igneous zeolites occur as well formed crystals, among which are chabazite, erionite, faujasite and mordenite. In some igneous rocks they occur as alteration products of aluminoslilicates such as the feldspars or nepheline (Deer, Howie & Zussman, 1963).

In addition to their occurrence in basic eruptive rocks and related late-stage hydrothermal environment, zeolites are known as authigenic minerals in sandstones and other sedimentary rocks. Authigenic silicates occur in a relatively large scale. The five most common zeolites in sedimentary deposits are analcime, clinoptilite, phillipsite, laumontite and heulandite (Dyer, 1984).

Several different zeolite types occur in low-grade (low temperature and/or pressure) metamorphic rocks.

The crystallisation process has developed over geological time scales, but the composition of the recrystallised zeolite, the nature of the co-occuring phases and the depth (which involves different temperature and pressure steps) of the deposit gives insight in which zeolite crystallisation has occurred. The ranges of physical and chemical conditions generating natural zeolites have been relatively restricted. For example, there are no known natural high siliceous zeolites like ZSM-5 and other members of the pentasil family.

1.3. Silicate Structures

The fundamental structural unit of silicates is the SiO_4 tetrahedron. The units are joined together in a variety of ways depending on the number of oxygen linkages involved. This structural dependence will be illustrated below.

1.3.1 Discrete Anions

The structure of the *orthosilicate anion* is shown in Figure 1.1. The simple silicate anion (SiO_4^{4-}) is present in olivine ($(Mg, Fe)_2SiO_4$). Other minerals containing the discrete anion are penacite (Be_2SiO_4), willmenite (Zn_2SiO_4) and zircon ($ZrSiO_4$). Also included in this group are the important class of minerals, known as garnets. These have the general formula: $M^A M^B (SiO_4)_3$, where M^A can be Ca^{2+}, Mg^{2+} or Fe^{2+}, and M^B is Al^{3+}, Cr^{3+} or Fe^{3+}.

The simplest of the condensed silicate anions - that is, those formed by combining two or more SiO_4 tetrahedra by sharing of oxygen atoms - is the *pyrosilicate anion* ($Si_2O_7^{6-}$) (Figure 1.1). This ion occurs for example in thortveitite ($Sc_2Si_2O_7$).

At a more complex level are the discrete cyclic anions. The structure of two such cyclic ion, ($Si_3O_9^{6-}$) and ($Si_6O_{18}^{12-}$) are shown in Figure 1.1. The *metasilicate anions* occur in benitiote ($BaTiSi_3O_9$) and beryl ($Be_3Al_2Si_6O_{18}$).

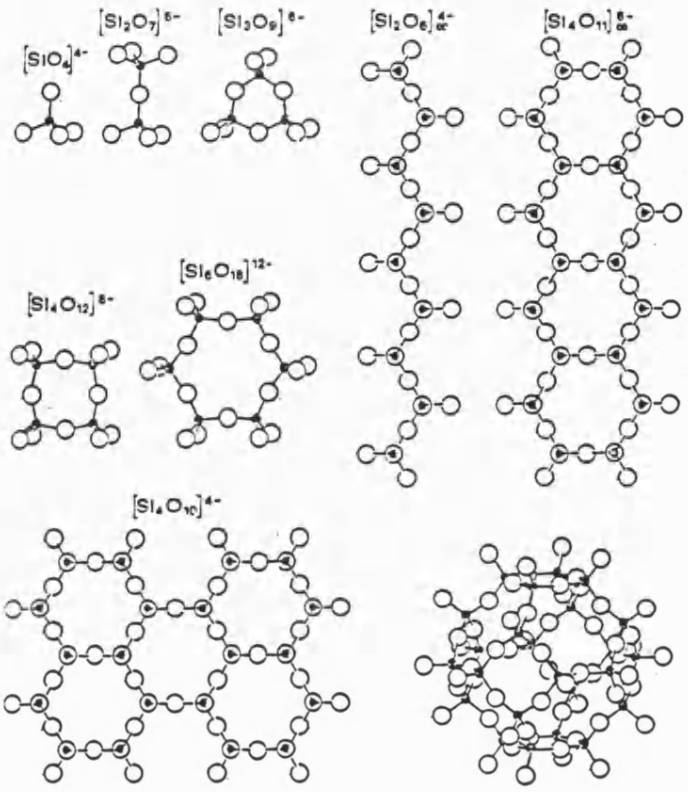

Figure 1.1: Various silicate structures

1.3.2. Extended Anions

An extension to the discrete anions are the *infinite chain anions*. These are of two main types: the pyroxenes, which contain singel-strand chains of composition $(SiO_3^{2-})_n$ (Figure 1.1) and the amphiboles, which contain double-strand, cross linked chains or bands of composition $(Si_4O_{11}^{6-})_n$ (Figure 1.1). Examples of pyroxenes are enstatite ($MgSiO_3$), diopside ($Ca\,Mg(SiO_3)_2$) and spodumen ($Li\,Al\,(SiO_3)_2$). A typical amphibole is tremolite ($Ca_2\,Mg_5\,(Si_4O_{11})_2\,(OH)_2$).

When SiO_4 tetrahedra are linked into infinite two-dimensional networks as shown in Figure 1.1, these are *infinite sheet anions*. The empirical formula for the anion is

$(Si_2O_5^{2-})_n$. Many important rock-forming minerals contain this silicate anion; examples are: kaolin ($Al_2(OH)_4Si_2O_5$), talc ($Mg_3(OH)_2Si_4O_{10}$) and the micas, like biotite ($K(Mg,Fe)_3(OH)_2(AlSi_3O_{10})$ and muscovite ($KAl_2(OH)_2(AlSi_3O_{10})$).

1.3.3. Three-dimensional Anions: Tectosliciates

The next logical extension in the progression above from simple (SiO_4^{4-}) ions to larger and more complex structures would be to three-dimensional framework structures in which every oxygen is shared between two tetrahedra. The empirical formula for such a silicate is $(SiO_2)_n$. However, silicon may be replaced by aluminium. The electrical imbalance created by the substitution is compensated through the presence of a cation. Aluminosilicates of this type are the feldspars, zeolites and ultramarines. The feldspars are the major constituents of igneous rocks and include such minerals as orthoclase ($KAlSi_3O_8$) and anorthite ($CaAl_2Si_2O_8$).

Ultramarines are characterised by an open framework with structural similarities to zeolites. They differ from the feldspars and zeolites, in having free anions and no water in the internal cavities of the structure.

The structure of the zeolites will be discussed below.

Tectosilicates may be sub-divided into porous and non-porous materials. The feldspars and the denser crystalline silicas (such as quartz) are non-porous as their internal spaces (interstices) are not large enough to admit even the smallest guest molecules in appreciable quantities. However, studies on tridymite and cristobalite (Barrer and Vaughen, 1967) revealed that the materials can take up considerable amounts of He and

Ne and so are considered porous.

Zeolites have extremely large internal cavities and channels, and are therefore highly porous. The structural features of zeolites are responsible for many of their unusual properties.

1.4. Structure of zeolites

1.4.1. Composition of zeolites

Zeolites are crystalline, hydrated aluminosilicates of alkali metal and alkaline-earth metal cations having infinite, three dimensional structures. They are produced by linking SiO_4 and AlO_4 tetrahedra by sharing all four oxygen. The structural feature which distinguishes zeolites from other tectosilicates is the presence of large internal cavities and pores. It is this feature which makes the framework porous, and is responsible for many of the relatively unusual and commercially very important properties of zeolites.

In zeolite structures some of the tetravalent silicon is replaced by trivalent aluminium, giving rise to a deficiency of positive charge. The framework is anionic, with a net negative charge equal to the number of aluminium atoms in framework T-positions. The charge is balanced by the presence of mono- and/or divalent non-framework cations, for example Na^+, Ca^{2+}, K^+ or by protons binding to framework oxygen. The non-framework cations are usually sited in or have access to the pore system and can be exchanged by treatment with a suitable salt solution or molten salt.

The framework may be considered as being derived from silica by:

$$(SiO_2)_n \xrightarrow{xM + x\ Al} M_x\ (AlO_2)_x\ (SiO_2)_{n-x}$$

where M stands for the cation compensating the overall negative charge created by the presence of aluminium.

In general hydrated zeolites can be presented by the empirical formula:

$$M_{a/n}\quad [(AlO_2)_a(SiO_2)_b]\quad wH_2O$$

Non-framework cations Framework Sorbed phase

where M is a cation of valence n, w is a whole number of water molecules, and a and b are small whole numbers. The sum (a+b) is the total number of tetrahedra in the unit cell and the ratio b/a varies from 1 to infinity. The square bracket contain atoms comprising the framework, while the remaining atoms reside in sites in the cavities. These cavity-atoms are usually mobile and are exchangeable with other species.

The ration b/a (Si/Al) varies from one framework to another, but can never be less than 1 (i.e. the Al content cannot exceed the Si content) due to a structural feature formulated as Loewensteins rule (Loewenstein, 1954), which prohibits Al-O-Al type linkages. This occurs because on replacing Si^{4+} by Al^{3+} the adjacent $[AlO_2]^-$ tetrahedra would then be adjacent effective negative charges and hence would be unfavorable.

In addition to Si-Al replacement, a range of T-atom heterosubstitutions are possible. For

example galloslilicates, aluminogermanate and gallogermanate with similar properties as zeolites. Transition metal substitution into several lower Si:Al ratio zeolites have been described and substitution of B, P, Fe, Ni, Sn and Ti in the high silica ZSM-5 have been claimed (Newsam, 1990).

All natural zeolites contain loosely bound water or larger molecules. Part or all of this water is given off continuously and reversibly on heating from room temperature to about 300℃. Once the water is removed the cations adopt positions on the inner surface of the channels and central cavities. The dehydration of a zeolite is an endothermic process. Conversely, rehydration is exothermic.

The three building units of a zeolite structure, the framework, the non-framework cations and the sorbed phase are each of interest and each plays a role of varying importance in applications.

1.4.2. Classification of zeolite structures

Although the chemical compositions are very similar, each zeolite species possess its own unique crystal structure, and hence, its own set of physical and chemical properties. In an attempt to classify zeolites, their structures have been described in terms of condensation of various building units. At the simplest level is the "Primary Building Units" (PBU). The PBUs are the SiO_4 and AlO_4 (these are often referred as TO_4 units, the T indicating "tetrahedral site" which may be occupied by either Si or Al tetrahedra). The individual TO_4 tetrahedra in zeolite structures are generally close to regular, but the shared oxygen linkage can accommodate a wide range of T-O-T angles from ~ 130°to ~160°. Thus the PBUs can be combined to from an infinite variety of different structures, and there is no known systematic procedure for deriving all of them.

Thus, the crystal structures were classified in terms of subunits. Several types of subunits can be found in a 3-dimensional (=3D) net. The simplest is an edge (Figure 1.2) between

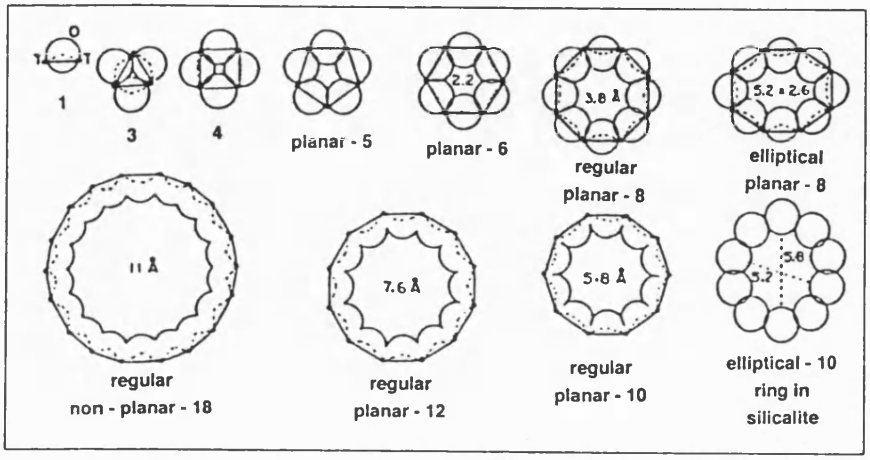

Figure 1.2: Geometrical properties of T-O rings and windows. Oxygen and T-atoms are shown respectively by large open and small filled circles. An arbitrary value for the "free diameter" is obtained by assigning a radius of 1.35Å to each oxygen atom and a distance of 3.1Å between adjacent T-atoms. The relative positions of the T and O atoms are chosen arbitrarily to give O-T-O angles near the tetrahedral value of 109.5°. Most rings are nonplanar in real structures with most O-T-O angles between 104 and 114° and most T-O-T angles between 130 and 160°. The importance of the regularity is shown by comparing a symmetrical planar 8-ring with an elliptical planar one. A regular planar 10-ring is compared with a non-planar 10-ring from silicalite. Two-thirds of the T-T linkages are tilted and shortened in the projection of the 18-ring.

two vertices. Others are rings (Figure 1.2), polyhedra (Figure 1.3), coplanar and non-planar chains (Figure 1.4) and 2D nets (Figure 1.5). All these types of subunits are useful for classification, and all can be linked together in various ways to make 3D-nets of zeolites and related materials. The possible subunits in 3D nets can be also considered as building units and polyhedral cages, rings and windows, channel systems and internal surfaces.

These subunits are useful for several reasons (a) any subunit is a potential candidate for

synthesis during growth of a zeolite or related material; (b) any cage or channel may be the container for an encapsulated species, which may even act as the template during synthesis; (c) each cannel system and window places and upper limit on the sorption of molecules; (d) each ring and internal surface provides sites for bonding of exchangeable cations to the framework oxygen; (e) each unit can be checked for possible ways of inventing new nets; (f) some units are convenient for classification (Smith, 1988).

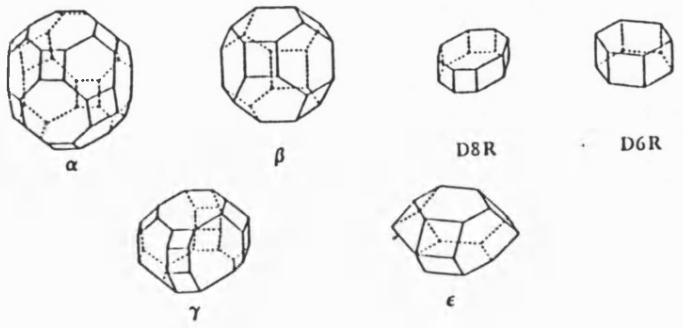

Figure 1.3: Selected cages and building units obtained from T-T linkages in the 3D frameworks of zeolites: α (26-hedron Type I) or truncated cuboctahedron; β (14-hedron Type I) or truncated octahedron; δ or double 8-ring (D8R); double 6-ring (D6R) of hexagonal prism; γ or 18-hedron; ε or 11-hedron.

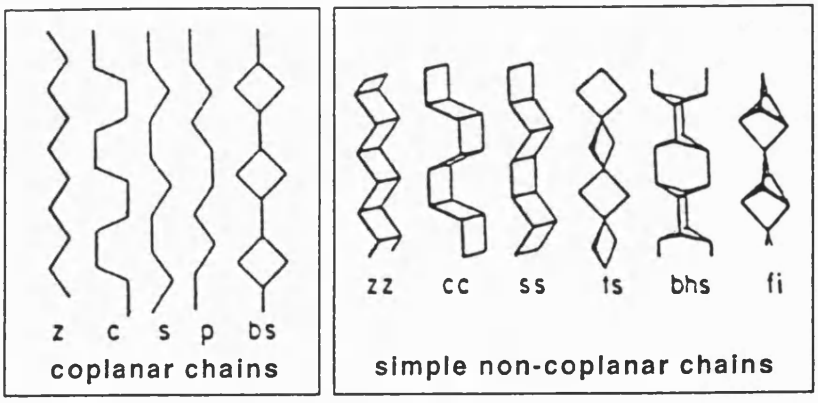

Figure 1.4: Simple coplanar and non-coplanar chains; z (zigzag), c (crankshaft), s (saw), p (pentasil), bs (bifurcated square), zz (double zigzag), cc (double crankshaft), ss (double saw), ts (twisted square), bhs (bifurcated hexagon plus square), fi (chain in the fibrous zeolites).

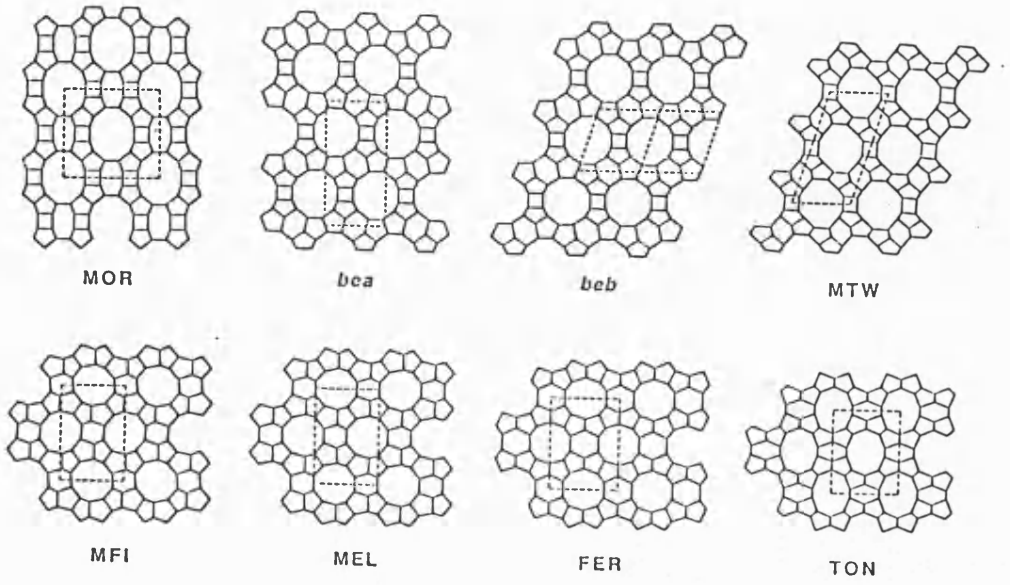

Figure 1.5: Two-dimensional nets of some zeolite structures

The concept of the "Secondary Building Units" (SBU) has been derived (Meier 1968, 1987) assuming the entire framework is made up of one type of SBU only. Actually many nets can be broken down into more than one type of SBU, therefore a unit cell always contains an integral number of SBUs. The ABC-6 group of zeolites, for example, are made up of single 4-rings and of parallel single and/or double 6-ring units and the stacking of these "12-valent" SBUs can be readily described like polytypic sequences of hexagonal layers (e.g. the hexagonal erionite net by AABAAC and the cubic sodalite net by ABC). The group of fibrous natural zeolites (e.g. edingtonite, natrolite or thomsonite) can be constructed from a single type of SBU, as they all share the 4=1 SBU. Most of the high silica zeolites (e.g. silicalite, mordenite) have a SBU based on the 5-ring. The SBUs in zeolite structures according to Meier and Olsen (1987) are shown in Figure 1.6.

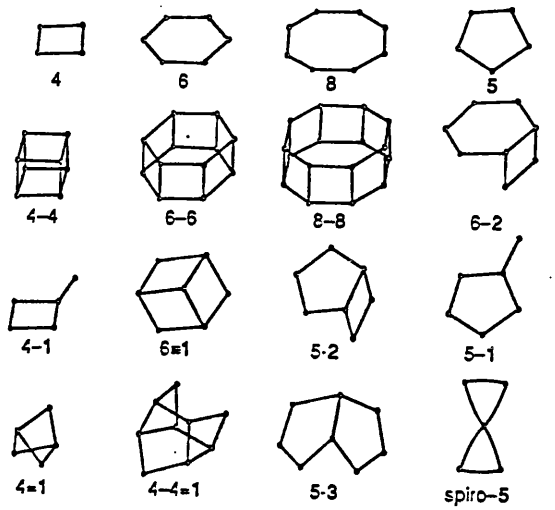

Figure 1.6: The secondary building units (SBU) in zeolite structures according to Meier (1987). Only the positions of tetrahdral (T) silicons and aluminiums are shown. Oxygen atoms lie near the connecting solid lines, which are not intended to mean bonds.

Another classification has been proposed by Breck (1973). This classification is based on a combination of framework topology as well as secondary building units. Breck's division of zeolites into seven groups are based on the criterions shown in Table 1.1.

Group	SBU	Example
1	Single 4-ring, S4R	Philipsite
2	Single 6-ring, S6R	Sodalite
3	Double 4-ring, D4R	Zeolite A
4	Double 6-ring, D6R	Faujasite
5	Complex 4-1	Natrolite
6	Complex 5-1	Mordenite
7	Complex 4-4-1	Stilbite

Table 1.1: The seven groups of zeolites as given by Breck (1973)

Breck also classified zeolites according to the cage structure of polyhedra they contain. Possible cage types are shown in Figure 1.3.

An important structural property of zeolites, which is particularly significant for the selectivity of zeolites is the pore size.The aperture dimensions of rings and windows which control entry into the internal pore volume primarily determined by the number of T-atoms and oxygen atoms in the ring which defines them. In Figure 1.2 geometrical properties of rings and windows are shown. A 3-ring must be planar and it cannot be a window for molecular adsorption. A 4-ring need not to be planar, but no matter how the angles are adjusted, the T-T constraint leaves little room. A hole of ~1.5Å diameter can be obtained for a regular planar 5-ring. A regular planar 6-ring has a hole of about 2.2Å diameter, but many 6-rings are distorted into ditrigonal or other shapes. Effective aperture sizes range from 3.8Å for a 8-ring structure (such as zeolite A or rho) through 5.8Å for 10-rings (like ZSM-5), 7.4Å for 12-rings (zeolite X or zeolite L) to 10.2Å for 18-rings (VPI-5).

The topology of the internal surface or an infinite channel system is also interesting, since the surface can be treated as an infinite curved net or infinite polyhedron (Wells, 1977). The term "tubular building unit" was invented (Meier et al, 1982) for the assemblage of T-T linkages around linear channels. Figure 1.7 shows the perspective drawings of tubular building units.

Because any sequence of edge-vertex-edge etc. is a chain, all 4-connected 3D nets contain chains which can be linked into sheets. Hence, the selection of chains in the 3D nets of zeolites is arbitrary. Some examples are given in Figure 1.4. The simplest chains are the five coplanar ones, which are given pictorial names zigzag (z), crankshaft (c), saw (s), pentasil (p) and bifurcated square (bs). The non coplanar chains include double zigzag (zz), double crankshaft (cc), the double saw (ss), the twisted square (ts), the bifurcated hexagonal-square chain (bhs) and the chain in the fibrous zeolites (fi) which contain

the 4-1 secondary building unit (Smith, 1988).

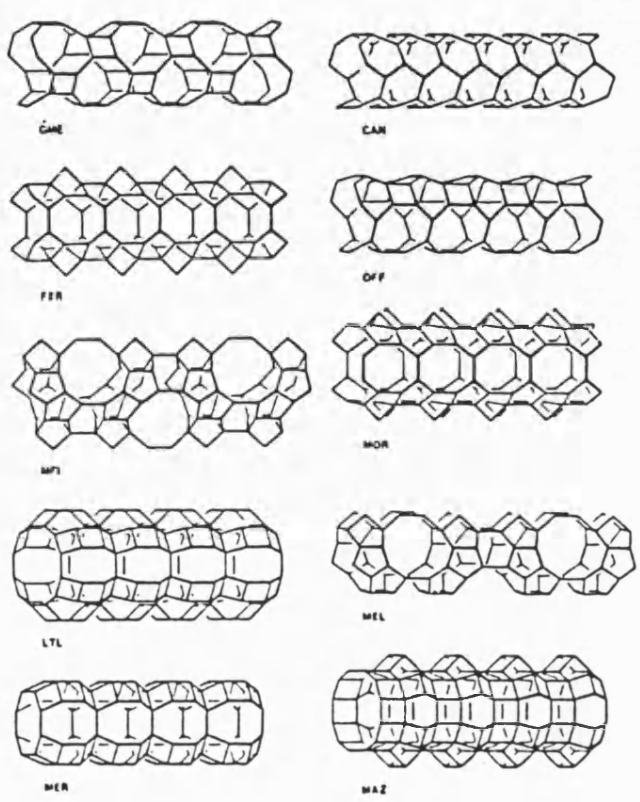

Figure 1.7: Tubular building units generated from T-T linkages in the 4-connected 3D nets of zeolites.

Many zeolite structures, when viewed in projection along one or more crystallographic directions appear as 2D 3-connected nets (Figure 1.5). The most obvious way to generate a 4-connected 3D net from a 2D net is to arrange one type of 3-connected 2D net into a parallel stack and to link each other vertex to only one another vertex. To form a 3D net some of the edges must point upward and some downward from the 2D net (otherwise a double sheet is formed). The character of the stacking of sheets along one axis is a good means of classifying many known zeolite structures. One example is the stacking of the 6-rings in the ABC-6 family, which will be discussed in greater detail in the next section.

An analysis of the enumeration of zeolite frameworks has been presented by Smith

(1979, 1988) who has investigated the great variety of zeolite structures that can be generated from 2D 3-connected nets. Recently also Akporiaye and Price (1989) developed a related method for the systematic enumeration of zeolite frameworks.

In addition to these, one approach based on the investigation of the topology of zeolite frameworks, a concept which is readily applicable to zeolite-type nets, has so far been largely overlooked, is that of co-ordination sequence and co-ordination network (Meier and Moeck, 1979, Brunner 1979, Akporiaye and Price, 1989). The same concept was under the name "Kaskadenfolgen" subsequently introduced by Fischer (1973) as a criterion in his derivation of homogeneous sphere-packing pertaining to cubic lattice complexes. This approach has been applied in this work and will be explained in further detail in chapter 7.

A summary of the essential topochemical features of selected structural types are in Table 1.2.

(a) Natural Zeolites and Related Aluminosilicates with a (4;2)-3D Net

type species	IUPAC code [a]	framework density [b]	types of rings [c]	types of chains [d]	types of 2D nets [e]	types of polyhedra	types of access [g]
Afghanite	AFG	15.9	4,6		4.6.12	canc	6-rings
Analcim	ANA	18.6	4,6,8	ts			3D-8,8,8
Cancrinite	CAN	16.7	4,6,12	zz	4.6.12	canc	1D-12
Chabazite	CHA	14.6	4,6,8,12		4.6.12	hp,chab	3D-8
Edingtonite	EDI	16.6	4,8	fi			3D-8,8,8
Erionite	ERI	15.6	4,6,8,12		4.6.12	hp,canc,erio	3D-8,8,8
Faujasite	FAU	12.7	4,6,12			hp,tp,fauj	3D-12,12,12
Ferrierite	FER	17.7	5,6,8,10	c,s	6^3;(5.6.10)	test	2D-8,10
Gmelinite	GME	14.6	4,6,8,12	cc	4.6.12	hp,gmel	3D-8,8,12
Heulandite	HEU	17.0	4,5,8,10	he			2D-8,10
Laumontite	LAU	17.7	4,6,10			laum	1D-10
Levyne	LEV	15.2	4,6,8		4.6.12	hp,levy	2D-8,8
Liottite	LIO	15.7	4,6		4.6.12	canc,liot,loso	6-rings
Mazzite	MAZ	16.1	4,6,81,2	c,ss	4.6.8.12	gmel	1D-12
Merlionite	MER	16.0	4,8	cc,bs	4.8^2	op	3D-8,8,8
Mordenite	MOR	17.2	4,5,6,8,12	c,s	6^3;(4.5.8.12)	test	2D-8,12
Offretite	OFF	15.5	4,6,8,12	ss	4.6.12	hp,canc,gmel	3D-8,8,12
Sodalite	SOD	17.2	4,6	ts		to	6-rings
Stilbite	STI	16.9	4,5,6,8,10	st		brew	2D-8,10

Table 1.2: Properties of selected microporous materials (Breck, 1973; Smith, 1988)

(b) Synthetic Aluminosilicates with a (4;2)-3D Net

type species	IUPAC code[a]	framework density[b]	types of rings[c]	types of chains[d]	types of 2D nets[e]	types of polyhedra	types of access[g]
Losod	LOS	15.8	4,6		4.6.12	canc,loso	6-rings
Linde A	LTA	12.9	4,6,8			cu,to,grco	3D-8
Linde L	LTL	16.4	4,6,8,12	ss	4.6.8.12	hp,canc	3D-8,8,12
Linde N	LTN	15.2	4,6,8			hp,canc,to,grco	6-rings
ZSM-11	MEL	17.7	4,5,6,7	p	(5.6.10)	test,mel,pent	3D-10,10,10
ZSM-5	MFI	17.9	4,5,6,7,8,10	p	(5.6.10)	test,pest,pent	3D-10,10,10
Nepheline		18.6	4,6,8	s,z,zz	6^3;4.6.8	hest	1D-8
Rho	RHO	14.3	4,6,8			op,grco	3D-8,8,8
Theta-1	TON	19,7	5,6,8,10	z	6^3;(5.6.10)	pest	1D-10

Table 1.2 (continued)

[a] IUPAC three-letter code assigned by International Zeolite Association Structure Commission.

[b] The framework density is expressed as the number of T sites per 1000Å^3. In some zeolites, the framework density can vary several percent in response to dehydration, change of Si/Al ratio, and ion exchange.

[c] Only the more obvious rings are listed in frameworks with comples connectivity.

[d] Only the simpler chains are listed.

[e] Only the simpler 3-connected 2D nets are listed. e Channels with access limited by 8-rings or larger windows are listed with the number of directions (1D, one-dimensional; 2D, two-dimensional; 3D, three-dimensional) and the rings size of the limiting windows.

1.4.3. ABC-6 zeolite structures

Different zeolite structures may be constructed from different stacking sequences of the same two dimensional layer structures. We will illustrate the development of 3D 4-connected structures by considering the different ways that structures can be built by arranging parallel 6-rings.

The ABC-6 (A, B and C are positional symbols) share the S6R or the D6R (see Figure 1.6), dependent on the stacking sequence, as a SBU (Figure 1.8). The simplest structures are based upon linking a 6-ring (labelled A) to another 6-ring vertically superimposed, resulting in a hexagonal prism or D6R (AA-sequence). Alternatively rings can be linked to adjacent, horizontal 6-rings through a tilted 4-ring, which can be denoted as AB-sequence (Figure 1.8). The third layer can be positioned above the first AAA or ABA, the second AAB or ABB, or it can be another adjacent 6-ring connected through a tilted 4-ring (C-sequence). The next, fourth layer must then stack over the A, B or C position.

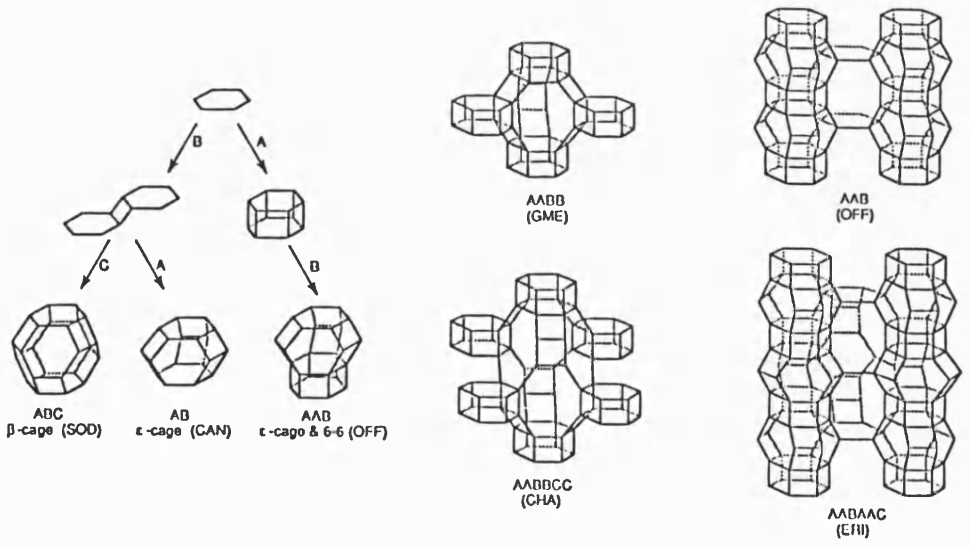

Figure 1.8: Schematic illustration of different stacking sequences of the ABC-6 zeolites.

The change of horizontal positions can involve either a clockwise operation (c) or an anti-clockwise (a) one and a tilted 4-ring is involved in both operations. The alphabetical order A → B, B → C, C → A is clockwise and A → C, C → B, B → A is anticlockwise. Because of the mirror symmetry there is no topological difference between a particular sequence and its a→c equivalent. Furthermore, the direction and starting point are meaningless (Newsam, 1990).

The centres of the hexagons and the hexagonal prisms are connected topologically in the same pattern as the centres of close-packed spheres in hexagonal structures (Breck, 1973). There is a whole family of related zeolitic structures of similar chemical composition with 6-membered rings that are stacked in 3 different ways along the hexagonal c-axes, giving rise to an almost infinite number of framework structures. Some of them are natural zeolites like cancrinite (AB), erionite (AABAAC), offretite (AABAAB) or sodalite (ABC), some of them are hypothetical structures like AAAB or AAAAB which have never been observed.

Included into this group is sodalite with a cubic ABC-sequence. The cubic symmetry is a result of the close packing of inter-connected six fold rings. These 6-rings are stacked parallel to {111} in an ABC type of sequence (Smith and Bennett, 1981).

Some stacking sequences are listed in Table 1.3.

If only two types of sequences are present (e.g. A and B) in a structure in any order, they will have large open channels in the c - direction. On the other hand, if ABC stacking is present, there will be large and small cages with 12-membered ring apertures, effectively blocked, depending on the precise sequence present (Figure 1.9).

Name	Abbr.	Space group	c-axis (Å)	Stacking sequence	No.of layers
Afghanite	AFG	P63/mmc	21.4	ABABACAC	8
Cancrinite	CAN	P63/mmc	5.1	AB	2
Chabazite	CHA	R$\bar{3}$m	15.1	AABBCC	6
Erionite	ERI	P63/mmc	15.1	AABAAC	6
Gmelinite	GME	P63/mmc	10.0	AABB	4
Levyne	LEV	R$\bar{3}$m	23.0	AABCCABBC	9
Liottite	LIO	P$\bar{6}$m2	16.1	ABABAC	6
Losode	LOS	P63/mmc	10.5	ABAC	4
Offretite	OFF	P$\bar{6}$m2	7.6	AAB	3
Sodalite	SOD	I$\bar{4}$3m	7.5	ABC	3
I			20.0	AABBCCBB	8
II			30.0	AABBCCAACCBB	12

Table 1.3 : Some possible zeolite structures from 6-rings; the structures I and II are unknown proposed structures, which are based upon arrangements of double 6-rings (Breck, 1973)

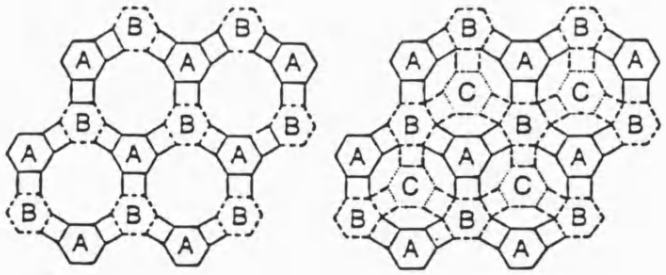

Figure 1.9 :Projection of stacking sequences along the c-axis; the AABB sequence (a) is characterised of gmelinite and the AABBCC (b) arrangements is characteristic of chabazite.

There are many structural complexities in the observed ABC-6 zeolites and intergrowths between structure types are common. Offretite (AABAAB) and erionite (AABAAC) were not originally distinguished as separate minerals, but combined X-ray and electron optical studies have revealed the ideal stacking sequence (Bennett and Gard, 1967; Kokotailo et. al. 1972; Gard and Tait, 1972). Levyne (AABCCABBC) occurs intergrown with offretite (Sheppard et al, 1974) and channel systems are compared for levyne and related zeolites in Barrer and Kerr (1959). Gmelinite with the ideal AABB stacking show frequent stacking faults (Fischer, 1966) which are presumed to be mainly of AABBCC type.

There is increasing experimental evidence (Thomas, 1989) to suggest intergrowths of two or more different, yet related framework structures. An example is zeolite L and offretite (or erionite). Figure 1.10 shows various types of intergrowths.

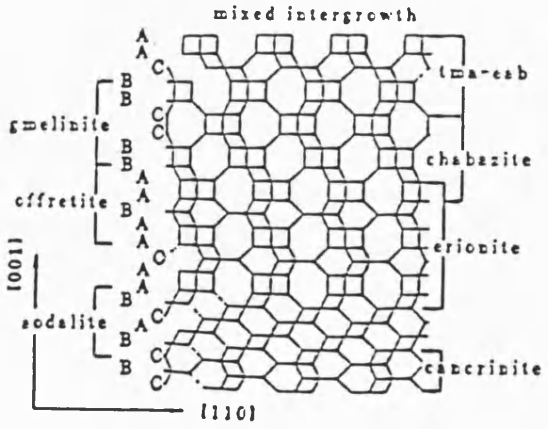

Figure 1.10: Various types of intergrowths occur, often at the subunit-cell level, in the ABC-6 family of zeolites.

1.5. Properties and applications of zeolites

The properties of zeolites are structure related, being governed by framework-topology, composition, channel dimensions, the presence, location, size of charge compensating groups within the framework, the presence of faults and occluded material. Therefore, structural information is very important in the understanding of the properties of zeolites.

1.5.1. Ion-exchanger

As mentioned in previous sections the net negative charge of a zeolite framework is balanced by the presence of charge compensating cations. The exchangeable cations of a zeolite are only loosely bonded to the framework and can be removed or exchanged easily by washing with an appropriate salt solutions or molten salt.

The maximum ion-exchange capacity is determined by the framework Si:Al ratio, although the actual capacity may be lower if a proportion of the cations are trapped within small, inaccessible cages.

In practice, however, the cation-exchange behaviour is dependent on a number of other factors as well, including (i) the nature of the cation species (size, charge etc.), (ii) temperature, (iii) concentration of the cation species in solution, and (iv) the structural characteristics of the particular zeolite under investigation (Flanigen and Mumpton, 1981).

The main areas where zeolites find applications as ion-exchanger are in radioactive waste water treatment, water purification, and agricultural, horticultural and medical uses. Natural zeolites such as clinoptilite or mordenite are mainly used. Synthetic zeolite A

has been widely used as a partial replacement for sodium tripolyphosphate (STPP) in low phosphate detergents. Zeolite A performs as a filler and exchanges Ca^{2+} and Mg^{2+} cation out of washing water (Newsam, 1990).

1.5.2. Catalysis

In the presence of certain zeolites, hydrocarbons may undergo one or more of a number of reactions: isomerisation, disproportionation, cracking, polymerisation and alkylation. The catalytic properties depend on chemical composition and acidity, zeolite structure and various pretreatments which may change locally the catalytically active sites in the zeolite.

The catalytic activity of zeolites is due to the high density of strong acid sites of Lewis and Brønsted activity. Figure 1.11 is a schematic representation of their formation.

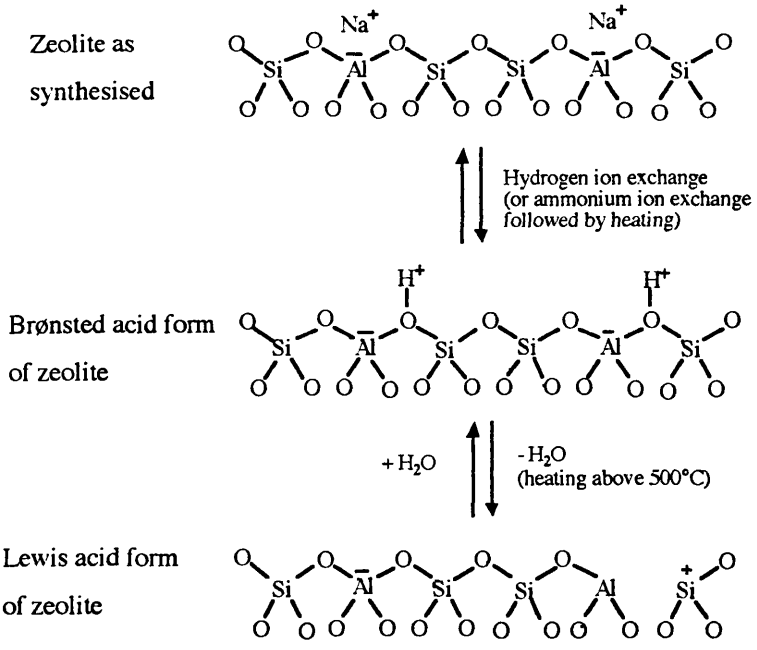

Figure 1.11: Schematic representation of Brønsted and Lewis acid sites in zeolites.

The acidity arises from the AlO_4 tetrahedra and thus to be reflected in catalytic properties. In fact, relative catalytic activity at first rises with Si:Al ratio, reaches a maximum between 8 - 40 and then declines. This behaviour has been interpreted as the operation of two opposing effects: increasing the Si:Al ratio raises the acidic strength, but decreases the number of available sites (Barthomeuf, 1984).

Most of the acidic catalytic reactions are related carbonium ion intermediates (Gates et al, 1979) are formed which can then participate in polymerisation, isomerisation and cracking.

Catalytic cracking is the process by which heavier components of crude oil or large hydrocarbons are converted into lower molecular weight fragments or smaller molecules, such as those are used in gasoline (Venuto et al, 1979). This process occurs via carbonium ion chemistry and is, therefore, catalysed by solid acid catalysts. The strong adsorption forces of the zeolite concentrate the substrate at the active site, favouring bimolecular reactions.

Chemically the reaction mechanisms are not fundamentally different from other acid catalysed reactions but the nature of zeolite structures results in specific catalytic activity.

Synthetic zeolites based on Zeolite Y whose pores (12Å) are sufficiently large to offer virtually no steric restrictions to most reagents, were first developed for catalytic cracking applications in the early 1960's (Venuto et al, 1979).

However, with the small and intermediate pore zeolites shape selective catalysis is observed. Csicsery (1976) and Weisz (1980) reviewed shape selectivity effects in catalysis and identified three types:

Reactant Selectivity (Dewaxing, M-forming) is found when the zeolite channels restrict

the reactant molecules, so that not all the potential reactants reach the active site (Figure 1.12 a). The conversion of alcohol to olefinic product over zeolite A (5A) is a good example for reactant selectivity under conventional conditions, the secondary alcohols form the more stable carbonium ions, and, therefore convert under acid catalysed conditions to olefins much more rapidly than the primary alcohols. Using reactant selectivity method, only the primary alcohols can reach the active acid sites and undergo relatively rapid conversion. The higher alcohols, are excluded and therefore effectively inert.

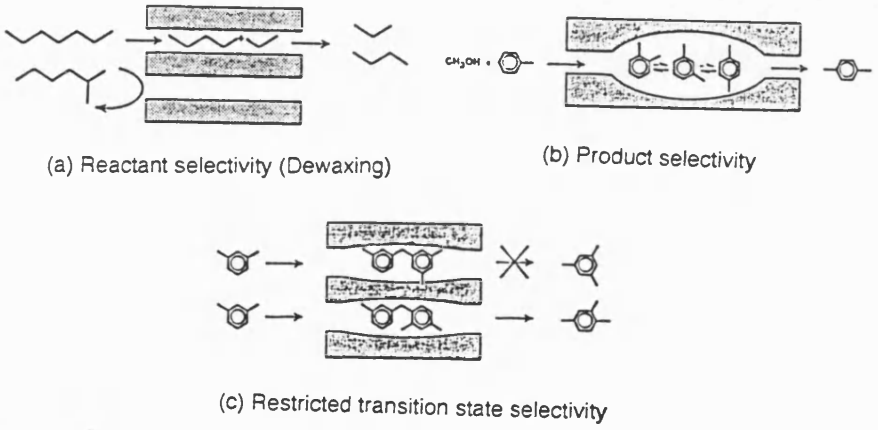

Figure 1.12: Idealised representation of typical shape selectivity effect in zeolite catalysis

Product Selectivity occurs when similar restrictions apply to the product molecules (Figure 1.12 b) so that only those molecules with appropriate geometric dimensions can diffuse out.

Restricted Transition State Selectivity takes place when certain reactions are inhibited due to geometric constraints on possible transition states. Thus reaction pathways leading to geometrically appropriate transition states are favoured (Figure 1.12 c). The

most important example of restricted transition state-type selectivity is the absence (or near absence) of coking in ZSM-5 type zeolites. Coking is less severe in ZSM-5 than in larger-pore zeolites because the pores are small enough to inhibit the polymerisation of precursors (Csicery, 1984). Coke formation is detrimental to catalytic activity.

Through the use of appropriate framework configurations, size constraints can limit the maximum size of the produced hydrocarbons, to be in the range suitable for petrol. In 1976 Meisel et al discovered that ZSM-5 could convert methanol to gasoline. The acidic catalytic properties of the zeolite effectively eliminate a molecule of water from the methanol. The carbene may be stabilised by the zeolite before it is inserted into another methanol molecule. The overall reaction scheme is as follows:

$$x\,CH_3OH \xrightarrow{\text{ZSM-5}} (CH_2)x + x\,H_2O \qquad (x= 4\text{-}10)$$

The commercial viability of the evolution of CH_3OH to olefinic and ultimately aromatic products on this acid zeolite arises in part from the intracrystalline constraints that limit the production of aromatic species larger than C_9 or C_{10} and hence reduce greatly de-activation via coke formation (Newsam, 1990).

Catalytically active metal species can also be introduced into a zeolite host by ion-exchange and subsequent hydrogen reduction. Zeolites are used increasingly in bi-functional catalysis; two types of active sites are presented: metallic sites whose function is to hydrogenate and dehydrogenate, and acid sites whose function is to crack or iso-merise. Zeolites containing palladium and platinum are used in hydrocracking, a process in which inferior fractions of crude oil are converted into valuable products such as jet

fuel and diesel oil.

1.5.3. Sorption

After dehydration the zeolite is a crystalline solid permeated by micropores, which fill and empty reversibly during adsorption. Molecules having effective cross-sectional diameters small enough to pass through the entry channels are readily adsorbed in the dehydrated energetically favourable sites of the channels and central cavities. Molecules too large to pass through the entry channels are excluded, giving rise to the well-known "molecular sieving" property of most zeolites.

Molecular sieves are able to discriminate between molecules on the basis of their size and shape. Todays applications are in one sense not strictly sieving (where the zeolites permits ongoing passage of the smaller component). Rather, processes are cyclical. After sorbing a component it is subsequently removed in a separate reactivation step. A reduction in external pressure (Pressure Swing), an increase in temperature (Thermal Swing) or the use of a desorbent such as ammonia are used commercially for this reactivation step (Flanigen and Mumpton, 1981; Newsam, 1990).

The adsorptive properties may be altered by a number of factors: Si:Al ratio, presence of certain cations and temperature effect.

Changing the Si:Al ratio from 3.0 to 1.18 increases the lattice constant from 24.60 to 24.95Å (Whan, 1981).

Highly siliceous zeolites are hydrophobic and can remove organic molecules from aqueous solutions. This hydrophobic feature is widely used as desiccants in laboratory scale applications, and, commercially for drying gas steams.

An increase in temperature allows larger molecules to be admitted into zeolites due to increased amplitude of lattice vibrations. In addition, the increased thermal energy of the diffusing molecule enables it to surmount the energy barrier created by the aperture (Newsam, 1990).

The application of sorption can be divided into two categories: purification, which depends on the surface selectivity for polar and polarisable molecules and bulk separations, many of which are based on molecular sieving properties.

Molecular sieving is a good example of how structure on an atomic scale can determine macroscopic properties, and how a detailed knowledge of structure can enable prediction of performance.

1.6. Synthesis of Zeolites

Zeolites are unique as crystalline porous materials, with structure as well as composition, controlling their properties. R. M. Barrer demonstrated in the 1940's and 50's that a series of zeolitic materials could be synthesised under hydrothermal conditions (Barrer, 1982; Breck,1973).

A review by Milton (1968) traced the early discoveries and synthesis of zeolite A, X and Y in the 1960's. Both zeolites, A and X have a high aluminium content; but the development of the more siliceous zeolite Y, resulted in a unpredicted effect on properties. This provided the base to synthesise even more siliceous zeolites.

Zeolite crystallisation occurs in alkaline aqueous gels, usually under autogenous

pressure, for a period of between a few hours to several weeks, at a temperature range from 60 to 200°C. The gels are normally composed of a source of silica and alumina, cations and organic bases. The source employed for silica and alumina effects the framework compositions and the cation is often a dominant factor in controlling the formations of specific structures (Flanigen, 1973).

Flanigen (1983) suggested that the nucleation process in low silica zeolites involves the formation of stabilized cation-aluminosilicate complexes, and is primarily controlled by aluminosilicate solution chemistry. The cations stabilise 4- and 6-membered rings and cages, the main structural features of low silica zeolites.

Barrer et al (1961a) first reported the use of organic (and inorganic) species in the form of alkylammonium cations in synthesis gels. This led to an increase in the framework Si:Al ratio which initially generated more siliceous framework compositions of known structures. The subsequent use of alkylammonium ions produced new structures with Si:Al ratios of 2 to 5. Mobil began using other nitrogenous organic molecules, such as tetrapropylammonium, which ultimately led to the formation of high-silica zeolite materials such as ZSM-5 (Argauer & Landolt,1972). The addition of alkylammonium cations to pure silica systems resulted in silica molecular sieves such as Silicalite-1 (Flanigen el al, 1978). The organic molecules may be liberated from the zeolite by high temperature treatment with no change of the framework topology.

In addition to altering the framework composition, organic (and inorganic) cations can lead to different zeolite structures. This "templating effect" has been discussed by Rollman (1979).

An alternative method of producing high siliceous zeolites is via the process of dealumination. One of the most widely used technique is the treatment of a zeolite with $SiCl_4$. Thomas et al (1983) dealuminated ZSM-5 with $SiCl_4$ vapour and showed the re-

sulting higher silica ZSM-5 to be isostructural with Silicalite-1. Dessau and Kerr (1984) have also shown that it is possible to reincorporate tetrahedra aluminium into very high-silica zeolites by treatment with $AlCl_3$ at high temperatures.

Neutral organic additives, such as n-propyamine have been used successfully in ZSM-5 synthesis, and also a series of microporous silicas (porosils or clathrasils) can be crystallised hydrothermally in the presence of neutral organic components. A large number of organic bases and amines as well as linear polyelectrolytes, alcohols, ketones etc. have been tested in various zeolite synthesis.

1.7. Physical Characterisation of zeolites

In this section an overview of the techniques employed in zeolite chemistry is given. These techniques are complementary and subsequent chapters will show that also computer-simulation is a further valuable technique in the understanding of zeolite structures and properties.

The scope includes aspects such as structure determination, framework ordering, sizes and shapes of crystals, pore sizes, void volumes and acidity.

1.7.1. Diffraction methods

Zeolite are crystalline and, therefore, diffraction methods are central to attempts to characterise atomic level-structure. The most frequently used method for identifying and

describing as zeolite structure, is by X-ray powder diffraction. Many zeolites have a similar chemical composition but differ structurally. The position and intensities of peaks in the powder X-ray diffraction pattern are therefore a basis for phase identification and definition.

Certain structural characteristics as i.e. cell dimensions, space group and atomic parameters (coordinates and temperature factors) can be probed by conventional single crystal X-ray diffraction, using as many Bragg reflections as possible. Pure single crystals of at least 20-50 μm are required but their preparation is difficult (Lechert, 1983). Careful manipulation of synthesis conditions has allowed the formation of larger crystals (<100μm) of a small number of synthetic zeolites such as zeolite A, Faujasite and ZSM-5, although particle sizes < ~ 5μm are more typical.

Synchrotron X-ray facilities offer significant advantages. It permits conventional measurements to be made on much smaller particles, and phase identification allows more complicated structures to be refined using Rietfeld methods and enhancing the possibilities for *ab initio* structure solution (Newsam, 1990). As a recent example Toby et al (1988) carried out a first refinement of the zeolite structure ZSM-11.

Fischer (1973) described problems associated with structure determination. One of these difficulties arises because X-ray scattering factors of silicon and aluminium are very similar due to the similarity of their surrounding electron density. Consequently the distribution of these atoms in the framework appears random resulting in the space group having a higher symmetry than it actually should. Si...O and Al...O may be distinguished in an ordered structure by differences in bond lengths.

The lattice parameters of zeolites vary with the degree of Al^{3+} substitution for Si^{4+} (Breck, 1973). Bibby et al (1981) were able to determine the aluminium content in ZSM-5 from the X-ray powder pattern using an empirical relationship in which the spacing

between to peaks varied inversely with the aluminium content.

To overcome some of the limitations of X-ray methods, i.e. distinguishing Si, Al and/or P, locating H^+ or Li^+, determine water or hydrocarbon sorbate configurations or measurements under non-ambient conditions, use is being made of neutron diffraction. The size of samples required for single crystal neutron diffraction are large (at least 1x1x1 mm) and relative to X-ray methods much longer exposure times are required. Despite these disadvantages powder neutron diffraction is a more attractive prospect for zeolite structures. The application of powder neutron scattering shows that the lengths of Si and Al are significantly different (Bacon, 1975), and the positions of "light" atoms in structures containing heavier elements can be determined more accurately. Structural refinements can be performed from powders using Rietveld profile analysis (Rietveld, 1969).

The first powder neutron diffraction study appeared in 1967 (Jirak et al, 1977) although those studies were restricted to cubic materials. Recent applications (Newsam, 1987) include lower symmetry materials and more complicated structures. Work on a series of gallosilicates has provided data on the effects of framework cation substitution. Several studies gave information about non-framework aluminate species generated by framework dealumination. Cheetham et al (1984) have also shown, using neutron diffraction, the location of hydrogen atoms in lanthanium zeolite Y. This provides evidence for cation hydrolysis and Brønsted acidity, both important factors in the catalytic activity of a zeolite.

Neutron diffraction, which yields the position of nuclei, can be used as a technique to complement X-ray diffraction, which produces the corresponding electron distribution.

1.7.2. Spectroscopic Methods

Zeolite elemental composition are generally analysed by microprobe, by inductively coupled plasma spectroscopy (ICPES) or by atomic absorption spectroscopy (AAS).

Electron microprobe analyses allows a quantitative analysation of elements with atomic numbers down to 8 (oxygen). The scanning transmission electron microscope offers an effective spatial resolution of the order of 100Å and therefore permits a full elemental analyses of discrete microcrystallites.

Using the ICPES or AAS method we get a bulk chemical analyses of a zeolite. These methods yields to averaged sample composition and do not distinguish between zeolite framework constituents and detrital or second phase material.

Spectroscopic techniques, like infrared- or Raman-spectroscopy and nuclear magnetic resonance (NMR) are being increasingly applied to zeolites. These methods have proven to be quite versatile, finding applications not only in structural and framework problems, but also in sorption and catalysis.

Infrared spectroscopy is usually used for identifying various functional groups that are present in a given sample by their different characteristic stretching and bending frequencies. Conventional infrared- and Raman-spectroscopy are sensitive to local structural features, but interpretations are generally limited to relatively simple dynamical models of framework vibrational modes (Cheetham & Day, 1987).

In zeolite structural applications it is normally used in situations where no unambiguous X-ray pattern can be obtained. A typical spectra of the aluminoslicate lattice is the so-called mid-infrared region of 400-1300 wavenumbers. Two types of vibrations exist in this region (Flanigen, 1976): internal vibrations which belong to the Si/AlO_4 - they are structure insensitive - and external vibrations, which are structure sensitive and depend

on the type of linkage of a TO_4 tetrahedron (T = Si or Al) in a given framework topology.

The infrared- and Raman spectra of silicate minerals, particular those of geological importance, e.g. forsterite, have been extensively studied (Wall and Price, 1988). Increasingly there have been infrared studies of zeolites particularly with a view to use this technique for characterisation (van Beest et al, 1989). Recent work by de Man et al (1990) has demonstrated the scope of lattice dynamics in modelling not only the infrared frequencies but also their intensities.

The technique which has a very great impact on zeolite chemistry is high resolution solid state nuclear magnetic resonance spectroscopy (NMR) with magic angle spinning (MAS). It is possible to study all primary zeolite constituent by NMR. Proper calibration of NMR signals intensities provides, in principle, one analysis method (Newsam, 1990).

The ability to create high magnetic fields using superconducting magnets led to an increase in both the sensitivity of the detection and the chemical shift of nuclei in different chemical surroundings. High resolution NMR has been widely applied to chemical species in solution. Solid-state spectra are dominated by direct dipole-dipole interactions of the nuclei which results in broad, featureless spectra. The Hamiltonia discribing this coupling contains a $(3\cos^2\theta - 1)$ term and by spinning the sample about an axis inclined at the so called "magic angle" of 54°44´to the magnetic field vector this term becomes zero (Fyfe et al, 1983). Hence the dipole-dipole interactions are reduced to a sufficiently low level to be able to detect the chemical shifts of nuclei in different local environments.

Engelhardt et al (1979) showed the result of the deshielding influence of aluminium, using the ^{29}Si resonance technique. A typical zeolite X spectra consists up to five peaks (separated by about 4.5ppm), corresponding to the five possible local environments, Si (nAl) where n can vary between 0 and 4. They were also able to assign characteristic ranges of chemical shifts for each configuration of nAl surrounding one Si. An

experiment on zeolite X (Si:Al = 1) gave one peak in the spectrum corresponding to Si (4Al). This indicated strict ordering of Si and Al on alternate tetrahedral sites which agrees with Loewensteins rule (section 1.4.).

Thomas et al (1982b, 1982c) have shown how MAS-NMR may also be used to determine the Si:Al ratio of zeolites.

Another MAS - NMR experiment can be undertaken using the ^{27}Al resonance technique. It was shown by Fyfe et al (1982) that ^{27}Al NMR can be used to analyse the relative amounts of aluminium in framework and extra-framework environments. Fyfe et al (1984a) monitored the dealumination with $SiCl_4$ of ZSM-5 into Silicalite-1, the ^{27}Al spectrum indicating that the aluminium atoms are in tetrahedral coordination.

MAS - NMR can be also used to study the effect of sorbate molecules in zeolite. Using the ^{29}Si MAS - NMR technique this effect was on the spectra of ZSM-5 by Fyfe et al (1984b). It was found that structural changes causing lattice distortions were occurring which were characteristic of the adsorbate used. These changes were found to be reversible on the removal of the sorbate.

Junger et al (1982) used ^{13}C and ^{15}N NMR to study the adsorption properties of exchangeable cations in various cation-exchanged zeolites, using acetonitrile as the probe molecule. A study by Lunsford et al (1985) used the ^{31}P resonance with MAS to study the interaction of trimethylphosphine with acid sites in zeolite Y.

Most non-framework species are also accessible by NMR. Water, hydrocarbon sorbates and templating species have been studied by ^{1}H, ^{13}C and ^{2}H (deuterium) NMR (Newsam, 1990).

Two other methods which should be mentioned are electron spin resonance spectroscopy (ESR) and Mössbauer spectroscopy. Electron spin resonance spectroscopy is used to investigate transition metals and transition metal complexes and Mössbauer spectroscopy is for example employed to investigate iron in its different oxidation states and local environments (Rees, 1982).

II. STRUCTURE AND PROPERTIES OF ALUMINOPHOSPHATES

2.1.Introduction to aluminophosphate chemistry

A novel class of crystalline, microporous aluminophosphate phases has been discovered in the early 1980's that represents the first family of framework oxide molecular sieves synthesised without silica. The materials are designed as compositional families e.g. $AlPO_4$-n, SAPO-n, MeAPO-n, MeAPSO-n, where n denotes a specific type of framework topology that is the same across various families. The aluminophosphate-based molecular sieves are an important new class of catalysts and adsorbent materials.

2.2. Composition of aluminophosphates

The aluminophosphates with the Al/P = 1 form a subgroup of the wide range of phosphates. The Al and P positions of each 1:1 aluminophosphate structure can be related to alternating nodes of a 4-connected 3D net. The framework Al and P alternating on the tetrahedral sites and some of the structure types are similar to those of the aluminosilicate zeolites.

In general hydrated $AlPO_4$-n can be presented by the empirical formula:

$$[AlPO_4] \quad yR \quad nH_2O$$

where R can be an organic amine or a quaternary ammonium salt which becomes entrapped or clathered within the crystalline products and y and n represents the amount needed to fill the microporous voids within the neutral framework. The framework can be considered comprised of $[AlO_2]^-$ and $[PO_2]^+$ units, strictly alternating and therefore the $AlPO_4$-n framework is neutral.

The crystal chemistry of $AlPO_4$-n is different from that of the zeolites for several reasons:

(a) The $AlPO_4$ moiety of the aluminophosphate structures is electrostatically neutral in contrast to the $Al_xSi_yO_{2x+2y}$ moiety of the zeolites. AlPO4-n structures have no compensating cations like Ca or Na and therefore there is no equivalent to the characteristic ion-exchange properties of the zeolites.

(b) In contrast to the strict occurrence of four-coordinated Al in the zeolite framework, the Al atoms of the 1:1 aluminophosphates have either 4-, 5- or 6 near oxygen neighbours. 5- and 6- coordinated Al occur in several anhydrous aluminosilicates like andalusite and kyanite. This range of coordination generates and additional geometrical and electrostatic flexibility which favours the adoption of new structure types not represented by zeolites. Recently synthesised aluminophosphates having partly 5- and/or 6- coordinated Al-atoms are $AlPO_4$-21 (Bennett et al, 1985) and $AlPO_4$-CJ2 (Yu et al, 1990).

(c) In all 1:1 aluminophosphate structures P and Al alternate around the tetrahedral nodes

of the four-connected nets. This contrasts with the zeolites for which there is a wide range of Al/Si ratio and order/disorder phenomena.

(d) Zeolites are hydrophilic due to the interaction of the dipole of the water molecule with the electrostatic fields of the anionic aluminosilicate framework and the balancing non-framework cations. But silicalite, with a neutral SiO_2 framework and no extra-framework cations is hydrophobic. In contrast, the neutral aluminophosphate frameworks with no extra-framework cations are moderately hydrophilic, apparently due to the difference in electronegativity between Al (1.5) and P (2.1). They exhibit less affinity for H_2O than the hydrophilic zeolites like zeolite A and X yet substantially more than hydrophobic silicalite.

2.3. Structure and topology of aluminophosphates

The new family of aluminophosphate materials currently includes about 30, 3-D framework structures, most of which are microporous and some 2-D layer type materials. Most of the 3-D structures are novel; however some appear to be structurally related to the zeolite family. $AlPO_4$-17 with the framework topologies of the erionite/offretite type (Smith et al, 1981; Pluth et al, 1986), $AlPO_4$-20 the sodalite type (Smith et al, 1981) and $AlPO_4$-24 the analcime type.

Three structures (berlinite, $AlPO_4$-cristobalite, $AlPO_4$-tridymite) are analogues of the well known polymorphs of silica (quartz, cristobalite and tridymite) and it is presumed

that the Al and P alternate in the latter two varieties as they do in berlinite (Schwarzenbach, 1966).

Some of the novel structures are $AlPO_4$-5, $AlPO_4$-8 and VPI-5 (Virgina Polytechnic Institute No. 5). $AlPO_4$-5 (figure 2.1) has a large pore opening, a 12-ring which circumscribes unconnected cylindrical channels parallel to the c-axis (Bennett et al, 1983). $AlPO_4$-8 is a 14-ring molecular sieve (Dessau et al, 1990) and VPI-5 is the largest molecular sieve with containing a one-dimensional channel, circumscribed by 18 tetrahedral atoms (Davies et al 1989).

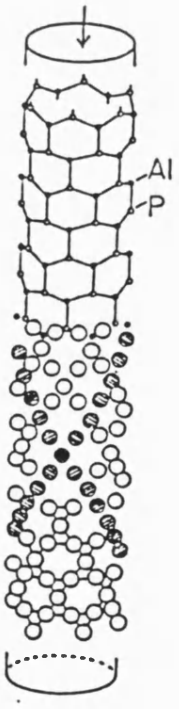

Figure 2.1: The topological descriptions of the cylindrical channel in $AlPO_4$-5 net.

(a) Synthetic Aluminophosphates with a (4;2)-3D Net

type species	IUPAC code[a]	framework density[b]	types of rings[c]	types of chains[d]	types of 2D nets[e]	types of polyhedra	types of access[g]
$AlPO_4$ -5	AFI	17.5	4,6,12	c	4.6.12	afi	1D-12
$AlPO_4$ -11	AEL	19.1	4,6,10	c	4.6.10	afi	1D-10
$AlPO_4$ -16	AST	16.7	4,5			cu,trd	6-rings
$AlPO_4$ -25	AFT	19.7	4,6,8	cc	4.6.8		2D-8,8
$AlPO_4$ -33	ATT	16.7	4,6,8	c,cc,ss	4.6.8		2D-8,8
$AlPO_4$ -46	AFS	13.7	4,6,8,12	esc	4.6.12	afo,afs,af	3D-8,8,12

(b) Other Aluminophosphates that can be related geometrically to a (4;2) - 3D Net

$AlPO_4$ -14		4,6,8	odc	4.8^2	odc
$AlPO_4$ -15		4,8		$4,8^2$	odc
$AlPO_4$ -EN3		4,6,8	z	4.6.8	
Variscite		4,6	c	6^3	
Meta-Variscite		4,6	c	6^3	laum

Table 2.1: Properties of Selected Microporous Materials

[a] IUPAC three-letter code assigned by International Zeolite Association Structure Commission.

[b] The framework density is expressed as the number of T sites per 1000$Å^3$. In some zeolites, the framework density can vary several percent in response to dehydration, change of Si/Al ratio, and ion exchange.

[c] Only the more obvious rings are listed in frameworks with comples connectivity.

[d] Only the simpler chains are listed.

[e] Only the simpler 3-connected 2D nets are listed. e Channels with access limited by 8-rings or larger windows are listed with the number of directions (1D, one-dimensional; 2D, two-dimensional; 3D, three-dimensional) and the rings size of the limiting windows.

At a fundamental level, aluminophosphate structures can be related to a four connected net. Each P-atom shares an oxygen atom with each of four adjacent Al atoms at ~3Å. Al can also interact with one or two extra-framework oxygens (OH, H_2O). The Al-P alternation does not allow the occurrence of 5-ring units, therefore the $AlPO_4$-n structures are mainly constructed from 4- and 6- ring units.

A summary of the topochemical features of selected structural types are in table 2.1.

2.4. Synthesis of aluminophosphates

The synthesis process yield structures which contain a large proportion of open space in the from of cages and channels. These are accessible to small molecules such as hydrocarbons, water, oxygen and nitrogen. Furthermore, the composition of the framework results to a highly acidic and reactive medium. These two factors of restricted accessibility and high acidity make $AlPO_4$-n immensely important in the chemical industry as chemical catalysts, drying and separating agents.

Despite their importance, there is a poor understanding of the factors that govern aluminophosphate crystal growth. To date most advances in $AlPO_4$-n development have been achieved by "trail and error" changes in the synthesis procedure.

The aluminophosphates are synthesised hydrothermally at 100-250℃ from reaction mixtures containing an organic amine or quaternary ammonium salt (Wilson et al, 1982). Gels are formed by adding an organic templating agent to a mixture of an active form of

alumina (typically CATAPAL - approximately Al_2O_3 $1.5H_2O$), orthophosphoric acid (H_3PO_4) and water. The pH of such gels (5-8) is notably much lower than those typically in aluminosilicate zeolite synthesis. The character of the synthesis products is determined largely by the nature of the organic additive, although the degree of specificity associated with a particular templating species varies considerably (Newsam, 1990).

The direct relationship between a templating agent and the resulting structure is illustrated in the synthesis of $AlPO_4$-17 (Pluth et al 1986). by using quinuclidine, neopentylamine or cycloheylamine. In each case chemical analysis corresponds to two template molecules per large cavity. Model building experiments indicate that (a) the three templating agents are similar size, (b) two template molecules essentially fill the large cavity and (c) there are no further voids in the erionite-type structure of sufficient volume to contain these templates. Similarly, TMAOH (tetramethylammonium hydroxide) templates the $AlPO_4$-20 sodalite framework topology (Wilson et al 1982, 1984). Some structures are much less template specific. $AlPO_4$-5 can be synthesised with 23 different amine and quaternery compounds. The large one-dimensional channel perhaps imposes fewer constraints on the template fit and because of the framework neutrality the template is not needed as a charge-balancing agent, therefore its incorporation into the structure is more a function of its size and shape relative to the channel volume to be filled (Bennett et al, 1986).

Recently Davis et al (1988) published the synthesis of a new structure type, called VPI-5, an 18-ring $AlPO_4$ material. VPI-5 can be synthesised by using n-dipropylamine or by using tetrabutyl ammonium hydroxide, n-dibutylamine or n-dipentylamine as templating agent at 423K (Davis et al, 1989). Since the report of the synthesis procedure for VPI-5 many workers have attempted a reproduction. A major problem proved to be

the unwanted formation of an impurity phase, $AlPO_4$-8, already described in the first Union Carbide patent (Wilson et al). $AlPO_4$-8 a 14-ring molecular sieve can be synthesised from identical gel composition. The differences between the synthesis of VPI-5 and $AlPO_4$-8 are only with respect to the aging and longer crystallisation period required, respectively, in the two cases (Prasad et al, 1990). Thus, all synthesis factors are common for both synthesis and the end products should therefore have the same identity. VPI-5 was found to transform to $AlPO_4$-8 upon heating to temperatures between 373 and 473K in the presence of moisture and low heating rate. This transition was also found to be reversible (Vogt et al, 1990). Phase transitions occurring in aluminophosphate molecular sieves have been described before (e.g. transition of $AlPO_4$-21 to $AlPO_4$-25 and $AlPO_4$-23 to $AlPO_4$-28 (Wilson et al)), but reversibility of a transition between two aluminophosphate molecular sieves has not been previously reported.

III) ATOMISTIC SIMULATION TECHNIQUES

3.1. Introduction

In solid state studies computer modelling techniques have achieved a high degree of precision in calculating energetic and dynamic properties. Atomistic simulation techniques have been successfully used to predict crystal structures, elastic constants, lattice dynamics, defect energies, phase transitions for a range of ionic and semi-ionic materials (Catlow et al, 1986; Parker et al, 1989, Matsui et al, 1984; Wall et al, 1986; Price et al 1988).

Computer simulation studies are also playing an increasing role in several aspects of zeolite chemistry. To name some of them, the calculations can be used to predict (i) framework structures and stabilities, (ii) the position of extra framework cations (iii) the location of sorbed molecules and (iv) reaction pathways of sorbed molecules (using quantum mechanical methods).

The primary motivation for computer simulation arises from the difficulties in experimental investigations. These difficulties are due first to the large number of parameters to be determined in structural studies of such systems and secondly from the large variety of mechanisms contributing to physical properties, such as spectroscopic, magnetic, and transport properties and thirdly from the problems in extracting local structure information. For this reason, the possibility of modelling solids, with the aid of high speed computers, is becoming an increasingly important complementary technique to experimental studies in solid-state chemistry.

The basis of classical computer simulation is the specification in mathematical terms of

the energy of the system as a function of particle coordinates. The reliability of the results of the simulations depends of the extent to which such models represent the system. The development of reliable potential models has become a key factor in the field of computer modelling. Their derivation is discussed in chapter 4.

In the calculations for static lattice simulation the computer code THBREL (which is supported by the SERC and the Daresbury Laboratory) and for the dynamic simulation, the computer program PARAPOCS (Parker and Price, 1989) was used.

This chapter aims to outline the methodology of the calculations. In the following sections it will be described how the energy is specified and evaluated computationally, the relationship of the energy derivatives to some physical properties and the simulation of the effects of temperature and pressure.

3.2. Static lattice simulation

3.2.1. Simulation of the perfect lattice

Ionic and semi-ionic crystals may be described as arrays of positively and negatively charged ions. The interactions between pairs or groups of ions are described by potential functions, the sum of which yields the lattice energy of the crystal. These interactions are divided into long-range and short-range terms.

The lattice energy, often referred as the cohesive energy is given by:

$$V(rij) = \sum_{ij} \frac{q_i q_j}{ij\, 4\pi\, \varepsilon_0 r_{ij}} + \sum_{ij} \phi_{ij}(r_{ij}) + \sum_{ijk} \phi_{ijk}(r_{ijk}) \qquad 3.1$$

where the first term is the long range interaction or Coulombic term, the second and third term represents short range interactions.

The Coulombic term corresponds to the sum of the interactions between the effective charges on each atom. q_i and q_j represents the full or partial charges of the interaction.; r_{ij} is the distance between ion i and j, ε_0 is the permittivity of free space. The summation is carried out over all pairs of atoms in the unit cell omitting the interaction on an ion with itself. The long range interaction is the major contribution to the lattice energy.

The second term in equation 3.1 represents the short range interactions between ions, which includes the repulsion between neighbouring charge clouds, van der Waals attraction, polarizability etc.

ϕ_{ij} is the short range interaction between ions i and j. The short range interactions are highly repulsive at low values of r which prevents the collapse of the crystal. They arise from overlap of electron charge clouds but may also include an attractive component at higher values of r arising from the effects of induction and covalency.

The final term in equation 3.1 represents the three body interactions, in order to reproduce the bond angle dependency found in covalent systems. The term is often called "bond-bending" term as it provides information on the directional nature of the bonding interaction. In the case of the silicates modelled in this study, we only consider the dependence of the lattice energy on bond angles such as the O-Si-O bond angle.

The short range interactions are described by an analytical expression, for which several parameterised functions are available. The form of the functions and the techniques for their parameterisation are presented in chapter 4.

Hence the lattice energy is the sum of the total Coulomb energy and the total short range energy.

The only difficulty that arises in the calculation of the electrostatic energy is that the summation of all Coulombic interactions is very slowly convergent in real space. The problem of slow convergence is overcome using the Ewald method, which is described in detail in Ewald (1921, 1939) and Tosi (1964). This method transforms the slowly convergent q_iq_j/r term into two rapidly convergent series, one of which is calculated reciprocal and the other one in real space.

The problem is to calculate the electrostatic potential experienced by one ion in the presence of all the other ions in the crystal. The Ewald method achieves this by deriving an analytical expression for the electrostatic potential energy, assuming the lattice as extends to infinity.

The approach is to consider the Bravais lattice which is represented as a series of point charges and a uniform neutralising charge. The two components are then resolved by a Gaussian function. Two new functions are generated and the total potential can be written:

$$\varphi = \varphi_1 + \varphi_2 \qquad 3.2$$

which is the sum of two distinct but related potentials.

The potential φ_1 is generated by a Gaussian distribution of charge situated at each ion site

(a continuous series of Gaussian distribution)(Figure 3.1 a). This function is smooth and thus the sum of the Fourier transformation of the Gaussian distribution converges rapidly in reciprocal space. The potential φ_2 is obtained from a lattice of point charges with an additional Gaussian distribution of opposite sign superposed upon the point charges (Figure 3.1b). This Gaussian function is used to describe the difference between the point charge distribution and the Gaussian distribution by which it is replaced. This second summation converges rapidly in real space.

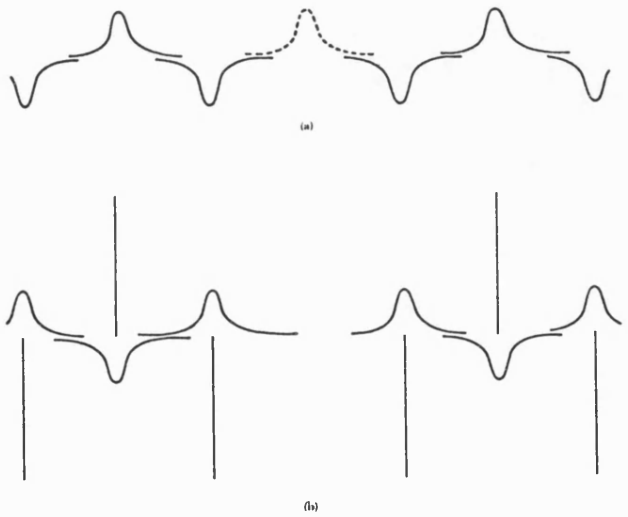

Figure 3.1: (a) charge distribution used for calculating φ_1; (b) charge distribution for φ_2 (Kittel, 1986).

The resultant summation when taken to infinity is independent of the choice of the half-width parameter η of the Gaussian peak shape. A large value of η will give rapid convergence to the reciprocal space part of the sum (the term vanishes in the limit $\eta \to \infty$),whereas a small value gives a rapid convergence of the real space term (the term vanishes in the limit $\eta \to 0$). To give an optimum convergence the value η is given by

$$\eta = (s\pi^3/V_C^2)^{\frac{1}{6}} \qquad 3.3$$

where s is the number of ions in the unit cell and V_c the unit cell volume (Catlow and Norgett, 1976).

3.2.2. Derivatives of the lattice energy

The lattice energy of a crystal would be at a minimum with respect to the ionic displacement for the observed crystal structure if the potential function perfectly described the crystal. However, this is usually not the case and hence the normal procedure is to minimise the lattice energy with respect to some structural parameters.

In addition to the calculation of the lattice energy of a system, derivatives of the lattice energy with respect to the internal and to the bulk strains are evaluated.These are used to determine crystal properties and are employed in energy minimisation procedures. For cubic systems, this corresponds to adjusting the lattice parameter to give zero bulk strains. However, for non-cubic systems the process is more complicated, and a detailed account is given by Parker (1982). Detailed mathematical descriptions are given by Catlow and Norgett (1976), Catlow and Mackrodt (1982).

The lattice energy U_C with N atoms per unit cell is calculated by expanding to second order about a lattice configuration **r**. The displacement of the lattice from equilibrium is represented by a vector δ, which contains the strain vector (δr) and a further 6 bulk components ($\delta\varepsilon$) which are discussed below. The strain vector generates a new configuration **r'** and by expanding the second order in δ we have:

$$U_C(\mathbf{r}') = U_C(\mathbf{r}) + \mathbf{g}^T.\delta + \frac{1}{2}.\delta^T .W .\delta \qquad 3.4$$

The strain vector has the dimension (3N+6). 3N components result from the 3N internal component $\delta\mathbf{r}=\mathbf{r}'-\mathbf{r}$, due to the displacement in x, y and z directions of the ions, denoted $\delta\mathbf{r}$, and the final 6 components are the independent bulk strain components of the symmetric strain matrix $\Delta\varepsilon$.

$$\Delta\varepsilon = \begin{bmatrix} \delta\varepsilon_1 & \frac{1}{2}\delta\varepsilon_6 & \frac{1}{2}\delta\varepsilon_5 \\ \frac{1}{2}\delta\varepsilon_4 & \delta\varepsilon_2 & \frac{1}{2}\delta\varepsilon_4 \\ \frac{1}{2}\delta\varepsilon_5 & \frac{1}{2}\delta\varepsilon_6 & \delta\varepsilon_3 \end{bmatrix} \qquad 3.5$$

The ions in configuration $\mathbf{r}$ are described by Cartesian vector $\mathbf{r}_s$; if the ions are displaced by a small amount $\delta\mathbf{r}_s$ then a new set of vectors $\mathbf{r}_s'$ are produced. The original configuration is related to the new configuration by the transformation:

$$\mathbf{r}'_s = \Delta\varepsilon\,(\mathbf{r}_s + \delta\mathbf{r}_s) \qquad 3.6$$

$\mathbf{g}$ is the vector of the first derivative of energy with respect to δ

$$\mathbf{g} = \left[\frac{\partial U_C}{\partial\,\delta\mathbf{r}}, \frac{\partial U_C}{\partial\,\delta\varepsilon}\right] \qquad 3.7$$

W is the corresponding second derivative matrix or Hessian matrix

$$W = \begin{bmatrix} \frac{\delta^2 U_C}{\partial\delta r\, \partial\delta r} & \frac{\delta^2 U_C}{\partial\delta r\, \partial\delta \varepsilon} \\ \frac{\delta^2 U_C}{\partial\delta \varepsilon\, \partial\delta r} & \frac{\delta^2 U_C}{\partial\delta \varepsilon\, \partial\delta \varepsilon} \end{bmatrix} = \begin{bmatrix} W_{rr} & W_{\varepsilon r} \\ W_{r\varepsilon} & W_{\varepsilon\varepsilon} \end{bmatrix} \qquad 3.8$$

3.3. Minimisation methods

The lattice energy of a system may be minimised either to constant volume or to constant pressure. These minimisation methods provide a powerful technique for the computer modelling of minerals. The methods offer a check upon the stability of a particular configuration and can be extended to the prediction of crystal structures (Catlow et al, 1982c). All energy minimisations simulated in this thesis were performed first at constant volume and afterwards at constant pressure. In the constant volume minimisation the atomic positions are adjusted until a minimum energy is obtained but the cell dimensions remain unaltered. In contrast, the constant pressure calculations allow both the ions and the unit cell parameters to be displaced to a position of minimum energy. Constant volume and pressure techniques employ the same principle for displacing the atomic parameters.

3.3.1. Minimisation to constant volume

In the constant volume minimisation the cell dimensions are kept fixed and all the forces which are acting on the ions are removed until the structure reaches a minimum potential or lattice energy. This method is useful for the determination of atomic coordinates and the crystal structure, but only if the cell dimensions are unambiguous defined.

The method we employ uses the first and second derivatives in the Newton-Raphson procedure. This approach is described in detail by Catlow and Norgett (1976).

For minimisation to constant volume the coordinate strain $\delta\mathbf{r}$ is removed using the Newton-Raphson matrix method and the equilibrium condition is expressed as

$$\frac{\delta U_C}{\partial \delta \mathbf{r}} = 0 \qquad 3.9$$

where $\delta\mathbf{r}$ represents a small displacement of the ions from configuration $\mathbf{r}$. When this condition is applied to equation 3.4, but neglecting the bulk strain components, the following result is found

$$0 = \mathbf{g} + \mathbf{W}_{rr}.\delta\mathbf{r} \qquad 3.10$$

and U(r) has a minimum when

$$\mathbf{g} = -\mathbf{W}_{rr}.\delta\mathbf{r} \qquad 3.11$$

$$\text{and} \quad \delta\mathbf{r} = -\mathbf{W}_{rr}^{-1}.\mathbf{g} \qquad 3.12$$

If the energy of the system were perfectly harmonic at **r** (equation 3.12) would yield the value of **r** at the minimum and hence the minimum energy of the system. However, the utility of this approach is that if this is not the case the new configuration will be closer to the minimum. The new minimum configuration can be found by updating the coordinates $\delta\mathbf{r}$ over several iterations. The equilibrium condition is reached when the displacements between successive iterations are less then a preset accuracy factor.

However, there are two computational difficulties when using the second derivative matrix. Firstly, the conversion of the second derivative matrix consumes much computer time; and secondly the inverted matrix, which has the dimension 3N*3N, may exceed the CPU memory for structures with a large unit cell.

The time required inverting the **W** matrix can be reduced using the method of Norgett and Fletcher (1970). The $\mathbf{W}^{-1}$ matrix is updated by an appropriate method and recalculated explicitly after a number of iterations. The new coordinate positions for the $(n+1)^{th}$ iteration are calculated using the Hessian, $\mathbf{H}_n = \mathbf{W}_n^{-1}$ and are given by

$$\mathbf{r}_{n+1} = \mathbf{r}_n - \mathbf{g}_n.\mathbf{H}_n \qquad 3.13$$

The approximation introduced by Davidon (1959) and developed by Fletcher and Powell (1963) is then used as an updating procedure for the inverse matrix

$$\mathbf{H}_{n+1} = \mathbf{H}_n + \frac{\delta\mathbf{r} \,.\, \delta\mathbf{r}^T}{\delta\mathbf{r}^T \,.\, \delta\mathbf{g}} - \frac{\mathbf{H}_n \,.\, \delta\mathbf{g} \,.\, \delta\mathbf{g}^T \,.\, \mathbf{H}_n}{\delta\mathbf{g}^T \,.\, \mathbf{H}_n \,.\, \delta\mathbf{g}} \qquad 3.14$$

where $\delta\mathbf{r} = \mathbf{r}_{n+1} - \mathbf{r}_n$ and $\delta\mathbf{g} = \mathbf{g}_{n+1} - \mathbf{g}_n$ are the vectors containing the differences in atomic positions and forces acting on each ion for subsequent iterations. The approximation for H_{n+1} can now be used to calculate the configuration $\mathbf{r}_{n+2}$. With this iterative scheme it is possible to advance towards the minimum without recalculating and inverting the second derivative matrix at every iteration. The calculation of the second derivative is necessary after a specified number of iterations (normally between 10 and 30 iterations) in order to maintain accuracy. This process is continued until the equilibrium configuration is reached.

The other problem associated with the Newton-Raphson minimisation method is the storage of the second derivative matrix. The size of the matrix can be reduced by symmetry considerations. The method requires only the calculation of interactions that are not equivalent by symmetry (Parker, 1982; Parker et al, 1984). Thus it is necessary to vary only the symmetry independent variables during the minimisation, and applying the weighting factors to the second derivatives in the calculation of the energy term. In this procedure a large amount of computer time and memory can be saved. However, in general such constraints should not be included and thus allow a structure to reduce its symmetry if it leads to a lower energy structure (Parker and Price, 1989).

If the second derivative matrix is too large to store, an alternative technique which uses just the first derivatives in a conjugate gradient method can be employed, although the minimisation process is much slower. The application of this method to do computer simulation of mineral structures has been discussed by Parker et al (1983).

3.3.2. Minimisation to constant pressure

The constant volume minimisation technique is inappropriate when the cell dimensions are unknown or if a comparison of the relative stability of two polymorphs is necessary. In this case a constant pressure minimisation is needed. When minimising the lattice energy to constant pressure the lattice coordinates the unit cell parameters are both adjusted to remove any remaining bulk and basis strains (ε and $\delta\mathbf{r}$) in the lattice. Coordinates and bulk strains are minimised in the following two stage procedure: firstly, the coordinates are adjusted to give an equilibrium configuration and secondly the lattice vectors are displaced to minimise the bulk and basis strains of the system.

The minimisation of the bulk strains require the calculations of the first and second derivatives of the lattice energy with respect to the strain. The first derivative is the stress or mechanical pressure and the second derivatives are the elastic constants. Catlow and Norgett (1976) give a detailed calculation of the strain derivatives.

The bulk strains are defined by using following relationship:

$$\mathbf{r}' = (\mathbf{I} + \varepsilon)\mathbf{r} \qquad 3.15$$

where $\mathbf{I}$ is the identity matrix, ε is the strain on the original coordinates and lattice vectors, $\mathbf{r}$; and $\mathbf{r}'$ are the final coordinates and lattice vector parameters.

After each adjustment of the lattice vectors, the symmetric strain (equation 3.5) is recalculated for the new configuration. This indicates the amount of residual strain in the system and new basis vectors are assigned to relieve the strain. The strain matrix can be written in vector form, using the Voigt notation, and therefore equation 3.15 can be written as:

$$\begin{pmatrix} x' \\ y' \\ z' \end{pmatrix} = \begin{pmatrix} 1+\delta\varepsilon_1 & \frac{1}{2}\delta\varepsilon_6 & \frac{1}{2}\delta\varepsilon_5 \\ \frac{1}{2}\delta\varepsilon_4 & 1+\delta\varepsilon_2 & \frac{1}{2}\delta\varepsilon_4 \\ \frac{1}{2}\delta\varepsilon_5 & \frac{1}{2}\delta\varepsilon_6 & 1+\delta\varepsilon_3 \end{pmatrix} \begin{pmatrix} x \\ y \\ z \end{pmatrix} \qquad 3.16$$

x, y and z are components of **r**.

The strains are calculated from the elastic constants and the stress of the crystal. Hook's law assumes that the stress is proportional to the strain, where the elastic compliance tensor is the constant of proportionality.

Considering the square of equation 3.15 the mechanical pressure or stress can be determined

$$\mathbf{r'}^2 = \mathbf{r'} + 2\mathbf{r}^T.\varepsilon.\mathbf{r} + \mathbf{r}^T.\varepsilon^2.\mathbf{r} \qquad 3.17$$

Hence the mechanical or static pressure is given by:

$$P_{si} = \frac{\delta U_C}{\delta \varepsilon_i} = \frac{\delta U_C}{\delta r} \cdot \frac{\delta r^2}{\delta \varepsilon_i} \cdot \frac{\delta r}{\delta r^2} \qquad 3.18$$

The derivatives of $\mathbf{r}^2$ with respect to the strain can be found at zero strain:

$$\frac{1}{2}\frac{\delta r^2}{\delta \varepsilon_i} = r^{\alpha} r^{\beta} \qquad 3.19$$

where $i = 1,2,3,4,5,6$

$\mathbf{r}^{\alpha} = x,y,z,y,x,x$

$\mathbf{r}^{\beta} = x,y,z,z,z,y$

The transformation from **r** to **r'** will result in a change of the reciprocal lattice vectors from G to G' and the unit cell volume from V_C to V_C', because the Ewald method sums much of the Coulombic interaction in reciprocal space and hence the effect of strain on the reciprocal lattice vectors and cell volumes must be considered.

The derivatives of G^2 with respect to the strain are analogous to equation 3.19

$$\frac{1}{2}\frac{\delta G^2}{\delta \varepsilon_i} = -G^{\alpha}G^{\beta} \qquad 3.20$$

with i, α and β as above and

$$\frac{\delta V_C}{\delta \varepsilon_i} = V_C' \qquad 3.21$$

where i = 1,2,3.

In addition the elastic constant matrix is required to evaluate the bulk strains. Elastic constants are defined as the second derivatives of the lattice energy with respect to the strain, normalised to the cell volume.

These are calculated by expanding equation and assuming the equilibrium condition:

$$U(\mathbf{r}') = U(\mathbf{r}) + \frac{1}{2}\delta\mathbf{r}^T.\mathbf{W}_{rr}.\delta\mathbf{r} + \delta\mathbf{r}^T.\mathbf{W}_{r\varepsilon}.\delta\varepsilon + \frac{1}{2}\delta\varepsilon.\mathbf{W}_{\varepsilon\varepsilon}.\delta\varepsilon \qquad 3.22$$

the equilibrium condition

$$\frac{\delta U_C}{\partial \delta \mathbf{r}} = 0 \qquad 3.23$$

gives

$$\delta\mathbf{r} = -(\mathbf{H}.\mathbf{W}_{r\varepsilon}.\delta\varepsilon) \qquad 3.24$$

where $\mathbf{H} = \mathbf{W}^{-1}$

substituting the equation $\delta\mathbf{r}$ into equation 3.22 gives the energy as

$$U(\mathbf{r}') = U(\mathbf{r}) + \frac{1}{2}\delta\varepsilon\,(\mathbf{W}_{\varepsilon\varepsilon} - \mathbf{W}_{\varepsilon r}.\mathbf{H}.\mathbf{W}_{re}).\delta\varepsilon \qquad 3.25$$

The second derivatives or elastic constant matrix is then

$$\mathbf{C} = \frac{(\mathbf{W}_{\varepsilon\varepsilon} - \mathbf{W}_{\varepsilon r}\,.\,\mathbf{H}\,.\,\mathbf{W}_{r\varepsilon})}{V_C} \qquad 3.26$$

and the bulk strains, $\delta\varepsilon$, are:

$$\delta\varepsilon = \frac{\delta U_C}{\partial \delta\varepsilon}\,\mathbf{C}^{-1} \qquad 3.27$$

and as

$$P_{si} = \frac{\delta U_C}{\delta \varepsilon_i} \qquad 3.28$$

$$\varepsilon_i = P_i(C)^{-1} \qquad 3.29$$

where P_i is the total pressure, which is the sum of the static and hydrostatic pressure.

Equation 3.27 is substituted into equation 3.15 which will yield to the new coordinates and cell dimensions. This calculation proceeds over a few iteration until all residual strains removed. In each iteration firstly a constant volume minimisation in order to remove the internal strains has to be done and secondly the constant pressure minimisation with respect to the cell dimensions.

This minimisation method gives a crystal structure at absolute zero.

3.4. Calculation of physical crystal properties

Once the equilibrium configuration of the crystal structure has been obtained, crystal properties like elastic constants, static dielectric and high frequency constants, piezoelectric constants and vibrational frequencies can be calculated.

Having evaluated the first (g) and the second (W) derivative matrices for lattice energy minimisation procedures they may be used to calculate the lattice properties.

3.4.1. Dielectric and piezoelectric constants

The derivatives of dielectric- and piezoelectric constants are given in detail by Catlow and Norgett (1976) and Catlow and Mackrodt (1982). The dielectric tensor $k^{\alpha\beta}$, required to find the dielectric constants is given by

$$\mathbf{k}^{\alpha\beta} = \delta^{\alpha\beta} + (4p/V_C) \cdot \mathbf{q}^T \cdot [W_{rr}-1]^{\alpha\beta} \cdot \mathbf{q} \qquad 3.30$$

where $\delta^{\alpha\beta}$ is the Krönecker delta and **q** the charge vector. For the static dielectric constant, the core-core and core-shell terms in $\mathbf{W}_{rr}$ are used, but the high frequency dielectric constant is only influenced by shell-shell terms.

3.4.2. Elastic constants

The derivatives of the elastic constants have been mentioned brief in section 3.3.2. Elastic constants are defined as the second derivative of the lattice energy with respect to the strain, normalised to the cell volume.

The elastic constants are calculated by

$$C_{ij} = \frac{\delta}{\delta\varepsilon_i}\left(\frac{\delta U_C}{\delta\varepsilon_j}\right) \qquad 3.31$$

thus the expression assume constant crystal volume and neglect entropy terms. If we integrate equation 3.31 twice the crystal energy $1/2C_{ij}\varepsilon_i\varepsilon_j$ from which comparing with equation 3.25 the expression for **C** is clearly.

The elastic constant tensor **C** is given by

$$\mathbf{C} = \frac{(\mathbf{W}_{\varepsilon\varepsilon} - \mathbf{W}_{\varepsilon r} \,.\, \mathbf{H} \,.\, \mathbf{W}_{r\varepsilon})}{V_C} \qquad 3.32$$

where the expression is normalised to the crystal volume.

3.4.3. Vibrational frequencies

The relationship between the interatomic potential and the normal modes of vibration of a structure has been described in detail by Born and Huang (1954), Ziman (1964) and Cochran (1973). The vibration of the atoms in a crystal can be described by a 3nN Newtonian equation of motion (n, number of atoms, N number of unit cells). If any atom i in the crystal is displaced by an amount u_i from its equilibrium position, it will experience a restoring force F_i

$$F_i = \delta U_C / \delta u_i \qquad 3.33$$

thus the equation of motion for each atom i of mass m_i, can be expressed as

$$m_i \frac{\delta^2 u_i}{\delta t^2} = \frac{-\delta U_C}{\delta u_i} \qquad 3.34$$

and from the theory of small displacements it can be shown

$$F_i = \frac{\delta U_C}{\delta u_i} = \sum \frac{\delta^2 U_C}{\delta u_i \, \delta u_j} u_j \qquad 3.35$$

where u_j is the displacement of all the other atoms j in the crystal.

Equation 3.34 and 3.35 must be translationally invariant (Ziman, 1964), so we can write the expression

$$u = e(\mathbf{q}) \exp(iq.R - \omega(\mathbf{q})t) \qquad 3.36$$

where **q** is the reciprocal lattice wave vector of lattice vibrations, $\omega(\mathbf{q})$ is the frequency of the vibrational mode, $e(\mathbf{q})$ is the polarisation wave vector describing the atomic displacements involved in the vibration and R is the interatomic separation. This method is reducing the number of equations, therefore we only need to consider 3n from 3nN, because all unit cells are equivalent and for calculating the dynamics only one unit cell need to be considered.

Substitution of equation 3.35 and 3.36 into equation 3.34 yields to the vibrational frequencies of a lattice related to the static lattice energy

$$m\omega^2(\mathbf{q})\, e(\mathbf{q}) = D(\mathbf{q})\, e(\mathbf{q}) \qquad 3.37$$

where $D(\mathbf{q})$ is the dynamical matrix.

$$D(q) = \sum \frac{\delta^2 U_C}{\delta u_i\, \delta u_j} \exp(iq.R) = \sum_r (W_{rr}) \exp(iq.R) \qquad 3.38$$

The vibrational frequencies are derived from $\omega^2(\mathbf{q})$. For a unit cell containing n atoms, there are 3n solutions for a given value of **q**.

Equation 3.38 gives 3n eigenvalues, which are the squared frequencies $\omega^2(q)$ of each normal mode and 3n sets of eigenvectors ($e_x(q)$, $e_y(q)$ and $e_z(q)$) which describe the atomic displacement associated with each normal mode.

3.5. Dynamic lattice simulation

As experimental studies at different pressures and temperatures are often difficult an attractive alternative is to use computer simulation methods.

The previous sections have described lattice energy minimisation techniques at zero Kelvin and zero pressure (and even neglected zero point motion). The development of the new computer code PARAPOCS (Parker and Price, 1989) which includes entropic effects in the calculation of free energy enables us to predict structures at elevated temperatures and pressures. The method used for calculating the free energy and thermodynamic properties is based on lattice dynamics and is an approach for calculating vibrational frequencies in periodic structures. This technique was pioneered by Born and Huang (1954). A major assumption of these calculations is the quasi-harmonic approximation, which assumes that the vibrational motions in the solid consists of quantised harmonic oscillators whose frequencies vary with the cell volume. The atoms in lattice dynamics are held fix when evaluating vibrational frequencies and thus only sample the energy at specific lattice sites where the shape of the potential energy-well is assumed to be harmonic.

The effects of temperature and pressure can be included in a static simulation by

evaluating the contribution from the internal mechanical, hydrostatic and kinetic pressure.

The approach used to calculate the free energy and the thermodynamic properties of a structure is summarised in Figure 3.2.

3.5.1. Lattice dynamics

The prediction of the crystal structure and the crystal properties at other temperatures other than zero Kelvin require the vibrational contribution to the free energy to be included. This is necessary to calculate the stress caused by the vibration of the constituent atoms. As stress is equal to the derivative of free energy with respect to the volume, the stress can be obtained from the phonon frequencies evaluated at different cell volumes.

The vibrational contribution to the free energy can be evaluated from the phonon frequencies derived from the dynamical matrix in section 3.4.3.

The phonon frequencies are dependent of the wave-vector, thus to determine phonon density of states and thermodynamic properties, a calculation of the frequencies over all possible wave-vectors is necessary. But in practise it is impossible to evaluate the phonon frequencies for each dispersion branch at all wave-vectors and therefore a sampling method must be devised. This is slightly reduced because of the periodic nature of the crystals, which allows phonon dispersion to be fully described by simply considering the behaviour of phonons within the first Brillouin zone (the Wigner-Seitz reciprocal lattice unit cell, Figure 3.3). The need to calculate the frequencies for all wave-vectors in the Brillouin zone is overcome in part by choosing only frequencies on a three-dimensional mesh of points within the Brillouin zone and using an appropriate weighting

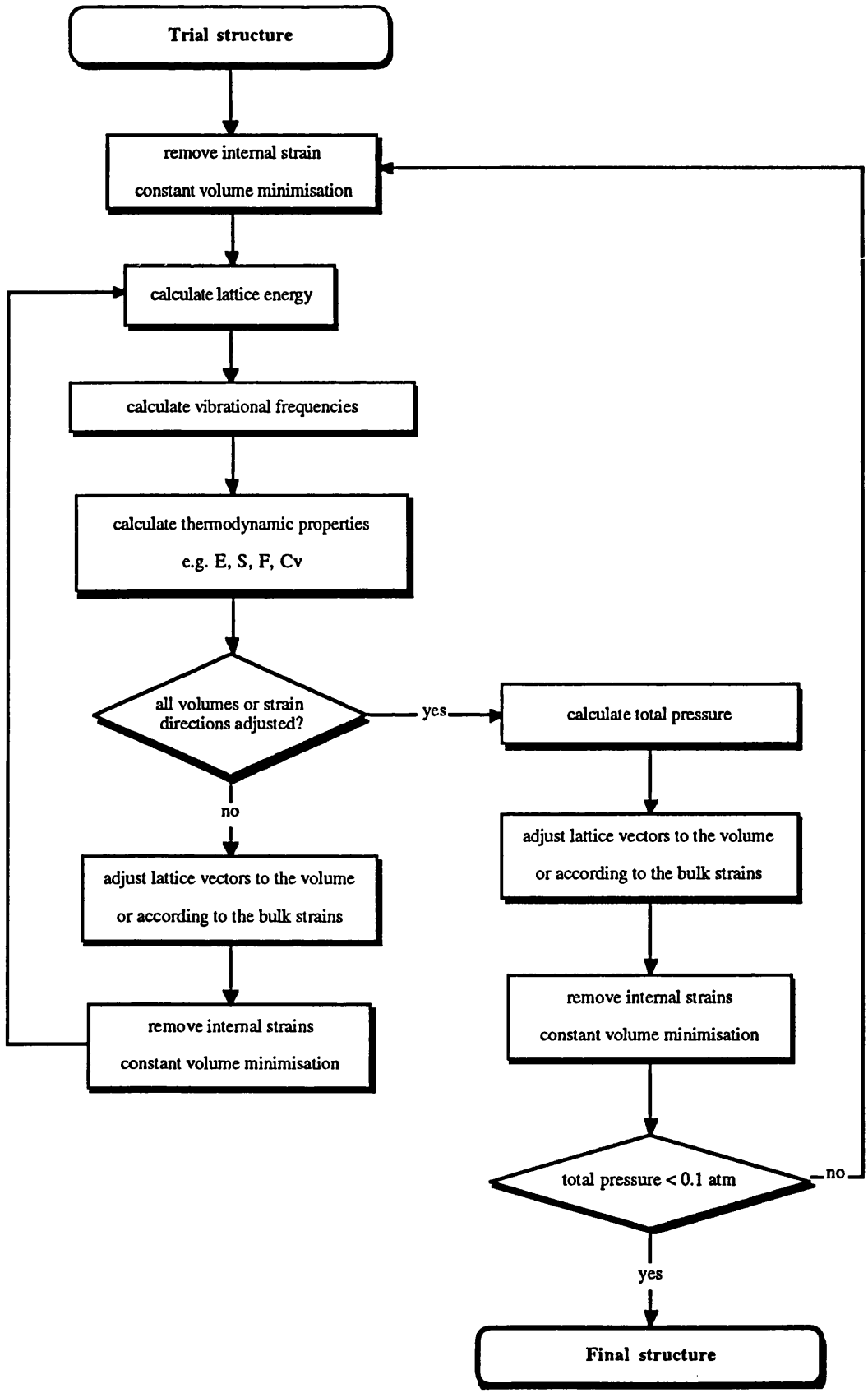

Figure 3.2: The approach of free energy minimisation using the computer code PARAPOCS

factor. Each point is weighted according to the number of times a point appears in the Brillouin zone, thus the zone-centre (Γ-point) **q** = (0,0,0), which appears only once has a weighting factor 1, while **q** = (0.5, 0.5, 0.5) for an orthorhombic crystal will have a weighting factor of eight.

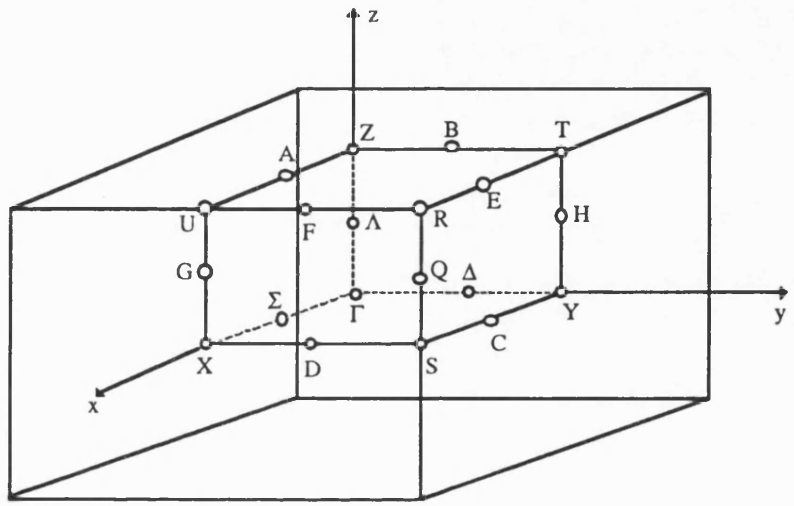

Figure 3.3: The Wigner-Seitz reciprocal lattice unit cell

The thermodynamic properties converge rapidly with the size of the mesh and the number of atoms in the unit cell, for temperatures above 50K.

The influence of the unit cell size is particularly significant for zeolites as they often have very large structures. This effect of the unit cell of mesh size was shown by comparison the two materials MgO and Mg_2SiO_4 (Price and Parker, 1988). MgO has 8 atoms in the full unit cell and the thermodynamic properties converged when integrating of 27 **q**-points, while for Mg_2SiO_4 with 28 atoms in the unit cell it was found that 8 **q**-points are sufficient. A similar comparison has been done for cancrinite. Cancrinite has 12 atoms in

the unit cell, which is compared to other zeolite structures small. As it can be seen in Figure 3.4 the heat capacity at constant volume is almost identical for 1 and 8 **q**-points, hence the thermodynamic properties converge for both points the same. For the zeolites described in this work it was found that 1 **q**-point was enough.

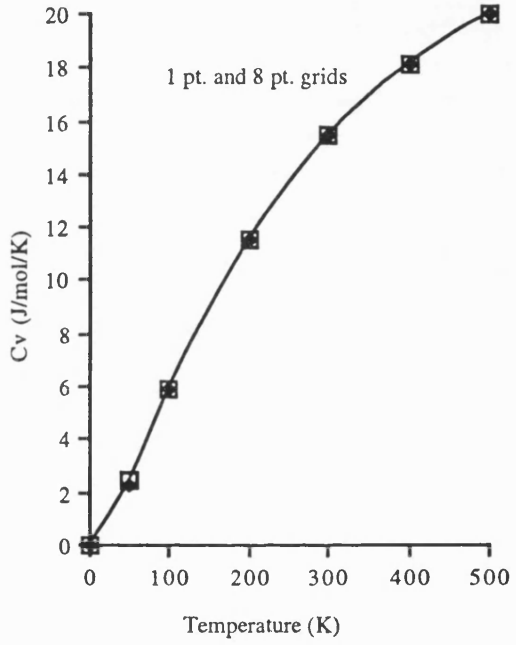

Figure 3.4: C_v versus temperature showing the effect of points in k-space for cancrinite.

Fillipini et al (1976) proposed that dispersion is greatest near the Brillouin zone centre and that at low temperatures acoustic phonons with wave-vectors close to the zone centre are the only thermally excited modes and therefore a more dense sampling is required in this region. In PARAPOCS this is overcome by using an "uneven" sampling technique, which give an appropriate weighting to wave-vectors near the zone centre. Although the Brillouin zone is sampled more densely near the centre, these frequencies do not make a contribution that is out of proportion to the total frequency sum (Wall,1987).

A calculation of the frequencies at the zone centre is useful as it correspond to generating large wavelength phonon frequencies with respect to the cell volume. These can be compared directly with those determined by infrared and Raman spectroscopy.

Once the phonon-frequencies have been determined the thermodynamic functions E, S, F and Cv i.e, the vibrational energy, entropy, free energy and heat capacity respectively can be calculated. A detailed description about the calculation of the thermodynamic properties follows in the next section.

3.5.2. Thermodynamic properties

After calculating the phonon frequencies for points within the irreducible Brillouin zone the thermodynamic properties can be evaluated. These thermodynamic functions need to be integrated over all values of reciprocal lattice wave vectors, **q** and they are determined from the following expressions:

$$E = kT \sum_{i}^{M} (x/2 + x(e^{x} - 1)) \qquad 3.39$$

$$S = k \sum_{i}^{M} (-\ln (1 - e^{-x}) + x (e^{x} - 1)) \qquad 3.40$$

$$F = kT \sum_{i}^{M} (x/2 + \ln (1 - e^{-x})) \qquad 3.41$$

$$C_V = k \sum_{i}^{M} (x^2 e^x)/(e^x - 1) \qquad 3.42$$

where E is the vibrational energy, S the entropy, F the free energy, and C_V the heat capacity at constant volume.

Each property is summed over the total number of phonon frequencies M and where $x = h\omega_i(q)/kT$ and all phonon dispersion branches, i. The zero point energy $\Sigma h\omega_i(q)/2$ is also included in the vibrational energy and free energy.

h is the Plank's constant, k the Boltzman's constant, T is the absolute temperature and $\omega_i(q)$ the normal mode frequency at reciprocal lattice wave vector **q** and dispersion branch i.

Alternatively the total vibrational density of states $G(\omega)$ may be estimated and the overall energy of a crystal can be calculated form the integral (Salje and Werneke, 1982):

$$U = U_C + \int_o^{\omega_m} h\omega(q) \left\{ \frac{1}{2} + [\exp (h\omega(q)/kT) - 1]^{-1} \right\} G(\omega) d\omega \qquad 3.43$$

where $G(\omega)d\omega$ is the number of modes summed over the entire Brillouin zone, with frequencies in the range between ω and $\omega+d\omega$, ω_m is the maximum vibrational frequency in the crystal and U_C is the static lattice energy. By differentiation of equation 3.43 the

heat capacity of a crystal at constant volume, C_V, is given by:

$$C_V = k\int_0^{\omega_m} (h\omega(q)/kT)^2 \exp(h\omega(q)/kT) \{\exp(h\omega(q)/kT) - 1\}^{-2} G(\omega)d\omega \qquad 3.44$$

The heat capacity at constant pressure (C_P) can be calculated from C_V and if the molar volume (V), the isothermal bulk modulus (κ_T) and the coefficient of volume expansion (β) of the mineral are know.

The heat capacity at constant pressure is calculated according to:

$$C_P = C_V + \beta^2 TV\kappa_T \qquad 3.45$$

The calculation of the coefficient of volume expansion (β) will be discussed in the next section.

3.5.3. Thermal expansion

Another property which can be calculated by using the technique mentioned in the previous chapters is the calculation of the thermal expansion.

One method to calculate the thermal expansion coefficient is to evaluate the crystal structure at two finite temperatures and determine the change in volume

$$\beta = \frac{1}{V}\frac{\delta V}{\delta T} \qquad 3.46$$

This approach is used in experimental techniques, where a dilatometer measures small changes in volume on heating (White et al, 1985).

Another method in calculating β, which is more difficult to determine theoretically, can be evaluated from following relationship:

$$\beta = \frac{\gamma C_V}{\kappa_T V} = \frac{\gamma C_P}{\kappa_S V} \qquad 3.47$$

where γis the thermal Gruneissen parameter, κ_T the isothermal compressibility and κ_s the adiabatic compressibility.

The thermal Gruneissen parameter (γ) can be evaluated first by calculating the mode Gruneissen parameters for each frequency:

$$\gamma_i = \frac{-\delta \ln(\omega_i)}{\delta \ln V} \qquad 3.48$$

The mode Gruneissen parameter (γ_i) is a measure of the change in vibrational frequencies of a normal mode (ω_i) as a function of the change in molar volume. As ω is a function of **q** there are in effect an infinite number of γ_i's for any one mineral.

The thermal Gruneissen parameter can be calculated then by taking the average of the heat capacity weighted mode Gruneissen parameters:

$$\gamma_T = \frac{1}{C_V} \sum C_i \gamma_i \qquad 3.49$$

where C_i is the contribution to the total heat capacity C_v, made by each mode i.

For non-cubic materials similar expressions can be used, which is shown in more detail in Parker and Price (1989).

3.5.4. Free energy minimisation

The basis of the computer code PARAPOCS is the free energy minimisation at a given temperature or pressure. The approach is similar to that described for lattice energy minimisation, the only difference is the calculation of the strain ε. In a constant pressure lattice energy minimisation the strain is defined as

$$\varepsilon = \mathbf{p}_s \cdot s \qquad 3.50$$

where s is the elastic compliance tensor and $\mathbf{p}_s$ the static stress. The static stress is the derivative of the lattice energy with respect to the strain. In the free energy minimisation the strain ε is defined as

$$\varepsilon = \mathbf{p}_s + \mathbf{p}_k \cdot s \qquad 3.51$$

where $\mathbf{p}_k$ is the kinetic pressure.

The kinetic pressure is the derivative of the vibrational free energy (F) with respect to the volume.

The kinetic pressure is found from the relationship

$$p_k = \frac{\delta F}{\delta V} \qquad 3.52$$

and is calculated by evaluating F at a given volume and reevaluating F after making a small adjustment to the cell volume.

For non-cubic materials the volume will not expand isotropically and therefore six different strain components have to be considered. In this case a small strain ($\delta\varepsilon$) is applied in each direction and the kinetic pressure is calculated from the change in F for each component.

$$p_k = \frac{1}{V}\frac{\delta F}{\delta \varepsilon} \qquad 3.53$$

Once the kinetic pressure is evaluated the constant pressure minimisation technique can be used, except that the total pressure is now defined as the sum of the kinetic, mechanical (internal) and hydrostatic pressure.

Each time the cell volume is modified a constant volume energy minimisation is performed where each atom position is adjusted so that it remains at a potential energy minimum. This is done to reduce the possibility that an atom will be moved to a position where the harmonic approximation breaks down, such as at a potential energy maximum, leading to imaginary frequencies. By minimising to constant pressure and including the

vibrational component of the free energy the crystal structure at a given temperature or pressure can be evaluated.

IV.) POTENTIAL MODELS

4.1. Derivation of the potential parameters

The accuracy of the results obtained from any computer simulation is dependent upon the accuracy of the chosen potential parameters. It is usually the reliability of the potential model rather than the approximation in the simulation methods which usually determines the success of the simulation. Thus the inclusion of important interatomic interaction and then the subsequent derivation of the appropriate parameters is critical in determining the outcome of the simulation.

The various ways the parameters can be derived are discussed in detail by Mackrodt and Stewart (1977) and Kendrick and Mackrodt (1983). We may divide the methods available for the derivation of potential parameters into two categories: those derived from fitting trial parameters to experimental properties (empirical methods) and those where the short-range energies are calculated theoretically (*ab-initio* methods). Hence all parameters cannot be obtained by *ab initio* methods; if the shell-model is used there must be some input from experimental crystal properties. Consequently it will be referred to the former methods as the empirical approach and the latter as the semi-empirical.

4.1.1. Semi-empirical methods

Potential parameters for solids can be obtained from full quantum mechanical calculations. The advantage of using this approach is that no experimental data for the solid is required, hence it can be applied to a wider range of compounds than fully empirical methods. It also has the advantage that the ion-ion interaction is evaluated over a wide range of separations.

One such method is the electron-gas method of Wedepohl (1967) and Gordon and Kim (1972). The parameters in the short-range potential are obtained by calculating the interaction energy between two ions at a series of interatomic separations, by approximate theoretical techniques based on a treatment of each ion as an "electron gas". The electron-gas approximation is based on following procedure:

(a) the wave functions and hence the electron density distribution of the isolated interacting ions are obtained by a Hartree-Fock procedure;

(b) the interaction energy (E_{TOT}) of two ions can be written as a function of electron density of the interacting ions using the expression:

$$E_{TOT} = E_{ELEC} + E_{KE} + E_{EX} + E_{COR} + E_{DISP} \qquad 4.1$$

where E_{ELEC} is the electrostatic energy, E_{KE} is the kinetic energy term, E_{EX} is the exchange energy, E_{COR} is the short range correlation energy in the region of the electron density overlap and E_{DISP} is the dispersive energy.

The dispersive energy cannot be calculated by the electron-gas method, but is included in the potential by adding extra terms to the potential function, for example the C_{ij} coefficient in the Buckingham potential.

The terms in equation 4.1 are then calculated from the electron density, which yields the short-range energy for a particular ionic separation. This process is repeated for a series of inter-ionic separations and then the potential parameters are determined by fitting the chosen form of the interaction to the calculated energies. Methods for calculating the terms in equation 4.1 are reviewed by Catlow et al (1982).

This approach works for several structures, but has been improved by consideration for the electrostatic potential found at crystal site (Mackrodt and Stewart, 1977). Potentials which are structure dependent and more representative were obtained.

This method has been successfully used to calculate F^-... F^- interactions (Catlow and Hayns, 1972) and the short-range interactions between O^{2-} ions (Catlow, 1977).

Quantum-mechanical cluster calculations are being applied increasingly to the development of interatomic potentials; the strategy is to vary the geometry of the cluster in a systematic way and to fit the resulting potential energy-surface to an effective-potential model.

Lasaga and Gibbs (1972, 1988) and Tsuneyuki et al (1985) derived potentials for silica based on ab-initio quantum-mechanical calculations on small clusters, but these force-fields give a less accurate description of α-quartz than the empirical force-fields.

Recently Kramer et al (1991) and van Beest et al (1990) derived a partial charge potential for SiO_2-polymorphs and aluminosilicates from quantum-chemical calculations. The derivation of these parameters is based both on a fit to the potential-energy surface of a small cluster, as determined by ab initio quantum-chemical methods and on fitting of

experimental data on α-quartz. In this work these potentials have been used for quartz, zeolite and aluminophosphate studies. The potential parameters are shown in Table 4.1.

The semi-empirical feature has two main advantages over the empirical method discussed in the next section. Firstly, empirical fitting gives a reliable potential for inter-ionic separations close to those observed in the crystal. However, the reliability of the potential for separations that deviate from this value is questionable. In contrast, semi-empirical potentials can be derived for a range of separations. Secondly, empirical methods depend on the availability of experimental measured data, which may not be available; semi-empirical methods can be used to obtain potentials for materials for which little data is available. However on extending the model to include polarisability (e.g. using the shell model) parameters cannot be obtained by ab-initio methods, hence a potential model which includes polarisation must have empirical input. Furthermore, parameters for three-body interactions have not been determined by ab-initio methods.

The next section discusses the method by which short-range potential parameters, and shell model parameters are obtained in the empirical approach.

4.1.2. Empirical Methods

Empirical methods adjust variable parameters to achieve the best agreement between calculated and observed crystal properties.

The method involves estimating the parameters A, φ, C, Y and k (see section 4.2.3. for detailed description of these parameters). Crystal properties, such as elastic, dielectric and piezoelectric constants are then calculated for a given crystal structure and compared with experimental determined values. Parameters are then adjusted iteratively using least square fitting procedures until the desired agreement is obtained.

A schematic representation of the operation of this procedure is summarised in Figure 4.1 (Lewis, 1983):

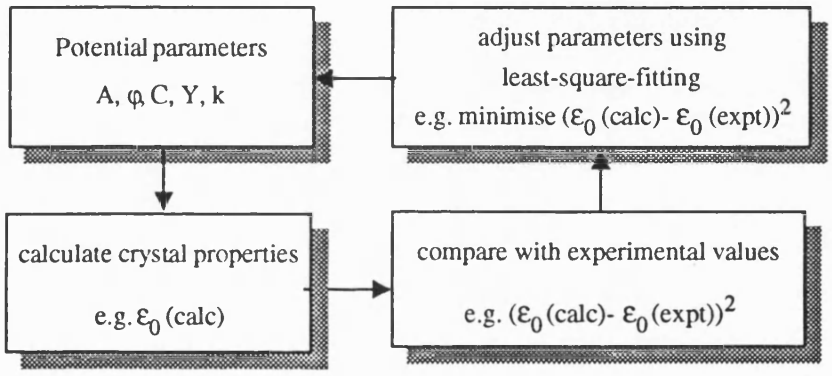

Figure 4.1: Schematic representation of the empirical method for deriving short-range potential energy function parameters.

This approach has two main drawbacks: firstly, accurate experimental data for the compound being modelled is required. Secondly, the number of variable parameters involved can be excessive when simple crystal structures are being considered. These problems can partially be solved by using data from compounds similar to that being studied. In particular parameters for the O-O interactions obtained by Catlow et al (1977) have been found transferable and have been used successfully in many studies (Sanders,

et al 1984; Jackson and Catlow, 1988; Parker et al, 1989; Parker and Price, 1989).

The advantage of the method is that it necessarily gives the best possible agreement between calculated and observed experimental properties. Thus empirical parameters were also used to study quartz and zeolite structures and they are shown in Table 4.2.

4.2. Short-range potential models

4.2.1. Basic features of the potential model

As mentioned in chapter 3 the main component of the lattice energy is the Coulomb interaction, but in order to calculate the total lattice energy the sum of the Coulomb energy and the total short range energy is necessary.

The Buckingham-potential gives a good representation for the short-range interactions:

$$\phi_{ij}(r_{ij}) = A_{ij} \exp(-r_{ij}/\varphi_{ij}) - C_{ij}/r_{ij}^{-6} \qquad 4.2$$

where r_{ij} is the separation distance of species i and j and A_{ij}, φ_{ij} and C_{ij} are parameters required for each pair of species i and j in the lattice. The parameters A_{ij} may be related to the ion size and φ_{ij} to the hardness of the ion. The first term represents the effective two

body repulsion between neighbouring charge clouds. The second term is attractive (van der Waals interaction) which in part models dispersive forces. For cation-anion interactions this term is commonly neglected. For long range anion-anion interactions this term is important and must be included. The sum of this short range interaction is rapidly convergent and may be truncated after a suitable distance.

This potential model has been successfully used in previous studies of ionic and partially ionic materials (Catlow, 1988; Parker et al 1984; 1989; Price et al, 1987; Kramer et al, 1991).

The method used to derive A, φ and C are discussed in section 4.1.

For fully ionic, rigid-ion, models, the above terms are generally the only components of the short-range potential which are considered. However, it is well known that bonding in a silicate or in quartz are generally considered covalently bonded networks with some degree of ionicity. In silicate studies three approaches have been used in attempt to model this more complex type of bonding. Price and Parker (1984) used non-integral or partial ionic charges, either alone or with a Morse potential function to model the cohesion of the covalent Si-O bond. Kramer et al (1991) used partial ionic charges with the Buckingham potential to model the covalency in quartz and silicates.

In contrast Sanders et al (1984), Catlow et al (1986) and Matsui and Busing (1984) retained a fully ionic description of the charges, but modelled the directionality of the Si-O bond by introducing a bond-bending term into the potential (section 4.2.4.).

Ionic polarisability has been described by a variety of models, the most successful of which is the shell-model (Dick and Overhauser, 1958). The shell model is discussed in greater detail in section 4.2.3.

4.2.2. The rigid-ion model

The rigid-ion model is the simplest type of an ionic model and neglects polarisability all together. Therefore, any attempt to simulate high-frequency dielectric properties of the lattice is impossible. In addition there are severe problems to reproduce the dynamical properties of a crystal accurately, since lattice vibrations are strongly influenced by ionic polarisation (Catlow and Mackrodt, 1982).

Models of this type were used and developed (Parker, 1982; Parker et al, 1984) for a range of ortho- and meta-silicates. A number of structures were modelled with reasonable accuracy, but it was also shown that such models have severe limitations. For some cases inaccurate bond lengths were calculated, physical properties like dielectric and elastic constants gave poor agreement with experiment, and the potential failed when applied to layer and framework structured silicates.

Nevertheless, the development of these models were important as they showed that Born-model potentials can be used to simulate the structures and properties of certain types of silicates.

This potential model has also been used with partial charges. Price and Parker (1984) studied models in which the effective charge on Si varied from ~1.4 to 2.1. They found that such models simulated very good structural and physical properties but are still unsuitable for framework structured silicates.

As mentioned before, Kramer et al (1991) developed new potential parameters with partial charges for the rigid-ion model to simulate silicate framework structures and aluminosilicates. This potential was used to calculate the stability of quartz and aluminophosphates and is discussed in greater detail in section 4.4. and 4.5.

The advantage of this model is the reduction in the number of parameters and in the

degrees of freedom needed to model a system.

The inclusion of polarisability doubles the number of degree of freedom for large structures, like zeolites, and the treatment is costly, both in computer time and and cpu-storage.

4.2.3. The shell-model

The discussion so far has assumed ions to be rigid interacting points in space. In practise however, this model is sometimes inadequate because it neglects ionic-polarisation. In order to model dielectric properties and dynamical properties of a crystal correctly, the development of the so called shell-model was necessary as an alternative to the rigid ion models described so far.

Dielectric constants depend on ionic polarisation as well as on short range forces. Polarisation arises from the distortion of electron charge clouds at ions by applied electrical fields. The short-range interactions between each ion and all the other ions of the lattice will be altered by such a displacement due to the overlapping charge clouds, hence polarisability has to be considered in the simulation of a real system.

The shell-model, originally proposed by Dick and Overhauser (1958) is a simple mechanical description of ionic polarisability and its use is therefore essential in the defect and high-frequency dielectric behaviour of a material.

In this model polarisability is coupled to the "effective" overlap forces (short-range repulsion). A simple diagrammatic illustration is given in Figure 4.2. The atom or ion (it is frequently assumed that the oxygen is the only polarisable atom in the structure) is

described having a core containing all the mass and assigned with the charge X and a massless shell assigned with the charge Y. The total ionic charge is the sum of the charges X and Y. Core and shell are connected by a harmonic spring with the force constant k. The development of a dipole moment is effected by the displacement of the shell relative to the core as shown in Figure 4.2.

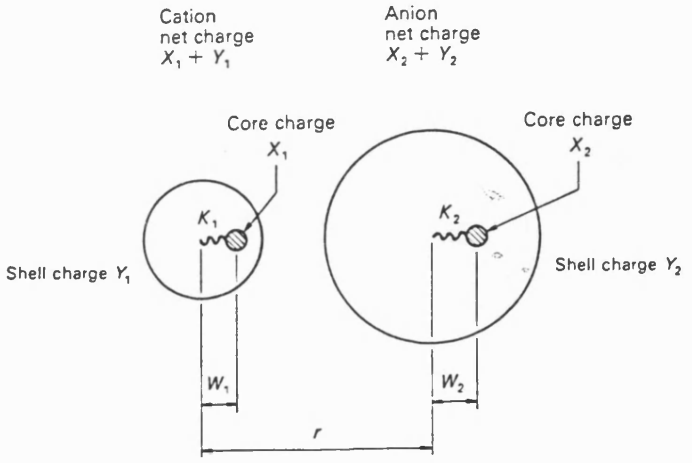

Figure 4.2: Schematic representation of the shell model (Catlow, 1988)

The core and shell of the same ion are not considered to interact electrostatically with each other and only the shell are included in the short- range force calculation. The core-shell interaction U_s is given by

$$U_s = \frac{1}{2}k_i^s r_i^2 \qquad 4.3$$

where k_i is the spring constant and r_i the relative displacement of core and shell. During the simulation a maximum value for r_i is specified to ensure that the core-shell separation does not become excessive and that the cores and shells remain in their original pairs.

The electronic polarisability (α) of the free ion is given by the expression:

$$\alpha_i = \frac{Y_i^2}{k_i^s} \qquad 4.4$$

where Y_i is the charge of the shell and k_i is as before. The spring constants k and shell charges Y are generally treated as variable parameters. They are evaluated from "fitting" to measured dielectric constants (section 4.1.).

Despite the simplicity, the shell model is very effective in modelling of properties such as defect energies, phonon dispersion curves and dielectric constants (Catlow, 1982; Cochran 1973). The only disadvantage is, that the spring constant and shell charge can only be obtained by empirical methods (section 4.1.). Thus, materials which have no measured dielectric and elastic data cannot easily be studied.

4.2.4. The bond-bending term

The inclusion of bond-bending terms into silicate potentials is a major development as they appear successfully to model the effective three body interactions and the bond directionality that has been recognised to play a significant role in determining the

structures and properties of silicates.

As discussed in the previous chapter, the two body potential is inadequate for materials with some degree of covalency. Thus a three-body or bond-bending term is incorporated into the model to include the directional nature of the covalent bonding.

The procedure involves assigning the bond acting between species i,j and k (i is at the centre with j and k the peripheral ion). The three body contribution to cohesive energy, is defined for the O-T-O (O-Si-O, O-Al-O) bond. It was found that the oxygen centred (T-O-T) model is difficult to parameterise and made only little contribution to the calculated properties (Sanders, 1984). Therefore only the Al or Si centred model will be considered in this simulation studies.

The bond-bending term has the form:

$$U_B = \frac{1}{2}k_{ijk}(\Theta_{ijk} - \Theta_0)^2 \qquad 4.5$$

where k_{ijk} is the spring constant, Θ_{ijk} is the simulated bond angle and Θ_0 is the equilibrium bond angle. Hence at values of Θ_{ijk} other than the equilibrium bond angle the energy expression is non-zero and therefore unfavourable. For modelling O-T-O interactions in zeolites or quartz Θ_0 is 109.47°, the ideal tetrahedral angle and for every tetrahedra atom (Si or Al) in the unit cell there will be six corresponding three-body interactions. The energies and derivatives of equation are exact and involve no approximations (Leslie, 1984).

Striefler and Barsch (1975) restricted the equilibrium bond angle to be at the minimum of the three-body energy. In this model there are no such constraints. It is therefore possible that the configuration in which the system has the minimum in the total energy may not be

the minimum when the three body term is added.

In this work Si-O potential both two-body and three-body additive terms, were used for the simulation.

4.3. Potential parameters employed in the simulation studies

As mentioned before, the accuracy of the simulation studies depends mainly on the reliability of the chosen potential parameters, therefore it is important which parameters are chosen for the calculations.

Several groups have in recent years studied the development of the Born-model potentials for silicates. Most modelling studies for silicates and quartz have been based on simulations using effective potentials, although a valuable set of Hartree-Fock calculations have been reported by Dovesi et al (1987) and Nada et al (1991). The polymorphs of quartz are of major interest to modelers, because their bonding is neither classical ionic nor ideally covalent. Therefore, the derivation of potential parameters for silicates are mainly based on the polymorphs of quartz.

Simple pairwaise-additive ionic models are unable to describe both the structural and elastic features of these phases. Other models describe short-range interactions and the directionality of the Si-O bond but ignore the longer-range components.

The first reliable potential parameters and possibly the most versatile potential to describe structural and thermodynamic properties of SiO_2 phases includes both, covalent

and ionic features, was developed 1984 by Sanders and coworkers. In this potential, Si and O are assigned to full, formal charges and the Si-O parameters for the short range interactions (three-body terms, shell model terms) were derived empirical.

A general feature of this potential is the $O^{2-}....O^{2-}$ interaction. The derivation was modelled on the interaction of two oxygen ions, using the Hartree-Fock molecular orbital method (Catlow, 1977). The additional electron in the O^{2-} ion (which is unbound in the free state) does not strongly influence the short-range potential.

Despite earlier speculations as to the importance of Si-Si forces (O'Keefe and Hyde, 1978), Parker (1983) found that these interaction gave an insignificant contribution to forces and energies and omitted the term.

The Al-O force field parameters were also derived empirically from α-Al_2O_3 by Lewis and Catlow (1985).

Parameters for interactions between cations and oxygens were taken from models developed from the appropriate oxide. The cation-anion parameters were calculated by using the 'electron-gas' method.

A recent quantum-mechanical derived potential for SiO_2 and $AlPO_4$-materials (Kramer et al, 1991) which successfully described the crystal properties of α-quartz and berlinite is also used for calculations in this work. The potential parameters are calculated for two-body rigid ion short-range potentials and Si, O, Al and P are assigned to partial charges.

The empirical and semi-empirical potential parameters are listed in Table 4.1 and 4.2 respectively.

4.4. Modelling of silica and silicates

4.4.1. The three-body shell model Si-O and Al-O potential

For certain classes of silicate structures, two-body rigid-ion models were used which yield to reliable structural data (Parker, 1982), but serious limitations remained, especially for modelling framework structured silicates. It was also found that in the case of α-quartz a two-body model could not consistently describe elastic, dielectric and dynamical data.

Work over the past few years has shown that the three-body potentials including the shell model treatment derived for α-quartz by Sanders et al (1984) when coupled with earlier empirical potentials derived for α-Al_2O_3, are able to yield to very good energy-minimised structural models for quartz-polymorphs and for a wide range of silicates (e.g. zeolites).

As mentioned in section 4.2.4. the bond-bending model has variable parameters. These parameters were determined by fitting to structural, elastic and dielectric properties of α-quartz. The fitting procedure was artificially weighted so that the importance of reproducing certain properties was exaggerated. Thus, the elastic and dielectric properties were weighted by a factor of ten, but during the procedure the weighting was transferred to the bulk and basis strains. The process was continued until the structural and observed properties were best reproduced (Sanders, 1984). In addition the ionic polarisability was fitted in the form of the shell model to observed crystal data of α-quartz.

The bond-bending an shell-model parameters used in this study are shown in Table 4.2.

4.4.2. Semi-empirical Si-O and Al-O potential

Section 4.2. highlighted recently derived potential parameters using *ab initio* quantum-mechanical methods which were evaluated for silica (Kramer et al, 1990). The derivation of the force field is based on both microscopic (*ab initio*) and macroscopic (experimental) data. Within this approach the interatomic interactions are described by simple two-body potentials.

Such macroscopic information can be obtained from the potential-energy surface of small representative clusters, which can be calculated by quantum-mechanical methods. H_4TO_4 (T=Si or Al) is the simplest cluster that contains the SiO_4 building units of the silica. The interaction within the cluster and the bulk, like the attraction between the central atom and the surrounding oxygen atoms and the oxygen-oxygen repulsion are separated and the potential energy surface along these two modes of distortion are determined. The short-range forces are only derived for Si-O to describe the silica bond and for O-O non-bonded interactions, which modifies the Coulomb repulsion and ensures the tetrahedral arrangement of oxygen atoms around the silicon.

The derivation of the force-field solely on the basis of cluster information is not accurate enough when applied to bulk silica and therefore fitting to macroscopic data is essential. A main characteristic of this potential model are the partial charges, which were fitted to the bulk properties. By iterating between fitting of the cluster parameters to the *ab initio* data and optimising the values of bulk parameters by comparison to the predictions of elastic constants and unit cell dimensions for quartz, a mixed *ab initio* empirical force field can be derived. A detailed description of the derivation of these force fields is given in Kramer et al (1991) and van Beest et al (1990). The parameters are given in Table 4.1.

4.4.3. Validity of the Si-O, Al-O potentials

Although the rigid-ion model of Parker (1982) has been successfully applied to several classes of silicates (Catlow et al, 1982; Parker et al, 1982) it failed to model framework structured silicates. The potential is limited because it can neither model polarisation or explicit covalent effects.

In contrast, covalent effects are modelled in the bond-bending potential and the inclusion of the shell-model allows ion polarisation to be modelled. In this potential formal charges are assigned, which is a major point of discussion in the simulation of 'semi-covalent' materials like quartz and silicates. As noted earlier, quartz and silicates are generally being accepted as being covalent bonded networks with some degree of ionicity. Whilst lattice dynamical studies clearly reveal the inadequacy of ionic models for quartz, work of Catlow (1983) and Sanders (1984) has shown that it is possible to reproduce the elastic and dielectric properties and structure of α-quartz with reasonable accuracy using the three-body shell-model with full ionic charges. More critical tests of the validity of these potential model including the calculation of dispersion curves, the application of pressure and temperature and the simulation of the properties of silica polymorphs were required. These calculations have been done to some extent (Sanders, 1984) and demonstrated the reliability of the potential. The results of these calculations and further tests using dynamic lattice simulation will be discussed in detail in chapter 5.

In addition this potential has been employed successfully for silicate materials, like zeolites. For example, Jackson and Catlow (1988) have shown that simple energy minimisation procedures using these potential parameters can model extra framework cations in zeolites and the dependence on the Al distribution in the framework. A recent application using these potential parameters was the energy minimisation of the zeolite beta polymorphs. Newsam et al (1988) have shown that the structure is essentially an intergrowth of two polymorphs, both of which have been modelled successfully using

energy-minimisation methods (Tomlinson et al, 1990).

Similar tests have been applied for the semi-empirical potential parameters. Although this is a two-body rigid-ion model the covalency of the simulated materials is given through the use of partial atomic charges. The tests for these force-field potentials have been performed on quartz and zeolites by Kramer et al (1991) and showed good agreement with experimental results. These results and further test for this potential will be discussed in further detail in chapter 5.

4.5. Modelling of aluminophosphates

4.5.1. The semi-empirical Al-O and P-O potential

Aluminophosphates are a novel class of compounds and therefore there is only little insight gained in their structural properties. Hence computer simulation is a perfect tool for studying these novel materials but until recently there where no potential parameters available.

Recently Kramer et al (1990) also developed a Al-O and P-O potential using ab initio quantum-mechanical methods. As with their Si-O parameters, the Al-O and P-O parameters were determined unambiguously from the potential-energy surface of a cluster and then fitted to the bulk properties of berlinite. Al and P are assigned to partial

atomic charges. In view of the applicability of the potentials to aluminophosphates, the charge 'difference' is set equal to the difference of formal charges. The O-O potential which was derived for use in the SiO_2 environment, also accounts for the O-O interaction in the $AlPO_4$-polymorphs. A detailed description of the force-field derivation is given in Kramer et al (1991).

The potential parameters are given in Table 4.1.

4.5.2. Validity of the Al-O and P-O potential

There are no potential parameters available to model aluminophosphates, except the semi-empirical force-field parameters discussed in this chapter. Hence no comparison with other potential models is possible.

The Al-O and P-O potential parameters have been applied to energy-minimisation procedures for berlinite (analog of α-quartz) and for microporous $AlPO_4$-polymorphs. The reliability of the force-field predictions were compared with available experimental data. Although, there are only structural information available about the $AlPO_4$-polymorphs and the accuracy of elastic properties is based on berlinite data, where there is relatively good agreement with experiment.

All these tests have been done at zero Kelvin and zero pressure. This potential is discussed and tested in greater detail in chapter 6.

	long range				two-body short range				unit
	Si	O	Al	P	Si-O	O-O	Al-O	P-O	
Z	+2.4	-1.2	+1.4	+3.4					e
A					18003.7572	1388.7730	16008.5345	9034.208	eV
φ					0.2052048	0.3623188	0.2084779	0.1926418	Å
C					133.5381	175.0000	130.5659	19.8793	$eV.Å^6$

Table 4.1: Semi-empirical potential parameters

	long-range					two-body short range					three-body	Shell-Core	unit
	Si	Al	O	K	Na	Si-O	Al-O	O-O	K-O	Na-O	O-Si(Al)-O	O	
Z	+4.0	+3.0	-2.0	+1.0	+1.0								e
A						1283.907	1460.3	22764.3	1000.30	5836.84			eV
φ						0.32052	0.29912	0.149	0.36198	0.2387			Å
C						10.66158	0.149	27.88	10.569	0.0			eV.Å^6
Θ_0											109.47		°
k											2.09724		eV/rad^2
Y												-2.86902	e
k												74.92	ev/Å

Table 4.2: Three-body shell-model potential parameters

V.) APPLICATION OF THE POTENTIAL MODELS TO QUARTZ-POLYMOPRHS

A key component of all simulation studies is the choice of the interatomic potential models. Thus a detailed comparison of the simulated data with experimental values is necessary to verify the validity of the potential models before using them for further simulation studies.

Thus one aim of this chapter is to describe the test of two potential models, the empirical three-body shell model (Sanders, 1984) and a recently derived semi-empirical two-body rigid ion model (Kramer et al, 1991) on quartz-polymorphs. One of the most effective test of a potential is the comparison of the simulated structural and elastic properties with available experimental values. and also at elevated temperatures and pressures. In addition, by using a newly developed computer code, PARAPOCS (Parker and Price, 1989), which is based on lattice dynamics, the vibrational spectrum and the thermodynamic properties will be calculated and compared to experimental data. Furthermore, by expanding the simulation to high pressure we aim to gain insights on the phase transitions.

5.1. Experimental structure of the quartz-polymorphs

In this section the two common polymorphic forms of silica, quartz and cristobalite, will be described, and along with some of their important structural features. The two silica

polymorphs investigated here belong to two different groups: low temperature phases (α-quartz and α-cristobalite) and high temperature phases (β-quartz and β–cristobalite). The low (α) and high (β) forms have different structures but the differences are so small that careful work is needed to detect them (Megaw, 1973). The structure of these polymorphs are shown in Tables 5.1 and 5.2.

5.1.1. The experimental structure of α- and β-quartz

On cooling, quartz undergoes a transformation at about 846K from a high-temperature hexagonal β-form into a trigonal α-form, which differs from the former by loss of 180° rotational symmetry about the c-axis (Megaw, 1973). With the determination of the structural relationship between α–and β–quartz it was realised that the transition from one phase to another involves only the bending, not the breaking of bonds. When β-quartz is cooled down to below the transition temperature the tetrahedral chains kink such that they are no longer related by the twofold rotation around *c* and this symmetry loss causes the space group $P6_222$ of β-quartz to degenerate to the subgroup $P3_121$ (or $P3_221$) of α-quartz. The produces twins: the so called Dauphinè twins (Heany and Veblen, 1991). Another important structural feature of quartz is that it has helical arrangements of atoms, which gives rise to optical activity. Both forms are enatiomorphous forms and therefore right- and lefthanded crystals can occur.

α-quartz

The calculations described in this chapter use as input the α-quartz structure determined

by X-ray diffraction by Jorgensen (1978). The structure is shown in Figure 5.1 (a).

α-quartz is trigonal and belongs to the space group P3121 (or P3212). The silicon atoms occupy (u 0 1/3), ($\bar{u}$ $\bar{u}$ 0) and (0 u 2/3) where u = 0.4697. There are nine atoms in each primitive cell. Referred to Cartesian axes, the basic vectors of the lattice are:

$\mathbf{a}_1 = a(1,0,0)$ $\mathbf{a}_2 = a(-1/2,\sqrt{3}/2,0)$ $\mathbf{a}_3 = c(0,0,1)$

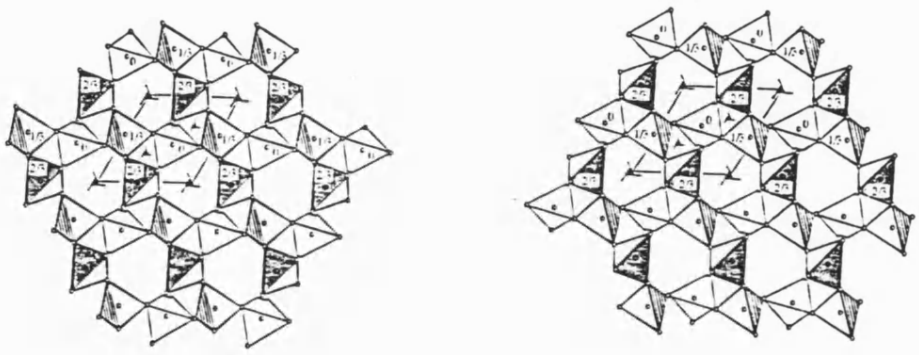

Figure 5.1a: Projection of the two Dauphiné twin orientations of α-quartz down the c-axis. The two structures are related by a 180° rotation around *c*.

β-quartz

The starting structure for the calculations was taken from Wykoff (1963). The structure is shown in Figure 5.1(b).

The structure of ß-quartz may be understood a s a special case of the α-quartz structure with hexagonal symmetry. ß-quartz is stable above 846K and belongs to the space group $P6_222$ (or $P6_422$). The reciprocal lattice is again hexagonal with the basis vectors:

$\mathbf{b}_1 = \mathbf{a}^{-1}\ (1,\ 1/\sqrt{3},\ 0)$ $\mathbf{b}_2 = \mathbf{a}^{-1}\ (0,\ 2/\sqrt{3},\ 0)$ $\mathbf{b}_3 = \mathbf{c}^{-1}\ (0,\ 0,\ 1)$

The silicon atoms occupy the symmetric positions (1/2 1/2 1/3), (1/2 0 0) and (0 1/2 2/3). The main change between α and β quartz is the placing and orientation of the tetrahedra.

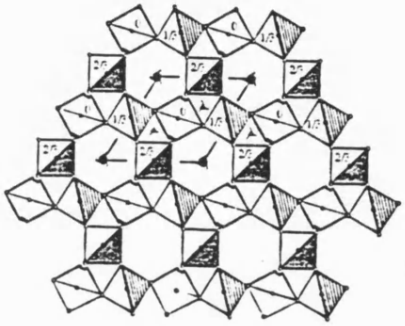

Figure 5.1b: The structure of β-quartz down the c-axis.

5.1.2. The experimental structure of α- and β-cristobalite

The high temperature phase of silica, β-cristobalite, is stable between 1746K and the melting point 2001K. On cooling it persists in a metastable form tō about 473K and inverts to the low temperature phase α-cristobalite (Hatch and Ghose, 1991). Hence β-cristobalite undergoes a first order phase transition from a cubic $Fd\bar{3}m$ to a tetragonal $P4_32_12$ or ($P4_12_12$) structure. The α–β phase transition is rapid and reversible, but shows a strong hysteresis effect (Leadbetter and Wright, 1976).

In contrast to β-cristobalite the structure of α-cristobalite is well established from single X-ray diffraction studies (Dollase, 1965; Peacor, 1973). The starting structure for the following calculations was taken from Peacor (1973) and is based on the pseudo-cubic tetragonal structure of α-cristobalite containing 4 silicon and 8 oxygen atoms in the unit cell.

The nature of the β-phase is highly controversial and the details of the microscopic transition mechanism are unknown (Hatch and Ghose, 1991). Different structure types of β-cristobalite have been reported. Wyckoff (1925) first proposed a cubic C9-type structure of β-cristobalite (space group $Fd\bar{3}m$) which is improbable because of two stereo- chemically features: a 180° Si-O-Si bond angle and a bond length of 1.54Å. These values are highly improbable assuming the silicate tetrahedra to behave as rigid groups through the transition the corresponding values in α-cristbalite are 146° and 1.609Å respectively.

In order to remove this inconsistency and to have a better fit to X-ray data Peacor (1973) and Wright and Leadbetter (1975) proposed a $Fd\bar{3}m$ model structure in which the 16 oxygen atoms are statistically distributed over the 96(h) positions resulting in a Si-O bond length of 1.609Å and a Si-O-Si bond angle of 146°.

For the simulation studies the crystallographic data were taken from Peacor (1973). The structure of α– and β-cristobalite are shown in Figures 5.2(a) and 5.2(b).

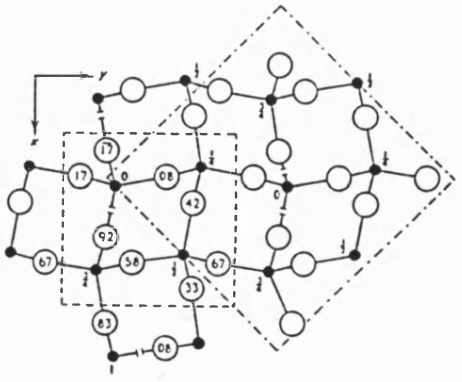

Figure 5.2a: The structure of α-cristobalite projected down the c-axis (the primitive unit cell is shown by broken lines and base-centred unit cell by dot-dash lines).

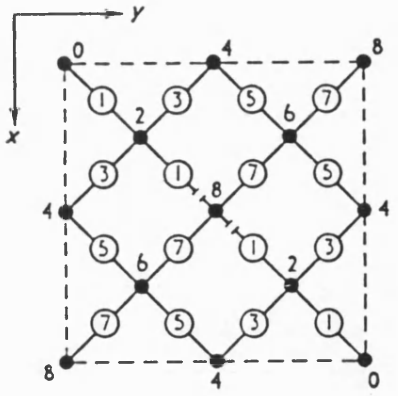

Figure 5.2b: The idealised structure of β-cristobalite projected down the c-axis.

5.2. Static lattice simulation of quartz

The discussion in chapter 4 highlighted the two applicable potential models for simulating silica and silicates. The empirical three-body shell model (Sanders, 1984) (E-model) and the semi-empirical two-body rigid ion model (Kramer et al, 1991) (SE-model).

The results of lattice energy minimisation using the SE potential parameters are very dependent on the chosen short-range potential cutoff. By using a cutoff smaller than 15Å the results, such as structural parameters and elastic constants show a big deviation from experimental results. Using potential cutoffs greater than 15Å the results converge and become close to experimental values. For example the volume of α-quartz is 130.42Å^3 using a short range potential cutoff of 3Å, 123.16Å^3 for 6Å, 114.70Å^3 for 11Å and 113.91Å^3 for 16Å. Also the elastic constant tensor c_{11}, for example, decreases from 100.9

GPa using a cutoff of 6Å to 89.4 GPa using a cutoff of 16Å. In addition the E-model cutoff should not be too short (<9Å). Compared to the E-model the SE-type has smaller long-range forces (because of the partial charges) and the short-range forces between nearest and next nearest neighbours are more significant and therefore a bigger cutoff is necessary.

Both potential models have been compared with experiment to some extent (Sanders, 1984; Kramer et al, 1991), but in order to have a complete comparison and the same basis for following calculations, this study begins with a systematic and thorough comparison of both potentials.

5.2.1. Calculated structure and elastic properties of α-quartz

In Table 5.1 the structure parameters for α-quartz after lattice energy minimisation using the E- and SE-potential model are shown. These results are compared with experimental data from Levien et al (1985), McSkimmin et al (1965) and Bechmann (1958).

Both models show very good agreement with experiment. Comparing the E- and the SE-model, the SE-model performs slightly better, although the differences are very small. The structural parameters of these two models, like the lattice constants, the Si-O-Si angle and the volume are better described by the SE force-field parameters. Also the elastic constants of the SE- potential parameters show a slightly better agreement with experimental results than the E-model. However, the static dielectric constants of the E-model are, in contrast, closer to experimental values, which is clearly a reflection of the fitting procedure.

Observable	Expt.	E - model	SE - model
a-axis [a]	4.916 [1]	4.867 (0.99)	4.920 (1.00)
c-axis	5.405	5.375 (0.99)	5.433 (1.01)
Si-O-Si	143.73°	149.05°(1.04)	147.38°(1.03)
c_{11} [b]	86.80 [2]	94.58	89.41
c_{12}	7.04	14.79	10.29
c_{13}	11.91	17.87	17.00
c_{14}	18.04	15.78	16.79
c_{33}	105.75	112.53	112.16
c_{44}	58.20	49.64	50.62
c_{66}	39.88	39.89	39.56
ε_{11}	4.52 [3]	4.58	1.97
ε_{33}	4.64	4.88	2.01
Volume [c]	113.13 [1]	110.25 (0.97)	113.91 (1.01)

Table 5.1: Calculated and experimental structural parameters of α-quartz; (a) in Å; (b) all elastic constant tensors in GPa; (c) $Å^3$; (1) Levien et al, 1985; (2) McSkimmin et al 1965; (3) Bechmann, 1958; the numbers in brackets show the statistical accuracy of the calculated structural parameters.

5.2.2. Calculated structure of β-quartz

The structural parameters for ß-quartz after lattice energy minimisation using the E- and SE- potential models are shown in Table 5.2. As a comparison experimental results from Kihara (1990) who measured the structural parameters above 846K and Ghiroso et al (1979) who investigated inverted high-temperature quartz are also listed in this table.

Again we find, as in α-quartz, that the simulated results of both models are very close to experimental values, except for the Si-O-Si bond angle.

A comparison of the two potential model shows that the structural parameters, like the lattice constants and the volume are better described by the E-model, in contrast to α-quartz, and the Si-O bond distance and the O-Si-O bond angle are slightly better reproduced by the SE-model. As in α-quartz, we have to stress that the differences between the simulated results are very small.

The calculated Si-O-Si bond angle is higher for both potential models than the experimentally bond angle. This is not surprising as there is no force restraining this angle to experimental value; however, this force is not a component of the potential model.

Observable	Expt.1	Expt.2	E - model	SE - model
a (Å)	4.9965	4.913	5.0018 (1.001)	5.0645 (1.01)
c (Å)	5.4570	5.402	5.5037 (1.01)	5.5906 (1.02)
Vol ($Å^3$)	117.983	112.920	119.243 (1.01)	124.187 (1.05)
Si - O (Å)	1.620	--	1.5777 (0.97)	1.6002 (0.99)
Si- O- Si (°)	145.1	--	158.84 (1.09)	158.82 (1.09)
O- Si - O (°)	109.63	--	109.48 (1.00)	109.53 (1.00)

Table 5.2: Comparison of the two force-field models for β-quartz with experimental observables; (1) Kihara (1990); (2) Ghiorso et al (1979); the numbers in brackets show the statistical accuracy of the calculated structural parameters.

5.3. Dynamic lattice simulation of quartz

In this section the lattice dynamics of α– and β-quartz are simulated using the computer-code PARAPOCS. This enables us to calculate crystal structures and thermodynamic properties such as the heat capacity, entropy and free energy at elevated temperatures and/or pressures.

The theory was outlined in detail in chapter 3.

As will be demonstrated the agreement between calculation and experiment is satisfactory if 8 grid points are sampled in reciprocal space. For the quartz-polymorphs the Γ-point and seven points on the faces of the Brillouin zone (0 0 1/2, 0 1/2 0, 0 1/2 1/2, 1/2 1/2 1/2 etc) were used. The reciprocal unit cell for quartz is shown in Figure 5.3.

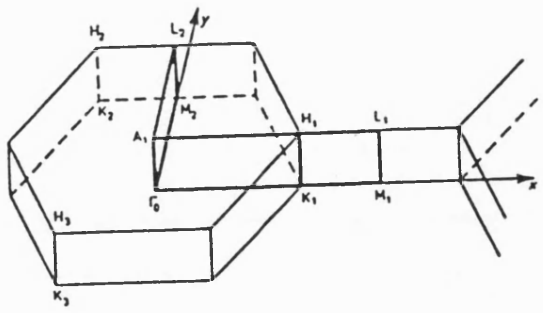

Figure 5.3: Part of the reciprocal unit cell for quartz, including the upper half of the first Brillouin zone (after Barron et al, 1979).

5.3.1. Structure of α- and β-quartz at different temperatures

α-quartz:

In section 5.2. it was shown that both potential models are able to simulate the structure and elastic properties at 0 Kelvin well.

Both lattice parameters *a* and *c*, for both potential models, are slightly decreasing between 0K and 40K and from 50K they show an increase with increasing temperature. This increase continues above the experimental determined transition point at 846K. Using the E- potential model α-quartz transforms to β-quartz at 1400K and using the SE-potential model α-quartz transforms at 1200K.

In Figure 5.4 the lattice constants *a* and *c* are shown in a temperature range from 0K to 900K for both potential models together with experimental data. The lattice parameter *c* (Figure 5.4b) of the E-model is in very good agreement with experimental measurements, except at higher temperatures. The SE-model shows a similar trend, but the deviation to the experimental result is larger.

The lattice parameter *a* (Figure 5.4a) shows a similar behaviour for both models and they are both in good agreement with the experimental values. From about 700K onwards both models do not differ with temperatures as observed in the experimental data, probably due to the onset of the phase transition which occurs at ~500K later in the simulation.

The value of *c/a* for both potential models decreases with increasing temperature, because the lattice has a greater coefficient of expansion in the basal plane than along the principal axis. The experimental values of the *c/a* ratio in Figure 5.4c of both potential models are higher, especially at the experimental determined transition temperature.

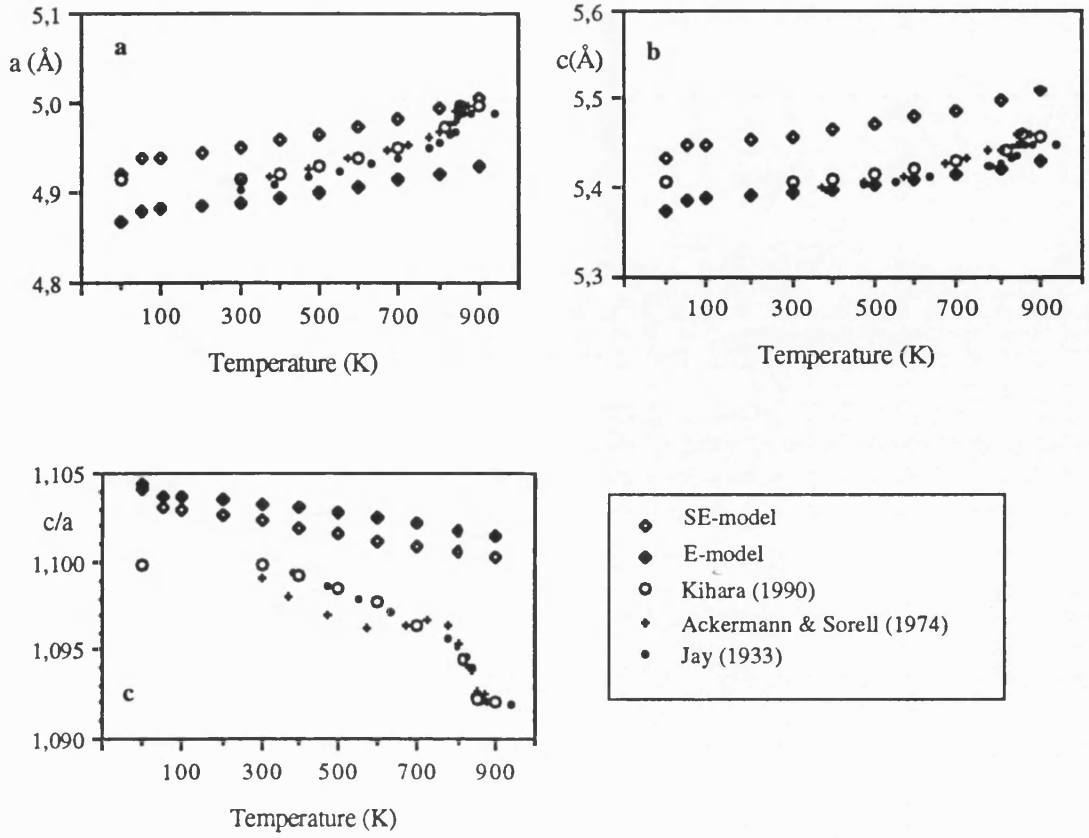

Figure 5.4: Experimental and calculated lattice constants with increasing temperature for α-quartz.

In an attempt to assess the individual components of the potential model we consider the bond distances and angles. The Si-O distances for both potential models increase with increasing temperature, whereas experimental results by Kihara (1990) show a decrease of the Si-O distance. Kihara (1990) calculated the bond distances and angles from the mean position of the atoms, which were determined using X-ray diffraction amplitudes at different temperatures. In a temperature range from 0K to 800K the Si-O distance for the E- model is increasing from 1.5745Å to 1.5787Å and for the SE-model from 1.6001Å to 1.6032Å, whereas the the experimental results show a decrease from 1.6097Å to 1.5944Å in a temperature range from 300K to 813K.

The Si-O-Si bond angles increase, but 1 to 2° with increasing temperature for both potential models. An increase of 6° was observed in the experimental studies (Kihara,1990). The calculated O-Si-O bond angles increase slightly (~0.1°) with increasing temperature, whereas experimentally (Kihara,1990) a decrease of 0.5° was observed.

Hill and Gibbs (1979) and some other authors (Taylor, 1972; Boisen et al, 1990; Downs et al, 1990) describe a structural interdependence between Si-O-Si angles and Si-O distance in silica polymorphs; the Si-O-Si angle increases when the Si-O distance decreases. Both potential models do not show this structural interdependence for α-quartz with increasing temperature. This feature will be discussed in further detail in section 5.3.5.

β-quartz:

The structural parameters of β-quartz have been calculated from 0K to 400K using both, the E- and the SE-potential parameters.

The minimised structure of β-quartz contained two imaginary frequencies for both potential models in a temperature range from 50K to 400K. This indicates that the structure is unstable, because turning points which are not minima in the multi-dimensional energy surface have been found. Using higher temperatures (from 400K onwards) for the simulation the structure collapsed, independent which potential model has been used. Although the structure is unstable according to the imaginary frequencies, a minimisation of β-quartz was possible up to 400K because energy derivatives are, of course, zero at saddle points.

In Figure 5.5 the structural parameters *a* and *c* of α-quartz and β-quartz are shown. As

mentioned above, the structural parameters for α-quartz are increasing with increasing temperature until the transition temperature is reached, which is compared to experimental results displaced towards higher temperatures. Beyond this point, at which the β-quartz configuration is attained the structural parameters *a* and *c* show a contraction, which is identical to experimental measurements. The absence of thermal expansion may indicate highly preferred atomic vibrations towards the free space in the structure. Comparing the two potential models, both show a contraction of the cell parameters of β-quartz with increasing temperature, but as in α-quartz, the E-model performs slightly better. The simulated lattice parameters *a* and *c* (Figure 5.5a, b) using the E-model are in good agreement with experimental data, whereas this lattice parameters using the SE-potential model are higher compared to experimental values.

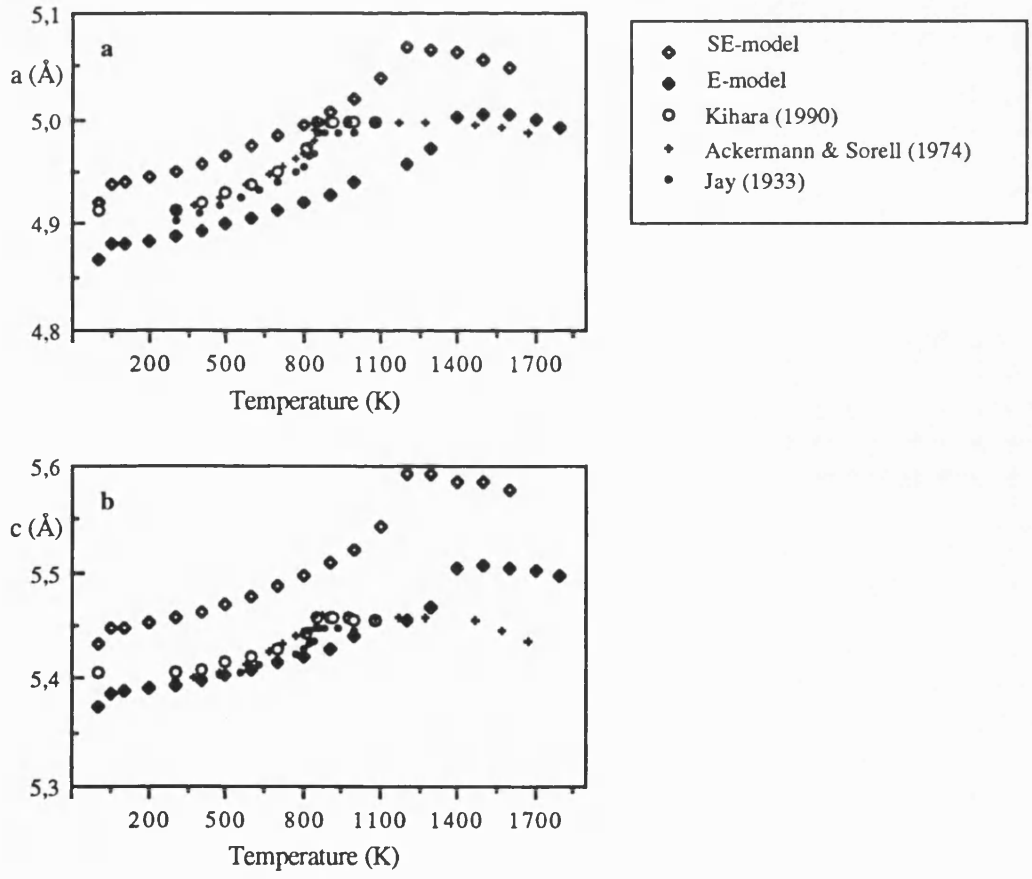

Figure 5.5:Experimental and calculated lattice constants with increasing temperature for α- and β - quartz

On calculating the bond distances and angles the same deviations from experiment were observed, which is perhaps not surprising given the similarity of the two phases.

Tilt angle

Quartz can be simply visualised as being composed of rigid SiO_4 units or tetrahedra. These tetrahedra are linked together at the corners and their relative orientation is determined by forces between them. From this viewpoint one can understand how the structure of the low temperature phase transforms into the one of the high temperature phase. Grimm and Dorner (1975) suggest that the α–β transition in quartz can be described as a simultaneous tilting of the SiO_4 tetrahedra around the two-folded axis perpendicular to *c*. In this way the structure of quartz can be formulated in terms of only one parameter, the tilt angle δ. Because of the tetrahedra being linked this tilt operations lengthens the dimension of the unit cell (*a*,*c*) of α-quartz with increasing temperature.

The tilt angle (δ) in the quartz structure is given by (Grimm and Dorner, 1975)

$$\tan \delta = \frac{2\sqrt{3}}{9} \frac{c}{a} \frac{1 - 6z}{x}$$

where *a* and *c* are the unit cell parameters and x and z are oxygen coordinates (referring to hexagonal coordinates $x = (x + y/\sqrt{3})/a$; $y = 2y/a\sqrt{3}$; $z = z/c$).

The tilt model for quartz gives a good overall description of the temperature dependence to the position parameters and explains qualitatively the lattice expansion data.

In Figure 5.6 the tilt angle for both potential models and the experimental tilt angle after Grimm and Dorner (1975) is shown. Both models show a decreasing tilt angle with increasing temperature as the experimental values and their deviation is small from experimental values at lower temperatures. At higher temperatures, where the tilt angle becomes zero (which corresponds to the α–β transition temperature), the deviation between calculated and experimental values becomes bigger, which corresponds to the much higher transition temperature for the simulated models (see section 5.3.7).

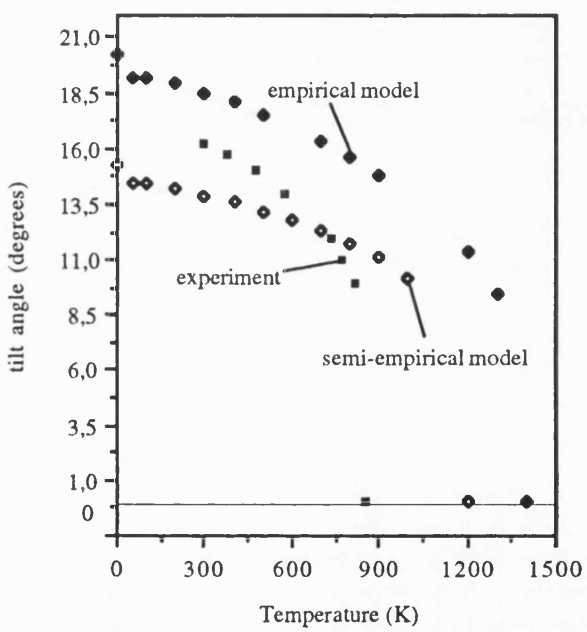

Figure 5.6: Comparison of experimentally determined tilt angle δ (Grimm and Dorner (1975)) with calculated tilt angle using the E- and SE- potential parameters.

Summary

Both models reproduce the structural parameters in α- and β-quartz with increasing temperature very well, although the E-models performs slightly better in the calculation of the lattice constants and the SE-model predicts the bond distances slightly closer to experimental values.

The Si-O-Si bond angles, which are predicted too high are perhaps due to the absence of a force restraining this angle to experimental value. As the SE-model is a simple two body rigid ion model, there are no bond-bending terms included, which could restrain this angle. However, including this term in the E-model, Sanders (1984) found that the oxygen centered (Si-O-Si) bond bending term made only little contribution to calculate the properties and consequently only the silicon centered (O-Si-O) term was included in the simulation studies. But according to the results in our simulation studies this term should be not neglected. No Si-O-Si bond bending term has yet been derived because of the difficulties to parameterise this term (Sanders, 1984).

With both potential models it was possible to reproduce the tilt model of quartz. Hence the temperature dependence of the position parameters and therefore the atomic displacements with increasing temperature is described by both models very well.

In both potential models it was not possible to simulate the α–β transition near 800K. The limitation of the lattice dynamical technique is that the anharmonic nature of the potential energy surface is neglected which is a major problem when considering very high temperatures or when a structure undergoes a displacive phase transition (Parker and Price, 1989). The atoms in lattice dynamics are stationary in contrast to molecular dynamics and thus only sample the energy of a specific lattice site where the shape of the potential well assumed to be harmonic. Therefore we can assume that the towards higher temperature shifted α–β - transition is due to a breakdown of the quasi-harmonic

approximation, which neglects the full anharmonicity of the potential energy surface.

5.3.2. Vibrational spectrum of α- and β-quartz

The structural and elastic parameters of α-quartz were used in both models to derive the potential parameters. But the models should be able to predict properties other than those used in fitting procedures. The phonon dispersion curves or the vibrational spectra therefore provide a good test.

Quartz has 9 atoms per unit cell, which gives rise to 27 normal modes of vibrations. Three of these are translational or acoustic modes. The remaining 24 modes (optical modes) have been assigned to various Si-O bending, stretching and deformation. The reciprocal unit cell for quartz is shown in Figure 5.3.

The spectroscopically active modes have frequencies that lie in the range between $1200cm^{-1}$ and $150cm^{-1}$, and they can be subdivided into vibrational classes. High frequency modes between $1200cm^{-1}$ and approximately $500cm^{-1}$ are the results of the Si-O stretching motions, while modes with frequencies below $500cm^{-1}$ are due to bending and torsion between the tetrahedra. Between $500cm^{-1}$ and approximately $750cm^{-1}$ there is a characteristic gap, the so called "quartz frequency gap" and modes with frequencies greater than $800cm^{-1}$ are separated by another about $150cm^{-1}$ wide gap, the "silicate gap" (van Beest et al, 1989). In Table 5.4 the experimental frequency ranges for stretching and bending modes and the characteristic gaps between them are summarised.

Normal mode frequencies can be predicted from the computer simulations and can be compared to available inelastic neutron scattering data. Long wave-length phonon

frequencies evaluated with **q** close to zero can be compared to the observed infrared and Raman spectra.

Calculations of the frequencies of infrared and Raman active modes which are close to the Γ-point were calculated using both models. The phonon calculations were performed by using a zero wave-vector and one wave-vector **q** with a length of 0.001 reciprocal lattice units in the direction of the x-axis.

frequency - range (cm^{-1})	modes
1100 -1200	anti-symmetric stretch
800 - 950	silicate gap
700 - 800	symmetric stretch
550 - 700	quartz frequency gap
100 - 550	bending mode

Table 5.4: Experimental frequency ranges for stretching and bending modes and characteristic gaps

Vibrational spectrum of α-quartz:

Experimentally the frequencies and symmetry of the 24 optical vibrational modes are known, allowing a detailed comparison between theory and experiment. Group theory calculations show that the optical modes can be divided up into symmetry modes (Etchepare et al, 1973. The decomposition of the 24 optic modes of α-quartz into symmetry species is:

$$4A_1 + 4A_2 + 8E_T + 8E_L$$

where the A_1 modes are Raman, the A_2 modes infrared active and the E modes are both.

In Table 5.3 the calculated infrared and Raman frequencies for the E- and SE- model at the Γ-point are shown. The experimental data from Scott and Porto (1967) are also listed in the table for comparison.

Symmetry	Experiment (cm^{-1})	E - model (cm^{-1})	SE - model (cm^{-1})
A_1	207	215.28 (1.04)	251.29 (1.21)
	356	333.01 (1.07)	429.99 (1.21)
	464	460.35 (1.01)	619.85 (1.30)
	1085	911.69 (0.84)	1120.37 (1.03)
A_2	364	344.29 (0.95)	467.74 (1.29)
	495	498.57 (1.01)	662.29 (1.34)
	778	817.19 (1.05)	761.85 (0.98)
	1080	900.23 (0.83)	1108.27 (1.03)
E_T	128	143.64 (1.12)	170.66 (1.33)
	265	269.38 (1.01)	319.32 (1.20)
	394	396.73 (1.01)	477.52 (1.21)
	450	438.14 (0.97)	587.26 (1.31)
	697	716.02 (1.02)	723.03 (1.04)
	795	821.80 (1.03)	769.30 (0.97)
	1072	898.23 (0.84)	1100.21 (1.03)
	1162	1021.46 (0.88)	1228.36 (1.06)
E_L	128	143.67 (1.12)	171.17 (1.34)
	265	272.19 (1.03)	319.38 (1.21)
	401	400,91 (1.00)	484.25 (1.21)
	509	512.24 (1.01)	684.45 (1.34)
	697	716.69 (1.03)	729.21 (1.05)
	807	827.96 (1.03)	846.24 (1.05)
	1162	1016.51 (0.87)	1208.16 (1.04)
	1235	1111.77 (0.90)	1242.22 (1.01)

Table 5.3: Experimental (Scott and Porto, 1967) and calculated infrared and Raman frequencies for α-quartz; the numbers in brackets show the statistical accuracy of the calculated frequencies.

The E-model shows a very good agreement with experiment for the optical modes lower

500cm^{-1}. The average discrepancy of 3% is very small. The SE-force-fields reproduce the frequencies below 500 cm^{-1} notably worse. The average discrepancy from experimental data using this model is 27%. Comparing the force field models for the vibrational modes above 500 cm^{-1} the result is changing. The E-model does not reproduce the high frequency modes as well as the SE- model.The discrepancies for both models are 9% and 3.5% respectively.Therefore the bending modes are better represented by the E-potential parameters, whereas the stretching modes are slightly more accurate using the SE-model.

Also calculations of all phonon dispersion curves along Γ-K-M, Γ-M_2 and Γ-A_1, which corresponds to (1/2,0,0), (0,1/2,0) and (0,0,1/2) respectively, have been performed for both models. The phonon dispersion curves for the E- and SE-model along the x and y direction are shown in Figure 5.7 and Figure 5.8.

Again the E-model does not reproduce the stretching modes in all three directions as well as the SE-model. There is also no gap between 800-950 cm^{-1} which divides the stretching modes into symmetric and anti-symmetric stretches. The SE-model reproduces this characteristic feature very well; it shows clearly the six anti-symmetric, the six symmetric stretching modes and the gap between them. The quartz-frequency gap between 550-700 cm^{-1}, which divides the stretching modes from the bending modes is only reproduced by the E-model, whereas the calculations using the SE-potential parameters do not show this gap. The bending modes between 550-100 cm^{-1} are also better reproduced by the E-model along all three directions. The calculation of the phonon dispersion curves along (0,1/2,0) using the E-potential parameters show between 550-700 cm^{-1} a pseudo-gap which contains one phonon branch. This pseudogap has also been calculated by Etchepare and Merian (1978) in this direction.

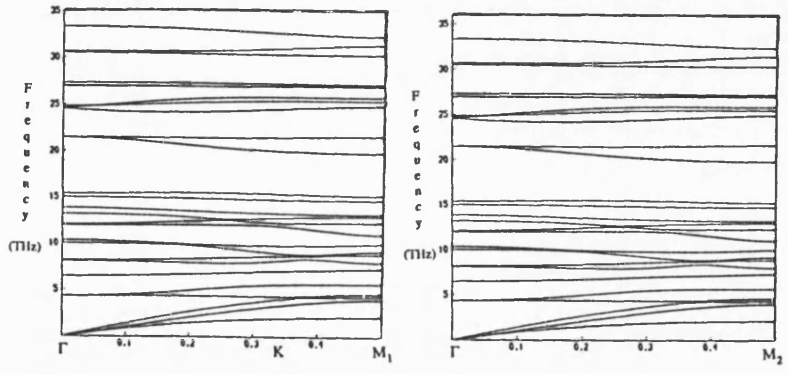

Figure 5.7: Calculated phonon dispersion curves for α-quartz using the E-model.

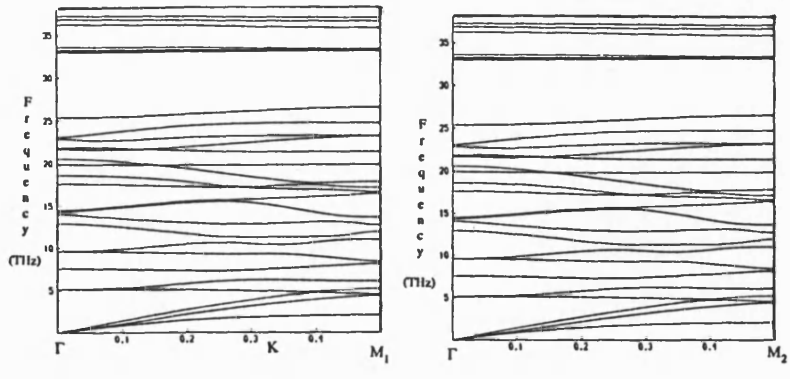

Figure 5.8: Calculated phonon dispersion curves for α-quartz using the SE-model.

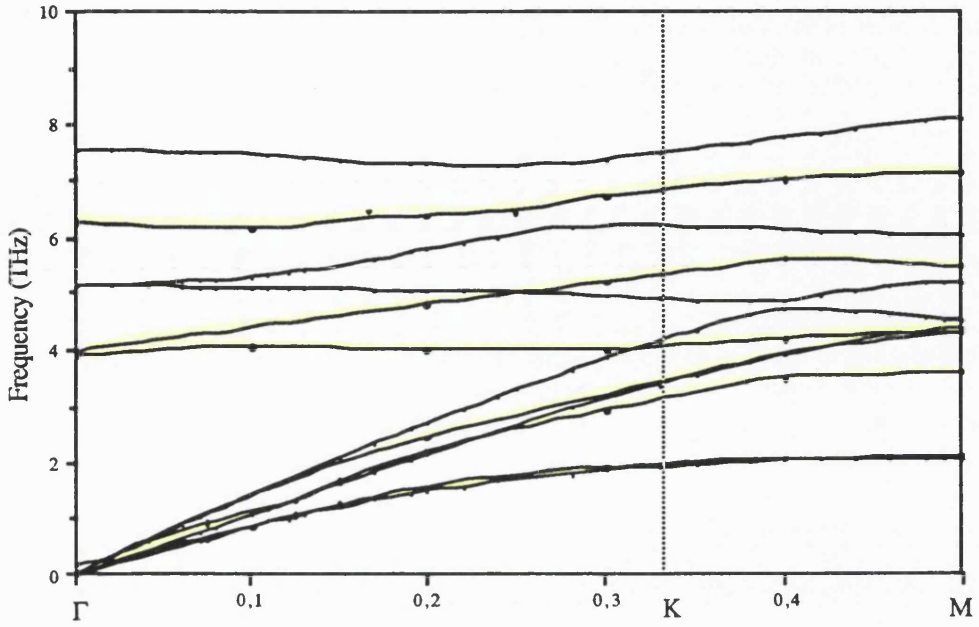

Figure 5.9: Calculated (black line) and measured (Dorner et al, 1980) (yellow line) phonon dispersion curves for α-quartz using the SE- potential model.

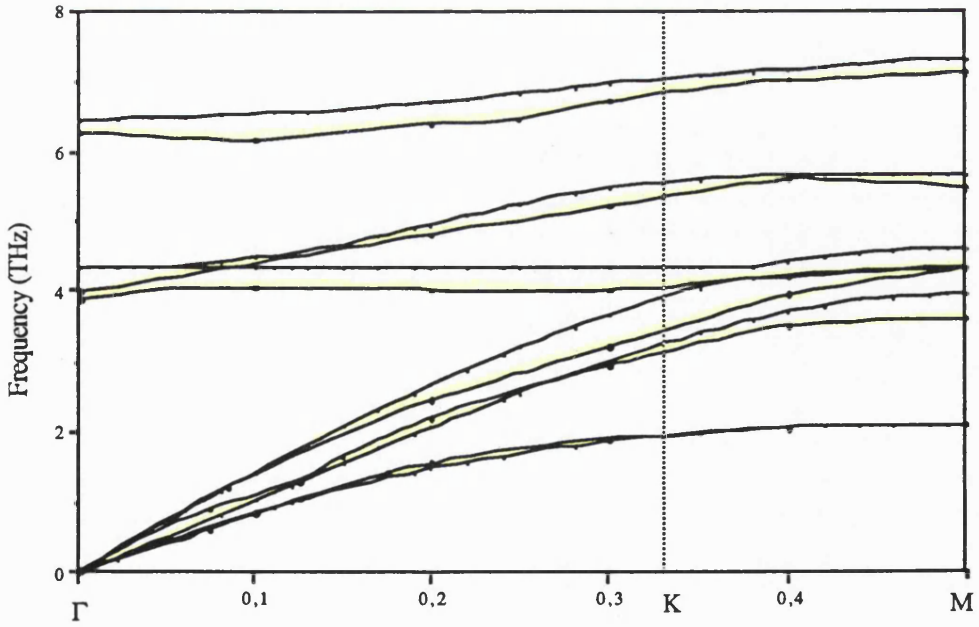

Figure 5.10: Calculated (black line) and measured (Dorner et al, 1980) (yellow line) phonon dispersion curves for α-quartz using the E-potential model.

Dorner et al (1980) measured the six lowest phonon dispersion branches in α-quartz at room temperature for the (1/2,0,0) direction using inelastic neutron scattering. The experimental results are shown together with the E and SE-force field calculation in Figure 5.9 and Figure 5.10. As expected, the E-model shows qualitative and quantitative very good agreement with experiment for the six lowest dispersion branches (Figure 5.10). The SE-force-fields show poor agreement with experiment compared to the E-model. Figure 5.9 shows that the three lowest optical branches calculated with the SE-model are much higher and in variance with the experimental data.

Vibrational spectrum of β-quartz:

Experimentally, (Gervais and Piriou, 1975; Bates and Quist, 1972) both the frequencies and the symmetry of the optical vibrational modes of β-quartz are known, enabling a comparison between theory and experiment. The separation of the vibrational modes into symmetry subgroups is supported by experimental evidence of α-quartz. In the low-temperature form there are four totally symmetric Raman-active modes of species A_1, four infrared-active A_2 modes and eight double degenerate Raman- and infrared-active modes of species E. According to group theory (Etchepare et al, 1973) three of the four A_1 modes and two of the A_2 modes become Raman- and infrared-inactive (B_1 and B_2) at the transition, whereas the E modes stay the same.The soft mode associated with the α–β transition has been shown to be the 207cm^{-1} A_1 mode of α-quartz (Scott, 1968; Scott and Höchli, 1971). The low frequency B_1 mode in β-quartz, which is purely torsional, with the wavenumber 72cm^{-1} is the equivalent mode of the 207cm^{-1} A_1 mode in α-quartz. Only the 461cm^{-1} mode of α-quartz can persist in the totally symmetry class A_1 of β-quartz, due to

the high symmetry of the atomic motions (Etchepare et al 1973). Most of the longitudinal optical frequencies of the E-type modes were not observed experimentally in β-quartz, therefore only the transversal optical frequencies will be considered in this comparison between calculated and experimental E-modes.

The symmetry species for the optic vibrations in β-quartz are (Etchepare et al 1973)

$$A_1 + 3B_1 + 2A_2 + 2B_2 + 4E_1 + 4E_2$$

In Table 5.5 the calculated infrared- and Raman-frequencies using the E- and SE-force-field parameters are shown.The experimental frequencies from Bates and Quist (1972), Gervais and Piriou (1975) and the calculated frequencies from Etchepare et al (1973) are also shown in the table for comparison. The calculation of the frequencies from Etchepare et al (1973) is based on lattice dynamics, but the potential parameters were fitted directly to the observed vibrational frequencies. In Figure 5.11 the calculated frequencies for both potential parameters and the experimental determined frequencies at the Γ-point are shown graphically.

As in α-quartz the E-potential model agrees to within 5% of the experimental determined frequencies below 500cm^{-1}.

In contrast the SE-potential parameters do not reproduce the bending frequencies so well. The average discrepancy from experimental data is 25%. In this statistical analysis the lowest B_1 mode (30cm^{-1}) given by Iishi (1978) is not considered, because this calculated frequency is, compared to the calculated mode by Etchepare et al (1973) and compared to both potential models ananomously low.

Between the bending modes and the symmetric stretch modes experimentally the quartz

frequency gap has been determined. This quartz frequency gap is only reproduced by the E-model.

Symmetry	Exptl [a]	Exptl [b]	Calc[c]	SE - model	E - model
A_1	464	461	491	599 (1.29; 1.30)	473 (1.02; 1.03)
B_1	30[d]	inactive	72	75 (2.50; 1.04)	72 (2.40; 1.00)
	350[d]	inactive	346	399 (1.14; 1.15)	346 (0.99; 1.00)
	1072[d]	inactive	1119	1229 (1.15; 1.10)	1050 (0.98; 0.95)
A_2	435	...	471	584 (1.34; 1.24)	425 (0.98; 0.90)
	1061	...	1074	1119 (1.05; 1.04)	926 (0.87; 0.86)
B_2	385 [d]	inactive	413	529 (1.37; 1.28)	380 (0.99; 0.92)
	777 [d]	inactive	754	741 (0.95; 0.98)	799 (1.03; 1.06)
E_1	98	99	98	123 (1.26; 1.24)	79 (0.81; 0.80)
	420	428	442	546 (1.30; 1.28)	396 (0.94; 0.93)
	779	788	775	762 (0.98; 0.97)	812 (1.04; 1.04)
	1057	1067	1074	1131 (1.07; 1.06)	933 (0.88; 0.87)
E_2	243	245	260	290 (1.19; 1.18)	243 (1.00; 0.99)
	400	409	387	524 (1.31; 1.28)	379 (0.95; 0.93)
	680	688	686	715 (1.05; 1.04)	704 (1.04; 1.02)
	1155	1173	1162	1254 (1.09; 1.07)	1127 (0.98; 0.96)

Table 5.5:Comparison between calculated and experimental determined infrared- and Raman modes for β-quartz; (a) Gervais and Piriou; 1975; (b) Bates and Quist; 1972; (c) Etchepare et al; 1973; (d) Iishi, 1978; the numbers in brackets show the statistical accuracy of the calculated frequencies compared with experimental data (a; b); (frequencies in cm^{-1}).

Comparing the two force-field models for the vibrational modes above $500cm^{-1}$ with the experimentally determined stretching modes, statistically both potential models show a discrepancy of 6% on average. The SE-force field parameters reproduce slightly higher frequencies and the E-potential parameters show slightly lower frequencies. The characteristic silicate gap between the symmetric and antisymmetric stretching modes is

clearly shown by the SE- model. The E-model does not reproduce the frequency gap very accurately.

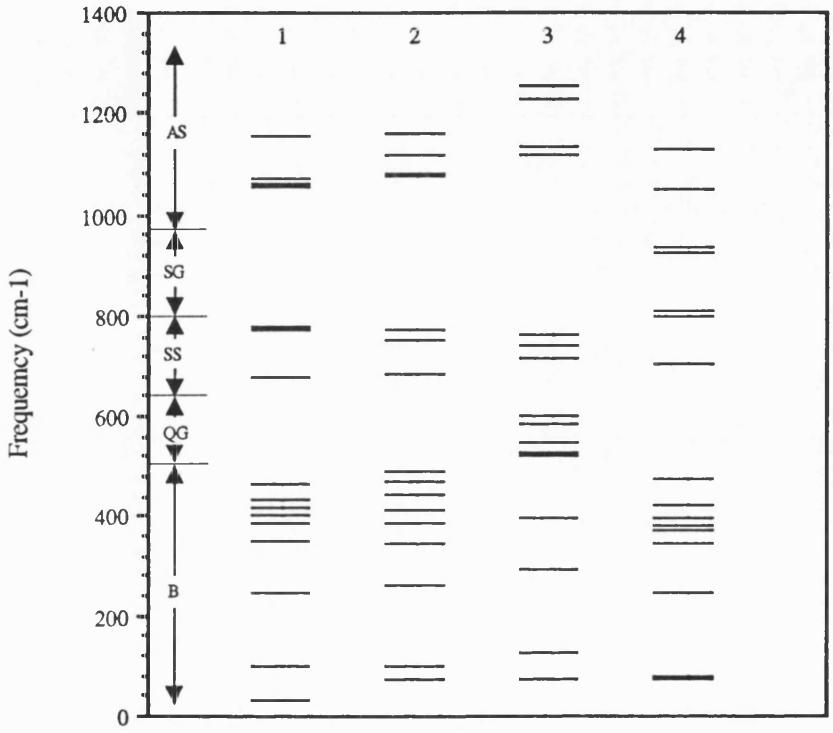

Figure 5.11: Comparison between the experimental q=0 vibrational model of β-quartz and the calculated spectra; (1) experimental frequencies from Gervais and Piriou (1975); (2) calculated frequencies by Etchepare et al (1973); (3) calculated frequencies using the SE-model; (4) calculated frequencies using the E-model; B denotes bending modes, SS and AS symmetric and anti-symmetric stretching modes, QG the quartz gap and SG the silicate gap.

Summary

The calculation of the vibrational frequencies show that independent of which potential model has been used the results for α and β-quartz are the same. The lower frequencies or

bending modes are better reproduced by the E-model, whereas the stretching modes are slightly more accurate if the SE-model is used.

In the SE-model the only forces are those due to Si-O and O-O interactions, whereas the E- model is a three-body shell model, where a O-Si-O bond-bending term is included. From the calculated results it can be seen that the SE-force fields show only poor agreement with experiment in the lower frequency ranges or in the bending vibrations of the O-Si-O and Si-O-Si angles and that further stiffening is needed. Therefore an additional force or bond-bending term or shell model included to the SE- model may lead to more accurate results.

As a conclusion both models are able to simulate the vibrational spectra of α-and β-quartz. However, in general the E-model performs better.

5.3.3. Elastic properties of α-quartz at different temperatures

In the static lattice simulation studies it was shown that the second order elastic constant tensors for α-quartz are slightly better reproduced by the SE-model. The elastic constant tensors have also been calculated at elevated temperatures and compared to experiment. Wang (1990) measured the six independent second order elastic constants from 243K to 400K. In Tables 5.6 a,b the measured and calculated elastic constants at 300K and 400K are shown. The calculated elastic constants using the E-model show reasonable agreement with experiment, except for c_{11}, c_{12} and c_{13} in both temperature ranges. Using the SE-potential model for calculating the elastic constants, good agreement with

experiment is obtained at 300K and 400K. Only c_{44} at both temperatures and c_{12} at 400K show a deviation of 14% form experiment.

	Wang (1990)	E - model	SE - models
c_{11}	84.84	95.59 (1.13)	88.44 (1.04)
c_{12}	5.31	12.08 (2.26)	5.18 (0.98)
c_{13}	12.24	16.70 (1.36)	12.49 (1.02)
c_{14}	17.66	16.31 (0.92)	18.11 (1.03)
c_{33}	105.44	111.52 (1.06)	102.05 (0.98)
c_{44}	57.75	50.57 (1.01)	49.35 (0.86)
c_{66}	39.77	41.75 (1.05)	41.63 (1.05)

Table 5.6a: Experimental (Wang, 1990) and calculated elastic constant tensors (in GPa) at 300K; the numbers in brackets show the statistical accuracy of the calculated elastic constants.

	Wang (1990)	E - model	SE -model
c_{11}	84.18	95.85 (1.14)	88.27 (1.05)
c_{12}	3.42	11.42 (3.33)	3.91 (1.14)
c_{13}	11.20	16.42 (1.47)	11.42 (1.02)
c_{14}	17.72	16.43 (0.93)	18.37 (1.04)
c_{33}	103.18	111.28 (1.08)	99.74 (0.97)
c_{44}	56.92	50.77 (0.89)	49.21 (0.86)
c_{66}	40.38	42.21 (1.04)	42.18(1.04)

Table 5.6b: Experimental (Wang, 1990) and calculated elastic constant tensors (in GPa) at 400K; the numbers in brackets show the statistical accuracy of the calculated elastic constants.

The elastic constant tensors are second derivatives of the lattice energy with respect to the strain. The temperature derivatives of the elastic constant tensors are third derivatives of the lattice energy and therefore they represent an even more stringent test on the validity of the potential models.

Atanasoff and Hart (1941) and Wang (1990) give experimental temperature derivatives for all six elastic constants in the temperature range from 273K to 363K and from 243K to 393K, respectively. In Table 5.7 the measured and calculated temperature derivatives of the elastic constants are listed. The temperature derivatives have been obtained by a least square fit method in temperature ranges as shown in Table 5.7.

Comparing the two experimental derivatives for the temperature range 273K to 363K some deviations are notable, especially the values of $(\delta c_{13}/\delta T)_{P,T=0}$, $(\delta c_{14}/\delta T)_{P,T=0}$ and $(\delta c_{66}/\delta T)_{P,T=0}$. But all of the $(\delta c_{ij}/\delta T)_{P,T=0}$ are negative, except the $(\delta c_{14}/\delta T)_{P,T=0}$ and $(\delta c_{66}/\delta T)_{P,T=0}$.

The temperature derivatives of the E-model show poor agreement with the experimental data. Only the values of $(\delta c_{13}/\delta T)_{P,T=0}$ and $(\delta c_{33}/\delta T)_{P,T=0}$ are in reasonable agreement. The derivatives $(\delta c_{11}/\delta T)_{P,T=0}$ and $(\delta c_{14}/\delta T)_{P,T=0}$ show instead of negative, positive signs.

Comparing the derivatives of the SE-potential model with experimental data much better agreement is obtained. In particular the theoretical and measured values of $(\delta c_{14}/\delta T)_{P,T=0}$ and $(\delta c_{33}/\delta T)_{P,T=0}$, agree well. All calculated temperature derivatives in the SE-model show the same signs as the experimental derivatives.

Thus in the simulation of the elastic constant tensors and their temperature derivatives the application of the SE-model is certainly better.

c_{ij}	$(\delta c_{ij}/\delta T)_{P,T=0}$				
	exp (273-363 K) [1]	exp (273-363 K) [2]	exp (243-393 K) [2]	E - model (200 - 400K)	SE - model (200 - 400K)
c_{11}	-0.00435	-0.0042	-0.0037	0.0024	-0.0017
c_{12}	-0.01821	-0.0243	-0.0228	-0.0061	-0.0118
c_{13}	-0.00765	-0.0026	-0.0049	-0.0026	-0.0099
c_{14}	0.00184	0.0041	0.0037	0.0011	0.0025
c_{33}	-0.02270	-0.0256	-0.0238	-0.0023	-0.0218
c_{44}	-0.00965	-0.0087	-0.0087	0.0018	-0.0029
c_{66}	0.00693	0.0101	0.0096	0.0043	0.0050

Table 5.7: The experimental ((1) Atanasoff and Hart (1941); (2) Wang (1990)) and calculated temperature coefficients of the elastic constants of α-quartz;

5.3.4. Thermodynamic properties of α-quartz

As a further test for the validity of the two potential models is the simulation of the thermodynamic properties of α-quartz.

The heat capacities at constant pressure C_p and entropies S were calculated at various temperatures and zero pressure using the empirical and semi-empirical potential parameters.

The results of the calculated heat capacities and the experimental results from Grønvold et al (1989), Hemingway (1987) and Richet et al (1982) are reported in Table 5.8 and plotted in Figure 5.12. The calculated results using the E-model are in very good agreement with experimental values, whereas using the SE-model a bigger deviation is obtained. The results of the E-model and SE-model are within 2.3% and 9.8% respectively using the predicted values from Richet et al (1982).

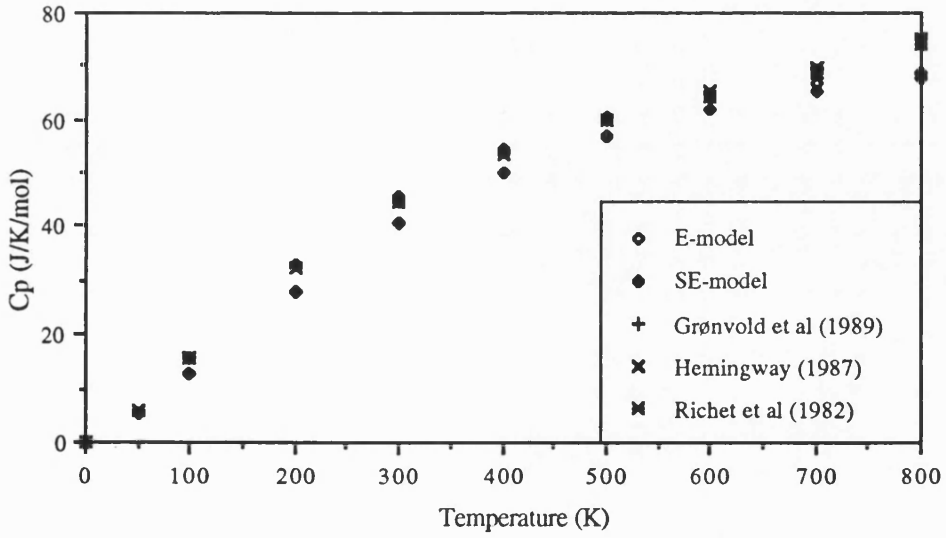

Figure 5.12: The experimental and predicted heat capacity (Cp) of α-quartz

Temperature (K)	Grønvold et al (1989)	Hemingway (1987)	Richet et al (1982)	E - model	SE - model
0			0	0	0
50			5.808	5.642 (1.03)	5.288 (1.10)
100			15.696	15.636 (1.004)	12.865 (1.22)
200			32.622	32.989 (0.99)	28.175 (1.16)
300	44.70	44.78	44.700	45.523 (0.98)	40.877 (1.09)
400	53.87	53.27	53.429	54.259 (0.98)	50.277 (1.06)
500	60.05	59.68	59.649	60.129 (0.99)	56.955 (1.05)
600	64.76	65.04	64.382	64.110 (1.004)	61.709 (1.04)
700	69.20	69.82	68.696	66.901 (1.03)	65.189 (1.05)
800	75.51	74.25	75.255	68.942 (1.09)	67.854 (1.11)

Table 5.8: Calculated and experimental heat capacity at constant pressure C_p for α-quartz (C_p=J K^{-1} mol^{-1}); the numbers in brackets show the statistical accuracy of the calculated heat capacity relative to the data from Richet et al (1982).

The calculated results of the entropies S, using both potential models are in a good agreement with experimental data, although the deviation at low temperatures (between 50K and 100K) is relatively high. The simulated and experimental results are listed in Table 5.9 and Figure 5.13.

Again the outcome of the E-model shows a slightly better agreement with experimental values than the SE-model.

Temperature (K)	Grønvold et al (1989)	Hemingway (1987)	Richet et al (1982)	E - model	SE - model
0			0	0	0
50			2.630	4.031 (0.65)	4.181 (0.63)
100			9.685	10.965 (0.88)	10.151 (0.95)
200			26.076	27.458 (0.95)	23.836 (1.09)
300	41.74	41.736	41.715	43.345 (0.96)	37.773 (1.10)
400	55.89	55.853	55.842	57.723 (0.97)	50.895 (1.10)
500	68.57	68.454	68.469	70.512 (0.97)	62.876 (1.09)
600	79.93	79.820	79.778	81.859 (0.98)	73.709 (1.08)
700	90.25	90.211	90.023	91.977 (0.99)	83.505 (1.08)
800	99.85	99.827	99.561	101.070 (0.99)	92.407 (1.08)

Table 5.9: Calculated and experimental entropy S for α-quartz (S = J K^{-1} mol^{-1}); the numbers in brackets show the statistical accuracy of the calculated entropy relative to the data from Richet et al (1982).

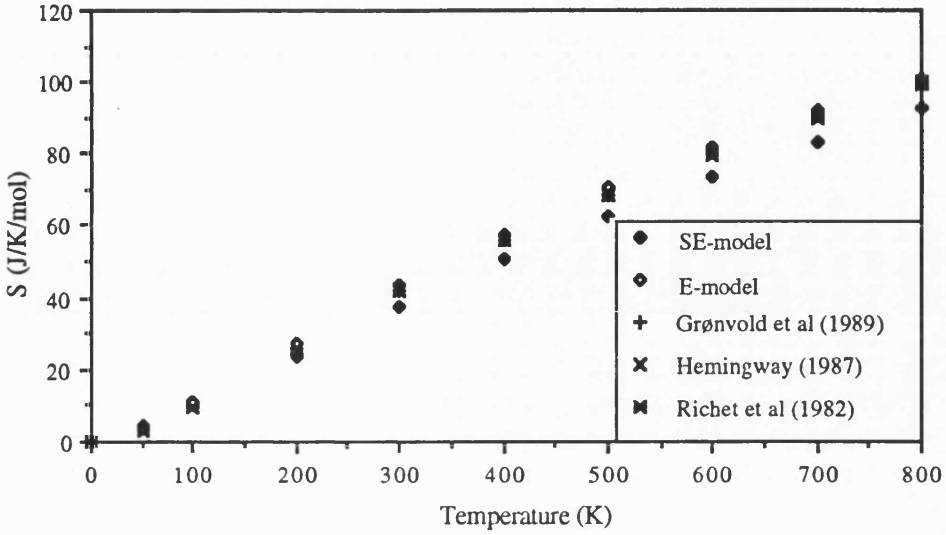

Figure 5.13:The experimental and predicted entropy (S) of α-quartz

5.3.5. Structure of α-quartz at different pressures

The simulation studies so far did not show clearly which of the two potential models performs better in order to employ it for further simulation studies. On the contrary, the outcome of the application of these two potential models is rather inconclusive. The E-model performs only slightly better in the simulation of the cell dimensions and thermodynamic properties at elevated temperatures, whereas the bond-distances and bond angles are slightly better reproduced by the SE-model. But the discrepancies in these studies between the models are very small. The simulation studies of the second order elastic constant tensors and their temperature derivatives showed clearly that the SE-model performs better. In order to get more clarity of the potential models, further

simulation studies will be performed at different pressures.

α-quartz is stable at room temperature between ambient pressure and 30 kbar and it persists metastable at room temperature at higher pressures. Above 150 kbar, however, quartz undergoes a gradual transition to an amorphous form (Hemley et al, 1987).

Free energy minimisation enables to simulate the structure and properties of quartz at elevated pressures. Again the two potential models are compared with available experimental data. The structure of α-quartz has been simulated in a pressure range from 0.01 kbar to 120 kbar at 0K and 300K. The differences in the results between 0K and 300K at elevated pressures do not show a large change and therefore the structure at 0K will be compared with experimental results in this study.

In Table 5.10 the lattice parameters and the volume for α-quartz at different pressures using the E- and SE-force field parameters are shown. For comparison the experimental determined lattice parameters and volumes from Levien et al (1980) and Hazen et al (1989) are also listed in this table. The calculated lattice parameters *a* and *c* using both potential models show a contraction with increasing pressure and are in very good agreement with experimental data. Comparing the compression of the lattice parameters in a pressure range from 0.01 kbar to 120 kbar the a-axis is reducing by 0.37Å after Hazen et al (1989), by 0.36Å and 0.37Å using the E- and SE-force field parameters respectively.

The lattice constant *c* shows excellent agreement with experimental data up to 50 kbar for both potential models. From 50 kbar onwards both models show a slight deviation from the experimental determined lattice parameter *c*. Comparing the reduction of the c-axis in a pressure range from 0.01 kbar to 50 kbar the experimental data by Levien et al (1980) show a decrease of 0.15Å, the E-model also by 0.15Å and the SE-model by 0.10Å. In a pressure range from 0.01 kbar to 120 kbar the compression is 0.23Å after Hazen et al (1989), 0.31Å and 0.17Å respectively for the E- and the SE-model.

	Levien et al (1980)			Hazen et al (1989)			E - model			SE - model		
pressure	*a*	*c*	Vol	*a*	*c*	Vol	*a*	*c*	Vol	*a*	*c*	Vol
0.001	4.9160	5.4054	113.13	4.9140	5.4060	113.06	4.8668	5.3748	110.25	4.9204	5.4328	113.91
1							4.8629	5.3715	110.00	4.9160	5.4295	113.64
5							4.8473	5.3581	109.03	4.8989	5.4170	112.59
10							4.8282	5.3419	107.84	4.8784	5.4031	111.36
20				4.8120	5.3272	106.84	4.7913	5.3106	105.58	4.8398	5.3792	109.12
20.7	4.8362	5.3439	108.24									
30							4.7561	5.2809	103.45	4.8039	5.3595	107.11
31	4.7850	5.3070	105.26									
37.6	4.7736	5.3010	104.61									
48.6	4.7390	5.2785	102.66									
50				4.7052	5.2502	100.66	4.6902	5.2254	99.55	4.7378	5.3284	103.58
55,8	4.7222	5.2673	101.72									
61.4	4.7022	5.2561	100.65									
80				4.6251	5.2162	96.65	4.6023	5.1506	94.48	4.6498	5.2939	99.12
95				4.5940	5.2002	95.03						
100							4.5504	5.1052	91.55	4.5973	5.2751	96.55
120							4.5033	5.0629	88.92	4.5491	5.2581	94.23
125				4.5353	5.1705	92.09						

Table 5.10:Experimental and theoretical unit cell parapmeters for α-quartz at several pressures (*a* and *c* = Å; Vol = $Å^3$; pressure in kbar)

The compression of α-quartz is anisotropic with the a-axis approximately 60% more compressible than *c* at room-pressure. The *c/a* axial ratio thus increases with pressure. The *c/a* cell parameter ratio is plotted vs pressure in Figure 5.14. For the *c/a* ratio to increase with pressure the *c* direction is elastically stiffer than *a*. Both potential models show again a very good agreement with the experimental data up to 50 kbar. From 50 kbar onwards a slight deviation of the theoretical results from the experimental values can be seen, which is due to the deviation of the lattice parameter *c* at higher pressures.

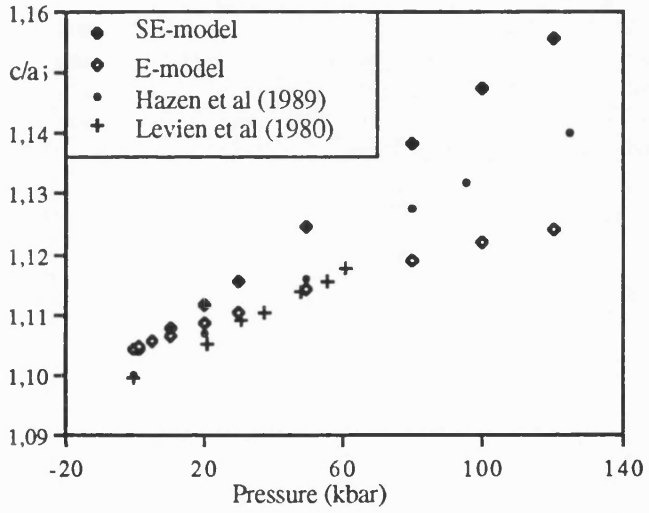

Figure 5.14: The c/a unit cell parameter ratio as a function of pressure for experimental and theoretical compressibility studies of α-quartz.

The calculated volume-pressure data for quartz plotted in Figure 5.15 show good agreement with the Birch-Murnaghan curve calculated from the bulk modulus and the pressure derivatives of the bulk modulus by Levien et al (1980) and Hazen et al (1989). A pressure-volume data fit to a Birch-Murnaghan equation of state yields a bulk modulus of 34 ± 4 GPa and a pressure derivative of 5.7 ± 0.9 by Hazen et al (1989) and Levien et al (1980) obtained 38.1 ± 0.2 GPa and 6.2 ± 0.1 respectively. The calculated bulk modulus

using the E-force fields us 44.8 GPa and the pressure derivative is 2.2. The bulk modulus employing the SE- potential model is with 42.18 GPa and a pressure derivative of 4.3 slightly closer to experimental values.

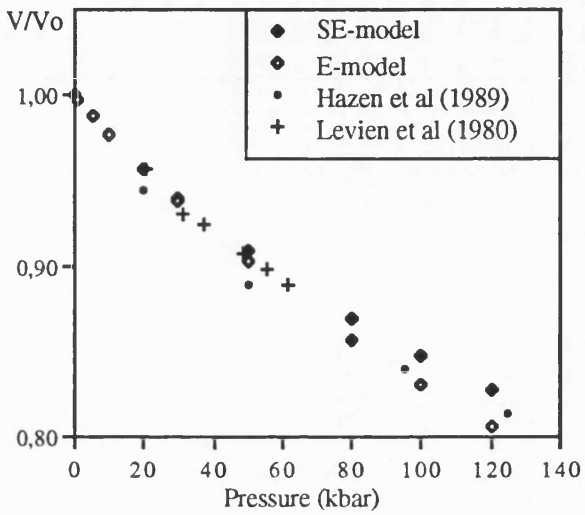

Figure 5.15: Experimental and calculated unit cell volume normalised to the ambient unit cell volume for the compressibility studies of α-quartz.

Most oxide crystals compress by two principal structural mechanisms: shortening of the T-O distance and reduction of the T - O - T angles. Only the second of these is important in quartz and undergoes a main structural change (Hazen and Finger, 1984).

The structural element responsible for the anomalously high compressibility of quartz is the Si-O-Si inter-bond angle which decreases non-linearly. In Figure 5.16 the Si-O-Si bond angle vs pressure using the E- and the SE-force-field parameters, compared to experimental data by Hazen et al (1989) and Levien et al (1980) is shown. Although the calculated bond angles are slightly higher compared to the the experimental values they show the same trend.

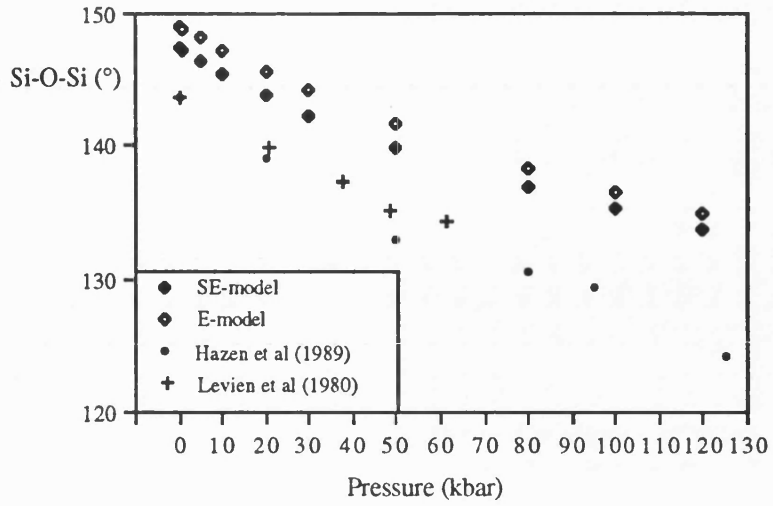

Figure 5.16: Experimental and calculated Si-O-Si bond angle as a function of pressure for α-quartz.

The Si-O distance of the experimental data from Hazen et al (1989) show no significant change with pressure; up to 125 kbar the average distance remains 1.61Å. Levien et al (1980) reported a decrease of the Si-O distance from 1.6009Å at room pressure to 1.6005Å at 61.4 kbar. Both potential models show a slightly bigger decrease of the calculated Si-O distances. Using the SE-force-field parameters the Si-O distance decreases from 1.6001Å at room pressure to 1.5928Å at 50 kbar and to 1.589Å at 120 kbar. The E-model shows a decrease from 1.574Å at 0.01 kbar to 1.562Å at 50 kbar to 1.552Å at 120 kbar.

The O-O distance within the silicate tetrahedron also decreases as pressure is increased. Levien et al (1980) measured an average decrease of 0.006Å in a pressure range from 0.01 kbar to 61.4 kbar and Hazen et al (1989) of 0.0147Å in a pressure range from 0.01 kbar to 95 kbar. Comparing the calculated O-O distances of the SE-model the distance is decreasing by 0.0127Å between 0.01 kbar and 50 kbar and 0.0211Å between 0.01 kbar

and 125 kbar and the E-model shows a decrease from 0.0210Å and 0.0435Å respectively.

The increased tetrahedral distortion is also reflected in the O-Si-O internal tetrahedral angles. Whereas the experimental data show a slight increase of the O-Si-O angle up to 50 kbar and above this pressure a slight decreasing angle, both theoretical models show a slight decrease of the O-Si-O angle throughout.

Summary:

As in the simulation studies at elevated temperatures both potential models reproduce the structural parameters very well. The lattice parameters are again slightly better reproduced by the E-model. The bond distances and the bond angles are in slightly better agreement with experiment using the SE-model, as in previous studies. As in section 5.3.1., where the effect of temperature on quartz was simulated, it has to be stressed that the differences between the simulated structural parameters of both potential models are small.

The Si-O-Si bond angles, which were simulated already too high at elevated temperatures (see section 5.3.1.) are also too high at elevated pressures compared to experimental values, independent which potential model was used, for reasons discussed elsewhere in this chapter.

Structural interdependence between Si-O-Si and Si-O:

As in the simulation studies at elevated temperatures (section 5.3.1.) the structural interdependence between the Si-O-Si angle and the Si-O distance as described by Hill and

Gibbs (1979) is also not given at elevated pressures . The relationship -sec(Si-O-Si) ∝ d(Si-O) suggests that as the Si-O-Si angle decreases the Si-O distance will increase. It would predict that with increasing pressures the Si-O distance might actually increase.

The theoretical calculations but also the experimental data by Levien et al (1980) show that this correlation does not persist with increased pressure, because a decrease of both, the Si-O-Si angle and the Si-O distance is observed.

Comparing the structural changes at elevated temperatures and pressures by plotting the unit cell volume against the Si-O-Si angle and the tetrahedral tilt angle, δ, respectively, it can be seen that the structural changes take place during thermal expansion and isothermal compression are not simply inverse. In Figure 5.17 the Si-O-Si angle of α-quartz as a function of the unit cell volume at elevated temperatures or pressures normalised to room-temperature-pressure volume is shown. Again the results of both potential models are shown. In this figure it can be seen that there is a break in the slope of the lines connecting the temperature and pressure points. This is showing that in these two regimes partially different structural changes must be responsible for the change of volume.

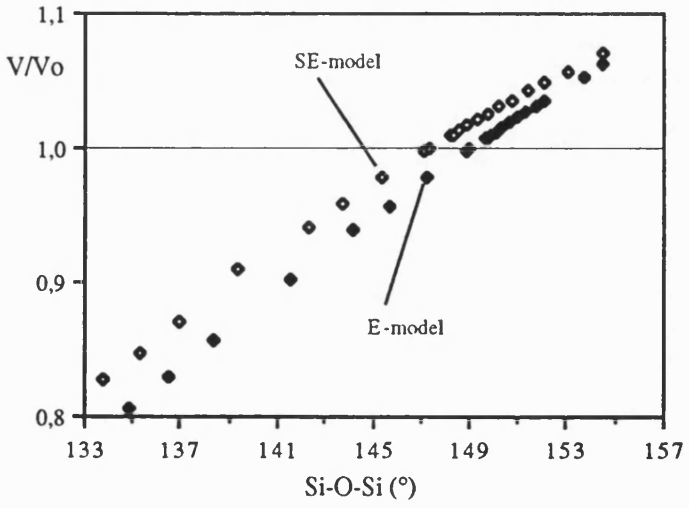

Figure 5.17: The Si-O-Si angle as a function of the unit-cell volume normalised to the room-temperature-pressure volume at elevated temperatures and pressures for α-quartz.

In Figure 5.18 the tetrahedral tilt angle for quartz, δ, is shown as a function of unit cell volume at temperature and pressure normalised to the room-temperature-pressure volume. The curve for both potential models shows that the tilt angle decreases from the connecting temperature and pressure point rapidly as the α–β transition is approached. The curve also shows that the tilt angle increases in magnitude more slowly as pressure is increased and therefore the unit cell volume is decreased. As temperature is increased there may be a small increase in distortion, when pressure is increased the tetrahedral distortion increases considerably.

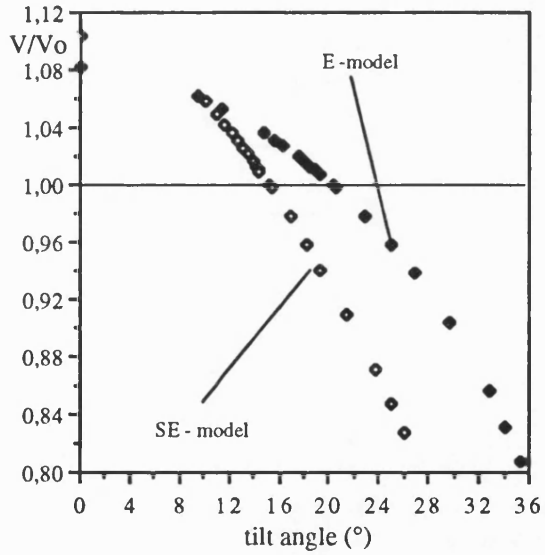

Figure 5.18: The tetrahedral tilt angle, δ, for α- quartz as a function of unit cell volume normalised to the room-temperature-pressure volume at elevated temperatures and pressures.

The volume increase with temperature is characterised through changes in the Si-O-Si angle and the tilt angle, whereas compression seems to be characterised by the Si-O-Si angle and increasingly by tetrahedral distortion. Therefore we can conclude that the

silicate tetrahedron does not show inverse effects.

As already mention in section 5.3.1. the described relationship between the Si-O-Si bond angle and Si-O bond distance was also not found with increasing temperature. But Gibbs and Hill (1979) and some other authors (Taylor, 1972; Boisen et al, 1990; Downs et al, 1990) showed, as mentioned already, an inverse relationship between the Si-O-Si bond angle and Si-O bond distance using multiple regression analysis for silica polymorphs and silicates.

Baur (1971, 1977) undertook a regression analysis of the Si-O bond length as a function of the Si-O-Si bond angle for a data set that included several silica polymorphs and silicates. He observed no inverse relationship between the bond angle and bond distance. Only 4% of the variation of the Si-O distances could be explained in terms of a linear dependence on the Si-O-Si bond angle and therefore he concluded that this relationship could not be viewed as a general property.

Liebau (1985) observed that more than 50% of the variation of the Si-O bond distance in a data set can be explained in terms of a linear dependence on B(O), the isotropic displacement factor of the oxygen ions. This result led him to the conclusion that the correlation between bond distance and bond angle for the silica polymorphs should be viewed with reservation. Thus B(O) may be included in a multiple regression analysis of the bond length and angle data observed in silica polymorphs, especially when their structures have been determined at a variety of temperatures.

The structural analysis for quartz at a number of temperatures and pressures seems to be supported by this assertion and thus it could be shown that the silicate tetrahedron does not show inverse effects.

5.3.6. Elastic properties of α-quartz at different pressures

The calculated elastic constant tensors and the bulk modulus at zero pressure and temperature are in good agreement with the measured quantities (table 5.1) for both potential models, although the SE-model appeared to be slightly better. The simulation of the second order elastic constant tensors and on when considering the temperature derivatives has shown that the SE-model performs clearly better compared to the E-model.

To test the outcome of the performed simulation studies the pressure dependence of the second order elastic constant tensors and the bulk modulus of α-quartz have been calculated from ambient pressure to 12 GPa at 0K and 300K respectively using both potential models.

In Figure 5.19 and Figure 5.20 it is shown that the calculated results of both potential models show non-linear dependence of the elastic constants on pressure. As an interesting feature c_{44} reaches a maximum at about 3 GPa, while c_{66} has a minimum at about 8 GPa using the SE-model. Using the E-model to calculate the elastic constant tensors this feature for c_{44} and c_{66} was not observed, but therefore c_{11} reaches a minimum at about 5 GPa.

Measurements have been made by Wang et al (1992) and McSkimin et al (1965) to obtain the hydrostatic pressure derivative of the six independent second order elastic constant tensors and the bulk modulus of α-quartz. In Table 5.11 the experimentally determined and the calculated values of the hydrostatic pressure derivatives of the elastic constant tensors are listed. The pressure derivatives of the second order elastic constants have been obtained by a least square fit method applied to the data from zero pressure to 0.5 GPa. The pressure derivatives obtained from the theoretical calculations do not show a

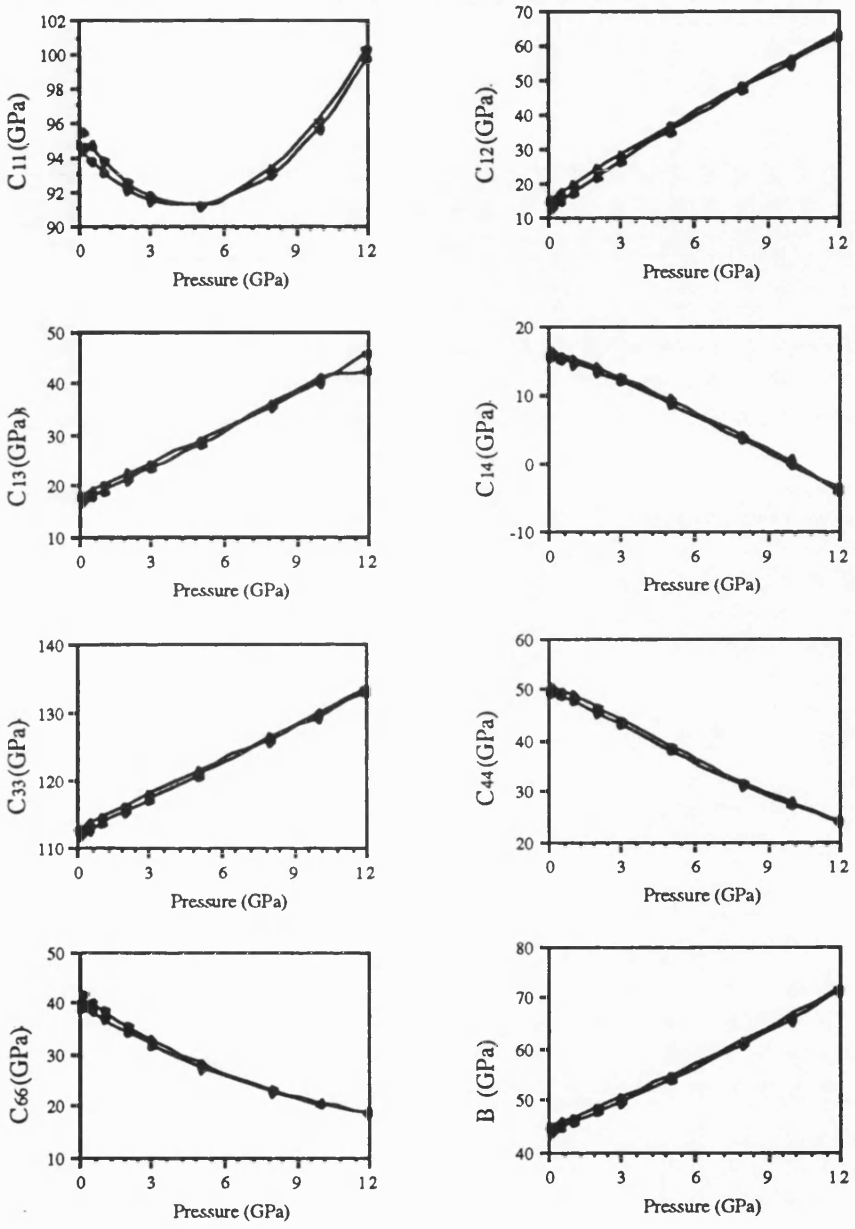

Figure 5.19: The hydrostatic pressure dependence of the elastic stiffness tensor components c_{ij} of α- quartz at 0K (open diamonds) and 300K (filled diamonds) calculated using the E-potential parameters.

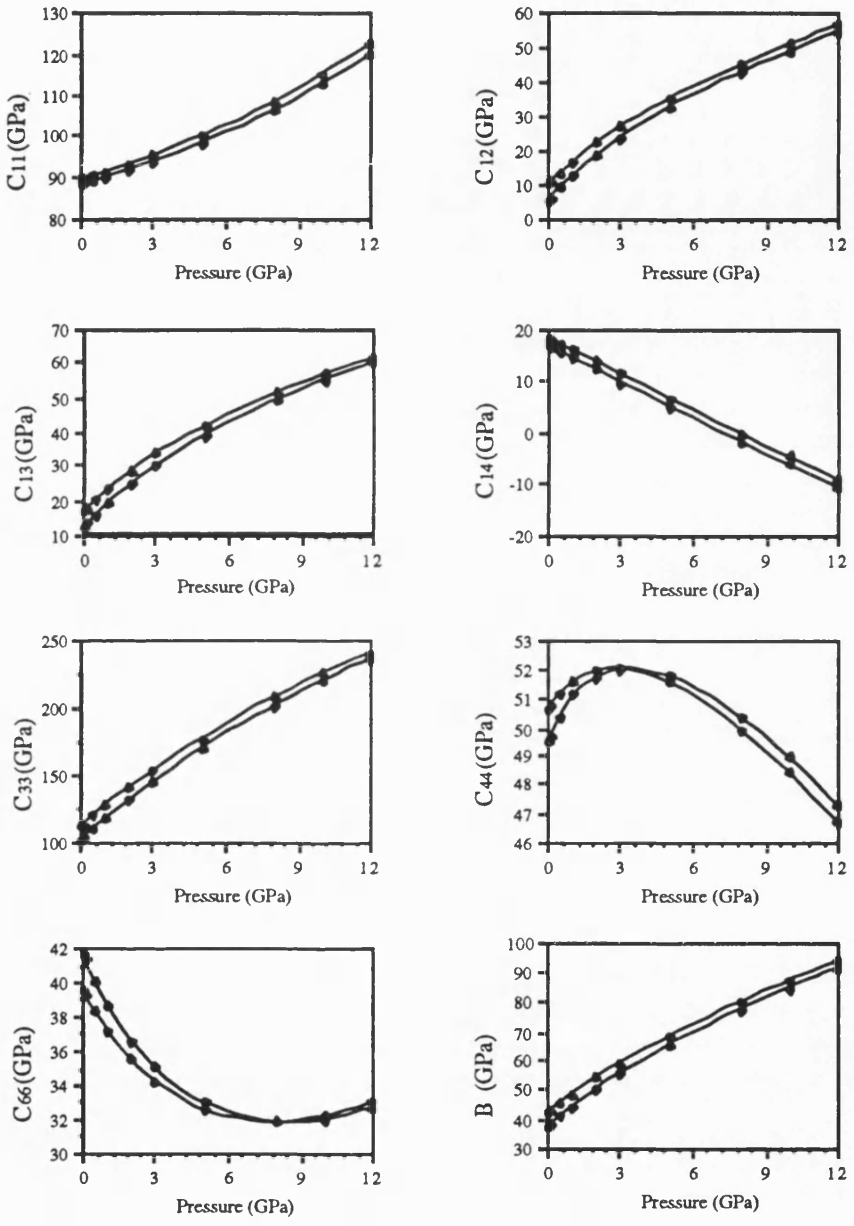

Figure 5.20: The hydrostatic pressure dependence of the elastic stiffness tensor components c_{ij} of α-quartz at 0K (open diamonds) and 300K (filled diamonds) calculated using the SE-potential parameters.

large change between 0K and 300K, independent which potential model was used.

Comparing the pressure derivatives of the two potential models with experimental results, the SE- model is in a better agreement with experimental data than the E-model. Especially $(\delta c_{11}/\delta P)_{T,P=0}$ and $(\delta c_{14}/\delta P)_{T,P=0}$ which show a negative sign, however results using the E-force-field parameters, do not agree with experimental results, which show positive signs for these derivatives. Only $(\delta c_{66}/\delta P)_{T,P=0}$ is in reasonable agreement with the experimental measurements. In view of the complexity of quartz the calculated pressure derivatives using the SE-force field parameters and the measured hydrostatic pressure derivatives by Wang et al (1992) and McSkimin et al (1965) are in good agreement. In addition the pressure derivative of the bulk modulus measured by Wang et al (1992) is very close to the calculated derivative using the SE-potential model.

All of the $(\delta c_{ij}/\delta P)_{T,P=0}$ using the SE-model are positive, except for the $(\delta c_{14}/\delta P)_{T,P=0}$ and $(\delta c_{66}/\delta P)_{T,P=0}$. Thus agrees very well with the measured data by Wang et al (1992), whereas McSkimin et al (1956) measured a positive $(\delta c_{14}/\delta P)_{T,P=0}$, which does agree with the E-model. However the key discrepancies of $(\delta c_{11}/\delta P)_{T,P=0}$ which is negative for both experiments, suggests here are problems with the E-model.

The negative pressure derivative of the elastic constants and the α-β phase transition:

In section 5.3.3. the calculation of the temperature derivatives of the elastic constants, using the SE-model, has shown that all $(\delta c_{ij}/\delta T)_{P,T=0}$ are negative, except $(\delta c_{14}/\delta T)_{P,T=0}$

	$(\delta c_{ij} / \delta P)_{T, P=0}$							
	c_{11}	c_{12}	c_{13}	c_{14}	c_{33}	c_{44}	c_{66}	Bulk Modulus
SE - model								
0K	1.72	6.79	6.31	-2.22	14.72	1.10	-2.53	6.33
300K	1.41	7.89	6.91	-1.98	15.39	1.75	-3.24	6.85
E - model								
0K	-1.58	4.73	2.14	-1.11	1.81	-1.93	-3.15	1.85
300K	-1.95	5.16	2.23	-1.01	1.89	-1.76	-3.55	1.92
McSkimin et al (1965)								
77K	3.40	7.40	5.41	2.00	10.26	1.77	-2.00	
298K	3.28	8.66	5.97	1.93	10.84	2.66	-2.69	
Wang et al (1992)								
298K	1.49	12.12	4.04	-3.96	9.51	1.84	-5.32	5.92

Table 5.11: Comparison between the calculated values of the hydrostatic pressure derivatives $(\delta c_{ij} / \delta P)_{T, P=0}$ of the elastic constant tensors of α-quartz and those measured experimentally. The pressure derivatives of the second order elastic constants have been obtained by a least squarte fit method applied to the data from zero pressure to 0.5 GPa.

and $(\delta c_{66}/\delta T)_{P,T=0}$, which are positive.

That the hydrostatic pressure derivatives $(\delta c_{14}/\delta P)_{T,P=0}$ and $(\delta c_{66}/\delta P)_{T,P=0}$ have negative signs and the temperature derivatives $(\delta c_{14}/\delta T)_{P,T=0}$ and $(\delta c_{66}/\delta T)_{P,T=0}$ have positive signs has an interesting consequence concerning the nature of the α–β displacive phase transition of quartz. The transition is driven by an optic phonon which is very soft in the (Γ00) direction (Axe and Shirane, 1970). In α-quartz there is only one irreducible representation for phonons with **q** in the (Γ00) direction so that one branch cannot cross another; as the optic branch softens it pushes the transverse-acoustic phonon in that direction down. The acoustic branch has a slope $\omega/\mathbf{q}$ equal to $(c_{66}/\rho)^{1/2}$ (Wang et al, 1992). The shear elastic stiffness c_{66} for α-quartz show an anomalous increase with temperature (section 5.3.3.) and $(\delta c_{66}/\delta P)_{T,P=0}$ has a negative value, features which identify acoustic-mode softening (Sidek et al, 1987; Hemely et al, 1988).

A decrease in the elastic constant under the influence of pressure and an increase under the influence of temperature can be driven principally by an elastic instability, because it corresponds to a reduction in crystal stiffness for the associated acoustic phonon mode. The anomalous derivative for c_{66} indicates that even at room temperature there may be an interaction between the soft optic phonon and the acoustic phonon in the same crystal direction (Wang et al, 1992).

The main contribution to the strain at the α–β transition is produced by rotation of the SiO_4 tetrahedra, which comprises the displacement parameter in the α-quartz structure. The displacement can be shown by the anomalous behaviour of c_{66}, but also by that of c_{14}. The

soft optic mode has B_1 symmetry in β-quartz. There is no plane wave of B_1 symmetry in quartz: c_{14} is always coupled to other elastic constants (Wang et al, 1992). Höchli and Scott (1971) showed that the soft elastic constant c_{14} in α-quartz is related to the displacement parameter x_0 by $c_{14} \sim x_0$ and ultrasonic measurements show that near the transition temperature the elastic constant c_{14} (T) behaves as the displacement parameter, as does the soft optic phonon frequency ω(T). Therefore it can be concluded that the negative $(\delta c_{14}/\delta P)_{T,P=0}$ and the positive $(\delta c_{14}/\delta T)_{P,T=0}$ is also one of the results of the interaction between the soft optic phonon and the acoustic phonon in quartz.

5.3.7. α–β quartz phase transition

Although the method allows us to simulate the transition from the low-temperature form to the high-temperature form, the calculated transition temperatures are much higher than the experimental temperatures much higher, which has been mentioned already in a previous section (5.3.1). The E-model the α-quartz structure transforms to the β-quartz polymorph at 1400K, whereas the SE-model transformation takes place at 1200K. This shifted transition temperature is probably due to the sensitivity of the quasi-harmonic approximation near an instability coupled with a difference in the potential parameters which results in the large error in simulating the phase-transition at the experimentally observed temperature.

The soft mode at 207cm^{-1}

The α- β phase transition has been commonly regarded as the classical example of a second order (displacive) phase transition. Second order or displacive phase transitions are characterised by certain symmetry restrictions and by the presence of anharmonic effects. A consequence of the presence of anharmonic effects is that the frequencies of some phonons may change drastically with temperature to attain zero value at the transition temperature. The idea behind this mode softening is that with decreasing frequency the atomic displacements become larger and at the transition temperature with ω=0, the dynamic atomic displacements become frozen in as a static displacement. Scott (1986) and Höchli and Scott (1971) presented evidence that the α-β phase transition is driven by an optic phonon mode at 207cm^{-1} (A_1 mode in α-quartz at room temperature) which is very soft in the [Γ00] direction. Kleinmann and Spitzer (1962) found that the eigenvectors of this A_1 mode correspond closely to the atomic displacements occurring at the transition and they attributed it to the movement of oxygen atoms as the quartz tetrahedra rotate from one Dauphinè twin orientation to the other.

In Figure 5.21 the calculated optic phonon mode at 207cm^{-1} at the Brillouin zone centre as a function of temperature for both potential models is shown. With increasing temperature this mode softens but it does not become zero at the transition point. Also neutron scattering experiments by Axe and Shirane (1970) indicated that this mode does not vanish entirely at the transition temperature. As the frequencies of this soft mode do not become zero this is indicating the structure at the transition temperature is not frozen in as a static displacement but that there is still a dynamic displacement present. Both potential models show the same trend with increasing temperature, although the mode calculated with the SE-force-field parameters is slightly higher (this result has been discussed in greater detail in section 5.3.2.). The observations at the Γ-point establish the picture of a displacive type of phase transition, that means the existence of a soft "optic"

phonon mode. The eigenvectors of which shows close similarity to the structural displacement at the phase transition.

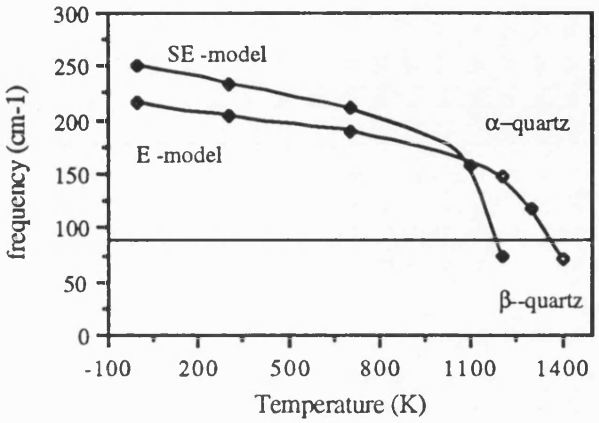

Figure 5.21: The optic phonon of the E- and SE- model which becomes very soft in the [Γ00] direction with increasing temperature.

The importance of the tilt angle

As described earlier in section 5.3.1.the conversion of α- to β-quartz can be described geometrically through the tilt angle δ; in the β-quartz structure the tilt angle is zero, but in the α-quartz structure the tilt angle is either positive or negative 16.3° at room temperature and decreases to about ±7° at the onset of the transition. The two possible directions of the tetrahedral tilt are equally and they correspond to two distinct α_1 (right handed) and α_2 (left handed) twin orientations, commonly denoted as Dauphinè twins. One Dauphinè twin can be transferred to the other by a 180° rotation around *c*.

From this model the β-quartz modification can be considered geometrically as a spatial average of the two Dauphinè twin configurations (Heaney and Veblen, 1991). Only by rotating the silica tetrahedra around the [100] axis in proper directions the α_1 configuration can be easily converted to the α_2. Considering that the tetrahedra oscillate from one modification to the other at very high frequencies, the resulting structure would be indistinguishable from the static structure of the ideal hexagonal β-quartz. This supports the hypothesis that the β-quartz polymorph is not a static structure with each atom position at a potential minimum, but that β-quartz is a dynamic structure oscillating in between the two opposite α_1 and α_2 modifications with each atom vibrating between two potential minima (Heaney and Veblen, 1991).

In Figure 5.22 and Figure 5.23 the Gibbs free energy and the lattice energy of both potential models as a function of the tilt angle is plotted for quartz. Considering the lattice energy as a function of the tilt angle, the tilt angle for each silica modification connects two energetically equivalent twin structures (α_1 and α_2) which correspond to the minima energy curves. The intermediate maxima at $\delta=0^\circ$ corresponds to the high temperature phase (β-quartz). Both potential models show the same trend, but the E-model shows a slow increase of the lattice energy until the transition point, whereas the the SE-model shows a continuous increase of the lattice energy with decreasing tilt angle.

Considering the Gibbs free energy as a function of the tilt angle, both silica modifications(α_1 and α_2) show an energetically minimum and for the high temperature modification a maxima, which corresponds to a more negative free energy (however, there is some uncertainty with the Gibbs free energy because of the imaginary modes).

A simplistic analysis of these figures leads one to discard the picture, that the high temperature modification is a static structure, which would be associated with an

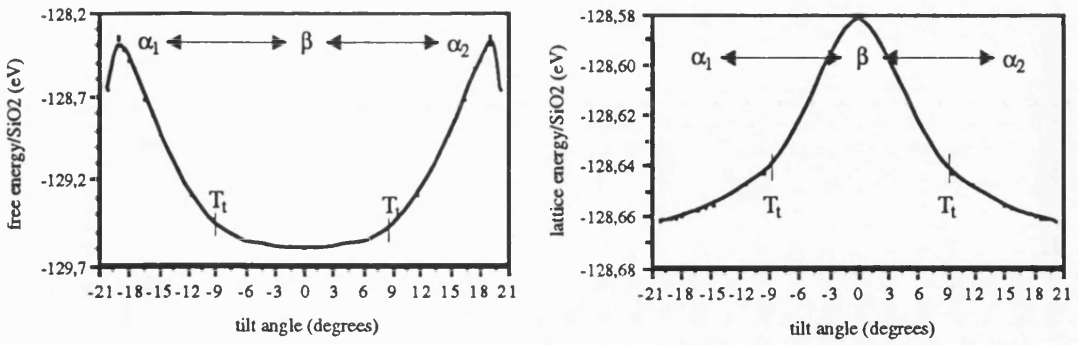

Figure 5.22: Gibbs free energy and lattice energy for quartz as a function of the tilt angle δ using the E-potential model (T_t corresponds to the transition temperature).

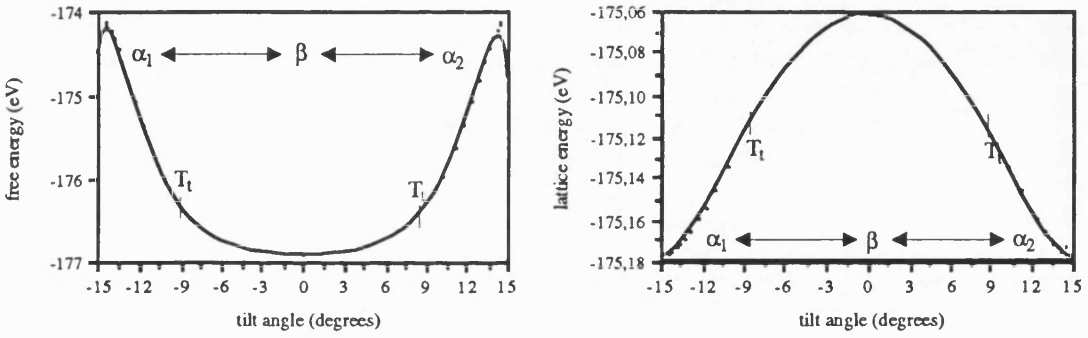

Figure 5.23: Gibbs free energy and lattice energy for quartz as a function of the tilt angle δ using the SE-potential model (T_t corresponds to the transition temperature).

additional local minimum for the lattice energy or an additional local maxima in the β-phase.

The results lead to the assumption of having a dynamic transition with one local energy minimum and maximum respectively for the lattice energy and the Gibbs energy corresponding to the α_1 and α_2 modification.

The structure of β-quartz

The phase transition in quartz is known for a quite long time already, it is therefore surprising to find that the mechanism of the transition is still somewhat in doubt, whether it is a displacive (second order), first order or order-disorder transition or a mixture of these types of transitions. There is also definite experimental evidence given whether the transition is of a static or dynamic form . If β-quartz exists as a static structure with true hexagonal symmetry, each atom should be restricted to a single equilibrium potential well, whereas the atoms in a dynamic structure would oscillate rapidly between two separate potential minima.

Results from both diffraction and spectroscopic experiments indicate that the structure of β-quartz is dynamic. Experimental results by van Tandeloo et al (1976) using electron microscopy and diffraction show that with rising temperature the region swept by a vibrating Dauphinè twin wall is clearly half of the time in the α_1-form and the other half in the α_2-form; the time averaged structure is then the β-form which is in a sense the geometrical average of the α_1 and α_2 form. The β-quartz polymorph can be thus regarded as the time averaged α_1- α_2 form.

On the basis of the electron diffraction experiments of Heaney and Veblen (1991) a model is supported in which at least the oxygen atoms vibrate between two potential minima separated by an extremely small potential maximum and that the silica tetrahedra oscillate between the two orientations corresponding to the Dauphinè twins and that over short ranges the tetrahedral rotations are temporally correlated.

Wright and Lehmann (1981) performed neutron diffraction refinements of powdered and single crystals of β-quartz. They also favour a disorder, dynamic model which is characterised by an additional screw motion about the ideal β-quartz position which

appears as an undamped overshot $\alpha_1 \overset{\beta}{\longleftrightarrow} \alpha_2$. The motion will be therefore on a much longer time scale than typical thermal vibrations corresponding to a very low frequency lattice mode propagated as a wave through the crystal. Transient occupancy of the ideal β-quartz sites is implicit in this model, but the local α-quartz symmetry is dominant.

Researchers who have studied β-quartz using single X-ray diffraction method favour a model in which each silicon and oxygen atom is characterised by high thermal vibration but occupies a single potential minimum (Kihara, 1990; Young 1962). Kihara (1990) presented an ordered model (or weakly disordered model) where the oxygen atoms are assumed to undergo liberational motion and silicon atoms to oscillate in correlation with oxygen motion. Young (1962) concluded on the basis of intensities of a number of chosen reflections in the α- and β-phase, that β-quartz is not a disordered structure and is defined by a potential minimum.

As mentioned already in section 5.3.1. the minimised structure of β-quartz is containing two imaginary frequencies, which is an indication that the structure is unstable. By heating up the α-quartz structure a transition to β-quartz is observable. This can be seen at the elastic constant c_{14} which is zero in the β-quartz structure. Also in this transformed β-quartz structure imaginary frequencies were found indicating again that this structure is unstable. The imaginary frequencies were found in both potential models.

The atomic displacements of the vibrational modes with imaginary frequencies can be used to generate new starting structures for the lattice energy and free energy minimisation. For both β-quartz structures, the original minimised and the transformed structure, a further relaxation was made after moving the atomic positions along the eigenvectors, which correspond to the imaginary frequencies. The cell volume or vectors were not changed. The resulting minimised structure was either a left- (α_1) or right- (α_2) handed α-quartz structure.

The calculations have been done again using both potential models and both of them gave the same result.

This result raises the prospect that the β-quartz polymorph is not a static disordered or static ordered structure with each atom moving about either the α_1 or α_2 site or occupying a single equilibrium position, otherwise there would be no imaginary frequencies indicating that this structure is unstable in this configuration. The β-quartz structure is rather a dynamic disordered structure with each atom liberating between the two potential minima of α-quartz.

Summary:

As both potential models show the same trend during the transition an error in the potential parameters, resulting in the simulation of too high transition temperatures can be excluded.

The higher simulated transition temperatures can be explained by neglecting the anharmonic effects in this lattice dynamic studies. Therefore further development in the simulation method should include anharmonic effects as they play an important role in the calculation of high quality thermodynamic data. Methods for including the anharmonic effects in lattice dynamics are already established but will increase the computational requirements (Parker and Price, 1989).

Nevertheless the applied method is an efficient way to determine phase stabilities and phase transition as it was shown in this studies. The simulation of the α–β transition was able to show that the transition is a displacive (second order) transition and it was given evidence that the transition is dynamic and that therefore β-quartz is a dynamic disordered structure.

So far it was not possible to demonstrate which of the two potential models perform better and should be used for further studies. As an additional test for the validity of the potential parameters a static and dynamic lattice simulation was performed on α- and β-cristobalite. This provides an even more stringent test for the potential models, because the structural and elastic parameters of α-quartz were used in both models to derive the potential parameters. But the model should be able to predict structural and elastic properties, vibrational spectra and thermodynamic properties for other structures than those used in fitting procedures.

5.4. Static lattice simulation of cristobalite

Lattice energy minimisation at constant volume and constant pressure has been performed on α-and β-cristobalite using both potential models.

5.4.1. Calculated structure of α-cristobalite

In Table 5.12. the calculated structural parameters for α-cristobalite using both potential models are shown. The experimental values from Peacor (1974) and Dolasse (1964) are also listed in this table for comparison. The simulated cell dimensions *a* and *c*, the Si-O bond distance and the O-Si-O bond angle of both potential parameters are in very good agreement with the experimental values. Comparing the two potential models the E-model appears to perform slightly better, but the differences are very small.

However, the Si-O-Si bond angle is interestingly because it is very well described by the SE-potential model but shows a big discrepancy from the experimental bond angle for the E-model .

Observable	Expt.	E - model	SE - model
a-axis (Å)	4.98 [a]	5.01 (1.006)	4.90 (0.98)
c-axis (Å)	6.95 [a]	7.06 (1.02)	6.54 (0.94)
Volume (Å^3)	172.18 [a]	177.37 (1.03)	156.8 (0.91)
Si - O (Å)	1.609 [b]	1.577 (0.98)	1.601 (0.995)
O - Si - O (°)	109.47 [b]	109.47 (1.00)	109.42 (0.999)
Si - O - Si (°)	144.67 [b]	156.91 (1.08)	142.72 (1.02)

Table 5.12: Experimental and calculated structural parameters for α-cristobalite; (a) Dolasse (1964); (b) Pluth et al (1984); the number in brackets show the statistical accuracy of the calculated structural parameters.

5.4.2. Calculated structure of β-cristobalite

Simulations of β-cristobalite show good agreement with experiment (Peacor, 1973) for the cell dimension *a*, the Si-O bond distance and the O-Si-O bond angle for both potential models. As in α-cristobalite the Si-O-Si bond angle is very close to experimental values with the SE-model, whereas the E-model shows a discrepancy of 12°from the experimental determined bond angle.The simulated and experimental data are shown in Table 5.13.

Observable	Expt. [a]	E -model	SE - model
a-axis (Å)	7.16	7.159 (1.00)	7.404 (1.03)
Volume (Å^3)	367.985	366.949 (0.997)	405.961 (1.10)
Si - O (Å)	1.609	1.577 (0.98)	1.603 (0.996)
O - Si - O (°)	109.47	109.47 (1.00)	109.42 (0.999)
Si - O - Si (°)	146	157.31 (1.08)	144.74 (0.99)

Table 5.13: Experimental and calculated structural parameters for β-cristobalite; (a) Peacor (1973); the number in brackets show the statistical accuracy of the calculated structural parameters.

5.5. Dynamic lattice simulation of cristobalite

5.5.1. The structure of α- and β-cristobalite at different temperatures

α-cristobalite

In the previous section it was demonstrated that both potential models simulate the structural parameters at 0 Kelvin very well.

The simulated structural parameters are compared over a range of temperatures for α-cristobalite. As in α-quartz both lattice parameters *a* and *c* are increasing with increasing temperature for both potential models. This increase continues as in α-quartz (see section 5.3.1.) above the experimental transition point at about 520K. In the simulations studies both potential models are indicating a structural change of α-cristobalite to about 1200K.

In Figure 5.24 a,b the lattice parameters *a* and *c* are shown in a temperature range from 0K to 700K for both potential models. As a comparison the experimental results from Leadbetter and Wright (1976) and Pluth et al (1984) are also plotted in this figure. The simulated lattice parameters of both potential models are in relatively good agreement with the experimental values at low temperatures. But as for α-quartz the deviation of the calculated lattice parameters is bigger at temperatures above the transition point, because of the higher simulated transition temperature for α-cristobalite.

With increasing temperature the Si-O bond distances are slightly increasing independent of which potential model has been used. In a temperature range from 0K to 500K the mean bond distance using the E-force-field parameters increases from 1.5773Å to 1.5805Å and using the SE-potential model the distance increases from 1.6005Å to 1.6019Å.

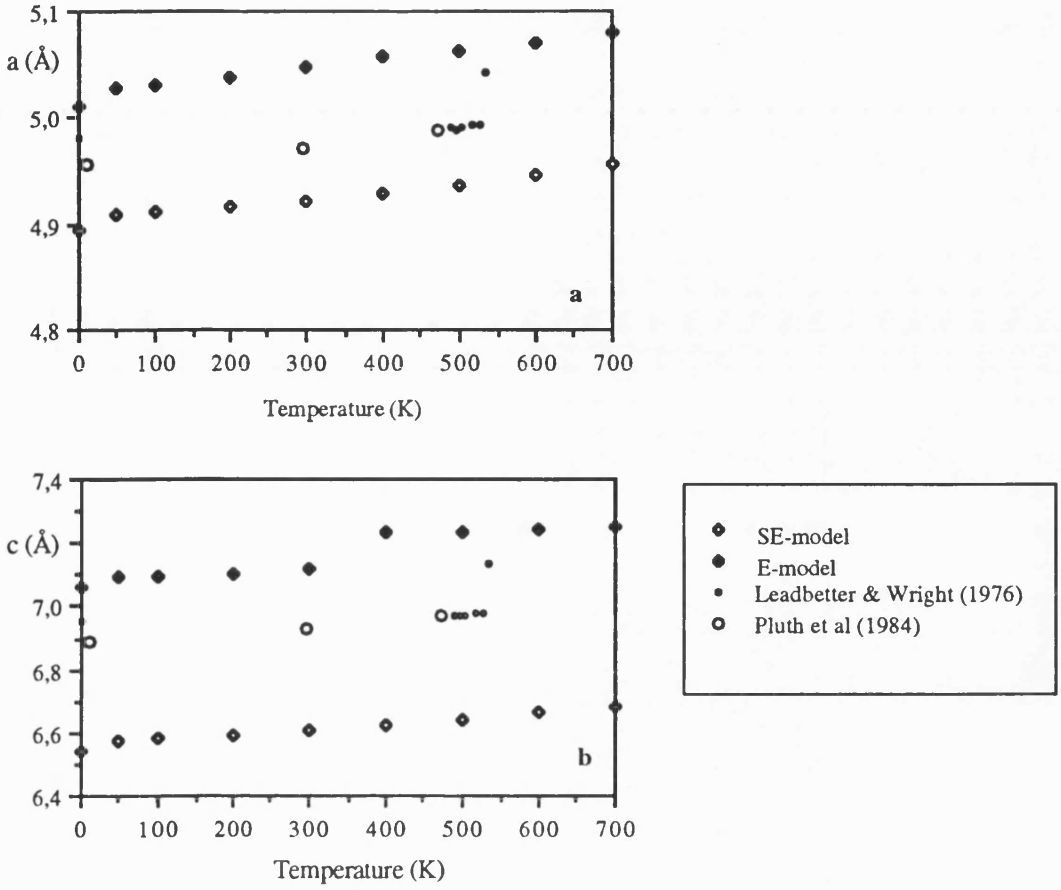

Figure 5.24: Calculated and experimental lattice parameter for α–cristobalite

Pluth et al (1984) measured a mean Si-O bond distance of 1.6095Å at 10K and 1.5975Å at 473K. But by adjusting the Si-O distance for riding motions between Si and O Pluth et al (1984) obtained a mean Si-O distance of 1.6125Å at 10K and 1.6155Å at 473K. Thus, the mean Si-O distance actually increases with temperature.

Also the simulated Si-O-Si bond angle using both potential parameters increases with increasing temperature. This has been observed experimentally (Pluth et al, 1984), although using the E-potential model much higher bond angles (about 10° difference) were obtained, in contrast to the SE-model, which calculates the bond angle very well.

The effect of temperatures has also been simulated by Sanders (1984) using the same potential parameters as in the E-model by adjusting the lattice parameter to the experimental values at each temperature from Pluth et al (1984) and Peacor (1973). Therefore the results of the simulated Si-O-Si bond angle are very close to experimental values and the Si-O bond distances are decreasing slightly with increasing temperature.

In section 5.3.5. the interdependence between the Si-O-Si bond angle and Si-O bond distance with increasing temperature has been discussed. As in α-quartz this relationship is not observed in α-cristobalite which confirms the experimental data by Pluth et al (1984). It is therefore obvious that there is not a unique relation for all silica polymorphs and silicates between the values of Si-O and Si-O-Si.

β-cristobalite

The effect of temperature also has been simulated on β-cristobalite using both potential models. However the SE-force-field parameters could not be used as the simulated structure of β-cristobalite collapsed from 50K onwards. Consequently more than 20 imaginary frequencies were obtained indicating that the structure in this form is unstable.

This result shows that the SE-potential parameters become dynamically unstable. But this has to be further tested with similar structures.

However, using the E-potential parameters a full minimisation was possible and no imaginary frequencies were obtained to indicate any instability. The model also accurately simulates the structural trends with changing temperature.

In Figure 5.25 the lattice parameter *a* is shown together with the experimental results

from Wright and Leadbetter (1975). Although there are only experimental data available around the transition temperature the simulated lattice parameter is in very good agreement in this temperature range and the deviation is below 1% from the measured lattice parameter.

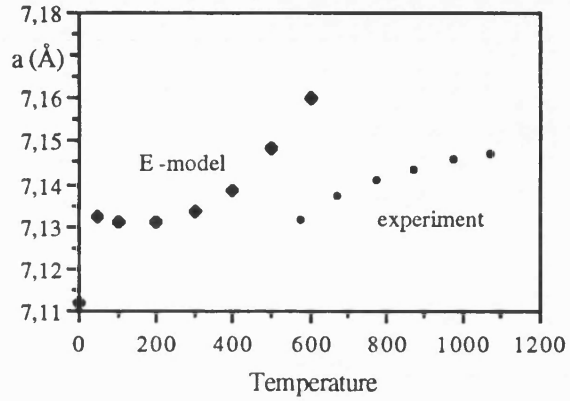

Figure 5.25: Calculated and experimental (Wright and Leadbetter, 1975) lattice parameter for β-cristobalite.

The simulated Si-O-Si bond angle is increasing with increasing temperature. This increase has been also observed experimentally (Wright and Leadbetter, 1975) and is shown in Figure 5.26.

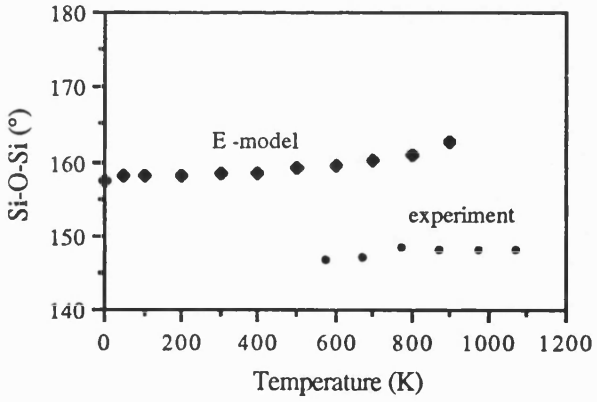

Figure 5.26: Calculated and experimental (Wright and Leadbetter, 1975) Si-O-Si bond angle for β-cristobalite.

As in α-cristobalite the trend is reproduced by this model, although the calculated bond angles are compared to the experimental values are higher.

Summary:

In α-cristobalite both potential models and in β-cristobalite the E-model reproduce the structural parameters very well. As in previous calculations the E-model performs slightly better in simulating the lattice constants and the SE-model in calculating the bond distances.

As in the static simulation of cristobalite the Si-O-Si bond angle is simulated higher compared to experiment, but only for the E-model, whereas the SE-model calculates the bond angle very good in α-cristobalite. In the simulation studies of quartz both potential models simulated higher bond angles.

The SE-model becomes dynamically unstable in the simulation studies for β-cristobalite. Although this has to be further tested, this is indicating that this potential model does not perform well in lattice dynamical simulation studies.

The tilt angle

The temperature variation of the crystal structure in cristobalite cannot be modelled by simple tilting of rigid tetrahedra as in quartz.

Although the α-β cristobalite transition is of the displacive type (Wright and Leadbetter, 1975), involving small movements of the the atoms with increasing temperature, it was

not possible to simulate a tilting of the tetrahedra with increasing temperature.

The calculation of the tilt angle in α-cristobalite did not show a decreasing tilt angle with increasing temperature like in α-quartz. Only very small changes in the tilt angle were observed, independent which potential model has been used. However, the tilt angle in β-cristobalite is zero.

The structure of α- and β-forms in cristobalite are closely related and this relationship is very similar to that between α- and β-quartz, except for the existence of long range disorder in the oxygen positions in β-cristobalite (Wright and Leadbetter, 1975). In quartz the positions of the oxygen and silicon atoms change continuously with increasing temperature towards the higher symmetry β-phase (Young,1962). Whereas in cristobalite this change occurs sharply at the transition temperature and therefore a gradual disordering apparently does not occur (Wright and Leadbetter, 1975).

The positions of the oxygen atoms show a considerable difference exists between quartz and cristobalite. In quartz the oxygen atoms move gradually to unique positions of the higher symmetry β-phase. For cristobalite there are on average in the β-phase six equivalent positions of higher symmetry for each oxygen position in the α-phase (Leadbetter and Wright, 1976).

As the tilt angle is calculated from the lattice parameters and the oxygen fractional coordinates (x and z) this explains why no tilting of the tetrahedra can be observed in cristobalite.

5.5.2. Vibrational spectrum of α-cristobalite

In section 5.3.2. the simulation of the vibrational spectrum of α- and β-quartz was performed. For both quartz-polymorphs the bending modes were better described by the E-model and the stretching modes slightly better by the SE-model.

In order to verify these results the normal mode frequencies of α-cristobalite at **q**=0 were calculated in the same procedure as described for quartz in section 5.3.2.

α-cristobalite has 12 atoms per unit cell which gives rise to 36 normal modes of vibration. Three of these are acoustic modes and the remaining 33 modes are optical modes. Experimentally (Bates, 1972; and Cherukuri et al, 1985) the frequencies and the symmetry of the 33 optical vibrational modes are known. This allows a detailed comparison between experimental and calculated values.

The decomposition of the optical modes of α-cristobalite into symmetry species is (Hua et al, 1988):

$$4A_1 + 4A_2 + 5B_1 + 4B_2 + 8E_T + 8E_L$$

where the A_1, B_1 and B_2 modes are Raman active, the A_2 modes infrared active and the E modes are both.

In Figure 5.27 the calculated infrared and Raman frequencies, using the E- and SE-potential parameters, of α-cristobalite at **q**=0 are shown. The calculated results of Etchepare et al (1977) and the experimental data from Bates (1972) and Cherukuri et al (1985) are also shown for comparison. Etchepare et al (1977) used in their simulation studies potential parameters fitted to the vibrational frequencies.

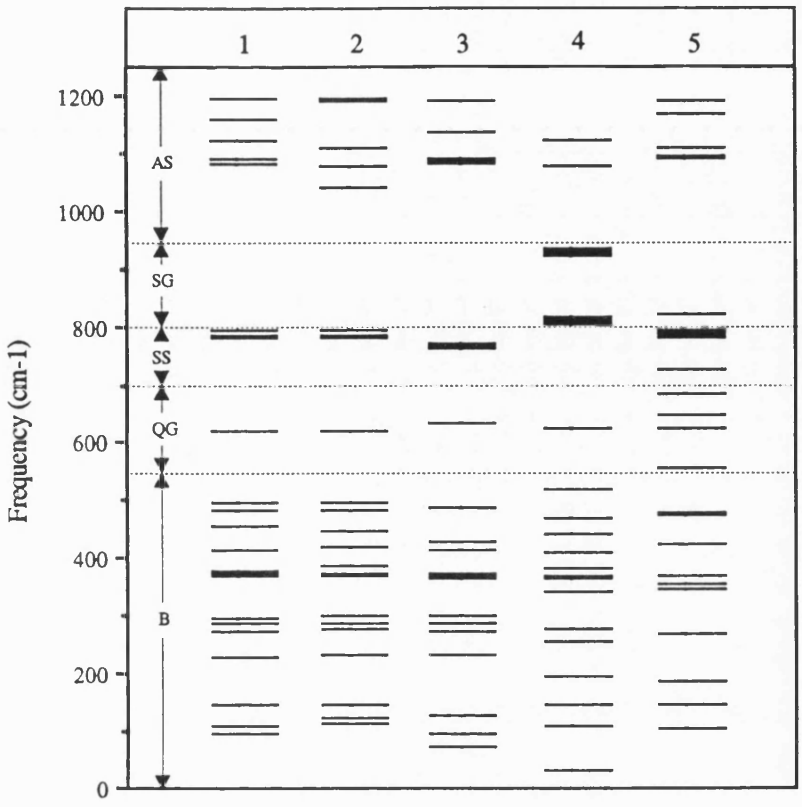

Figure 5.27: Comparison of the $q=0$ frequencies for α-cristobalite using the E-(4) and the SE- (5) potential model, with the experimental Raman and infrared data of (1) Bates (1972) and (2) Cherukuri et al (1985), together with the results calculated by (3) Etchepare et al (1977). B denotes the bendinge modes, SS and AS the symmetric and anti-symmetric stretching modes; QG the quartz gap and SG the silicate gap.

Comparing the outcome of the two potential models we find similar results to α– and β–quartz. The E-potential parameters reproduce the bending modes better than the SE-potential parameters. The quartz-frequency gap between the bending and stretching mode is characterised in α-cristobalite by a single mode, which is clearly reproduced by the E-model. The calculations using the SE-force-field parameters do not show this characteristic feature.

A comparison of the two force-field models for the stretching modes, which are observed above 700cm^{-1}, with experimentally determined modes, shows that these modes are better reproduced by the SE-model. Also the characteristic silicate gap between the symmetric and anti-symmetric stretching mode is clearly shown by the SE-model. The E-model does not reproduce this gap very accurate.

5.5.3. Thermodynamic properties of α- and β-cristobalite

As in quartz, the heat capacity at constant pressure (C_p) and the entropy (S) was calculated for α-cristobalite at elevated temperatures using the SE- and the E-potential parameters.

In Figure 5.28 the results of the calculated heat capacity (C_p) and the experimental values from Richet et al (1982) and Leadbetter and Smith (1976) are shown as a function of temperature. Although the agreement between the calculated and experimental values is good, the simulated data show with increasing temperature a slight deviation from the experimental values. However using the SE-force-field parameters a slightly better agreement with the measured heat capacity is given.

The calculated results of the entropy (S) together with experimental values are shown in Figure 5.29 as a function of temperature. The simulated data are in good agreement with the measured values. Again the results of the SE-model show a better agreement with the measured values.

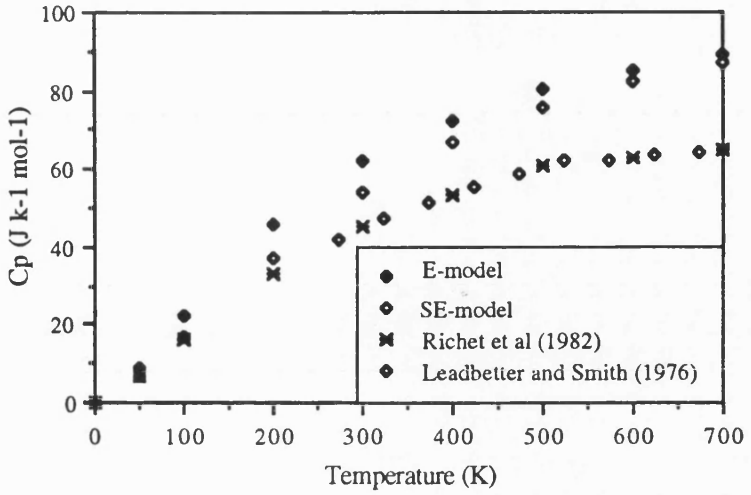

Figure 5.28: The experimental and predicted heat capacity (C_p) of α–cristobalite.

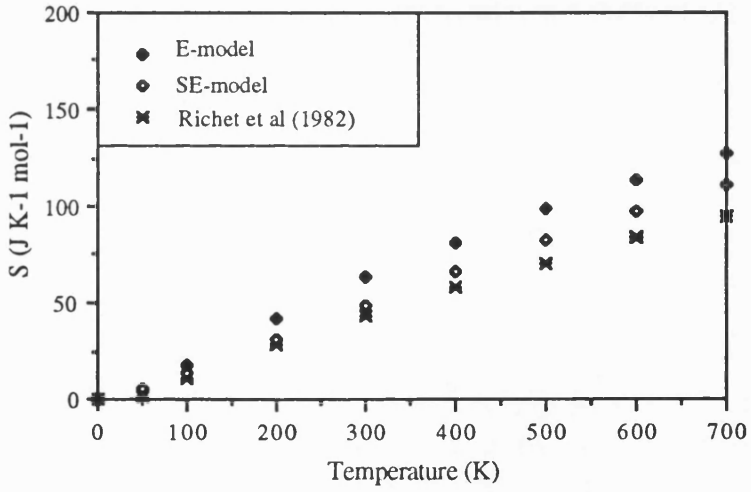

Figure 5.29: The experimental and predicted Entropy (S) of α–cristobalite

The heat capacity (C_p) of β-cristobalite was also calculated with the E-model parameters. The results of the simulated heat capacity in α– and β–cristobalite are shown in Figure 5.30 together with the experimental values from Richet et al (1982) and Leadbetter and Smith (1976). The calculated heat capacity for both phases show the same trend with in-

creasing temperature and they are also in good agreement with the experimental data. The heat capacity is not a very sensitive function of the structure (Richet et al, 1982), hence α and β-cristobalite have nearly identical heat capacities and do not show any major change at the transition temperature.

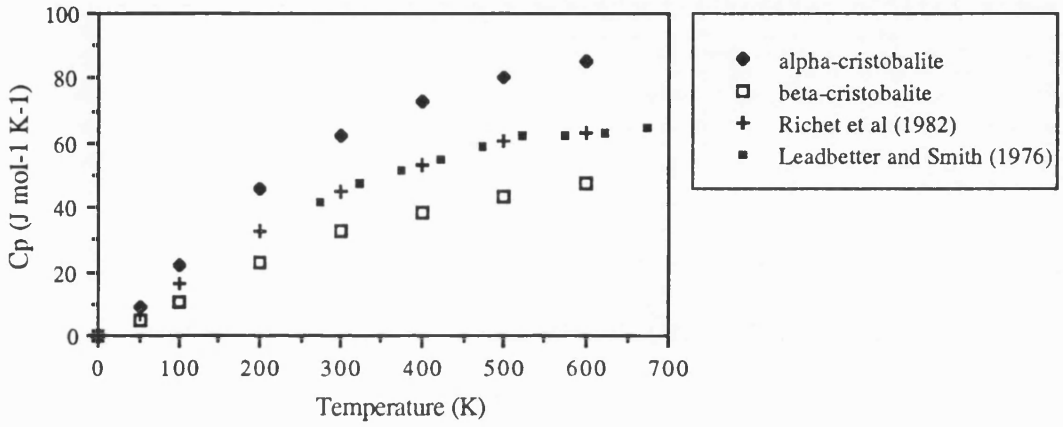

Figure 5.30: Calculated and experimental heat capacity (Cp) for α- and β-cristobalite using the E-model

Summary:

The calculation of the heat capacity (Cp) and entropy (S) in quartz (section 5.3.4.) showed that the E-model performs slightly better than the SE-model. Till now the calculated results in cristobalite indicated that both potential models show the same trends as in the simulation studies in quartz. Confusingly the simulation of the thermodynamic properties in cristobalite demonstrated that the SE-model performs better than the E-model. Although the discrepancies are small this result is opposite to the simulated results in quartz.

5.5.4. The α–β cristobalite phase transition

Cristobalite undergoes a first order transition from the α- to β-phase (Hatch and Ghose, 1991), which is characterised of discontinuities at the transition temperature.

This first order phase transition is clearly shown by comparing the cell dimensions of α- and β-cristobalite. The simulated results show a discontinuous change in the lattice dimensions for both phases. In Figure 5.31 the calculated cell dimensions for α- and β-cristobalite using the E- potential parameters are shown. Despite the gradual nature of the transition both phases coexisting over a range of temperatures and the lattice parameters of each phase show a small variation in the simulated temperature range. There is no continuity between these two phases but there is a discrete change of the lattice parameters between these two phases, which indicates that the transition is of first order.

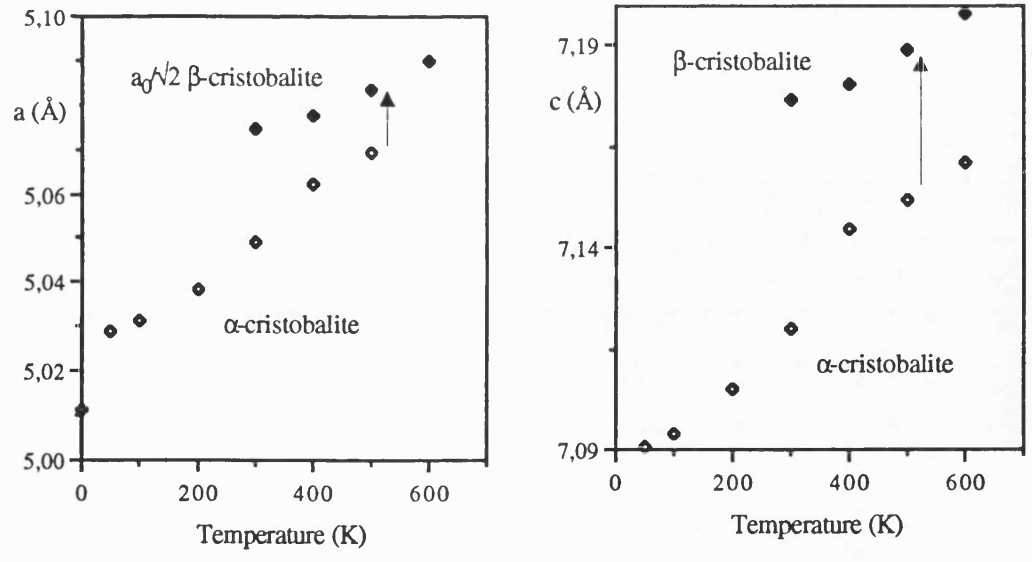

Figure 5.31: Calculated lattice parameter *a* and *c* for α and β-cristobalite using the E-potential parameters.

Also the non-existence of a continuous change of the tilt angle with increasing

temperature indicates that the transition is of first order and that there is a sharp change between these two phases.

Hua et al (1989) expect because of their lattice dynamic studies that the lowest A_1 mode in α-cristobalite is softening with increasing temperature. A soft mode is characteristic for a second order (displacive) phase transition as shown in quartz (section 5.3.7.). The calculation of the vibrational spectrum in α-cristobalite at different temperatures has shown that the lowest A_1 mode does not soften with increasing temperature. Although the α–β transition is of the displacive type, involving small movements of the atoms and no breaking of the bonds (Leadbetter and Wright, 1976) a gradual disordering does not occur. The change of the phases occurs sharply at the transition point.

5.6. Summary

Applying static and dynamic lattice simulation methods we compared the E-potential models and the SE-potential model to a range of experimental data of quartz-polymorphs in order to verify the validity of these two models. In addition, determining their limitations also show under what situation each is most reliable.

The static lattice simulation showed that in general both potential models simulate very accurately the structural and elastic properties of the the quartz polymorphs. Hence both models can be applied for further studies at 0 Kelvin. Only the Si-O-Si bond angle was simulated too high in β-quartz using both potential models and in cristobalite using the E-model.

However, dynamic lattice simulation studies of the quartz-polymorphs using both potential parameters gave a slightly inconclusive outcome.

The structural parameters are described very well by both models, although the E-model performs slightly better in the simulation of the lattice constants and the SE-model gives slightly more accurate results for the calculated bond distances and angles.

As in the static simulation studies we found that the Si-O-Si bond angle has been simulated too high for α- and β-quartz using both potential parameters and for α- and β-cristobalite using the E-model.

The calculation of the vibrational spectrum of the quartz-polymorphs showed that the E-model performs in general better than the SE-model.

In the simulation of the second order elastic constants at elevated temperatures and pressures and their derivatives of α-quartz it appeared that the SE-model is clearly better, whereas the results of the E-model are notably worse.

The thermodynamic properties like the heat capacity (Cp) and entropy (S) are better reproduced by the E-model in quartz. In contrast in cristobalite these thermodynamic properties are better reproduced by the SE-model. But as in the simulation studies of the structural properties the discrepancies between the two potentials are small.

Interestingly the SE-model becomes dynamically unstable in the simulation studies for β-cristobalite. This indicates that the SE-model does not perform well in lattice dynamical studies and the E-model is therefore a better choice for lattice dynamical studies.

Further we demonstrated that static lattice simulations, but especially lattice dynamics are very efficient methods. The only major problem in lattice dynamics is that because of the quasi-harmonic approximation the anharmonicity of the potential energy surface is

neglected and therefore transition temperatures cannot be modelled accurately. The structural, elastic and thermodynamic properties, and also the nature of the phase transition in quartz polymorphs can be quite accurately modelled.

VI. APPLICATION OF THE POTENTIAL MODEL TO BERLINITE ($AlPO_4$)

As noted earlier, aluminophosphates ($AlPO_4$'s) are an important new class of compounds. Recently derived semi-empirical potential parameters (Kramer et al, 1991) enable us to simulate these structures. The potential parameters are listed in Table 4.1 (chapter 4).

In this chapter the validity of this potential model will be tested on α-berlinite (α-$AlPO_4$), in order to apply this model for further simulation studies on aluminophosphates. The reliability of this potential has been tested to some extent by Kramer et al. (1991) at 0 Kelvin, but these parameters were never tested at elevated temperatures and pressures using lattice dynamics. As in the quartz studies this will be done by comparing systematically the calculated structural and elastic properties of berlinite with available experimental data at 0 Kelvin and at elevated temperatures and pressures. Also the simulated vibrational spectrum will be compared to the experimental spectra.

6.1. Experimental structure of α-berlinite and β-berlinite

The aluminophosphate α- and β-berlinite is isostructural with α- and β-quartz; half of the silicon is replaced by aluminium and half by phosphorous. The ordered distribution of the Al^{3+} and P^{5+} ions results in a doubling of the unit cell along the c-axis (Wyckoff, 1965).

The close relationship between berlinite and quartz is shown by their nearly identical physical properties. Also all high-temperature modifications of SiO_2 show analogous behaviour in AlPO4.

Berlinite undergoes a transformation from the low-temperature form to the high temperature-form at 853K, which is only a few degrees higher than that for quartz. In addition the form of the transition is the same as in quartz (Kosten and Arnold, 1980; van Tandeloo et al, 1976).

The experimental α-berlinite structure described in this chapter was determined by X-ray diffraction from Ng and Calvo (1976).

α-berlinite is trigonal and crystallises under ambient conditions in the space group $P3_121$ or in the enatiomorphic space group $P3_221$.

There are 18 atoms (3 formula units) in each primitive cell. The Al atoms occupy (u_1 0 1/3) (0 u_1 2/3) ($\bar{u}_1$ $\bar{u}_1$ 0) and the P atoms occupy (u_2 0 5/6) (0 u_2 1/6) ($\bar{u}_2$ $\bar{u}_2$ 1/2), where u_1 = 0.4660 and u_2 = 0.4675.

The experimental starting structure of β-berlinite for the calculations in this chapter was taken from Wyckoff (1965).

β-berlinite is hexagonal and crystallises above 850K in the space group $P6_422$ (or $P6_222$). There are 18 atoms in each primitive cell. The Al atoms occupy the symmetric position (1/2 0 1/2), (0 1/2 1/6) and (1/2 1/2 5/6) and the P atoms occupy the positions (1/2 0 0), (0 1/2 2/3) and (1/2 1/2 1/3).

6.2. Static lattice simulation of α- berlinite

As a first test for the validity of this potential model energy minimisation was performed at 0 Kelvin using the experimental crystal coordinates as a starting structure. A detailed study of the structure and elastic properties of α-berlinite provides a good test for the potential model as these are calculated from the first and second derivatives of the lattice energy.

In Table 6.1 the calculated structural parameters; the lattice constants, bond distances and bond angles are shown. As a comparison the experimental results for Ng and Calvo (1975) and Thong and Schwarzenbach (1979) are also listed in this table.

Observable	this work		Expt.[1]	Expt.[2]
a (Å)	5.0281	(1.02) ; (1.02)	4.9429	4.9423
c (Å)	11.1657	(1.02) ; (1.02)	10.9476	10.9446
Vol (Å3)	242.117		231.640	231.52
Al - O (Å)	1.7395	(1.004) ; (1.002)	1.7330	1.736
P - O (Å)	1.5077	(0.99) ; (0.99)	1.5215	1.523
O - Al - O (°)	110.56	(1.01)	110.00	
O- P - O (°)	109.86	(1.004)	109.41	
P - O - Al (°)	149.23	(1.05) ; (1.05)	142.6	142.3

Table 6.1: Calculated and experimental structural parameters of α-berlinite; (1) Ng and Calvo (1975); (2) Thong and Schwarzenbach (1979); the numbers in brackets show the statistical accuracy of the calculated parameters.

The agreement between calculated and experimental structural parameters is very good. Except for the P-O-Al bond angle, the calculated parameters are in general correct within 1-2%.

Furthermore the six independent elastic constants have been calculated as this provides and even more rigorous test to the potential model.

The calculated elastic constant tensors are listed in Table 6.2. together with experimental values from Sidek et al (1987) and Chang and Barsch (1976). The calculated results are in very good agreement with the experimental values. Only c_{11} shows a significant deviation from the experimentally determined c_{11}.

C ij (GPa)	this work	Expt. [1]	Expt.[2]
c_{11}	82.99	64.88	64.01
c_{12}	8.78	8.98	7.24
c_{13}	15.16	14.60	9.57
c_{14}	13.71	12.17	12.35
c_{33}	96.25	87.14	85.76
c_{44}	46.41	43.12	43.17
c_{66}	37.11	27.95	28.38

Table 6.2: Calculated and experimental elastic constant tensors for α-berlinite; (1) Sidek et al (1987); (2) Chang and Barsch (1976)

However, the calculation of the structural and elastic properties of α-berlinite demonstrated that the potential model performs very well in the static lattice simulation.

6.3. Dynamic lattice simulation of berlinite ($AlPO_4$)

In this section the lattice dynamics of berlinite is simulated. The method applied is the same as in the quartz (section 5.3.) and cristobalite (section 5.5.) simulation studies.

6.3.1 Structure of α- and β- berlinite at different temperatures

In section 6.2 it was shown that the applied potential model for $AlPO_4$'s is able to simulate the structural and elastic properties of α-berlinite at 0 Kelvin very well. As an additional test of this potential model the simulated structural parameters of α- and β-berlinite at elevated temperatures will be compared to experimental values. To date there are only few experimental data available for β-berlinite (Ng and Calvo, 1976), and these are the structural parameters around the transition temperature. Hence we will consider β-berlinite only in this section.

The structural parameters of α-berlinite have been calculated in a temperature range from 0K to 800K. At higher temperatures the calculated structure of α-berlinite became unstable, indicating the transition to β-berlinite. In contrary to the simulation studies of quartz the simulated transition temperature for berlinite is close to the experimental transition temperature at 853K.

Furthermore the structural parameters of β-berlinite from 0K to 300K have been calculated. As in the simulation studies of β-quartz the minimised structure contained, dependent on the temperature, between one and two imaginary frequencies, indicating

that the calculated structure is unstable. Although the calculated structure is unstable according to the imaginary frequencies a minimisation was possible up to 300K, because energy derivatives are zero at saddle points (see chapter 5). At temperatures above 300K the calculated structure collapsed in the simulation studies.

In Figure 6.1.the calculated lattice parameters *a* and *c* for α- and β-berlinite are shown. The experimental lattice parameters from Chang and Barsch (1976) are also shown in this figure for comparison.

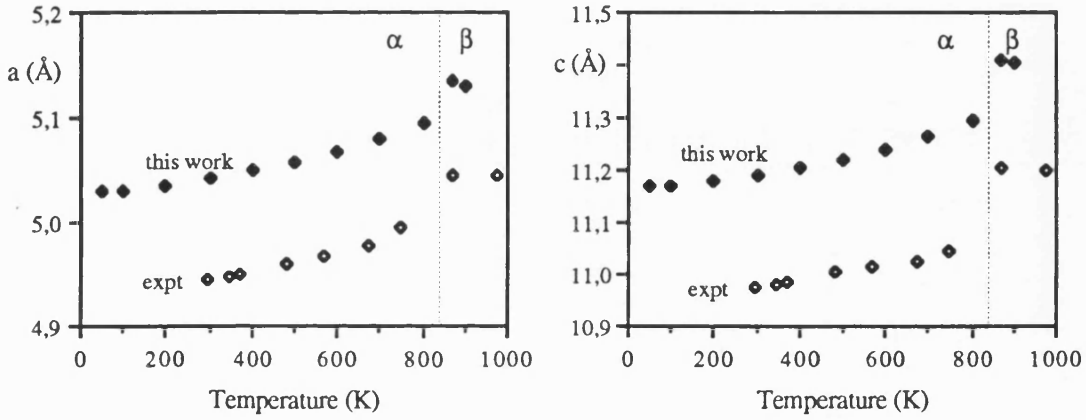

Figure 6.1: Calculated and experimental (Chang and Barsch, 1976) lattice parameters of α – β berlinite.

Both lattice parameters *a* and *c* in α-berlinite are increasing with increasing temperature until the transition temperature is reached. The lattice parameters show an apprupt change between 800K and 900K resulting from the α-β phase transition. The lattice constants of β-berlinite are compared to α-berlinite higher and show a slight decrease with increasing temperature. Because of the structural similarities between berlinite and quartz these characteristics were also observed in α- and β-quartz.

Although the calculated lattice parameters for α- and β-berlinite are slightly higher than

experimental they do show the same trend with increasing temperature is given.

In contrast the average Al-O and P-O bond distances of α-berlinite are calculated to increase until the transition temperature is reached, whereas the experimental results by Ng and Calvo (1976) show a decrease of the bond distances. In a temperature range from 0K to 800K the calculated mean Al-O and P-O distances increase from 1.741Å to 1.746Å and from 1.508Å to 1.509Å respectively . However, the experimental results show a decrease from 1.733Å to 1.690Å for the Al-O and from 1.522Å to 1.515Å for the P-O bond distances in a temperature range from 298K to 803K.

In the structure of β-berlinite the four equal Al-O and P-O bond lengths are shorter than in α-berlinite. Experimentally (Ng and Calvo,1976) the Al-O and P-O bond distances are respectively 1.694Å and 1.505Å, whereas the calculated bond distances are 1.741Å for Al-O and 1.597Å for P-O.

In quartz the Si-O bond in the α-phase is also shortened from an average of 1.607Å to 1.594Å in the β-phase.

The calculated average P-O-Al, O-P-O and O-Al-O bond angles in α-berlinite also increase with increasing temperature. The increase of the mean P-O-Al angle was also observed in the experimental studies, whereas the O-T-O (T=Al or P) bond angles show experimentally a slight decrease.

Ng and Calvo (1976) measured an average P-O-Al bond angle from 142.57°to 152.12°in a temperature range between 298K and 803K. The calculated bond angle is slightly higher compared to the experimental values and increases from 150.21° to 154.17° in a

temperature range from 0K to 800K.

Above the transition temperature the P-O-Al angle is still increasing. Experimentally this bond angle is, in the β-phase, 152.2° (Ng and Calvo,1976). The calculated P-O-Al angle is 159.02° in the β-phase, which is again slightly higher compared to the experimental values.In quartz the Si-O-Si angle increases from 144.0° in the α-phase to 152.5° in the β-phase.

Despite their similarities, there are differences between quartz and berlinite. In quartz it is possible to describe the structural change with increasing temperature by simply rotating or tilting the SiO_4 tetrahedra around the two-folded axis perpendicular to *c* (see section 5.3.1.). The tilt model for quartz gives an overall description of the temperature dependence to the position parameters and therefore to the atomic displacements.

In α-berlinite it is not possible to describe the structural change with increasing temperature solely in form of a tilting of the AlO_4 and PO_4 tetrahedra. The atomic displacement with temperature can thus be approximated by a rotation of the AlO_4 and PO_4 tetrahedra around the two-folded axis, but in contrary to quartz, this is accompanied by a simultaneous translation of the tetrahedra along the same axis (Ng and Calvo, 1976).

As the temperature is raised, both the AlO_4 and PO_4 tetrahedra rotate around their two-folded axis. At the same time the tetrahedra moves as a whole along the crystallographic two-folded axis. As adjacent AlO_4 and PO_4 tetrahedra must rotate in opposite directions in a cooperative manner, this rotation leads to and increase of the Al-O-P angle, but cannot be expressed in form of a tilt angle.

Summary:

The potential model reproduces the structural parameters, for example the lattice constants and the bond angles for α- and β-berlinite at elevated temperatures very well. But like in the simulation studies of α-quartz and α-cristobalite (see chapter 5) we found that the bond distances in α-berlinite are slightly increasing with increasing temperature, whereas experiment shows the opposite.

It was also found that the simulated transition temperature of berlinite is very close to the experimental transition temperature. However, in quartz and in cristobalite it is not possible to simulate the transition temperature close to the experimental determined temperature (see chapter 55). It is assumed that the high simulated α-β transition temperatures in quartz and cristobalite are due to a breakdown of the quasi-harmonic approximation in the applied lattice dynamical technique.

Although it was possible to simulate the α-β berlinite transition temperature very accurately, this limitation of the lattice dynamical technique still exists. Hence it may be assumed that the applied potential model in berlinite is not so sensitive to the quasi-harmonic approximation and therefore to the lack of the full anharmonicity of the potential energy surface in the dynamic lattice simulation technique.

6.3.2. Vibrational spectrum of α-berlinite

Another critical test of the potential model is to compare the calculated and experimental phonon frequencies of α-berlinite. Like in quartz the calculation of the infrared- and Raman frequencies was performed by using a zero wave-vector and one wave-vector **q**

with a length of 0.001 reciprocal lattice units (see section 5.3.2.).

As mentioned in section 6.1. the replacing of the Si-ions by Al- and P-ions results in a doubling of the unit cell along the c-axis and therefore the first Brillouin zone is half. Hence the phonon modes located in the direction of the A-point of the Brillouin zone in α-quartz have equivalents in α-berlinite which are located near the Γ-point and observable by optical methods (Scott, 1971). They may be directly compared to each other (the points Γ and A have the same symmetry). Table 6.3. summarises the symmetries and the number of phonon modes of α-berlinite at the the centre of the Brillouin zone Γ, and those of α-quartz at the Γ and A points (Etchepare and Merian, 1978).

	optic modes	acoustic modes
α- berlinite	$8\Gamma_1 + 9\Gamma_2 + 17\Gamma_3$	$\Gamma_2 + \Gamma_3$
α- quartz	$4\Gamma_1 + 4\Gamma_2 + 8\Gamma_3$ $4A_1 + 5A_2 + 9A_3$	$\Gamma_2 + \Gamma_3$

Table 6.3: Symmetries of the phonon modes of α-berlinite and α-quartz at the points Γ and A of the first Brillouin zone.

Experimentally the frequencies and symmetry of the 51 optical vibrational modes are known. The decomposition of these modes is shown in Table 6.3, where the Γ_1 modes are Raman- the Γ_2 modes are infrared-active and the Γ_3 modes are both.

In Table 6.4 the calculated and experimental Raman- and infrared-frequencies are shown. The experimental frequencies were taken from Goullet et al (1990) and Etchepare and Merian (1978).

Symmetry	this work	Expt. [1]			Expt. [2]
		Raman	Infrared		
			TO	LO	
A_1	187.75	162			158
	234.65	221			216
	331.85	335			336
	436.81	435			-
	515.46	461			456
	710.59	726			729
	1083.76	1103			1105
	1090.95	1110			1112
A_2	56.68		48	(48)	
	149.46		149	(150)	
	257.03		277	(248)	
	512.79		447	(454)	
	554.70		495	(554)	
	687.29		-	-	
	806.55		691	(714)	
	1086.44		1108	(1252)	
	1199.38		1167	(1167)	
E_1	119.43	107	112	(112)	105
	119.55	118	126	(126)	116
	187.62	160	157	(162)	192
	193.74	196	193	(196)	-
	331.85	306	286	(288)	296
	377.41	373	373	(382)	-
	392.56	418	413	(414)	417
	443.98	438	464	(524)	460
	521.76	467			-
	567.54	566			-
	644.71	650	645	(648)	697
	703.19	701	706	(722)	713(?)
	732.30	748	739	(742)	-
	1083.82	1104	(1096)	(1242)	1100
	1097.47	1121	(1125)	(1125)	1175
	1199.88	1180	1171	(1171)	1231(?)
	1233.14		1231	(1231)	1239(?)

Table6.4: Calculated and experimental infrared and Raman frequencies for α-berlinite; (1) Goullet et al (1990); (2) Etchepare et al (1978); frequencies in cm^{-1}.

In Figure 6.3 these calculated and experimental frequencies are shown graphically. The success of the potential can be also judged by comparing with other theoretical calculations. Therefore the theoretical calculation from Goullet et al (1990) is also shown in Figure 6.2. The theoretical calculation from Goullet et al (1990) is based on lattice dynamics, with the potential parameters fitted to the observed vibrational frequencies.

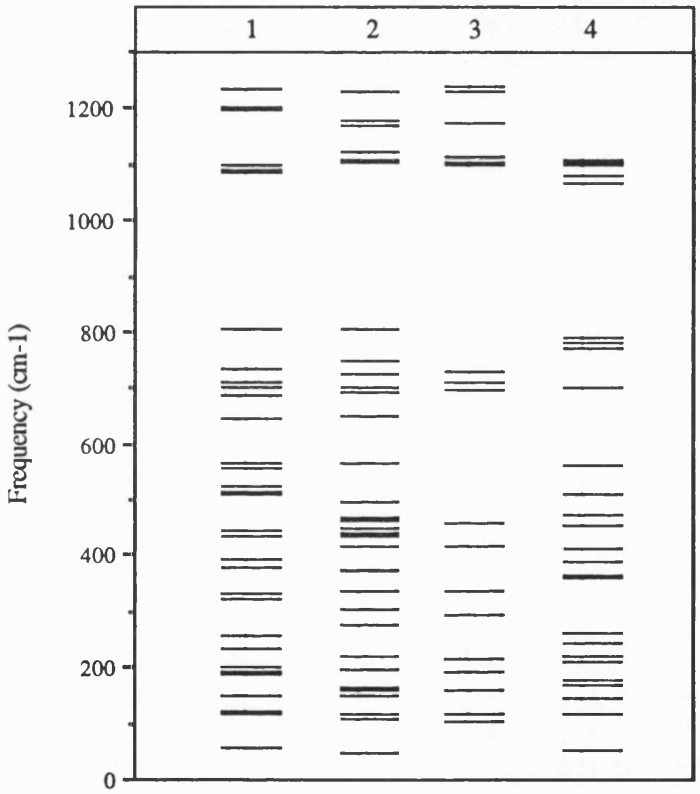

Figure 6.2: Calculated and experimental infrared and Raman frequencies for α-berlinite; (1) this work; (2) experimental frequencies (Goullet et al; 1990); (3) experimental frequencies (Etchepare et al; 1978); (4) calculated frequencies from Goullet et al (1990) using lattice dynamics.

The agreement between the calculated frequencies of the present studies and the experimental frequencies is very good. There are only 5 frequencies which show a

discrepancy of more than $30cm^{-1}$ from experimental values, whereas in the theoretical calculations from Goullet et al (1990) 10 frequencies are in error by more than $30cm^{-1}$. The main discrepancies in our calculations are in the frequency range between $300cm^{-1}$ and $600cm^{-1}$, which correspond mainly to T-O-T and O-T-O (T=Al or P) bending vibrations (Etchepare and Merian, 1978). However, there also appears to be some experimental uncertainty over the exact frequencies of some modes, which makes the exact quality of the prediction of these modes difficult to estimate.

Between $800cm^{-1}$ and $1050cm^{-1}$ is a very characteristic frequency-gap. As α-quartz and α-berlinite show a concordance between the modes this gap corresponds to the "silicate-gap" which has been determined already in the quartz polymorphs (van Beest el al, 1989) and divides the symmetric stretching modes from the anti-symmetric stretching modes (see section 5.3.2.).

However, the applied potential model reproduces the known **q**=0 lattice dynamics of α-berlinite very accurately, which enables to apply the parameters for further calculations of aluminophosphates.

6.3.3. The elastic properties of α-berlinite at different temperatures

In the static lattice simulation studies it was demonstrated that the applied potential model reproduces the second order elastic constants at 0 Kelvin very well. Now the elastic constants have been calculated at elevated temperatures and compared to experiment.

The six single crystal elastic constants of α-berlinite have been measured between 80K and 298.15K by Chang and Barsch (1976). In Table 6.5 the calculated and measured second order elastic constants are shown. The elastic constant c_{14}, c_{33} and c_{44} are in very good agreement with the experimental values, whereas the other calculated elastic constants are in reasonable agreement with the measured values.

With the exception of c_{66} and c_{14} all elastic constants show the usual decrease with increasing temperature. The shear modulus c_{66} and c_{14} increase monotonically with increasing temperature. This behaviour is in qualitative agreement with the observed values in α-quartz.

Temperature	c_{11}	c_{12}	c_{13}	c_{14}	c_{33}	c_{44}	c_{66}
this work							
50	81.93	5.89	12.68	14.17	91.06	45.55	38.02
100	81.84	5.62	12.45	14.20	90.60	45.46	38.11
200	81.56	4.81	11.78	14.30	89.21	45.20	38.39
300	81.27	3.73	10.91	14.40	87.44	44.85	38.77
Chang & Barsch (1976)							
80	64.60	9.32	10.22	12.03	88.99	44.12	27.64
100	64.56	9.20	10.18	12.04	88.82	44.06	27.68
200	64.35	8.36	9.91	12.17	87.43	43.72	28.00
298.15	64.01	7.24	9.57	12.35	85.76	43.17	28.38

Table 6.5: Calculated and experimental second order elastic constants (in GPa) of α-berlinite at different temperatures.

A more stringent test on the validity of the potential model are the temperature derivatives of the elastic constants, which are calculated from the third derivatives of the lattice energy. The temperature derivatives have been obtain by a least square fit in the temperature ranges between 50K and 300K for the calculations in this work and between 80K and 298.15K for the measured values from Chang and Barsch (1976).

In Table 6.6, both, the experimental and calculated temperature derivatives are shown. The values of $(\delta c_{14}/\delta T)_{P,T=0}$; $(\delta c_{33}/\delta T)_{P,T=0}$ and $(\delta c_{66}/\delta T)_{P,T=0}$ are in excellent agreement with the experimental values. For the other derivatives good agreement is obtained. As in the experimental derivatives all calculated temperature derivatives show negative signs, except for $(\delta c_{14}/\delta T)_{P,T=0}$ and $(\delta c_{66}/\delta T)_{P,T=0}$ which are positive.This behaviour is also in qualitative agreement with the observed and calculated values for α-quartz. The positive temperature derivatives for $(\delta c_{14}/\delta T)_{P,T=0}$ and $(\delta c_{66}/\delta T)_{P,T=0}$ are associated with the α–β transformation. This characteristic has been discussed in greater detail in section 5.4.6.

The results in α-berlinite are in general systematically smaller than the data for α-quartz. This demonstrates that α-berlinite is less elastically "stiff" than α-quartz, also when temperature is applied.

However, the results demonstrate, that this potential model is also able to simulate the second order elastic constants and their temperature derivatives very well.

	$(\delta c_{ij} / \delta T)_{P.\ T=0}$						
	c_{11}	c_{12}	c_{13}	c_{14}	c_{33}	c_{44}	c_{66}
α-berlinite							
this work	-0.0026	-0.0085	-0.0071	0.0009	-0.0145	-0.0028	0.0030
Chang & Barsch (1976)	-0.0049	-0.0107	-0.0038	0.0009	-0.0187	-0.0068	0.0029
α-quartz							
this work (SE-model)	-0.0017	-0.0118	-0.0099	0.0025	-0.0218	-0.0029	0.0050
Wang et al (1992)	-0.0037	-0.0228	-0.0049	0.0037	-0.0238	-0.0087	0.0096

Table 6.6: Comparison between the calculated values of the temperature derivatives $(\delta c_{ij} / \delta T)_{P.\ T=0}$ of the elastic constant tensors of α-berlinite and α-quartz and those measured experimentally.

6.3.4. Structure of α-berlinite at different pressures

High pressure Raman scattering experiments showed that α-berlinite does not undergo a phase transition up to 12 GPa, and that there are at least three high-pressure phases which are stable above 6 GPa and 1173K (Jarayamann, 1987).

Because of the structural similarities between α-quartz and α-berlinite it is supposed that their high-pressure behaviour is comparable. This has been confirmed by Raman scattering studies (Jarayamann, 1987) and will be also shown in this simulation studies.

The structure of α-berlinite has been calculated in a pressure range between 0.001 GPa and 85 GPa at 300K. In Figure 6.3 the calculated lattice parameters *a* and *c* are shown together with the experimental values from Sowa et al (1990). Both lattice parameters show a contraction with increasing pressure as in α-quartz. They are also in a very good agreement with the experimental values: the reduction of the a-axis is 0.336Å after Sowa et al (1990) and 0.296Å in our simulation studies, whereas the reduction of the c-axis is 0.382Å and 0.371Å respectively.

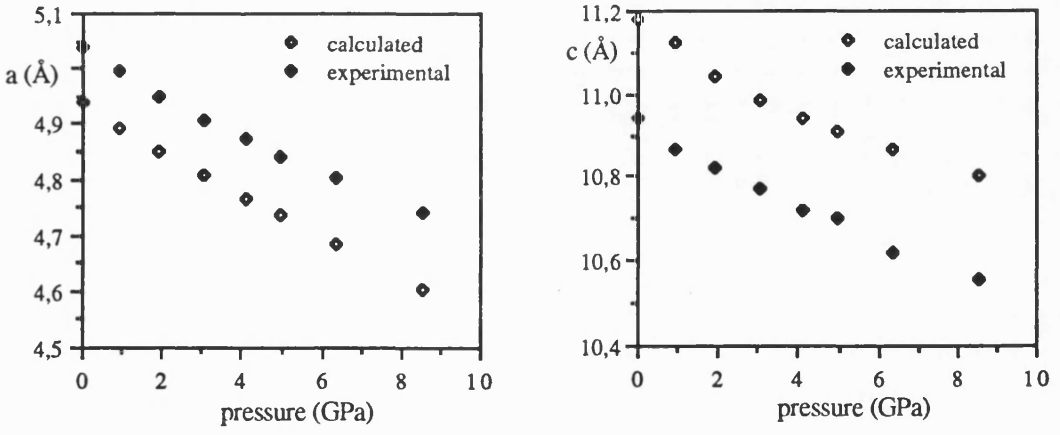

Figure 6.3: Calculated and experimental (Sowa et al, 1990) lattice parameters of α-berlinite as a function of pressure.

As in α-quartz the compressibility of α-berlinite is anisotropic, with the a-axis more compressible than the c-axis. Thus the c/a ratio increases with increasing pressure. In Figure 6.4 the experimental and calculated c/a cell parameter ratio as a function of pressure is plotted for α–berlinite and α-quartz. The calculated value for α-berlinite is very close to the experimental ratio and both, quartz and berlinite, show the same trend, an increasing c/a ratio with increasing pressure.

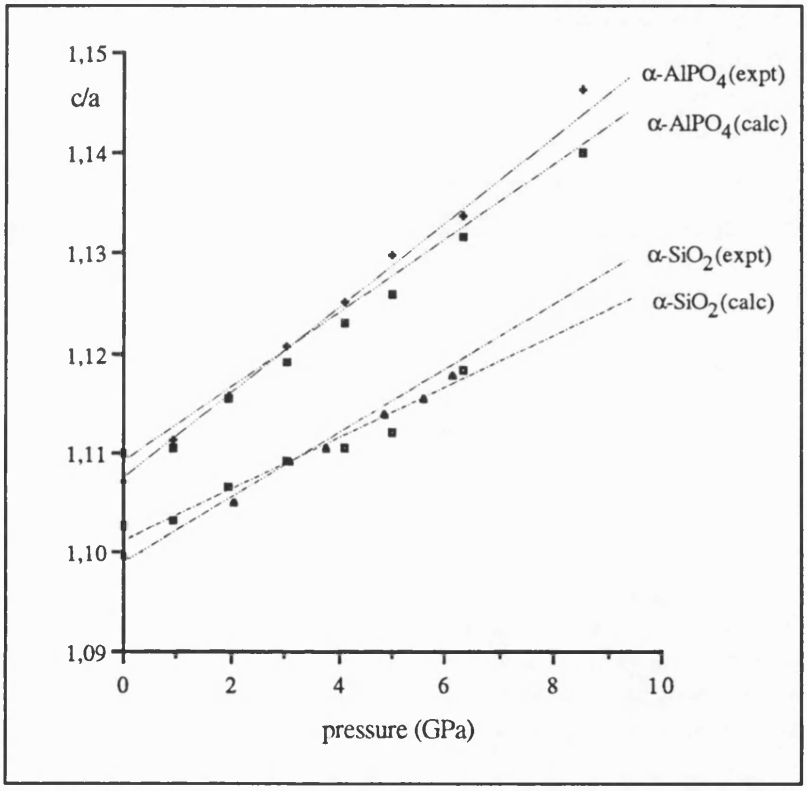

Figure 6.4: c/a ratios of experimental and calculated α-quartz and and α-berlinite (for α-berlinite c/2a is given)

Goiffon et al (1983) found that the higher the c/a ratio the more distorted are the tetrahedra, and supposed that this ratio can be a measure for the distortion in berlinite and quartz. This assumption was confirmed by Glinnemann et al (1990) and Sowa et al

(1990), where high-pressure structural investigations on SiO_2 and $AlPO_4$ show increasing distortions of the tetrahedra with increasing c/a ratios.

From the altering of the O-Al-O and O-P-O angles it can be seen that the $AlPO_4$ tetrahedra become more and more distorted when pressure is applied. In Table 6.7 the calculated and experimental mean O-T-O angles are shown. Both, the experimental and calculated O-T-O bond angles are decreasing with increasing pressure, although the calculated angles show compared to the experimental angles a smaller decrease with pressure.

In Table 6.7 the experimental and calculated average bond distances and angles are given. Both, the experimental and calculated Al-O bond distances are decreasing with increasing pressure. The calculated values show also excellent agreement with the experimental values. Sowa et al (1990) reported a decrease of the Al-O distance of 0.02Å in a pressure range from 0.001 GPa to 85 GPa, which is identical with the calculated Al-O bond distance.

In contrast, the experimental P-O bond distances are increasing with pressure (Sowa et al, 1990), whereas in the simulation studies the P-O bond distances are decreasing.

The decrease of the P-O-Al angles under pressure are clearly visible, although the calculated bond angles are slightly higher as the experimental values (see Figure 6.5). The experimental bond angles show a decrease of 14.1° in a pressure range between 0.001 GPa and 85 GPa, which is very close to the calculated decrease of 12.2°. The experimental and calculated values are also shown in Table 6.7. As in α-quartz, where the Si-O-Si bond angles are decreasing with pressure, this reduction of the P-O-Al bond angle in α-berlinite is indicating that cooperative tilting of the tetrahedra takes place.

pressure (GPa)	Al - O (calc)	Al - O (expt)	P - O (calc)	P - O (expt)	O- Al-O (calc)	O-Al-O (expt)	O-P-O (calc)	O-P-O (expt)	P-O-Al (calc)	P-O-Al (expt)
0.001	1.7416	1.7350	1.5084	1.5195	109.485	110.075	109.475	109.250	150.700	142.550
1.95	1.7409	1.7345	1.5081	1.5180	109.477	110.250	109.473	109.375	150.160	140.300
19.5	1.7349	1.7320	1.5062	1.5255	109.462	110.200	109.470	109.325	146.365	138.100
30.6	1.7317	1.7300	1.5052	1.5250	109.455	110.250	109.470	109.350	144.550	136.300
41.0	1.7290	1.7295	1.5042	1.5270	109.443	110.125	109.470	109.200	143.105	134.500
49.8	1.7270	1.7325	1.5035	1.5170	109.440	110.250	109.472	109.350	142.020	134.100
63.4	1.7240	1.7235	1.5024	1.5360	109.437	109.975	109.470	109.125	140.525	131.050
85.1	1.7199	1.7150	1.5008	1.5445	109.430	109.575	109.472	108.900	138.480	128.450

Table 6.7: Calculated and experimental (Sowa et al. 1990) mean bond distances and bond angles for α-berlinite at elevated pressures (bond distances in Å; bond angles in degrees)

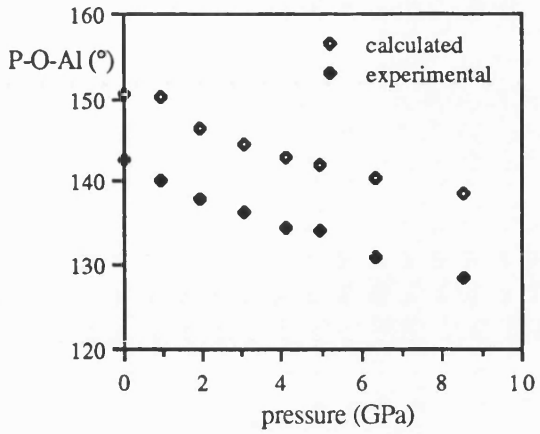

Figure 6.5: Calculated and experimental (Sowa et al, 1990) average P-O-Al bond angle of α-berlinite as a function of pressure.

Using a Birch-Murnaghan equation of state, Sowa et al (1990) calculated a bulk compressibility for α-berlinite of 36 GPa. In this simulation studies, the calculated bulk modulus is 35.3 GPa, which is very close to the experimental value. The bulk compressibility of α-berlinite is also very similar to the compressibility of α-quartz, which is after Levien et al (1980) 38.6 GPa.

Summary:

As in the simulation studies at elevated temperatures it could be demonstrated that the applied potential model predicts very accurately the structural parameters at elevated pressures.

However, the calculated decrease of the P-O bond distances with increasing pressure is opposite to the experimental results. In the simulation studies so far, it could be shown, that the calculated results of α-berlinite are in qualitative agreement with α-

quartz.Therefore it can be assumed, that the structural interdependence between Si-O and Si-O-Si, which was shown in α-quartz, can also be transferred to α–berlinite. Hence with increasing pressure the Al-O and P-O distances and the Al-O-P bond angles would decrease, which would support the outcome of this calculations. This structural interdependence has been discussed in detail in section 5.4.5.

6.3.5. Elastic properties of α-berlinite at different pressures

So far it was demonstrated that the second order elastic constants at 0 Kelvin but also at elevated temperatures are in good agreement with experimental values. Because of the structural similarities the elastic constants of α-quartz at 0 Kelvin and elevated temperatures are very similar to those in α-berlinite. The, in general, smaller elastic constants in α-berlinite show that it is less elastically stiff than α-quartz, a feature which is consistent with reduced covalent and enhanced ionic contribution to the interatomic binding as compared with quartz (Sidek et al, 1987).

Finally as a further test for this potential model the second order elastic constants and their pressure derivatives have been calculated from ambient pressure to 12 GPa at 300K.

In Figure 6.6 the six independent second order elastic constants are shown as a function of pressure. As in α-quartz they all show a non-linear dependence of the elastic constants on pressure. As an interesting feature c_{66} reaches a minimum at about 4 GPa. Compared to the calculated results of α-quartz using the SE-model the pressure dependence of the elastic constants in α-berlinite are very similar.

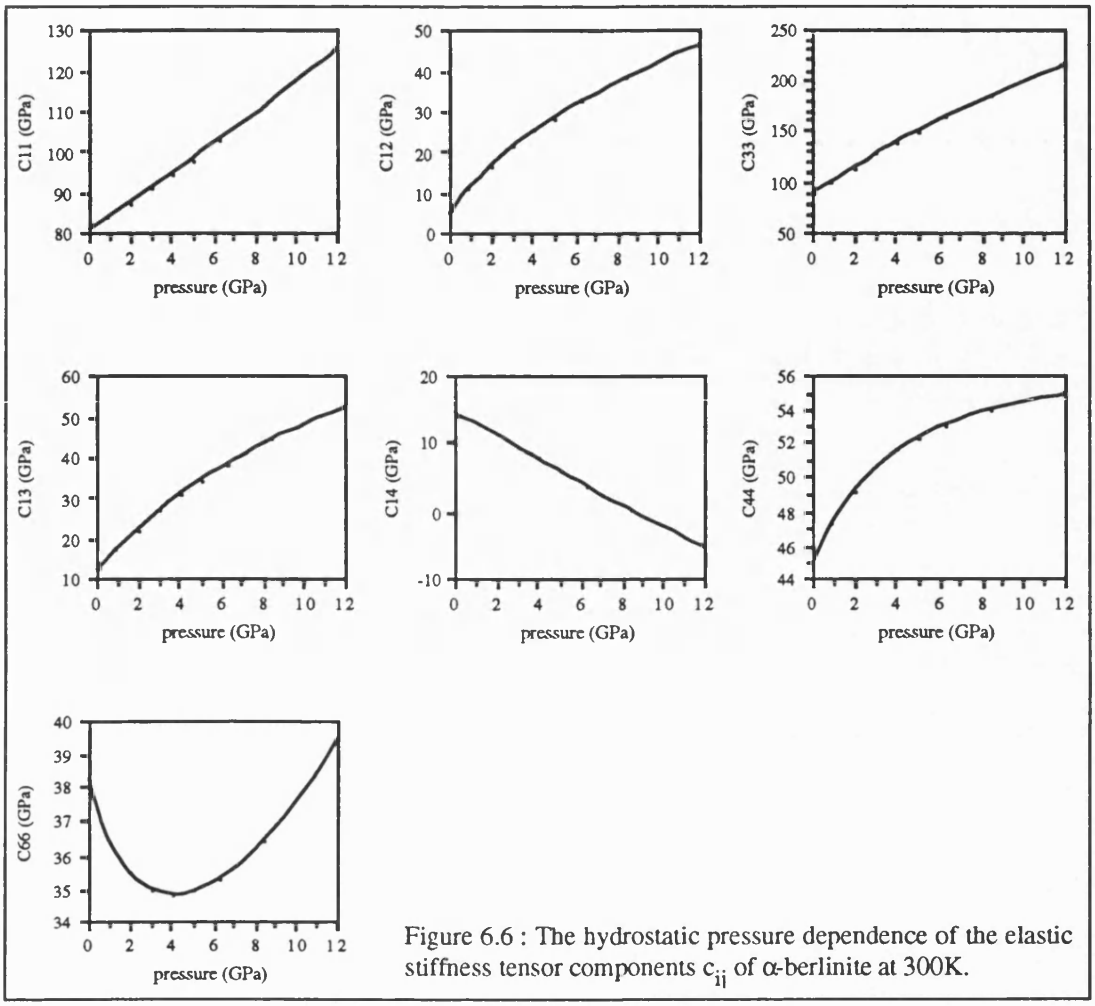

Figure 6.6 : The hydrostatic pressure dependence of the elastic stiffness tensor components c_{ij} of α-berlinite at 300K.

Sidek at al (1987) measured the second order elastic constants in α-berlinite in order to obtain the hydrostatic pressure derivatives.

In Table 6.8 the experimentally determined and the calculated values of the hydrostatic pressure derivatives for α-berlinite are listed. The pressure derivatives of the second order elastic constants have been obtained by a least square fit to the data from zero pressure to 0.2 GPa in our simulation studies and to 0.3 GPa in the experimental studies.

Considering the complexity of berlinite the calculated pressure derivatives are in a good agreement with the experimental values. Especially the theoretical and measured values

	$(\delta c_{ij} / \delta P)_{T, P=0}$						
	c_{11}	c_{12}	c_{13}	c_{14}	c_{33}	c_{44}	c_{66}
α-berlinite							
this work	2.60	7.10	5.73	-0.95	13.79	3.08	-2.25
Sidek et al (1987)	8.79	12.96	3.34	2.20	12.24	1.66	-2.08
α-quartz							
this work (SE-model)	1.41	7.89	6.91	-1.98	15.39	1.75	-3.24
Wang et al (1992)	1.49	12.12	4.04	-3.96	9.51	1.84	-5.32

Table 6.8: Comparison between the calculated values of the hydrostatic pressure derivatives $(\delta c_{ij} / \delta P)_{T, P=0}$ of the elastic constant tensors of α-berlinite and α-quartz and those measured experimentally.

of $(\delta c_{33}/\delta P)_{T,P=0}$ and $(\delta c_{66}/\delta P)_{T,P=0}$ agree very well.

All calculated pressure derivatives show a positive sign, except $(\delta c_{14}/\delta P)_{T,P=0}$ and $(\delta c_{66}/\delta P)_{T,P=0}$. This agrees with the measured data by Sidek et al (1987), although they obtained for $(\delta c_{14}/\delta P)_{T,P=0}$ a positive sign.

Considering the calculated and measured pressure derivatives in α-quartz, $(\delta c_{14}/\delta P)_{T,P=0}$ has also a negative sign. Because of the structural similarities of α-quartz and α-berlinite it can be assumed that the calculated negative $(\delta c_{14}/\delta P)_{T,P=0}$ is the right value. In section 6.2.3. the temperature derivatives of the second order elastic constants of α-berlinite have been calculated. All calculated temperature derivatives show a negative sign, except $(\delta c_{14}/\delta T)_{P,T=0}$ and $(\delta c_{66}/\delta T)_{P,T=0}$, which are positive. This is in addition supporting the assumption, that the calculated $(\delta c_{14}/\delta P)_{T,P=0}$ is accurate.

As shown in Table 6.8, the elastic constants and their pressure derivatives of α-berlinite have a similar pattern to those of α-quartz. Because of the in general lower elastic constants in berlinite it was already concluded that berlinite is less stiff elastically than quartz. The smaller pressure derivatives of berlinite show that also the application of pressure does not result in an increase of the stiffness of berlinite as it does in the case of quartz.

Again as in α-quartz, α-berlinite has a negative pressure derivative $(\delta c_{66}/\delta P)_{T,P=0}$ and $(\delta c_{14}/\delta P)_{T,P=0}$. This anomalous behaviour of $(\delta c_{66}/\delta P)_{T,P=0}$ and $(\delta c_{14}/\delta P)_{T,P=0}$ indicates that there may be even at room-temperature influence of the zone-centre optic phonon, whose softening is associated with α-β transformation (Sidek et al, 1987; Wang et al 1992). This behaviour has been discussed in greater detail in section 5.4.6.

Finally it could be demonstrated that the potential model also reproduces very well the second order elastic constants at elevated pressures and their pressure derivatives.

6.4. Summary

Using static and dynamic lattice simulation techniques a recently developed potential model for aluminophosphates (Kramer et al, 1991) was tested on berlinite ($AlPO_4$) to verify the validity of this potential model.This has been performed by comparing the calculated results with available experimental data.

The $AlPO_4$-berlinite is isostructural with quartz, therefore the outcome of the simulation studies of berlinite is in qualitative agreement with the simulated and observed values of quartz.

The static lattice simulation studies demonstrated that the applied potential model simulates very accurately the structural and elastic properties of α-berlinite.

In the dynamic lattice simulation studies, where temperature or pressure effects on berlinite were calculated, the potential model also performed very well.

Hence the potential model reproduces the structural parameters of α- and β-berlinite at elevated temperatures or pressures very close to experimental values. The results are also

in qualitative agreement with the experimental and calculated values in α- and β-quartz.

In the simulation studies of the second order elastic constants at different temperatures or pressures and their derivatives the agreement between calculated and experimental values in α-berlinite is again very good.

The applied potential model also reproduces the experimental known infrared- and Raman frequencies (q=0) of α-berlinite very accurately.

It was also possible, in contrary to the quartz and cristobalite simulation studies, to calculate the α-β transition temperature of berlinite very close to the experimental transition temperature. However, this potential model is in contrast to the applied potential models in quartz, probably not so sensitive to the quasi-harmonic approximation.

This potential model performs very well, both in static and dynamic lattice simulation studies, hence this model can be applied for further studies of aluminophosphates.

In addition it was again demonstrated that static and dynamic lattice simulations are very efficient methods, where structural and elastic properties, vibrational spectra and phase transitions can be quite accurately modelled, at very low computational expense compared to quantum-mechanical methods.

VII. STATIC LATTICE SIMULATION OF ZEOLITES

The potential models used earlier were able to model the quartz-polymorphs very accurately. Because of its superior performance in the dynamical lattice simulations the E-model was selected for the following calculations on zeolites.

In this chapter lattice energy minimisation is used to calculate structural and energetic properties of zeolites. The primary aim is to rationalise zeolite stability in terms of structural features. There are some methods described which enable stabilities to be studied in terms of some structural motif. The ABC-6 family of zeolites are used as a model system, although the approach is quite general.

7.1. Relative stability of zeolites

The comparison of lattice energies gives a measure of the relative stability. The experimental determined structures were taken as starting structures. In the minimisation procedure both, the unit cell dimensions and the atomic coordinates were varied until the most stable configuration with the minimum lattice energy was obtained (at 0 Kelvin).

The results of these stability calculations on a set of siliceous zeolites and quartz-polymorphs expressed as lattice energy per SiO_2 unit, are presented in Table 7.1. A comparison of the lattice energies shows, that the structures like quartz, silicalite,

sodalite and cancrinite have the lowest energy structures, whereas zeolite A, zeolite L and faujasite are one of the highest energy structures and therefore the less stable configurations.

zeolite - type	lattice energy/SiO_2 (eV)	density (T/1000Å)	ring - ratio (%)				
			4R	5R	6R	8R	12R
FAU	-128.4575	12.7	63		29		8
LTL	-128.4651	16.4	63		13	20	4
LTA	-128.4653	12.9	52		34	13	
RHO	-128.4746	14.3	56		22	22	
MAZ	-128.4876	16.1	58	19	6	10	6
GME	-128.4877	14.6	68		18	14	
MER	-128.4889	16.0	65		35		
CHAB	-128.4898	14.6	64		14	21	
OFF	-128.4914	15.5	64		27	9	
ERI	-128.4948	15.6	57		29	14	
LEV	-128.4973	15.2	60		28	12	
BOG	-128.5137		17	42	41		
bea	-128.5140	15.5	26	63	10		
CAN	-128.5254	16.7	54		46		
LIO	-128.5267	15.7	35		65		
AFG	-128.5287	15.9	35		65		
SOD	-128.5318	17.2	43		57		
MFI	-128.5680	17.9	5	76	19		
Tridymite	-128.6335	22.7			100		
Cristobalite	-128.6420	23.0			100		
Alpha-Quartz	-128.6610	26.6			100		

Table 7.1: Lattice energy/SiO_2, density and ring ratio for several zeolite types and α–quartz

A more detailed analysis of the characteristic features of these structures shows that the relative stability of these zeolites can be correlated with some structural changes. One important structural characteristic in zeolite structures is the type of rings from which a

framework is built. Considering the polyhedral building units and cages of a zeolite framework, described in detail by Smith (1989), the number of specific ring sizes can be evaluated for each zeolite type. The polyhedral building units and cages give an exact mathematical description for the topology and geometry of specific framework types, but it has to be stressed that this does not include all the pore and channel structures.

In Table 7.1 the calculated ratio of specific ring sizes for some zeolite types are reported. From a comparison of the lattice energy with the ring ratio it can be concluded that in general the most stable structures are characterised by the presence of mainly 5- and/or 6-rings, a smaller number of 4-rings and the absence of 8- and 12-rings. The high energy or less stable structures are characterised by a predominance of 4-rings, but also by a smaller number of 6-, 8- and 12-rings.

Stixrude and Bukowinski (1990) related the ring size to the framework density of tectosilicates by performing a ring statistic on the basis of a framework-specific characteristic ring size. In an algorithm they calculated an average number of rings of a size K passing through a single T (T = Al or Si) atom averaged over all T atoms in a structure. This characteristic ring size increases with increasing framework density.

The calculated ring sizes from Stixrude and Bukowinski (1990) were correlated to the calculated lattice energies of some zeolites and quartz-polymorphs. A correlation between the lattice energy and the ring size is given and illustrated in Figure 7.1. The ring size (K) increases with increasing stability.

The observation that a characteristic ring size increases with stability is consistent with the above observed trend, that with an increasing number of 5- and/or 6-rings and a decreasing number of 4-rings the stability increases.

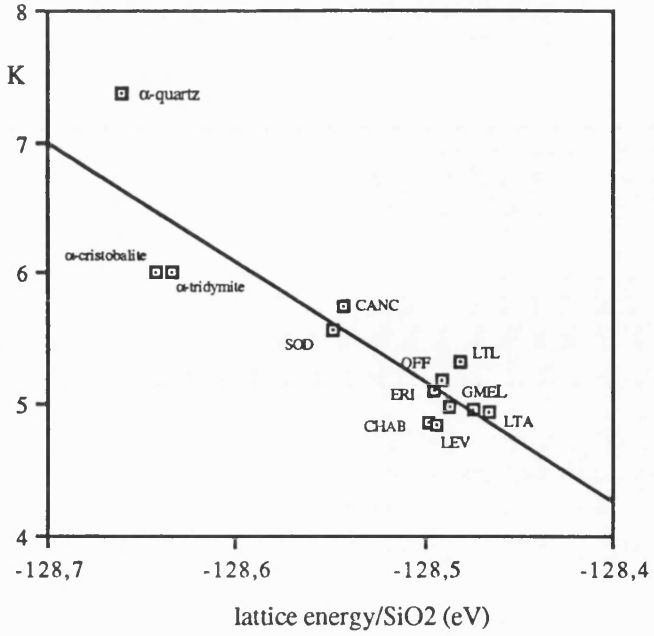

Figure 7.1: The lattice energy/SiO_2 as a function of the ring size K.

The ring size is obviously related to the framework density. Consequently a relationship between density and stability must follow. This relationship is illustrated in Figure 7.2.

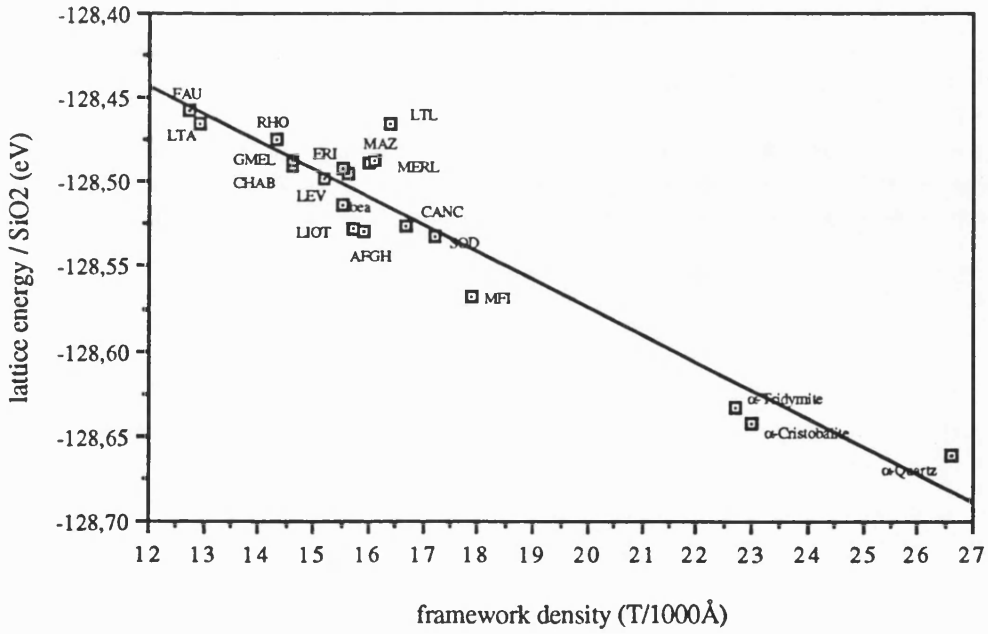

Figure 7.2: The lattice energy per SiO_2 of zeolites and quartz-polymorphs as a function of density

A linear correlation of the framework density with the calculated lattice energies for several zeolite structures and the quartz-polymorphs is observed; stability increases with density. Akporiaye and Price (1989) observed this relationship also for a range of zeolite structures. Hence faujasite, zeolite A or zeolite L, structures with large micropore volume are less stable structures compared to the very dense structures like sodalite or silicalite.

All these studies were performed on purely siliceous zeolites. As a further step the effect of alumination on the zeolite stability in different structure types was studied. Therefore silicon was substituted in a random distribution by aluminium (considering Loewenstein's rule) and charge balancing cations in different Al/Si ratios. The effect of the Al/Si ratio on the stability was studied on cancrinite, sodalite, zeolite L and faujasite.

Generally in all zeolites a decrease of the lattice energy with increasing aluminium content was observed.

Changing the aluminium content has also a significant effect on the relative stability of zeolites with different structural characteristics. An increase of the Al/Si ratio from 0 to 0.333 shows that the relative stability of faujasite and zeolite L is less affected than the stability of cancrinite and sodalite; e.g. the energy difference between siliceous faujasite and aluminium/silicon faujasite of the above mentioned ratio is -7.239eV, whereas the energy difference in sodalite is -8.139eV. Hence the stability of dense structures like sodalite or cancrinite is more affected by the incorporation of aluminium in the framework in contrast to the more porous structures like faujasite or zeolite L. The calculated relative stability of the above mentioned zeolite structures with different Al/Si ratios is illustrated in Figure 7.3.

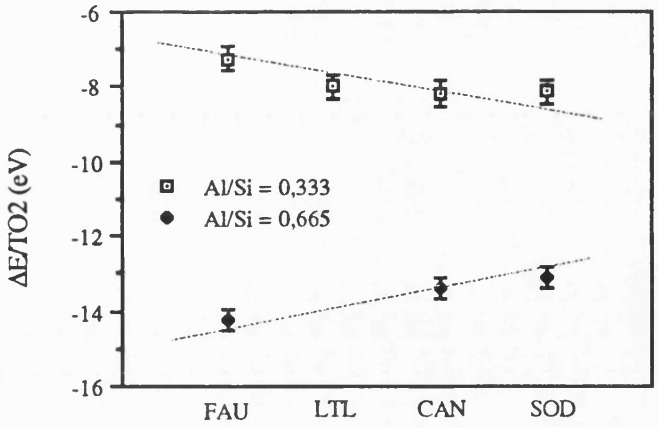

Figure 7.3: Relative lattice energy of zeolites with different Al/Si ratios ($\Delta E = E_{\text{Si- zeolite}} - E_{\text{Al+Si zeolite}}$).

However, an increase of the Al/Si ratio shows an opposite trend. Having an Al/Si ratio of 0.665 the energy difference for faujasite is -10.863eV and for sodalite -10.850eV. Although the energy differences in faujasite and sodalite are very close, there is clearly a change of the above mentioned trend visible.

So far it could be demonstrated that the relative stability for a range of siliceous, but also non-siliceous zeolite types is governed by their structural characteristics. In addition to the crystallographic significance the relationship between stability and framework structure or stability and density is central to the design and synthesis of new zeolite structures. This also provides further support for the importance of structures containing mainly 6- and/or 5-rings in the search for stable zeolite structures.

7.2. Relative stability of ABC-6 zeolites

In the previous section it was shown that the relative stability of zeolites is related to structural characteristics, like ring size, density and silicon to aluminium ratio. It would be desirable to have simple empirical rules to predict the stability of frameworks in order to provide an aid to synthesis. In order to illustrate this approach some preliminary studies on the ABC-6 family of zeolites will be described. It will be focussed mainly on siliceous end-members so that it will be possible to distinguish the influence of the framework structure from the Al/Si ratio.

The ABC-6 family of zeolites are used here as a model system. The structural features of the ABC-6 zeolites have been discussed in detail in chapter 1. Because of their relatively complex structural construction some basic structural features will be recalled. ABC-6 zeolites can be distinguished by their stackings of single 6-rings. These single 6-rings can be stacked in 3 different ways (A, B and C) along the hexagonal c-axis and therefore an infinite number of different structures are possible.

Only a small number of possible ABC-6 zeolite structures occur in nature. Hence to have a set of many different stacking sequences for systematically comparison, a computer programme was written. This approach generates series of hypothetical ABC-6 structures systematically. More details about this approach are given in Appendix I.

7.2.1 Relative stability of ABC-6 zeolites in terms of stacking sequences

The lattice energies for several different ABC-6 zeolite structures with different stacking

sequences have been calculated. Some structures correspond to known ABC-6 zeolite structures others represent hypothetical structures.

The result of the lattice energy minimisation are shown in Figure 7.4. It can be seen that the ABC-6 group can be divided into sub-groups based on their stability. These sub-groups contain sequences with only single 6-rings (S6R) and with single 6-rings and double 6-rings (D6R). The structures containing S6R only are much more stable than the structures containing both S6R and D6R. But the energy differences within the sub-groups are small.

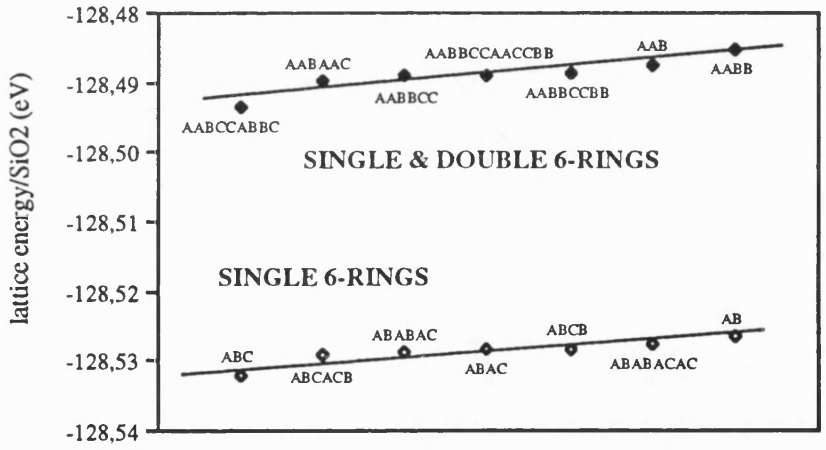

Figure 7.4: Lattice energy/SiO_2 as a function of different stacking sequences

The hypothetical stacking sequences AAAB, AAAAB and AAAAAB are not shown in this figure, because of graphical reasons. These stacking sequences are compared to the other sequences the lowest energy structures.

The stability is independent of the amount of stacking sequences, it is dependent on the

way they are stacked. The more different 6-ring sequences are in a unit the more stable is the structure.

7.2.2. Relative stability of ABC-6 zeolites in terms of structural features

In the above section it was demonstrated that the stability of the ABC-6 zeolites is dependent on the stacking sequence. Hence S6R structures are more stable than structures containing S6R and D6R. A description of the local geometry, e.g. cell parameters, bond distances and bond angles, might explain the variation in the stability of the stacking sequences.

In order to get more detailed information about the stacking sequences of the ABC-6 zeolites the lattice parameters were calculated and compared to the stacking sequences and consequently to the stability.

As a logical consequence of the structural construction of the ABC-6 types, the cell dimension *c* becomes larger as the number of stacking sequences increases.

However, within the ABC-6 family it was observed that the calculated cell dimension *a* becomes larger as the number of D6R increases and similarly becomes smaller as the number of S6R increases. In Figure 7.5 the relative lattice parameter (*a*-*a*') is illustrated; *a* corresponds to the lattice parameter before minimisation and *a*' represents the lattice parameter of the minimised structure. It is clearly shown that stacking sequences containing only S6R show a decrease of the lattice parameter, whereas the sequences containing S6R and D6R show an increase. Stacking sequences containing only D6R show the biggest increase of the lattice parameter *a*.

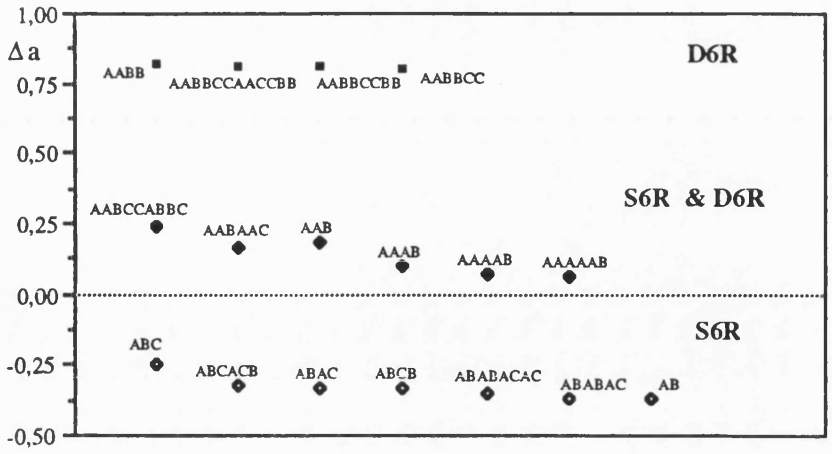

Figure 7.5: The relative lattice parameter (Δa) for a set of different stacking sequences (Δa = a - a'; a = lattice parameter before minimisation; a' = lattice parameter after minimisation); (S6R = single 6-rings; D6R = double 6-rings)

The increase or decrease of the lattice parameter a is independent of the amount of stacking sequences; it is only dependent on the number of S6R and D6R are present in a sequence.

Compared to the calculation of the relative energies of the stacking sequences, the calculation of the lattice parameter a allows a more detailed classification of the stacking sequences into sub-groups. Hence these sub-groups consist of stacking sequences containing only S6R, S6R and D6R and D6R. These sub-groups can also be related to the calculated stability of these sub-groups.

The stability order within the sub-groups does not correspond exactly to the calculated order of the lattice parameter. But as the energy differences are very small within a sub-group these slight discrepancies might be expected.

Once a chemical composition of a framework is known then it will be possible to estimate the number of S6R and D6R in a member of the ABC-6 family from the length of the a dimension and consequently it can be assigned to the corresponding stability field. This

may be particularly useful in assigning intergrowths where direct experimental observations may be difficult.

Within the ABC-6 family the calculated structural parameters as the bond angle and bond distances also reveal a classification into sub-groups and therefore into stability fields.

Hence the Si-O distances increase and the O-O distances decrease as the number of D6R increases, which is consequently connected with a stability loss.

In addition the O-Si-O bond angles show a characteristic decrease from ~109.5° to ~105.8° as the number of D6R increases. The calculated O-Si-O bond angles allow also a distinct subdivision of the ABC-6 group into stacking sequences containing only S6R, S6R and D6R and sequences built up of D6R only. Hence a decreasing bond angle indicates decreasing stability within the ABC-6 zeolites. This is illustrated in Figure 7.6, where the stability of the ABC-6 zeolites is shown as a function of the O-Si-O bond angle.

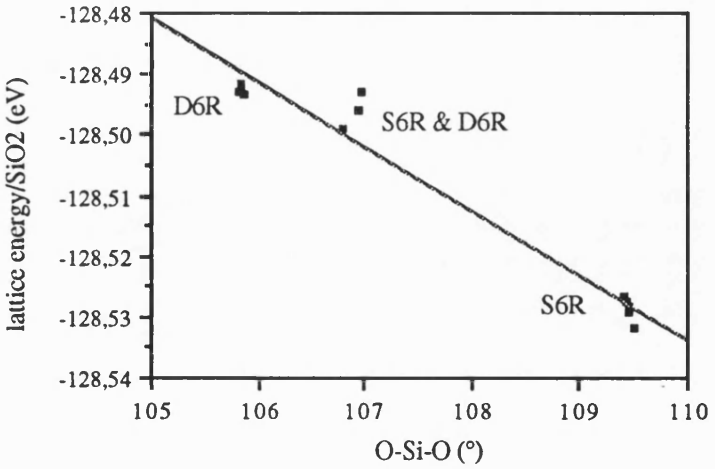

Figure 7.6: The lattice energy of different ABC-6 zeolite structures as a function of the O-Si-O bond angle (S6R = single 6-rings; D6R = double 6-rings)

As illustrated in section 7.1., there is a close relationship between the density of zeolite frameworks, the characteristic features of their structures and their stability. Thus a description of the geometric and topological variations among different stacking sequences on which framework density depends is important to an understanding of the construction of the ABC-6 zeolites and their relative stability.

The framework density of several ABC-6 zeolites has been calculated and correlated with the corresponding lattice energy. The outcome of this relationship is shown in Figure 7.7.

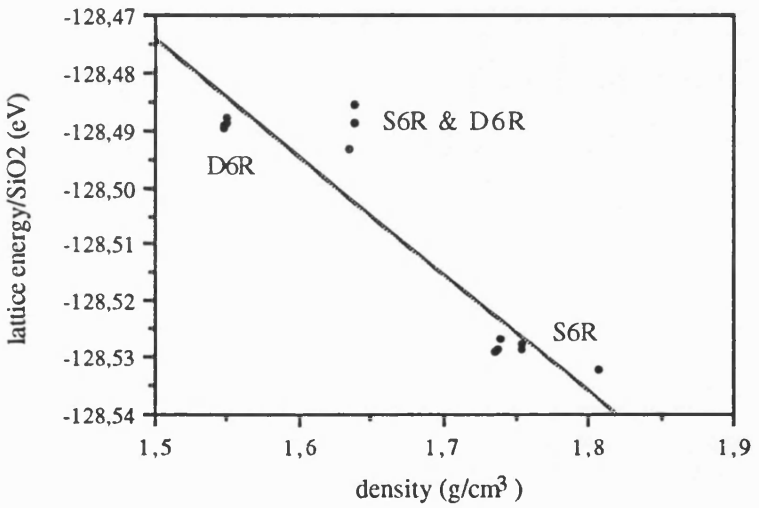

Figure 7.7: The lattice energy of different ABC-6 zeolite structures as a function of the framework density (S6R = single 6-rings; D6R = double 6-rings)

As expected the stability increases with increasing framework density. Additionally a clear classification of the stacking sequences into sub-groups is given. Hence stacking sequences containing only S6R are the most dense and therefore most stable structures and in contrast, stacking sequences built up of only D6R are the less stable and consequently the less dense structures. ABC-6 structures, which contain both, D6R and S6R are in between the high and low density structures.

7.2.3. Relative stability of ABC-6 zeolite structures in terms of the coordination sequence

The topology of framework structures may be characterised by the coordination sequence (CSQ). In the present work the CSQs are primarily investigated with a view to broadening the basis for the topological classification of ABC-6 zeolite type structures. Additionally the ABC-6 zeolite structures are used in this study to examine the relationship between CSQ and stability. The concept of the CSQ was first described by Brunner and Laves (1971) and applied to tectosilicates by Brunner (1979), Meier and Möck (1979) and Akporiaye and Price (1989).

The CSQ is a method to describe the number of atoms in a coordination shell around a central atom. For example in a zeolite structure the first nearest neighbour atoms are always four (the number of vertices of a tetrahedron). The number of the next nearest neighbour atoms are dependent on the structure. In principle as shown in Figure 7.8 the CSQ is an infinite sequence of numbers; the CSQ = $\{N_k\} = N_1, N_2, N_3 .... N_k$ is indicating the number of atoms in a shell k which are connected to atoms in a shell (k-1). The maximum possible CSQ for such a system is given by $N_k = 4, 12, 36, 108, ...$

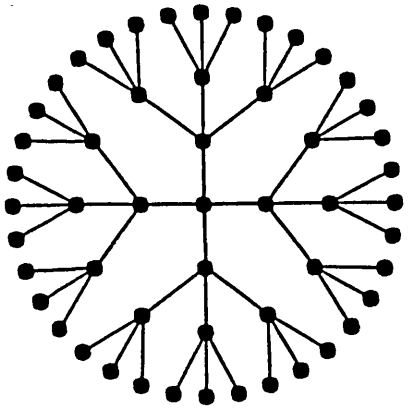

Figure 7.8: Planar example demonstrating the derivative of the CSQ; the framework shows the atoms of "sphere k" which are connected to atoms of "sphere k-1".

In the case of zeolite frameworks the values of the coordination numbers are much reduced because of the presence of closed rings. Therefore the CSQ is dependent of the smallest ring in the structures. Small rings lower the values of the CSQ substantially.

The CSQ for each T-atom (T = Si, AL) in a zeolite structure depend only on the topology of the framework, but not on the actual symmetry, cell dimensions and other structural data (Brunner, 1979). Many zeolite framework types having a homogeneous net, where the T-atoms are topologically equivalent, will yield an identical CSQ. In other zeolite structures there are as many as 12 topologically distinct T-atoms and therefore a mean CSQ must be defined. These topologically heterogeneous nets can be assigned to weighted mean values $\{N_k\}$, the weights being given by the respective number of T-sites per unit cell.

The CSQ up the 10^{th} shell (k=10) has been calculated for a set of ABC-6 zeolite structures (the program used to calculate the CSQ was made available from Akporiaye and Price (1989)). The mean values $\{N_k\}$ for these are listed with the corresponding lattice energy in Table 7.2. For closely related framework structures, as the ABC-6 sub-group structures, containing S6R, S6R and D6R and D6R only a complete match of $\{N_k\}$ up to the 4^{th} shell is observed for each. In these cases the structural differences lie primarily in the stacking sequence within a sub-group. But at higher terms of the CSQ also differences within the sub-groups are observable.

However, considering all ABC-6 structures, differences between the sub-groups are observed from the 2^{nd} shell. This also applies for the stacking sequences AAAB, AAAAB and AAAAAB.

As an interesting feature it was observed that all stacking sequences containing D6R are homogeneous nets, whereas sequences containing D6R and S6R are heterogeneous

stacking sequence	lattice energy/SiO_2 (eV)	CSQ									
		1st	2nd	3rd	4th	5th	6th	7th	8th	9th	10th
ABC	-128.5321	4	10	20	34	52	74	100	130	164	202
ABCACB	-128.5292	4	10	20	34	52.67	75.33	102	133.33	168.67	208.67
ABABAC	-128.5287	4	10	20	34	53.33	76.67	103.33	134.67	169.33	209.33
ABAC	-128.5283	4	10	20	34	53	76	103	135	170	210
ABCB	-128.5283	4	10	20	34	53	76	103	135	170	210
ABABACAC	-128.5277	4	10	20	34	53.5	77	103.5	134.5	169	209
AB	-128.5266	4	10	20	34	54	78	104	134	168	210
AABCCABBC	-128.4973	4	9.33	18	30.67	48	68.67	91.33	117.33	147.33	183.33
AABAAC	-128.4948	4	9.33	18	30.67	48.67	71.33	95.33	120.67	150.67	188.67
AABBCC	-128.4945	4	9	17	29	45	64	85	110	140	173
AABBCCAACCBB	-128.4922	4	9	17	29	45	64.33	86.33	112	141.67	175.33
AABBCCBB	-128.4916	4	9	17	29	45	64.5	87	113	142.5	176.5
AAB	-128.4914	4	9.33	18	30.67	48.67	72	96.67	121.33	150	187.33
AABB	-128.4899	4	9	17	29	45	65	89	116	144	175
AAAB	-128.3537	4	9	16.25	27	43.75	66.5	92	116	139	169
AAAAB	-128.2838	4	8.8	15.2	24	38.40	60	86	112	134.8	159.2
AAAAAAB	-128.2376	4	8.67	14.5	22	34	53	78.17	105.67	131.33	155.33

Table 7.2: The CSQ and lattice energy of the ABC-6 zeolite structures.

structures. In the stacking sequences built up of S6R, homogeneous and heterogeneous structures were found. From this observation it can be concluded that stability is independent from equivalent or non-equivalent T-sites in a framework structure.

The CSQ contains essentially 2 pieces of information: (1) the coordination number N_1, which is four for all zeolite-types mentioned here and (2) the lower terms of the CSQ are a measure of the relative abundance of small rings (Brunner, 1979). For example if N_2 is lower than 9 this would require either two or more three-membered rings, or four or more four-membered rings to be connected to a T-atom. Therefore the lower terms of $\{N_k\}$ may be used to characterise the topology of the ABC-6 structures discussed here.

Brunner (1979) found a good correlation between $\{N_k\}$ and the framework density in zeolites. Similar correlations have been found by (Meier and Möck, 1979) and Akporiaye and Price (1989). With decreasing framework density they related a decreasing size of the smallest ring in the framework. Especially the 2^{nd}, 4^{th} and 5^{th} shell were shown to correlate with the density very well.

In the previous section a correlation between framework density and stability of ABC-6 zeolite was shown. Consequently a relationship between stability and CSQ should be given for the ABC-6 zeolite types. In Figure 7.9 the relationship between stability and CSQ for different shells (N_2, N_5, N_6 and N_{10}) is illustrated. For all different shells, considered in this graph, a distinct separation of the sub-groups of the ABC-6 stacking sequences can be observed. The CSQ of the 5^{th} shell shows the best correlation with stability. With decreasing stability the number of surrounding T-atoms decreases independent which shell was considered. The coordination number is also independent on the amount of different stacking sequences.

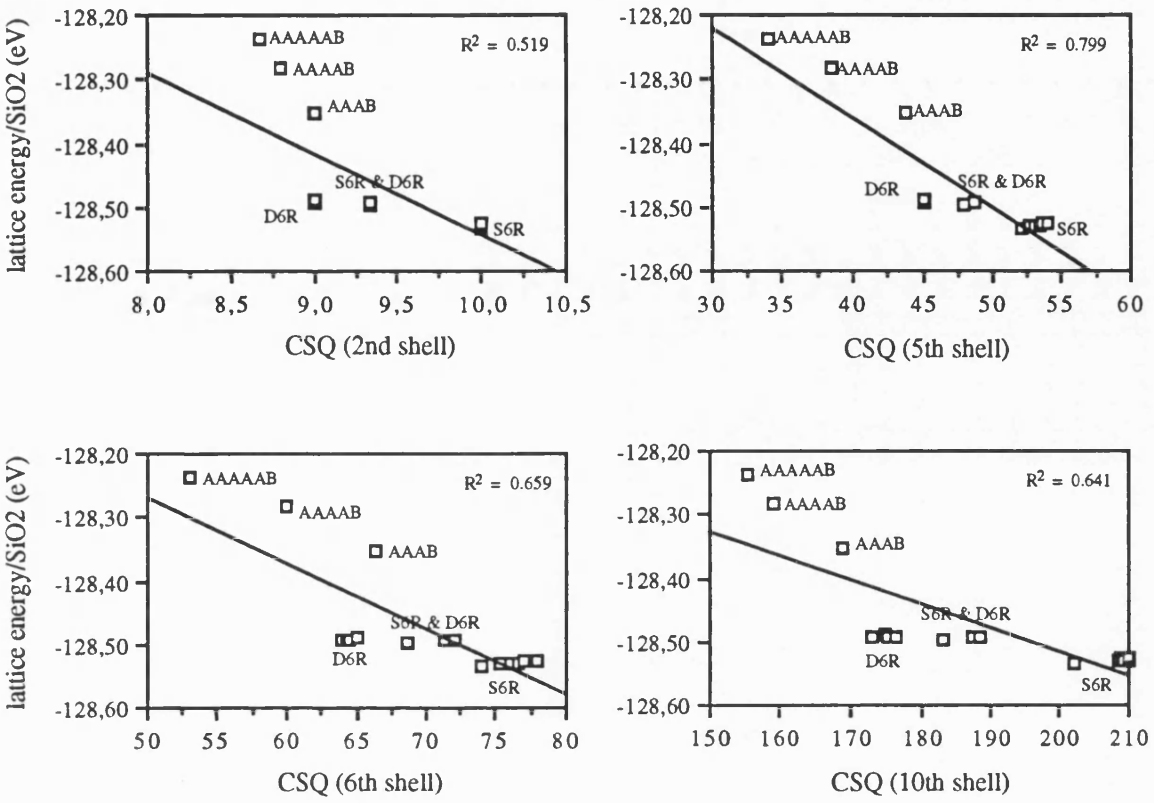

Table 7.9: The relative stability of the ABC-6 zeolite structures as a function of the CSQ.

This agrees with the observations from section 7.1, that the size of the smallest rings seems to be of more importance for obtaining the lowest possible framework density and therefore the less stable structure. Hence the CSQ is a measure of the increasing size and decreasing number of the smallest rings in a structure as the stability increases. Additionally the CSQ is also a measure of the stacking sequence. The coordination number decreases as the number of D6R increases, which corresponds to less stable configurations within the ABC-6 stacking sequence.

The CSQ of the 2nd shell has for each sub-group the same coordination number. But with increasing shell number a scatter of the coordination numbers within the sub-groups can be seen (Figure 7.9). In Figure 7.10 the values of the CSQ of the 6^{th} shell for the stacking

sequences containing S6R only and for those containing D6R only are shown. Again a correlation between the coordination number and the stability can be observed. But surprisingly and in contrast to the correlation observed above the coordination number is decreasing with increasing stability within a sub-group. This observation was also made for the sub-group containing S6R and D6R.

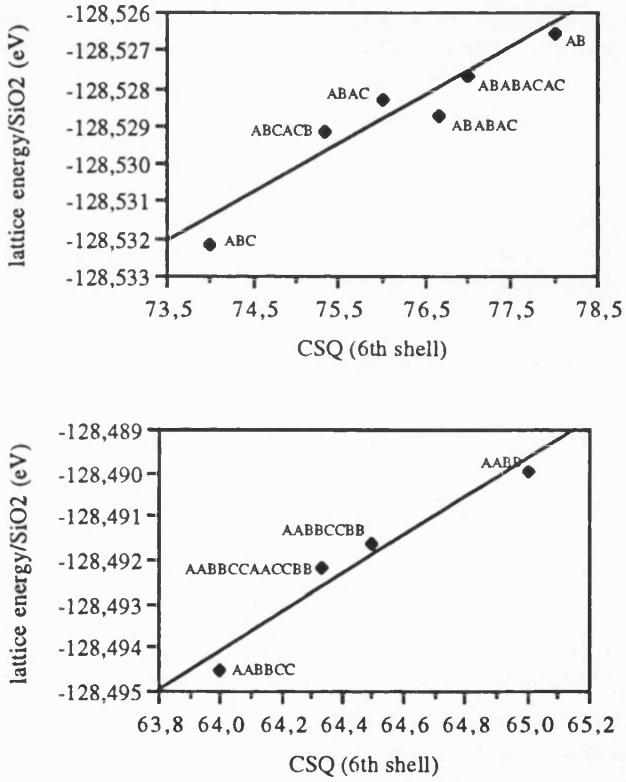

Figure 7.10: The lattice energy of the stacking sequences containing S6R and D6R as function of the CSQ.

However, this trend within a sub-group is not so distinct, as the coordination number increases and the number of the smallest rings also increases (e.g. ABC-stacking has compared to the AB-stacking a smaller number of 4-rings). Within a sub-group it might be concluded that the relationship between stability and coordination number depends in

a complex manner on the ring size, but also on the ring connection or stacking sequence.

A correlation of the stability with the CSQ was possible up to the 7^{th} shell for the stacking sequences containing S6R and to the 8^{th} shell for the sequences containing D6R. At higher values of the CSQ no correlation could be observed.

The concept of the CSQ has proved to be very useful in this studies as it broadens the basis for classifying the ABC-6 zeolite structures on purely topological grounds. Thus for an as yet unsynthesised zeolite its stability relative to known zeolite structure types may be assessed by computing the CSQ number up to the 6^{th} shell.

7.2.4. Relative stability of the ABC-6 zeolite structures in terms of the ANNNI-model

In order to make an analysis of the stacking sequence more predictive a method analogous to the ANNNI-model (Axial Next Nearest Neighbour Ising) was implemented. The ANNNI-model is a statistical mechanical model and was used to describe ordering in magnetic systems. The application of the ANNNI-model is discussed in detail by Price (1983), Price and Yeomans (1984) and Angel et al (1985). In the model they assume that the internal energy of any given polytypic structure is a function of both of the internal energy of the component structural modules and of the interaction energy between neighbouring modules. Additionally they assume that the internal energy of the modules is invariant and that the differences in energy of the polytypic phases is solely dependent upon the interaction energies between the structural units. The interactions between the units were presented by a Hamiltonian with competing first and second neighbour interactions.

For zeolites with different stacking sequences this correspond to write down an energy

which is the sum of the internal energy of a ring (E_0) and the interaction energy of a ring with its nearest neighbour ring (E_I) and an interaction energy with its next nearest neighbour ring (E_{II}); i.e.

$$E = E_0 + E_I + E_{II}$$

So for example, the expression for the energy for a zeolite with an AB stacking sequence would be:

$$E = 2E_0 + 2E_{I\,(AB)} + 2E_{II\,(ABA)}$$

and for an ABC stacking sequence the energy would be:

$$E = 3E_0 + 3E_{I\,(AB=AC=BC)} + 3E_{II\,(ABC)}$$

The approach employed in calculating the energy parameters was to fit them to the calculated lattice energies and to check the reliability of the method by comparing the predicted lattice energies of zeolite structures not used in the fitting procedure to those calculated directly using energy minimisation procedure. Initially poor agreement was obtained until the E_0 term was examined. The E_0 term is the self energy of an isolated 6-ring. By calculating the energies of isolated 6-rings it was found that they differed considerably for different stacking sequences. Hence the E_0 term can no longer be assumed as invariant.

The energy differences of the isolated 6-rings are due to the oxygen arrangement within a ring. These in-plane oxygen atoms can either alternately point in and out of a ring, or, all point into the ring. However, the oxygen arrangement within a ring is dependent on the stacking order; for example if an isolated ring is stacked between different S6R or

between D6R. Some examples are shown in Figure 7.11. From this figure it can be seen that as long as the single 6-ring is between two equal layers the oxygen positions alternately point in and out (favoured energetically). But if the 6-ring is in between two different layers the oxygen positions point into the ring.

Thus the assumption made in the ANNNI-model that only E_I and E_{II} are significant in determining the stabilities of stacking sequences and that the interaction between next nearest neighbours is independent of the intervening layer is not the case for calculating the stabilities of the ABC-6 zeolite stacking sequences.

To show the influence of the neighbour and next nearest neighbour interactions the self energies of single 6-rings in different stacking sequences have been calculated.

The results of some ring-self energies out of sequences containing only two different layers (A and B) are shown in Figure 7.12. It can be seen from this figure that the self energy of a single 6-ring decreases the more equal layers are in a stacking present.

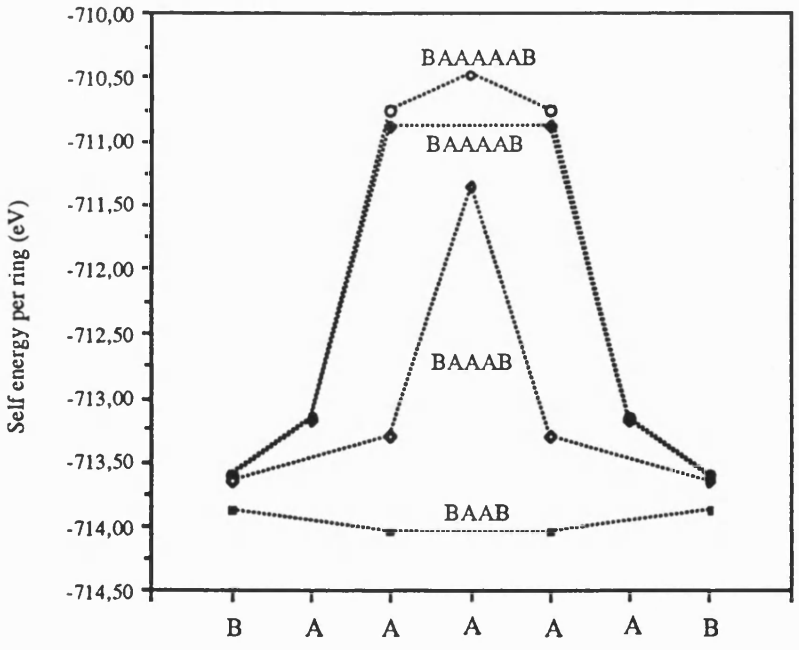

Figure 7.12: Calculated self energies per ring for different stacking sequences

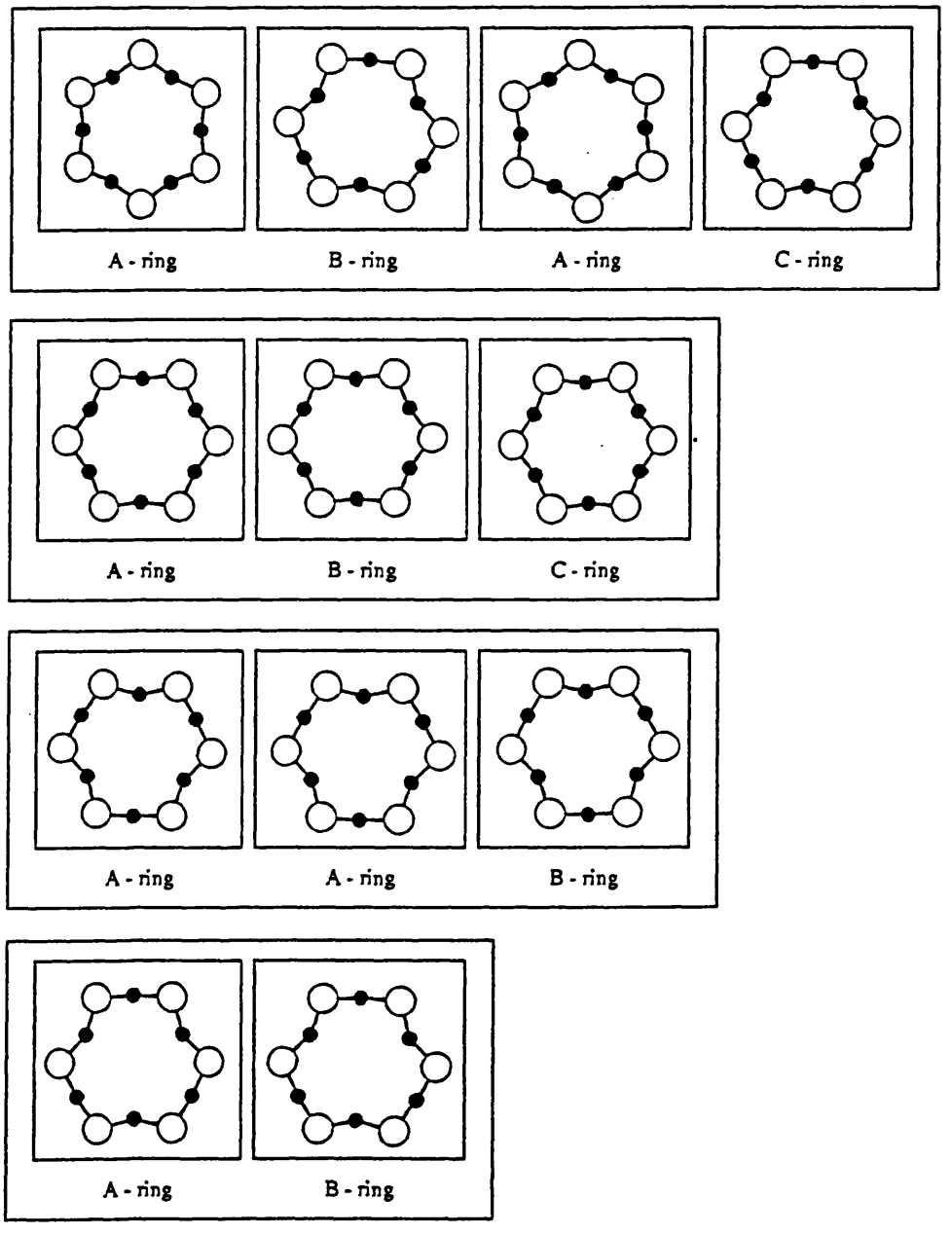

Figure 7.11: Minimised single 6-rings of an ABAC, ABC, AAB and AB stacking sequence (white circles = silicon atoms, black circles = oxygen atoms).

Additionally the self energies of single 6-rings out of a set of different stacking sequences containing three different layers (A, B and C) have been calculated. The averaged ring-self energy for each possibility appearing in a stacking-sequence is listed in Table 7.3. They all show significant differences in their energies.

	self energy (E_0)/ring (eV)
AAA	-710.85
ABA	-713.583
AAB	-713.422
ABC	-712.834

Table 7.3: Calculated average self energy for 6-rings in different sequences (the bold letter indicates the calculated ring)

From these averaged values the self energies of all stacking sequences employed in this study were evaluated and the interaction energies between the nearest (E_I) and next nearest (E_{II}) neighbours. The results are listed in Table 7.4. Considering the ring-self energies within the subgroups containing S6R, S6R and D6R an increasing self energy per ring is observed with decreasing stability. For stacking sequences containing D6R only, the self energy per ring is always the same. Consequently the interaction energies between nearest and next nearest neighbours ($E_I + E_{II}$) are decreasing with decreasing stability within each sub-group. The self energies (E_0) and also the interaction energies ($E_I + E_{II}$) are independent on the amount of layers in a sequence are present. They are dependent on how many different layers or rings are stacked in succession .

Stacking sequence	self energy/ring (E_0)	interaction energy ($E_I + E_{II}$)	
ABC	-712.834	-58.357	S6R, decreasing stability
ABCACB	-713.084	-58.091	
ABABAC	-713.330	-57.842	
ABAC	-713.209	-57.959	
ABCB	-713.209	-57.959	
ABABACAC	-713.396	-57.769	
AB	-713.583	-57.576	
AABCCABBC	-713.226	-57.768	S6R + D6R, decreasing stability
AABAAC	-713.473	-57.504	
AAB	-713.474	-57.475	
AAAB	-712.845	-57.305	
AAAAB	-712.426	-57.295	
AAAAAB	-712.162	-57.277	
AABBCC	-713.422	-57.539	S6R, decreasing stability
AABBCCAACCBB	-713.422	-57.535	
AABBCCBB	-713.422	-57.533	
AABB	-713.422	-57.518	

Table 7.4: Calculated self energies (E_o) and interaction energies ($E_I + E_{II}$) per ring for different stacking sequences (E_o, E_I and E_{II} in eV).

Although it is not possible to calculate E_I and E_{II} explicitly following assumptions can be made:

$E_I >> E_{II}$;

for the nearest neighbour interaction (E_I): AB > AA

and for the next nearest neighbour interaction (E_{II}): A<u>B</u>C > A<u>B</u>A > A<u>A</u>B > A<u>A</u>A

Thus by modifying self energies to reflect local geometry, better agreement is obtained. It appears that the stability of a given stacking sequence is dependent upon the self energy of the 6-rings in a sequence and their nearest and next nearest neighbour interactions.

This method has also proved to be very useful to determine zeolite stability as a function of the internal energy of the component structural modules and of the interaction energies between neighbouring modules.

7.2.6. Calculation of the relative stability of the ABC-6 zeolite cancrinite with different Si:Al ratios and different locations of framework atoms and non-framework cations

In section 7.1 it was shown that there is a relation between the silica and alumina ratio of zeolite and its relative stability. The more siliceous zeolites tends has a lower lattice energy.

In this section the silicon to aluminium ratio, the positioning of these atoms within the framework and the location of non-framework cations was thoroughly examined. Cancrinite, with the stacking sequence AB was chosen as it is the most simple stacking sequence of the ABC-6 type structures.

First the stability of cancrinite was calculated by increasing the alumina content gradually. Silicon was replaced randomly by aluminium, always considering Loewensteins rule. According to this rule the maximum number of aluminium atoms in

the cancrinite structure can be six. The charge balancing cations chosen were sodium.

In Figure 7.13 the effect of alumination on the stability of cancrinite is shown. With increasing aluminium content the stability relative to the free ions decreases non-linearely. This demonstrates that the alumination plays an important role in zeolite stability.

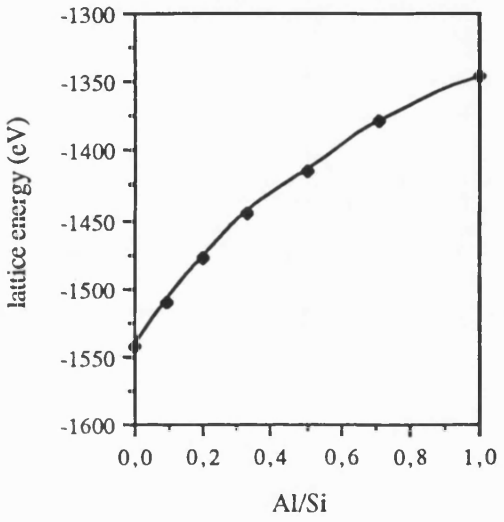

Figure 7.13: The effect of alumination on the stability of cancrinite.

However, when considering zeolites with a low aluminium content problems occur as a large number of ordering schemes may be proposed. A low aluminium content also has another problem related to the cation distribution. As the number of cations decreases, in response to the decreasing aluminium content, the cations may be placed in increasingly varied arrangements. Therefore the identification of the most stable positions requires the consideration of a large number of configurations.

Such calculations were performed on cancrinite with the aim of predicting and

rationalising the stability of non-siliceous ABC-6 zeolites in terms of the silicon and aluminium order and the cation position.

In the cancrinite structure there are two sites where the cations can be placed. Site I is in the S6R of the cancrinite cage and site II in the 12-ring channel. A simplified schematic of the cation sites in cancrinite is shown in Figure 7.14.

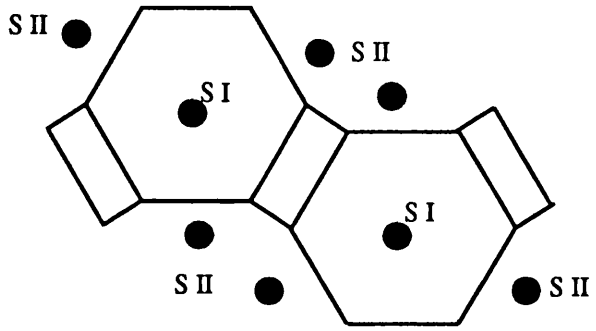

Figure 7.14: Cation sites in cancrinite; SI = Site I; SII = Site II

Initially the stability of cancrinite with the silicon to aluminium ratio of 11:1 was studied. Some of the possible schemes are illustrated in Figure 7.15. Additionally the calculated lattice energy, the relative energy (ΔE) with respect to the most stable configuration is also shown in this figure. In this example the aluminium atom was kept at the same position and only the cation positions were changed. The results show that in the most stable configurations the cations positioned in site II are more stable than when the cations are placed in site I. This trend was also observed for different aluminium positions, which are not shown in this figure.

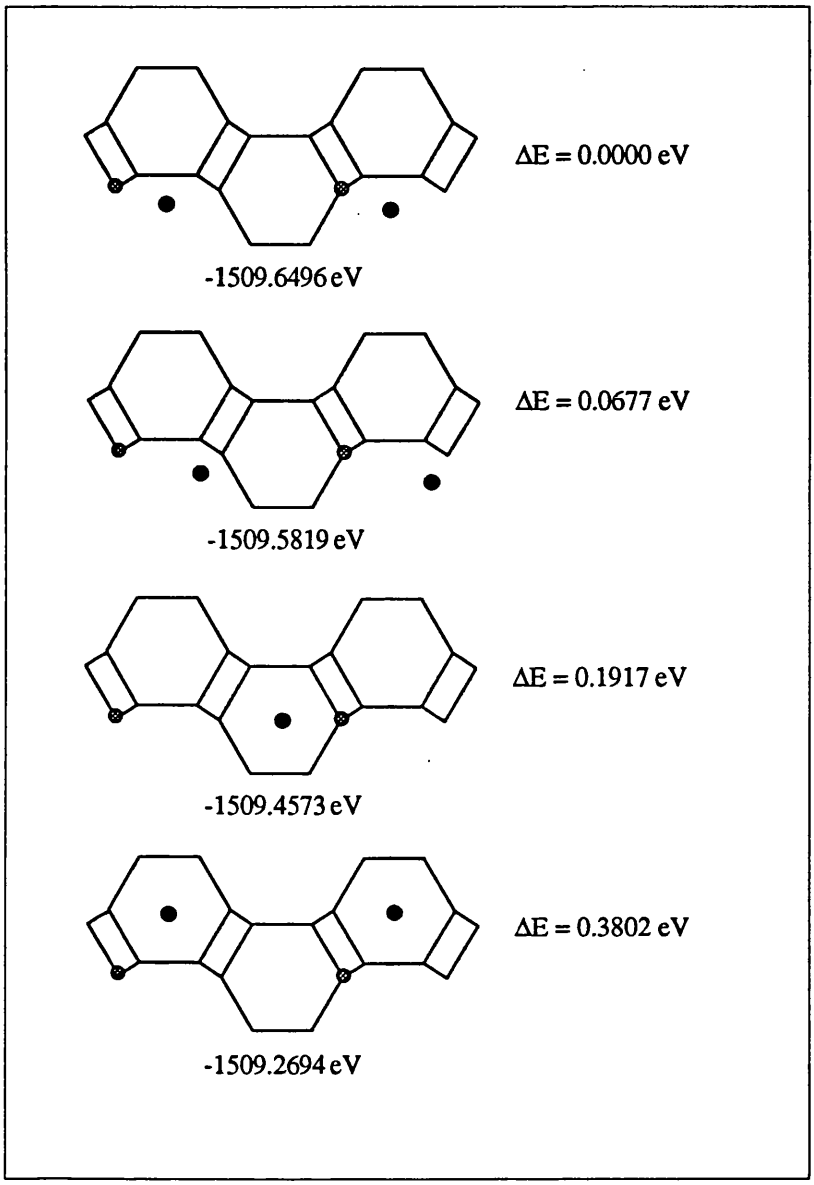

Figure 7.15: The stability of cancrinite having a Si:Al ratio of 11:1 with different aluminium and sodium positions (grey circle = aluminium, black circle= sodium; silicon and oxygen atoms are not shown).

As a consequence of this result the silicon to aluminium ratio was increased in order to obtain similar results. The stability of cancrinite having a silicon to aluminium ratio of 5:1 with different ordering was calculated. In Figure 7.16 a simplified illustration is shown of the different aluminium, silicon and cation positions in the cancrinite framework of which the energies were calculated. They are pictured in this figure with

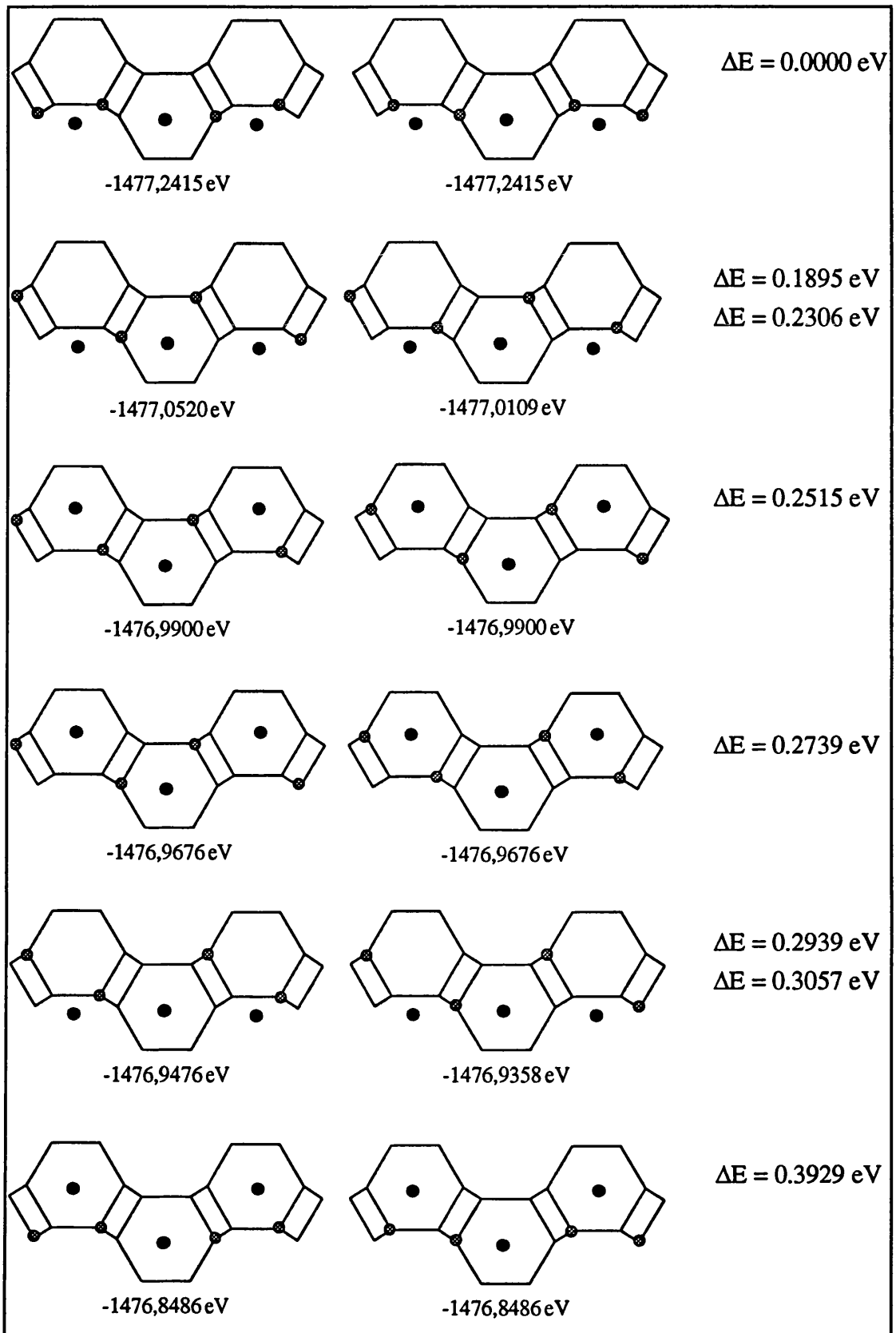

Figure 7.16: The stability of cancrinite having a Si:Al ratio of 5:1 with different aluminium and sodium positions (grey circle = aluminium, black circle = sodium; silicon and oxygen atoms are not shown).

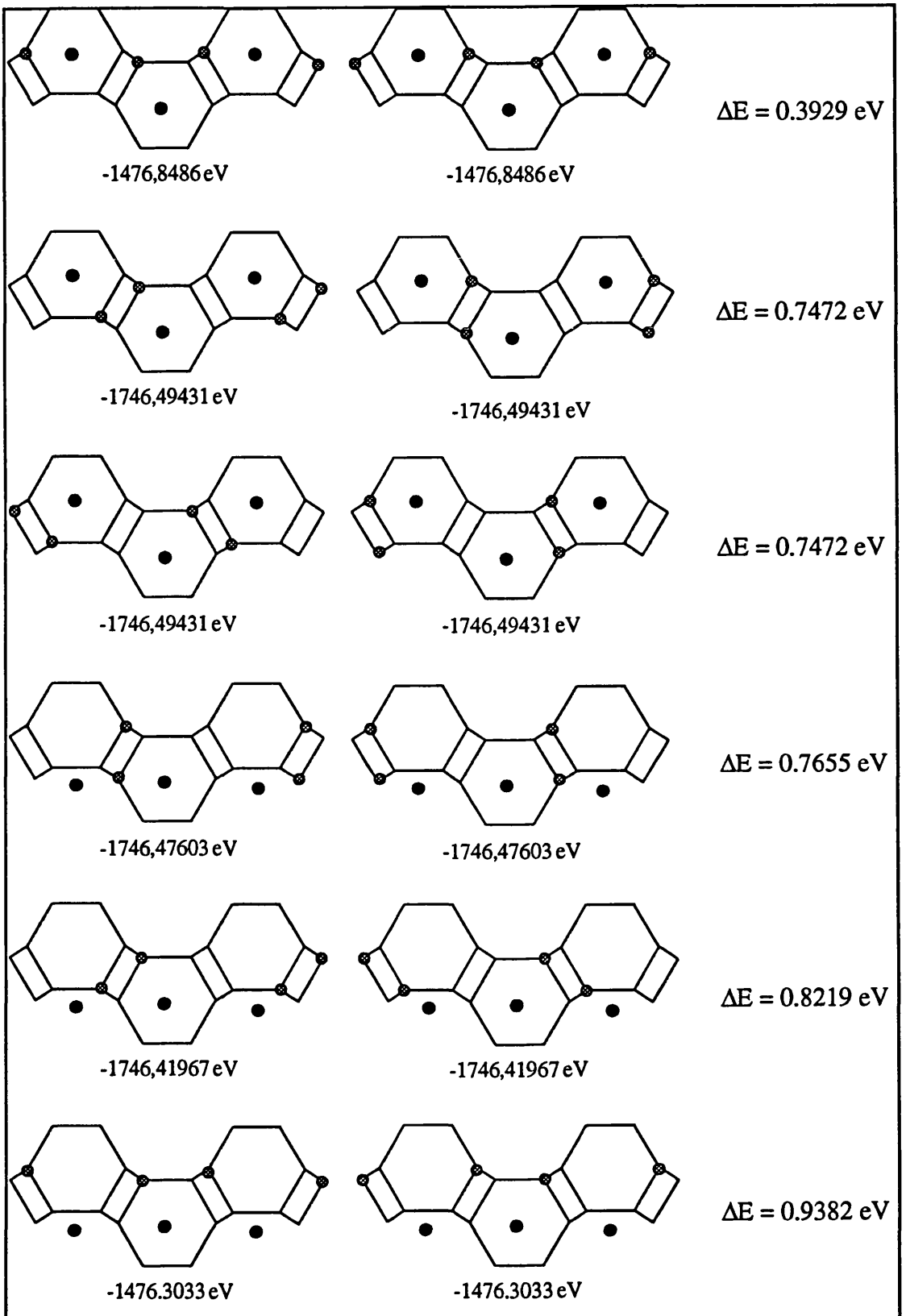

Figure 7.16: continued

decreasing stability together with the calculated lattice energy and their relative energy (ΔE).

Considering these results no definite rationalising of the stability is possible. In general the most stable configurations were found when each aluminium was placed in different 4-rings, which are joining the 6-rings. The less stable configurations were obtained when both aluminium atoms were positioned in one 4-ring. There was also no clear evidence that a certain cation site is energetically preferable.

These studies were also performed with higher silicon to aluminium ratios but again it was not possible to find a scheme of predicting and rationalising the zeolite stability in terms of the silicon, aluminium and cation positions. However, further work is in progress which might give some more informative results.

7.3. Summary

The relative stability of siliceous, but also non-siliceous zeolite types is governed by their structural characteristics. There is a relationship given between stability and framework structure and stability and framework density.

Additionally to these relationships it could be shown on the ABC-6 family of zeolites, which were taken as a model system, that the stability can be rationalised in terms of basic structural features.

Hence the stability can be expressed in terms of stacking sequences or estimated from the cell dimension.

The CSQ a topological feature of the the zeolite framework provides an effective method to indicated zeolite stability. The CSQ has proved to be very useful for classifying the ABC-6 zeolite structures on purely topological grounds.

Another method which enables stability to be studied in terms of a structural motif is the method analogous to the ANNNI model. Applying this method stability can be expressed by the internal energy of the component structural modules and the interaction energy between the nearest and next nearest neighbouring modules.

Finally calculations were performed on cancrinite with the aim to predict and rationalise the stability of ABC-6 structures in terms of the silicon, aluminium and cation positions at different silicon to aluminium ratios. Except that the stability decreases with increasing aluminium content no definite rationalising of the stability concerning the positioning of silicon, aluminium and the cations was possible.

VIII. STATIC LATTICE SIMULATION OF ALUMINOPHOSPHATES ($ALPO_4$)

Aluminophosphates are microporous structures, structurally related to zeolites, and interest in them has risen since the discovery of VPI-5 a $AlPO_4$-structure with unique 18-ring pores. Simulation studies play an important role for this new class of materials in order to understand factors governing their stability, similarities and differences to zeolites.

To date no detailed simulation studies on aluminophosphates have been performed using atomistic simulation methods, mainly because of the lack of a reliable potential model.

In chapter 6 it was shown that the semi-empirical P-O, Al-O and O-O potential parameters perform very well in the simulation studies of berlinite. Therefore these parameters were applied in the simulation studies for the microporous $AlPO_4$-structures.

The aim of the work described in this chapter was to use lattice energy minimisation to calculate the structural and energetic properties of $AlPO_4$-structures in order to demonstrate first, that the potential model calculates the structural properties accurately and second, to gain insight into the factors govern the stability of aluminophosphates.

8.1. Modelling of aluminophosphate structures

This section describes the calculation of the structural properties, i.e. cell dimension, bond distances and bond angles of aluminophosphates and compare them to experimental values. The structural features of aluminophosphates are very complex. Hence this study was restricted to structures for which good data have been published. To calculate the structural properties, the experimental structure was energy minimised, both, to constant volume and constant pressure.

In Table 8.1 the calculated cell dimensions for several aluminophosphates are reported together with the experimental values. All calculated values are in good agreement with the experimental data; only the lattice parameter *b* of the orthorhombic $AlPO_4$-8 structure is inaccurate being 4Å larger.

Structure	experimental	calculated
$AlPO_4$ - 17	a = 13.2371 [1] c = 14.7708	a = 13.3553 c = 15.6341
$AlPO_4$ - 8	a = 33.292 [2] b = 14.762 c = 8.257	a = 34.169 b = 18.603 c = 8.404
$AlPO_4$ - 5	a = 13.726 [3] c = 8.484	a = 14.178 c = 8.677
VPI - 5	a = 18.9752 c = 8.1044	a = 19.0981 c = 8.6619
$AlPO_4$ - 52	a = 13.73 [5] c = 28.95	a = 14.10 c = 29.99

Table 8.1: Calculated and experimental cell dimensions (Å) for several $AlPO_4$ - structures ((1) Pluth et al, 1986; (2) Dessau et al, 1990; (3) Bennett et al, 1983; (4) McCusker and Baerlocher, 1991; (5) Bennett el al, 1989)

Additionally to the lattice parameters the interatomic bond distances and angles have been calculated. Table 8.2 gives the energy minimised values together with available experimental data. The calculated bond distances and O-T-O (T = Al, P) bond angles are all within 1% of accuracy compared to the experiment. Only the P-O-Al bond angles show slightly bigger deviations.

Structure		Al - O	P- O	O - P - O	O - Al - O	P - O - Al
$AlPO_4$ - 5	calc	1.746	1.509	109.447	109.428	162.55
	expt [1]	1.742	1.528	109.467	109.450	145.78
$AlPO_4$ - 17	calc	1.749	1.510	109.442	109.372	158.51
	expt [2]	1.757	1.520	109.475	109.388	147.20
VPI - 5	calc	1.751	1.510	109.415	109.455	164.48
	expt [3]	1.740	1.510	109.580	109.580	149.00
$AlPO_4$ - 8	calc	1.747	1.509	109.44	109.37	157.65

Table 8.2: Calculated and experimental interatomic distances (Å) and angles (°) for some $AlPO_4$ - structures ((1) Bennett et al, 1983; (2) Pluth et al, 1986; (3) McCusker and Baerlocher; 1991).

In summary the agreement with experiment is very good and shows that the potential model is able to predict the structural properties of microporous aluminophosphates accurately.

8.2. Relative stability of aluminophosphates

8.2.1. Calculation of the relative stability

The experimental structures of some aluminophosphates were also taken as starting structures to evaluate their relative stabilities. As in the calculations of the structural properties a full lattice energy minimisation was performed.

The results of the stability calculations, expressed as lattice energy per TO_2 (T = Al,P) are listed in Table 8.3. A comparison of the energies shows that α-berlinite is as expected the most stable structure followed by $AlPO_4$-8, whereas the less stable configurations are $AlPO_4$-17 and $AlPO_4$-52, both ABC-6 structures with a stacking sequence of AABAAC and AABBCCAACCBB respectively.

Structure	lattice energy/TO_2 (eV)	pore structure (1)
Alpha - Berlinite	-59.2978	–
$AlPO_4$ - 8	-58.9967	**14** (7.9 x 8.7 *)
$AlPO_4$ - 5	-58.9787	**12** (7.3 *)
VPI - 5	-58.8819	**18** (11.2 *)
$AlPO_4$ - 17	-58.8543	**8** (3.6 x 5.1 ***)
$AlPO_4$ - 52	-58.8106	**8**

Table 8.3: Calculated lattice energies/TO_2 and the pore structures for several $AlPO_4$-framework structures ((1) bold numbers are indicating the number of T (or O) atoms in the defined ring; numbers in brackets are approximate aperture free diameters in Å; the number of asterisks are indicating if the channel system is 1, 2 or 3-dimensional).

8.2.2. Relative stability of aluminophosphates in terms of basic structural features

Some of the $AlPO_4$-structures considered in this study are characterised by very large channel systems and it might be expected that these large pore structures are influencing the stability.

By considering the lattice energies of these aluminophosphates it can be shown that the stability of these structures are independent of the channel system or the pore structures (listed in Table 8.3). For example, the relative stability of VPI-5, the first 18-ring molecular sieve, is more stable than a 8-ring but less stable than a 12-ring.

However, a more detailed analysis of the characteristic features of these structures show that the stability can be correlated with some structural features, e.g. ring size. For some aluminophosphates the ring-ratio can be correlated with stability. The ring-ratio within the framework was evaluated using the method described in section 7.2. The alternation of Al and P in $AlPO_4$-frameworks restricts the order of a ring to an even number; therefore aluminophosphates with 5-rings analogue to zeolites have not yet been reported.

In Table 8.4 the calculated ratio of two specific ring sizes, the 4- and 6-rings, are listed for some aluminophosphates. A comparison of the stability with the ring ratio reveals following trend: with increasing stability the number of 6-rings increases within the framework and the number of 4-rings decreases.

This observation, that a characteristic ring size increases with stability is consistent with the observed trend for zeolite structures; namely that the stability increases with an increasing number of 6-rings (for zeolites also 5-rings) and a decreasing number of 4-rings.

Structure	lattice energy/TO_2 (eV)	ring - ratio (%)	
		4 R	6 R
$AlPO_4$-17	-58.85427	67	33
VPI - 5	-58.88188	22	78
$AlPO_4$ -5	-58.97872	13	87
Alpha-Berlinite	-59.29780	0E-30717	100

Table 8.3: The lattice energy/TO_2 and the 4- and 6- ring-ratio for some aluminophosphates.

For zeolites a relationship between stability and framework density was observed. This relationship was also tested for $AlPO_4$-framework structures.

In Figure 8.1 the relationship between the calculated density and stability is illustrated. As calculated for the zeolite structures a linear correlation between density and stability for several aluminophosphates is also observed, and shows the same result, that with increasing density the stability increases. Hence $AlPO_4$-structures with a large microporous volume, like $AlPO_4$-52 or $AlPO_4$-17 are less stable structures compared to the dense structures like α-berlinite or $AlPO_4$-8.

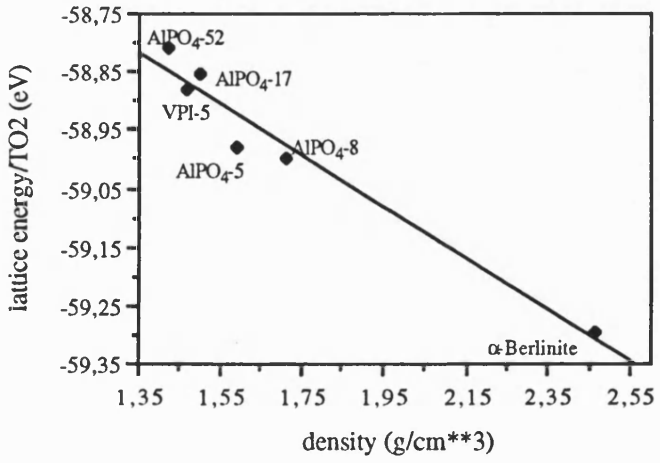

Figure 8.1: The lattice energy /TO_2 for $AlPO_4$ - structures as a function of the density.

From these results it can be concluded that also the stability of $AlPO_4$-structures is governed by structural characteristics and that the large pore structures found in some of the aluminophosphates have no major influence on stability; moreover the stability is governed mainly by the amount of 4- and 6-rings present in the structure. These results provide further support for the synthesis of stable aluminophosphates with large channel systems and a predominance of 6-rings.

8.2.3. Relative stability of aluminophosphates in terms of the coordination sequence

In chapter 7 it was demonstrated that the relative stability of zeolites can be expressed in terms of the coordination sequence (CSQ). The CSQ, characterised by the topology of the framework, is dependent on the ring size in the structure. Hence small rings lower the values of the CSQ substantially. A more detailed definition about the CSQ is given in chapter 7.

The lower terms of the CSQ {Nk} especially may be used to characterise the topology of the structures discussed here. Hence for the aluminophosphate structures the CSQ has been calculated up to the 6^{th} shell (k=6). The mean $\{N_k\}$ for these structures are listed in Table 8.5. Except for the 1^{st} shell all aluminophosphate structures show different coordination numbers of each sequence considered.

As already mentioned, zeolite structures show a relationship between the topological features contained in the CSQ and the lattice energy. For aluminophosphate structures there is also a correlation given between stability and the CSQ. The variation of the lattice

$AlPO_4$ - structure	CSQ					
	1st	2nd	3rd	4th	5th	6th
Berlinite	4	12	30	52	80	116
$AlPO_4$-8	4	11.11	21.33	35.56	52.89	75.33
$AlPO_4$-5	4	11	21	35	53	77
VPI-5	4	10.67	19.33	30.67	44	60.67
$AlPO_4$-17	4	9.33	18	30.67	48.67	71.33
$AlPO_4$-52	4	9	17	29	45	64.33

Table 8.5: The CSQ of several $AlPO_4$-structures.

energies and the CSQ of the 3rd, 4th, 5th and 6th shell is illustrated in Figure 8.2. All of them show a linear correlation between the CSQ and the stability. Although all considered $\{N_k\}$ show a good correlation, the best correlation was found to be in the 3rd shell, showing an increasing stability with increasing CSQ. This correlation is a measure of the increasing ring size and decreasing number of the smallest rings in the structure. Berlinite, which is the most stable structure considered here, is composed of 6-rings only and has the highest values of each CSQ considered, whereas $AlPO_4$-52, the less stable structure, is characterised by a predominance of 4-rings and has therefore the lowest values of the CSQ.

These results show that the lower terms of the CSQ $\{N_k\}$ can also provide an effective indication of the stability of aluminophosphate structures.

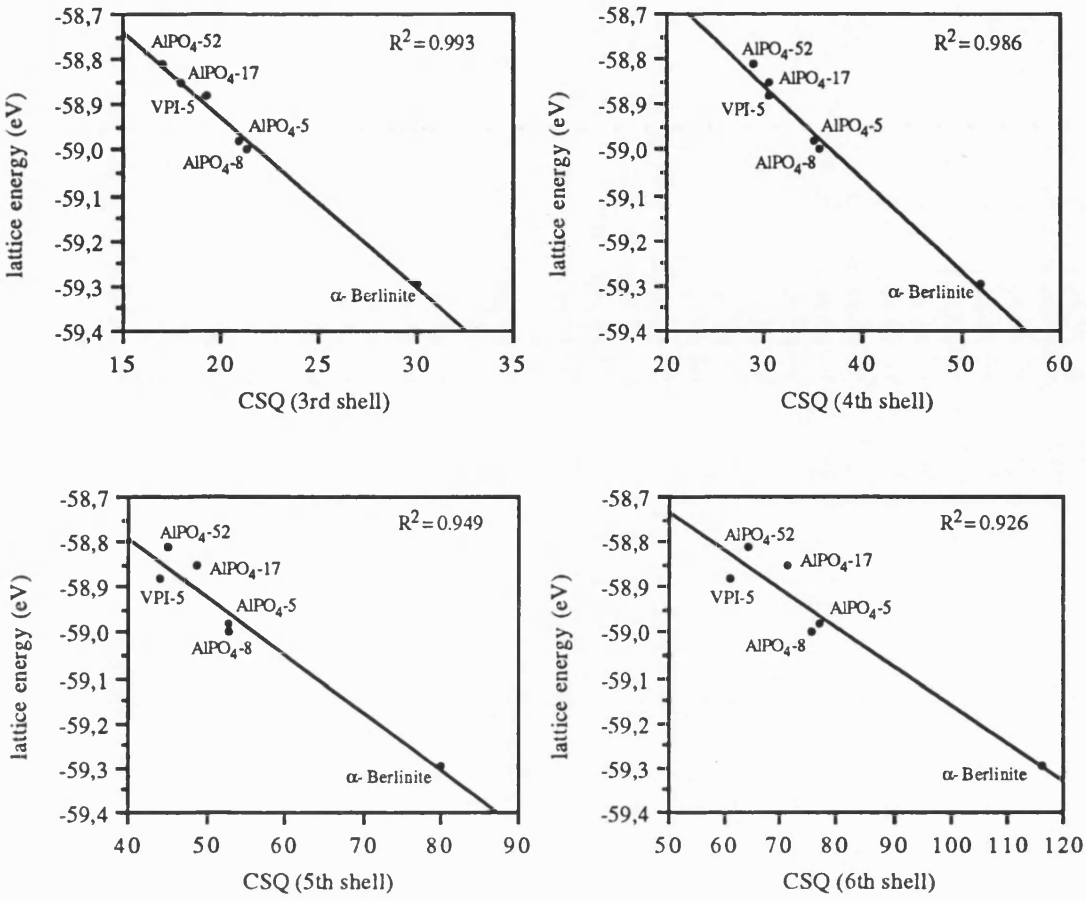

Figure 8.2: The lattice energy/TO_2 of $AlPO_4$-structures as a function of the CSQ.

8.3. Summary

The potential parameters applied for the simulation studies of the microporous $AlPO_4$-structures were able to calculate the structural properties very accurately.

Additionally to the structure prediction the relative stability of aluminophosphates is of major interest. As in the simulation studies of zeolites the relative stability of aluminophosphates is governed by structural characteristics. The stability of aluminophosphates is mainly characterised by the amount of 4- and 6-rings present in a framework and is not influenced by the observed large channel systems. There is also a relationship given between stability and framework density; stability increases with density.

The relative stability of aluminophosphates can also be expressed by the CSQ. The results show that the lower terms of the CSQ {Nk} provide an effective indication of their stability and confirm that the stability of aluminophosphates is dependent of the ring size in the structure. The stability of aluminophosphates increases with an increasing number of 6-rings and a decreasing number of 4-rings.

IX. DYNAMIC LATTICE SIMULATION OF ZEOLITES

The main limitation of the lattice energy simulation applied so far to zeolites is the neglect of temperature; i.e. the simulation is performed at 0 Kelvin and even neglects zero point motion. The extension to the static lattice simulation technique is to include the effects of temperature and/or pressure leading to the calculation of free energy and the thermodynamic properties of zeolites (as embodied in the computer code PARAPOCS (Parker and Price, 1989) described in chapter 3).

Dynamic lattice simulation studies of the quartz-polymorphs (chapter 5) demonstrated the ability of lattice dynamical methods. The structural, elastic and thermodynamic properties of the quartz-polymorphs were modelled accurately. Therefore, this type of simulation method is clearly predictive and may be used to avoid the experimental determination of these properties, which often present serious difficulties.

The aim of this chapter is to apply the techniques to zeolites. We will be able to provide insight into the factors which govern the energetic and thermodynamic properties and structural changes of zeolites at different temperatures. We note that such thermochemical data are necessary, for example, understanding solution-mineral equilibria in an number of important geochemical systems (Donahoe et al, 1990).

9.1. Free energy minimisation of zeolites

9.1.1. The relative free energy of siliceous zeolites at different temperatures

For several siliceous zeolites the Gibbs free energy (G) was calculated at elevated temperatures and zero pressure to provide a measure of their relative stability. The Gibbs free energy for each zeolite was compared to α-quartz such that the relative free energy is expressed as $\Delta G = G_{Zeolite} - G_{Quartz.}$

In Figure 9.1 the Gibbs free energy relative to quartz is illustrated for these zeolites. The siliceous zeolites have a more positive free energy than α-quartz, indicating that zeolites are metastable with respect to quartz.

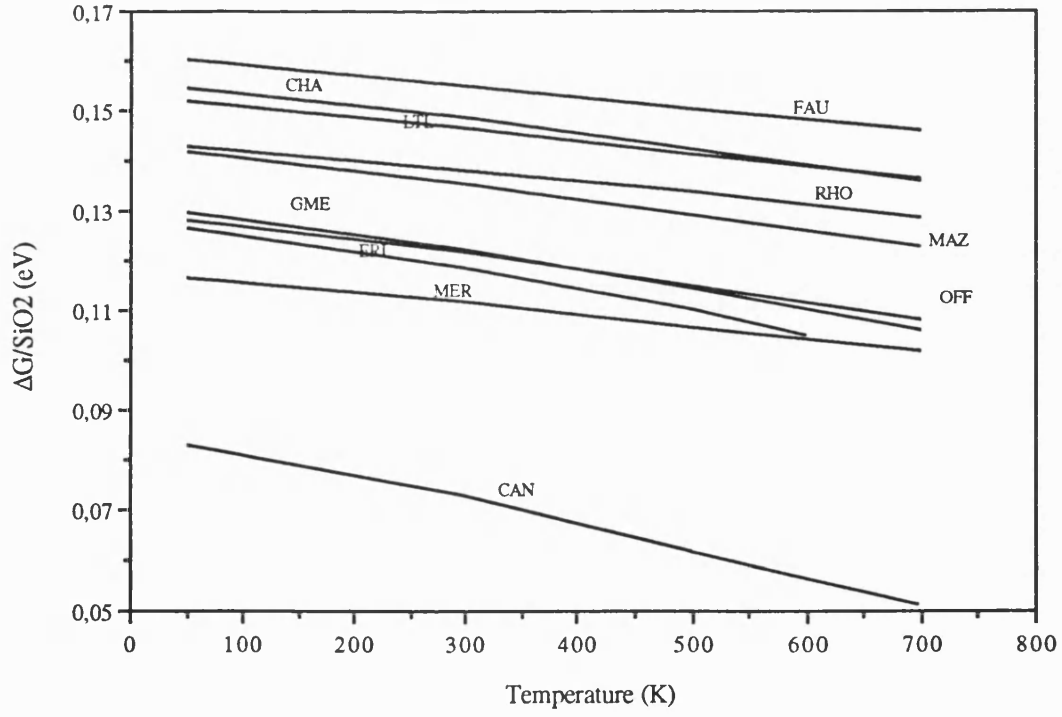

Figure 9.1: The Gibbs free energy relative to quartz for several zeolites as a function of temperature ($\Delta G = G_{Zeolite} - G_{Quartz}$).

All zeolites show an increasing negative free energy with increasing temperature. The plot free energy vs temperature gives a straight line for all zeolites as shown in Figure 9.1. The calculated values differ from each other, dependent on their stability, but they all show the same trend with increasing temperature.

The zeolites, sodalite and zeolite A are not shown in this figure as they show signs of instability, as indicated by imaginary frequencies, at 200K and 300K respectively. The reasons for their instability at higher temperatures are not fully understood yet, but could suggest a phase transition. This suggestion is supported by NMR studies (Janssen et al, 1989) on Na-zeolite A, in which a phase transition has been observed above room temperature.

9.1.2. The relative free energy of non-siliceous zeolites at different temperatures

The Gibbs free energy of some non-siliceous zeolite structures was calculated in order to study the effect of alumination on the thermal stability of zeolites.

In Figure 9.2 the calculated Gibbs free energy of siliceous and non-siliceous faujasite and zeolite L is plotted as a function of temperature. For the non-siliceous zeolites faujasite and zeolite L a silicon to aluminium ratio respectively of 1.52 and 3.0 is given. As charge balancing cations sodium is present in faujasite and potassium in zeolite L. The Gibbs free energy of the siliceous zeolites is more negative than the free energy of the zeolites containing aluminium and cations in their framework. This is because the electrostatic energy of silicon is higher than aluminium and cations.

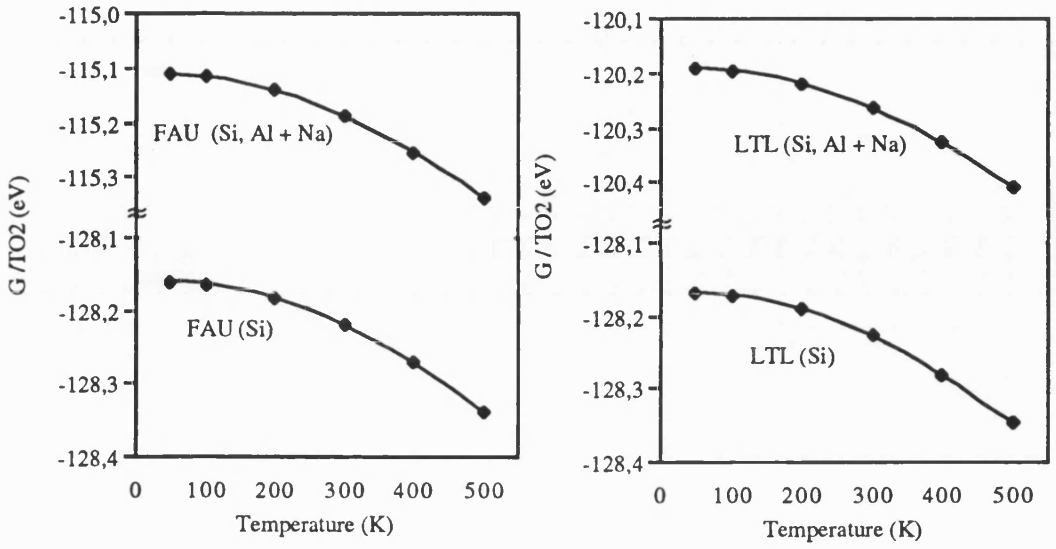

Figure 9.2: Gibbs free energy of siliceous and non-siliceous faujasite and zeolite L as a function of temperature (Si:Al ratio in faujasite = 1.52; Si:Al ratio in zeolite L = 3.0).

But independent if siliceous or non-siliceous zeolites are considered, they all show the same trend with increasing temperature; an increasingly negative free energy.

In Figure 9.3 a and b the effect of different silicon to aluminium ratios on the thermal stability of cancrinite and sodalite at 300K and 50K respectively is shown. As in the static lattice simulation studies the silicon was substituted in a random distribution by aluminium and as charge balancing cations sodium was chosen.

It is demonstrated that the siliceous forms being again the most stable forms relative to the free ions and that the thermal stability of cancrinite and sodalite decreases linearly with increasing aluminium and cation content.

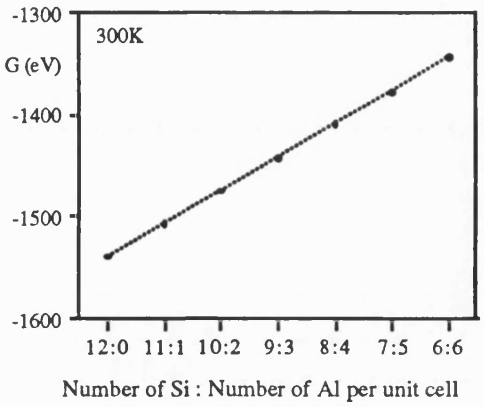

Figure 9.3 (a): The Gibbs free energy of cancrinite at different Si:Al ratios.

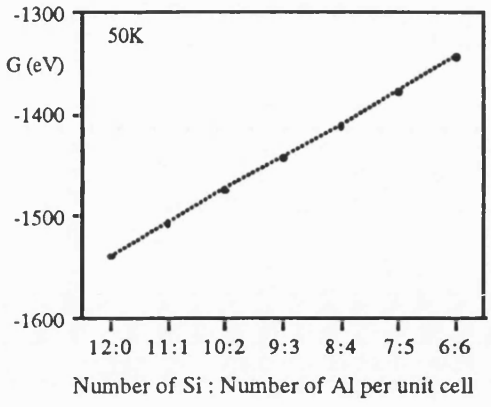

Figure 9.3 (b): The Gibbs free energy of sodalite at different Si:Al ratios.

9.1.3. The free energy of zeolites in terms of basic structural features

In the static lattice simulation studies of zeolites it was demonstrated that the stability can be expressed in terms of basic structural and topological features; e.g. ring size, density or CSQ. The Gibbs free energy of zeolites at different temperatures can also be correlated with some structural changes.

The from Stixrude and Bukowinski (1990) calculated characteristic ring size (K) was correlated with the Gibbs free energy at different temperatures of several zeolite structures and α-quartz. In Figure 9.4 the interdependence between the ring size (K) and the Gibbs free energy at 50K, 300K and 500K is illustrated. The ring size (K) increases with increasing negative free energy. Hence it can be concluded that with an increasing number of 5- and/or 6-rings and a decreasing number of 4-rings the Gibbs free energy becomes more negative in each temperature range.

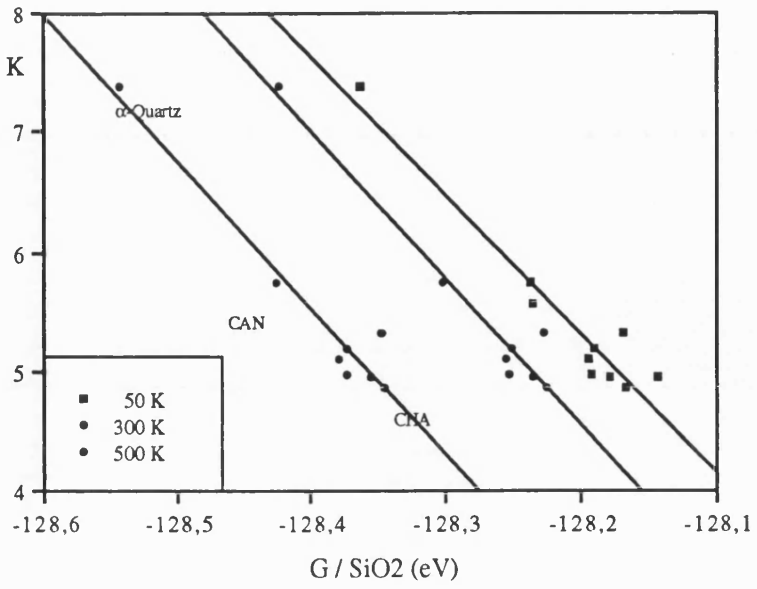

Figure 9.4: The Gibbs free energy of several zeolites and α-quartz at 50K, 300K and 500K as a function of the ring size K.

This result is also supported by the calculation of the CSQ of these zeolite structures. In chapter 7 it was shown that the topology of framework structures may be characterised by the CSQ, which may also be correlated with the stability of zeolites.

The Gibbs free energy at different temperatures for several zeolites and quartz shows a linear correlation of the CSQ of the 3^{rd}, 4^{th} and 5^{th} shell. This relationship is shown in Figure 9.5. The number of surrounding T-atoms increases independent of which shell is considered with increasing negative free energy which is again consistent with an increasing ring size.

This result agrees with the above observation that the variations of the Gibbs free energy is independent of which temperature is considered, and becomes more negative with reduction of the number of the smallest ring-size.

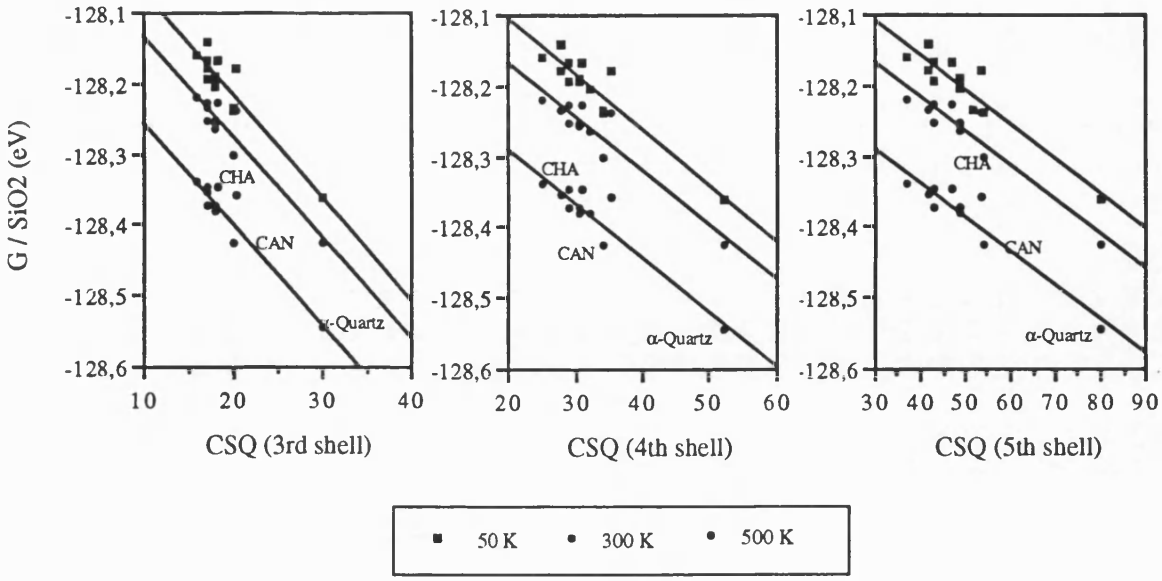

Figure 9.5: The Gibbs free energy at 50K, 300K and 500K as a function of the CSQ.

The ring size was also shown to be related with the framework density (see chapter 7). Consequently a relationship between the Gibbs free energy and the density must follow. In Figure 9.6 a correlation between the free energy at 50K, 300K and 500K and the framework density is illustrated. It can be seen that the free energy becomes increasingly negative as the density of the framework structure increases, and again is independent of which temperature range is considered.

The conclusion is that the stability of any hypothetical structure may be routinely predicted before synthesis by computing factors such as the CSQ and density, and using the graphs provided in this work to 'read off' the relative stability. Of course this does not mean that the hypothetical structure can necessary be synthesised, because this depends on many other factors, such as chemical kinetics of the formation and the availability of suitable templates.

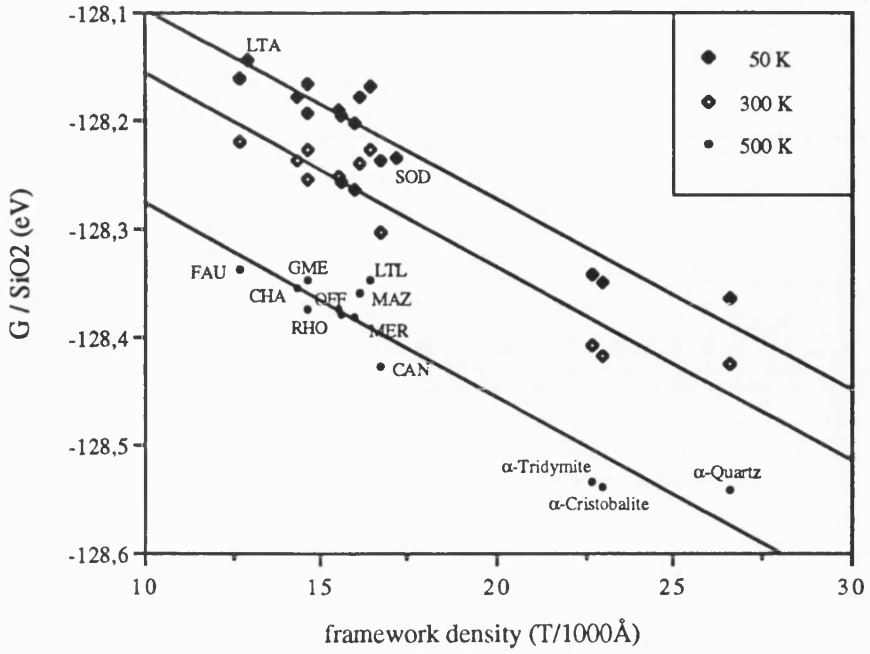

Figure 9.6: Correlation of the framework density (number of T atoms per 1000Å) with the Gibbs free energy at 50K, 300K and 500K.

9.2. The structure and thermal expansion behaviour of zeolites at different temperatures

The structural parameters and the thermal expansion coefficients have been calculated for several zeolites at elevated temperatures. The most surprising aspect and result of these calculations was that with increasing temperature the cell volume contracts significantly for all zeolites considered, except sodalite and cancrinite. This result is surprising as one intuitively believes that the crystal should expand on heating.

The thermal expansion coefficients of some siliceous zeolites at elevated temperatures are shown in Figure 9.7. These results show that most zeolites have a negative thermal expansion, which means a contraction of the cell dimensions on heating. In contrast, cancrinite and sodalite show a converse behaviour; their lattice parameters show expansion on heating.

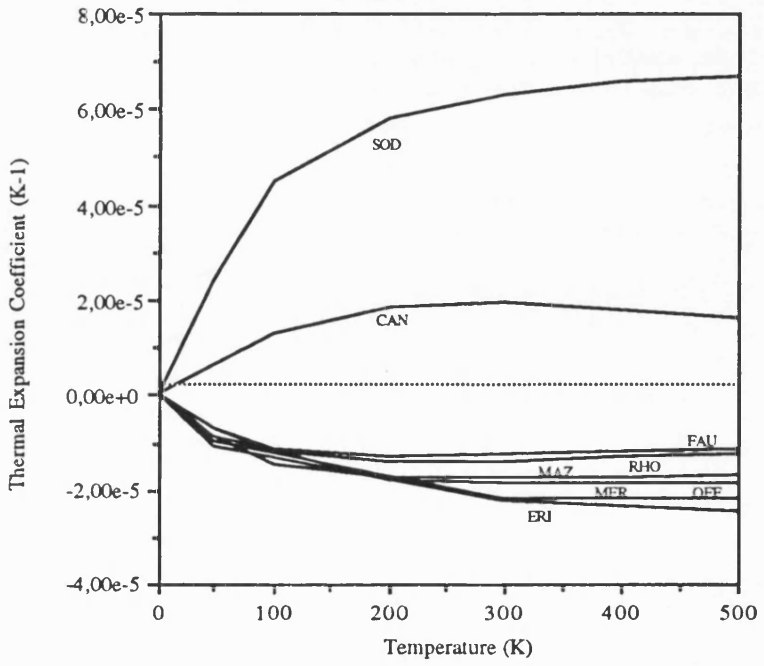

Figure 9.7: The predicted thermal expansion coefficient for several siliceous zeolites.

The calculation of the Si-O and O-O bond distances of these zeolites show that there is at the same time a contraction of both the Si-O and O-O bond lengths with increasing temperature for all zeolites, except for sodalite and cancrinite. The Si-O and O-O bond distances of sodalite and cancrinite are increasing with increasing temperature. In Figure 9.8 the mean Si-O and O-O bond distances for some zeolite structures are illustrated as a function of temperature. All zeolites having a negative thermal expansion coefficient show a slight increase of the interatomic distances between 0K and 100K but then they

are decreasing rapidly. Only cancrinite shows a continuous increase of the bond distances with increasing temperature.

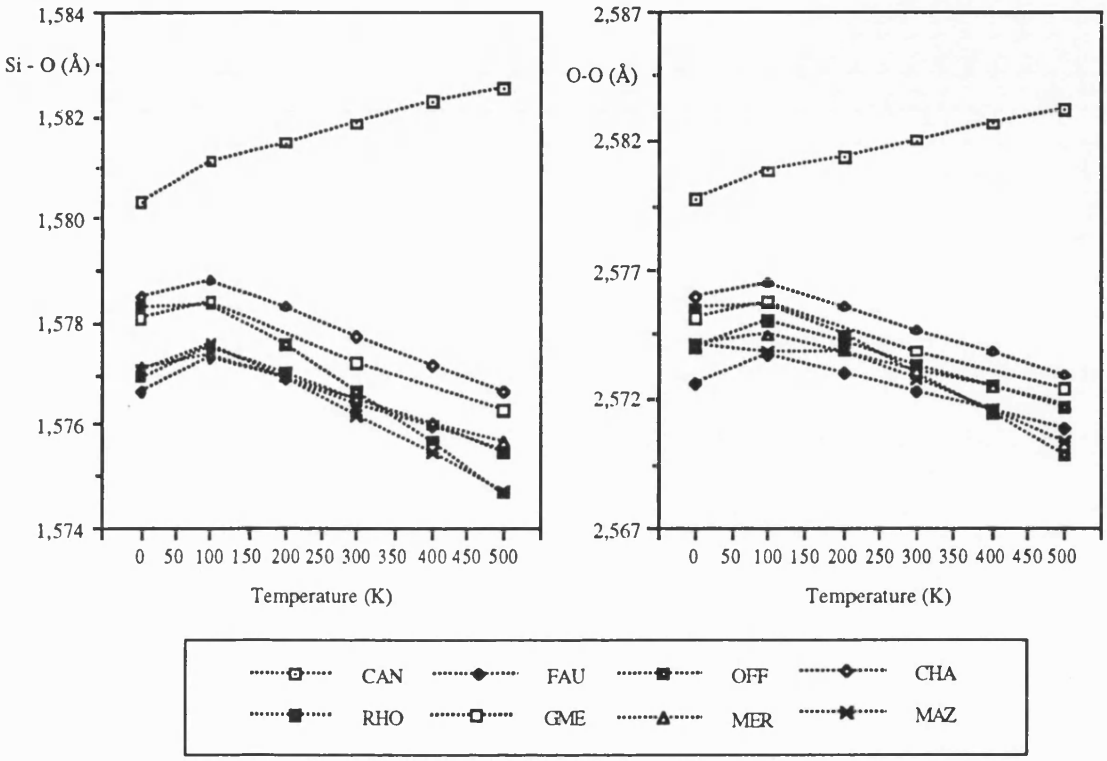

Figure 9.8: Calculated Si-O and O-O bond distances at elevated temperatures for several siliceous zeolite structures.

Additionally the thermal expansion behaviour of some non-siliceous zeolites was calculated. In Figure 9.9 the thermal expansion coefficients of non-siliceous zeolites and as a comparison their siliceous analogues are illustrated. As with the siliceous zeolites, all the non-siliceous analogues show a negative thermal expansion on heating with the exception of non-siliceous sodalite and cancrinite.

Comparing the thermal expansion behaviour of siliceous and non-siliceous zeolites, the

contraction or expansion of non-siliceous zeolites is much smaller compared to the siliceous zeolites.

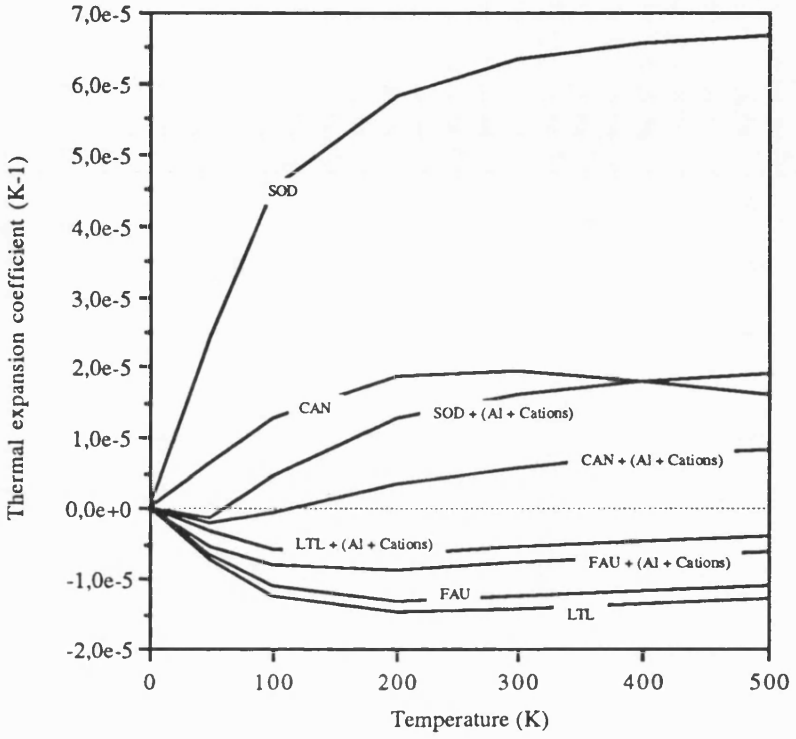

Figure 9.9: The predicted thermal expansion coefficient for several siliceous and non-siliceous zeolites.

Also the mean bond distances of non-siliceous zeolites are decreasing with increasing temperature for those zeolites where a negative thermal expansion was observed. The mean bond distances for non-siliceous sodalite and cancrinite are increasing with increasing temperature.

To show the effect of the aluminium and cation content on the thermal contraction and the anisotropic nature of this effect the unit cell parameters for siliceous and non-siliceous zeolite L at different temperatures are listed in Table 9.1 as example. The contraction of zeolite L is anisotropic with the a-axes approximately 70% (for siliceous

zeolite L) and 40% (for non- siliceous zeolite L; Si:Al = 3:1) more compressible than the c-axes for siliceous and non- siliceous zeolite L respectively. Similar results have been obtained for other zeolites which show a contraction on heating.

Temperature (K)	Zeolite L		K - Zeolite L	
	a	*c*	*a*	*c*
50	18.051	7.547	18.199	7.607
100	18.048	7.545	18.200	7.607
200	18.041	7.540	18.194	7.605
300	18.034	7.534	18.190	7.604
400	18.026	7.529	18.187	7.602
500	18.020	7.524	18.184	7.601

Table 9.1: Unit cell parameters (Å) for siliceous and non-siliceous zeolite L at several temperatures (the Si:Al ratio of non-siliceous zeolite L is 3:1).

The anisotropy is also reflected by those zeolites which show a positive thermal expansion and is affected by the aluminium and cation content. For example the a-axes of siliceous cancrinite is about 68% and of non-siliceous cancrinite (Si:Al = 1:1) about 40% more extensible than the c-axes. The cell parameters for siliceous and non-siliceous cancrinite are listed in Table 9.2.

Temperature (K)	Cancrinite		Na - Cancrinite	
	a	*c*	*a*	*c*
50	12.3707	5.1713	12.7591	5.2898
100	12.3720	5.1722	12.7587	5.2897
200	12.3778	5.1764	12.7595	5.2900
300	12.3838	5.1806	12.7616	5.2908
400	12.3902	5.1849	12.7648	5.2920
500	12.3948	5.1878	12.7686	5.2934

Table 9.2: Unit cell parameters (Å) for siliceous and non-siliceous cancrinite at several temperatures (the Si:Al ratio of non-siliceous cancrinite is 1:1).

Above it was shown that non-siliceous zeolites show a smaller contraction or expansion on heating than siliceous zeolites. Hence a decreasing thermal expansion coefficient with increasing aluminium and cation content was expected. The influence of aluminium and cations on the thermal expansion behaviour was studied in sodalite and cancrinite, where the Si:Al ratio was increased in a stepwise fashion.

In Figure 9.10 the calculated thermal expansion coefficient of cancrinite with different Si:Al ratios is pictured. Again it is shown that siliceous cancrinite has a much larger thermal expansion coefficient than non-siliceous cancrinite.

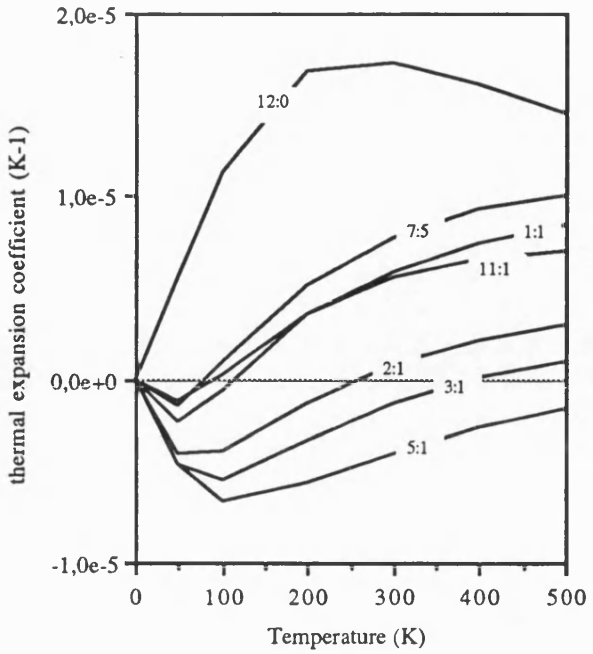

Figure 9.10: Calculated thermal expansion coefficient of cancrinite with different Si:Al ratios.

But considering the expansion behaviour of cancrinite with different Si:Al ratios a rather confusing result was obtained. The thermal expansion behaviour cannot be related with the Si:Al ratios. The only feature the different Si:Al ratios have in common is a contraction of the cell dimensions at lower temperatures.

In attempt to resolve this confusing outcome the influence of the aluminium and cation positions within the framework on the thermal behaviour was studied. In Figure 9.11 (a,b) two examples are shown. In these two examples the thermal expansion coefficient at a Si:Al ratio of 5:1 and 11:1 with different silicon, aluminium and cation positions was calculated. As illustrated in the graphs the positioning of the aluminium atoms and non-framework cations are influencing the expansion behaviour remarkably.

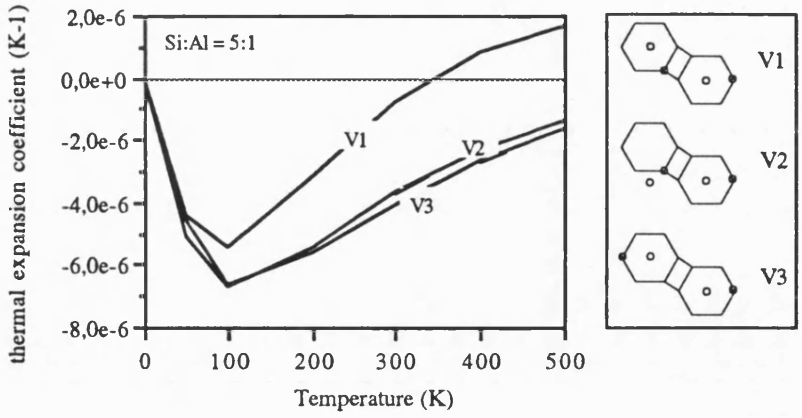

Figure 9.11 (a): Calculated thermal expansion coefficient of cancrinite with a Si:Al ratio of 5:1 and different Al, Si and Na positions (the Na and Al positions are presented simplified on the right hand side).

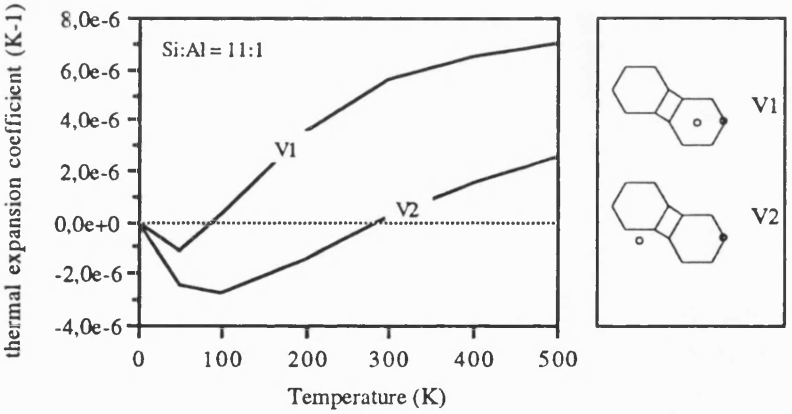

Figure 9.11 (b): Calculated thermal expansion coefficient of cancrinite with a Si:Al ratio of 11:1 and different Al, Si and Na positions (the Na and Al positions are presented simplified on the right hand side).

The thermal expansion behaviour was also calculated for sodalite with different Si:Al ratios. In section 9.1. it was mentioned that the simulated structure of siliceous sodalite collapsed from 200K onwards. However non-siliceous sodalite does not show this

instability with increasing temperature independent of which Si:Al ratio is considered. This suggests that the presence of substituted aluminium or interframework cations confers thermal stability to the sodalite structure. (Although the thermal expansion coefficient for siliceous sodalite cannot be calculated explicitly at higher temperatures it can be approximately calculated from the thermal expansion coefficient between 50K and 200K.)

In Figure 9.12 the calculated thermal expansion coefficient of sodalite with different Si:Al ratios is illustrated. Again the siliceous form expands more than the non-siliceous sodalite. In addition there is also no recognisable correlation between the Si:Al ratio and the thermal expansion behaviour. Although for certain Si:Al ratios the thermal expansion of sodalite is, as in cancrinite, dependent on the positioning of silicon, aluminium and the cations.

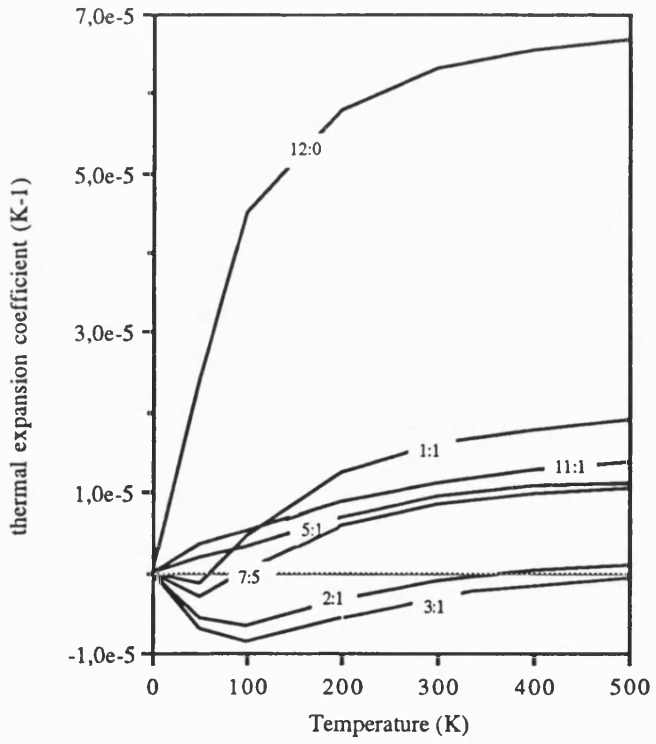

Figure 9.12: Calculated thermal expansion coefficient of sodalite with different Si:Al ratios.

Hence the thermal expansion coefficient of non-siliceous zeolites is not decreasing with increasing aluminium and cation content furthermore it is dependent on where the silicon, aluminium and cations are positioned.

Unfortunately there has been little detailed work on the thermal expansion behaviour of framework silicates, apart from the silica minerals and feldspars. However, a negative thermal expansion for silicas is not so surprising. For example α-quartz shows a negative thermal expansion below 50K and above the transition temperature of quartz, where the β-quartz configuration is obtained, a slight but measurable contraction in the cell volume was observed and calculated. This apparently anomalous behaviour of β-quartz is interpreted as being due to an increase in the amplitude of the anisotropic motion of the oxygen atoms on increasing the temperature, resulting in a further shortening of the Si-O bond distances (Taylor, 1972)

However, the results of the negative thermal expansion behaviour of zeolites have now been verified by high resolution powder diffraction studies of dehydrated Na-zeolite X by Couves et al (1992). The experimental results indicate that the qualitative predictions of the simulations are correct, although the calculations underestimate the magnitude of the negative coefficient of expansion. The calculated and experimental results are shown in Figure 9.13 and Table 9.3. The experimental results indicate that Na-Zeolite X is expanding at temperatures above 200K, whereas the calculations predict continuous contraction. The discrepancies may be due to uncertainties concerning the samples (e.g. the presence of significant quantities of water and other sorbents or the amount and positioning of aluminium and cations) or to approximations in the models.

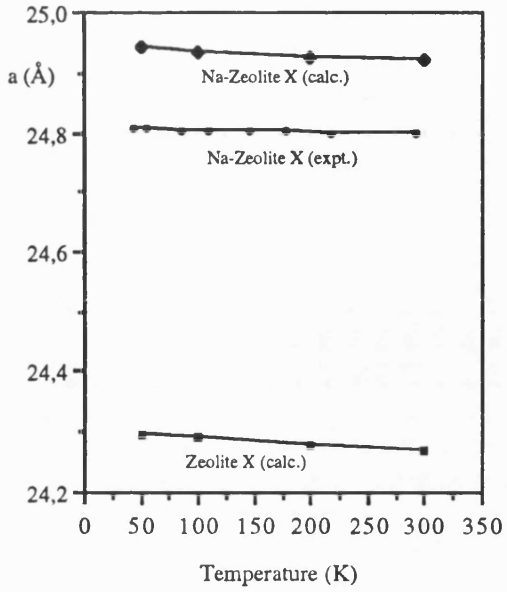

Figure 9.13: Calculated and experimental (Couves et al, 1992) lattice parameters for Na-zeolite X and siliceous zeolite X as a function of temperature.

Calculated Lattice Parameters			Experimental Lattice Parameters	
Temperature (K)	Lattice Parameter (Å)		Temperature (K)	Lattice Parameter (Å)
	Zeolite X [1]	Na-Zeolite X [2]		Na-Zeolite X [3]
50	24.2946	24.9409	24.9(5)	24.8047(5)
100	24.2908	24.9337	43.3(5)	24.8059(5)
200	24.2804	24.9261	54.6(5)	24.8062(7)
300	24.2695	24.9189	84.7(5)	24.8042(6)
400	24.2593	24.9125	109.9(5)	24.8021(1)
500	24.2494	24.9067	145.5(5)	24.8005(7)
			179.2(5)	24.8006(1)
			217.2(5)	24.7988(8)
			293.0(5)	24.7998(8)

Table 9.3 : Calculated and experimental (Couves et al, 1992) lattice parameters of zeolite X ((1) purely siliceous faujasite; (2) Na-zeolite X, Si:Al = 1.525; (3) Na-Zeolite X, Si:Al = 1.54).

Moreover, the positive thermal expansion behaviour of sodalite is also verified. Thermal expansion data for synthetic aluminosilicate sodalites were determined by powder X-ray diffraction from Henderson and Taylor (1978). These data are illustrated in Figure 9.14. For comparison the calculated cell parameters of non-siliceous sodalite with different Si:Al ratios and at elevated temperatures are also shown in this figure. The illustrated sodalite structures show a range of cell edges. These variations of the cell parameters may be related to the expansion characteristics of the bond between the cavity cations, the positioning of the cations and the amount of cations are present in the different sodalite structures. However, the calculated thermal expansion curves show the same trend with increasing temperature.

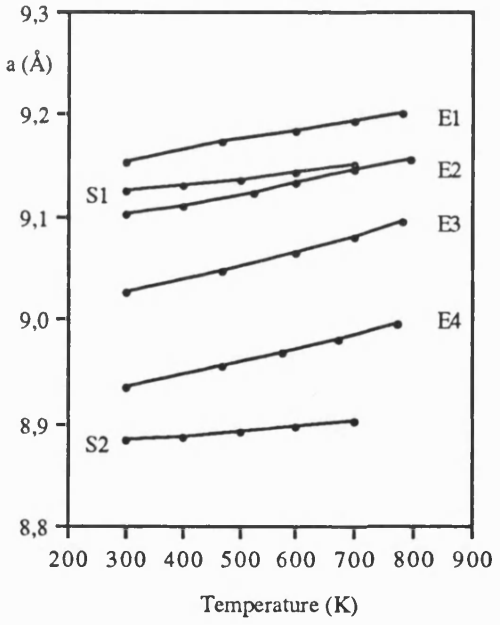

Figure 9.14: Calculated (S1, S2) and experimental (E1-E4; Henderson and Taylor, 1978) thermal expansion curves for sodalite (S1- $Na_6Si_6Al_6O_{24}$; S2 - $Na_1Si_{11}Al_1O_{24}$; E1 - $Na_{3.2}K_{4.8}(Si_6Al_6O_{24})Br_2$; E2 - $Na_{3.3}K_{5.8}(Si_6Al_6O_{24})Cl_2$; E3 - $Na_{5.6}K_{2.4}(Si_6Al_6O_{24})Br_2$; E4 - Na_8 (Si6Al6O24) Br_2.

Couves et al (1992) measured also the thermal expansion behaviour of dehydrated gallosodalite using a high resolution powder diffractometer. A comparison of the cell parameters between the calculated siliceous sodalite and the experimental gallosodalite show an excellent agreement. The results are reported in Table 9.4.

Calculated Lattice Parameters	
Temperature (K)	Lattice Parameter (Å) Sodalite [1]
50	8.8046
100	8.8267

Experimental Lattice Parameters	
Temperature (K)	Lattice Parameter (Å) Gallosodalite
15.4	8.8190(3)
35.2	8.8190(2)
62.5	8.8212(5)
92.5	8.8230(4)
125.9	8.8270(3)

Table 9.4 : Calculated and experimental (Couves et al, 1992) lattice parameters of sodalite ((1) purely siliceous sodalite).

The reason for these results are not yet fully understood, but a possible explanation may be found by considering the zeolite structures itself. Both sodalite and cancrinite are more stable and dense structures then the other zeolites. They also have only a one-dimensional channel system, which seem to allow no reduction of their cell dimension on heating. All other zeolites studied have a more porous framework and a two- or three dimensional channel system which seems to allow a structural 'expansion' towards the pores and channels on heating, leading to these zeolites showing a negative thermal expansion.

Further information about this unusual thermal behaviour of zeolites may be obtained by

considering also the macroscopic properties. As a crystalline substance is heated there is an increase in the amplitude of the bending and stretching modes of the different combinations of the atoms, which translates macroscopically into thermal expansion or contraction. Therefore the unusual thermal behaviour of zeolites should be analysed by examining the magnitude and location of the atomic vibrations which appear to cause expansion into the pores and channels on heating. However, this and further analysis of the calculations are in progress.

9.3. The heat capacity, Cp, of zeolites at different temperatures

An important thermochemical parameter often measured and used in studies of mineral behaviour in geochemical systems is the heat capacity.This thermodynamic property the heat capacity, C_p, has been calculated for several zeolite structures.

In Figure 9.15 the heat capacity for several siliceous zeolites relative to quartz ($\Delta C_p = Cp$ *Zeolite - Cp Quartz*) at different temperatures is illustrated. Generally all siliceous zeolites show similar behaviour at different temperatures, which is an increasing heat capacity with increasing temperature, and there is no major difference in their results.

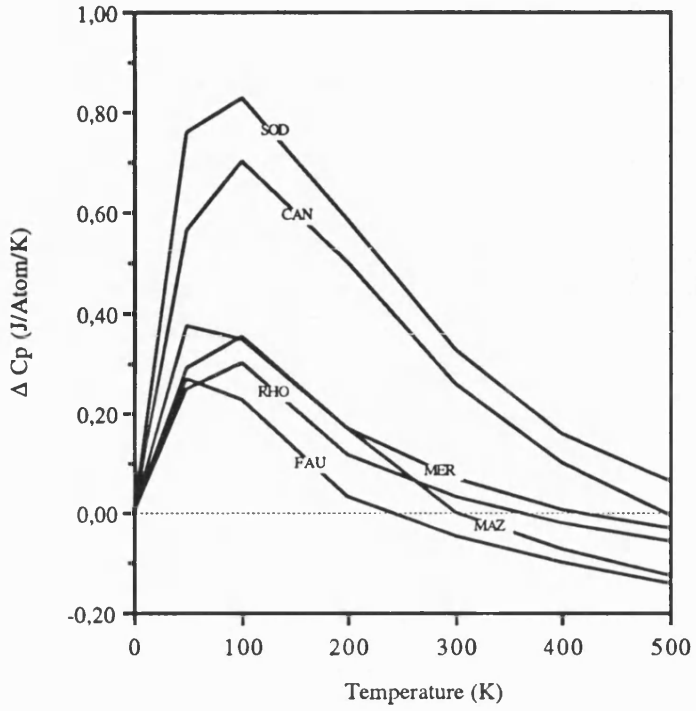

Figure 9.15 : The heat capacity, C_p, relative to quartz, of siliceous zeolites as a function of temperature ($\Delta C_p = C_{p\,\text{Zeolite}} - C_{p\,\text{Quartz}}$).

However, sodalite and cancrinite show a much higher heat capacity. This may arise from their greater stability compared to other zeolites . Also all other zeolites show a decreasing heat capacity with decreasing stability. Hence the stability of several siliceous zeolites was correlated with their heat capacity. In Figure 9.16 the relationship between the heat capacity at 300K and the lattice energy of these zeolites is shown. From this graph it can be seen that all siliceous zeolites considered show a decreasing heat capacity with decreasing stability.

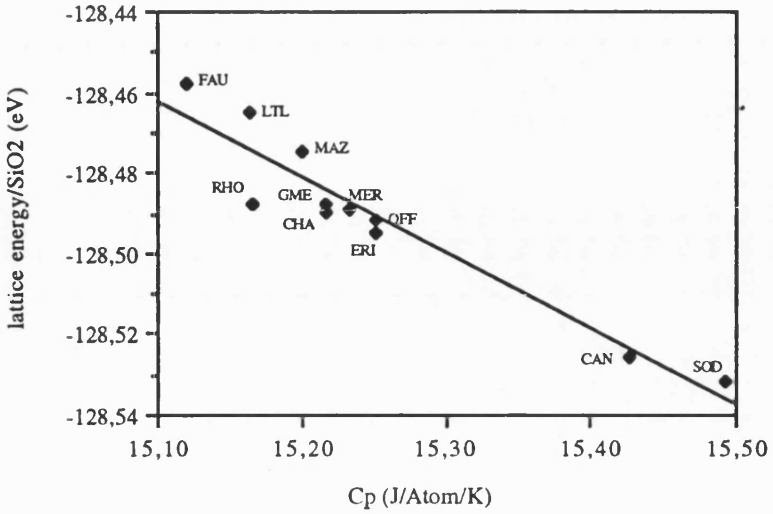

Figure 9.16: The lattice energy/SiO_2 of several siliceous zeolites as a function of the heat capacity, *Cp*, at 300K.

The calculation of the heat capacity of non-siliceous zeolites contrasts with this behaviour. With increasing temperature non-siliceous zeolites show the same trend as their siliceous analogous, except that their overall heat capacity is much higher, although non-siliceous zeolites are less stable.

Hence relative small changes in the composition of a zeolite can lead to significant variation in its heat capacity. In Figure 9.17 the heat capacity of non-siliceous and their siliceous analogues is shown.

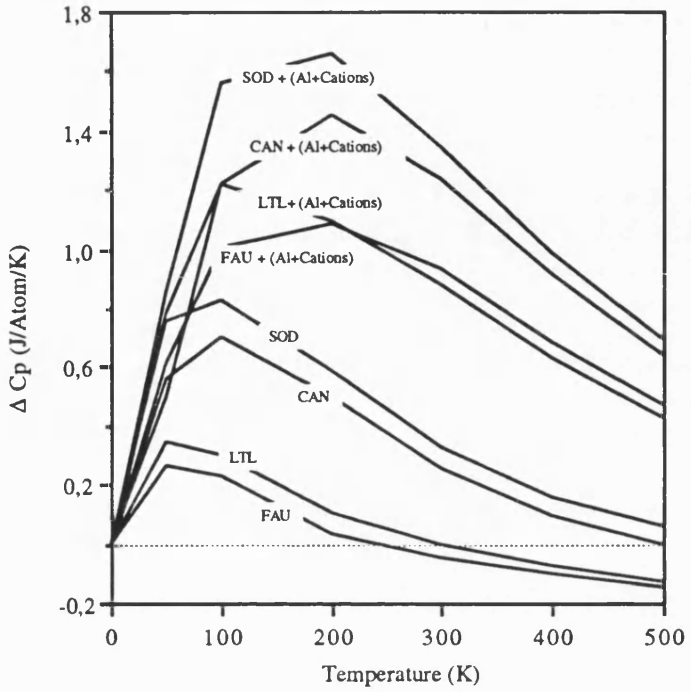

Figure 9.17 : The heat capacity, C_p, relative to quartz, of siliceous and non-siliceous zeolites as a function of temperature ($\Delta C_p = C_{pZeolite} - C_{pQuartz}$); the Si:Al ratio for cancrinite and sodalite is 1.0, for faujasite 1.52 and for zeolite L 3.0.

Because of the above made observations the heat capacity of zeolites can be expected to vary as a function of composition. Figure 9.18 shows the effect of variation in the Si:Al ratio on the heat capacity of cancrinite. Compositional differences have less effect at lower temperatures for all Si:Al ratios. However, at higher temperatures the heat capacity of cancrinite is increasing with increasing aluminium and cation content. The same observations were made for sodalite with different Si:Al ratios.

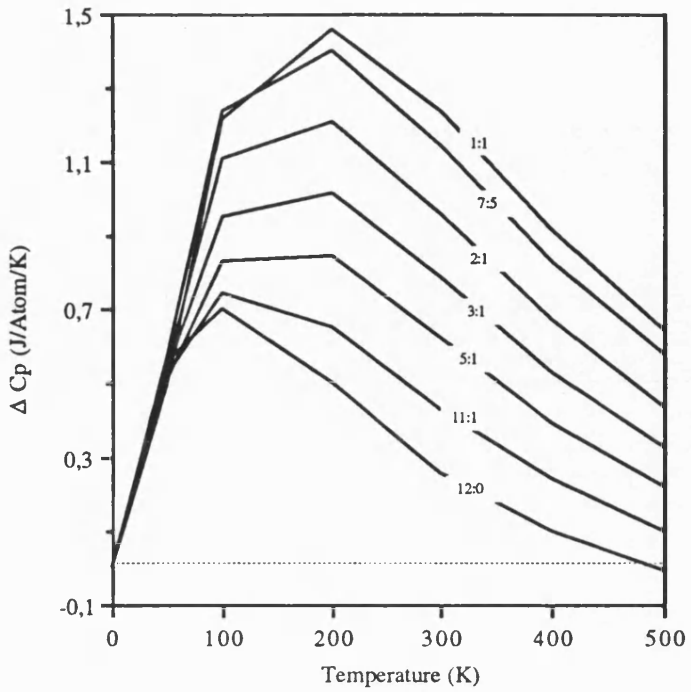

Figure 9.18: The heat capacity, C_p, of cancrinite with different Si:Al ratios as a function of temperature ($\Delta C_p = C_{pZeolite} - C_{pQuartz}$).

In chapter 7 it was demonstrated that the stability of non-siliceous zeolites decreases with increasing aluminium and cation content. Hence it can be concluded that the heat capacity of non-siliceous zeolites is increasing with decreasing stability.

In the previous sections it was demonstrated that the positioning of silicon, aluminium and the cations play an important role. In the calculations of the heat capacity this positioning has no significant effect.

To date there are little experimental heat capacity data of zeolites to compare with the calculated values. Donahoe et al (1990) measured the heat capacity of merlinoite. The

experimental and calculated results relative to quartz are shown in Figure 9.19. A comparison between both, the calculated and experimental data show that the overall trend with increasing temperature is the same; an increasing heat capacity with increasing temperature. However, the calculated heat capacity of merlinoite is smaller due as purely siliceous form was considered.

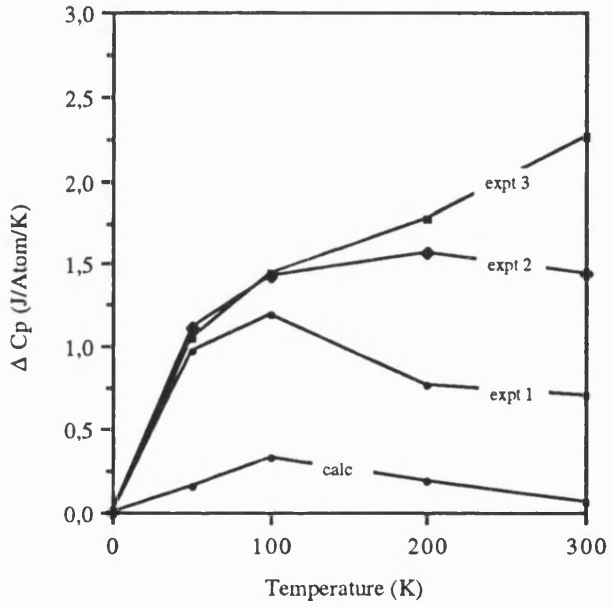

Figure 9.19: Calculated and experimental (Donahoe et al, 1990) heat capacity, C_p, of merlinoite as a function of temperature ($C_p = C_{pZeolite} - C_{pQuartz}$; expt 1 = $K_{0.91}Na_{0.09}AlSi_{1.81}O_{5.62}.1.79H_2O$; expt 2 = $KALSi_{1.94}O_{5.88}.1.69H_2O$; expt 3 = $K_{0.80}Na_{0.20}AlSi_{1.94}O_{5.88}.1.81H_2O$).

9.4. Summary

The free energy calculations of zeolites have shown that the change of the Gibbs free energy with increasing temperature is constant for all zeolites. Hence all zeolites show an increasing negative free energy with increasing temperature.

Siliceous zeolites have compared to non-siliceous zeolites a more negative free energy. The thermal stability of non-siliceous zeolites decreases linearly with increasing aluminium and cation content.

The work on sodalite might also offer the possibility in the future of using these techniques to predict possible ways of increasing the thermal stability of zeolites. The simulations have shown that the stability of purely siliceous sodalite, which shows a phase instability at 200K, is removed by aluminium exchange. This approach could be exerted to zeolites at high temperatures to improve their stabilities.

The relative free energy of zeolites is also governed by their structural characteristics and topological features. The simulations have shown that there is a relationship between the Gibbs free energy and the framework density, the framework structure and the CSQ independent of which temperature range is considered.

The most interesting result in this chapter was the outcome of the thermal expansion behaviour of zeolites. Most of the considered siliceous and non-siliceous zeolites show a negative thermal expansion, which means a contraction of their cell dimensions on heating. Only cancrinite and sodalite (both, siliceous and non-siliceous) contrast this behaviour.

The contraction or expansion of non-siliceous zeolites is compared to their siliceous analogous smaller. Furthermore, the calculations of the thermal expansion behaviour of non-siliceous zeolites have shown, that the contraction or expansion cannot be correlated with the Si:Al ratio but is strongly influenced by the positioning of silicon, aluminium and the cations within the framework.

The calculation of the heat capacity, C_p, of zeolites at elevated temperatures demonstrated that all zeolites show an increasing heat capacity with increasing temperature. Additionally the heat capacity of zeolites can be related to the stability of zeolites. Siliceous zeolites show a decreasing heat capacity with decreasing stability. In contrast, non-siliceous zeolites, which have a overall higher heat capacity than their siliceous analogous, show a decreasing heat capacity with increasing stability.

X. DYNAMIC LATTICE SIMULATION OF ALUMINOPHOSPHATES

In chapter 8 the relative stability of aluminophosphates and their structural characteristics were calculated at 0 Kelvin. Especially for the novel class of aluminophosphates, which are characterised through their unique large pores and channels, the free energy calculations are of great interest and importance, and possibly offer an insight in extending their size and complexity.

The aim of this chapter is, as in the dynamic lattice simulation studies of zeolites, to use free energy minimisation to calculate the energetic, thermodynamic and structural properties of aluminophosphates and to gain insight into the factors which govern these properties at elevated temperatures.

10.1. Free energy minimisation of aluminophosphates

10.1.1. The relative free energy of aluminophosphate at elevated temperatures

For several aluminophosphate structures the Gibbs free energy was calculated at elevated temperatures and zero pressure to provide a measure of their relative stability with increasing temperature.

The calculated Gibbs free energy per TO_2 (T = Al or P) of these aluminophosphate structures and of α-berlinite is illustrated in Figure 10.1.

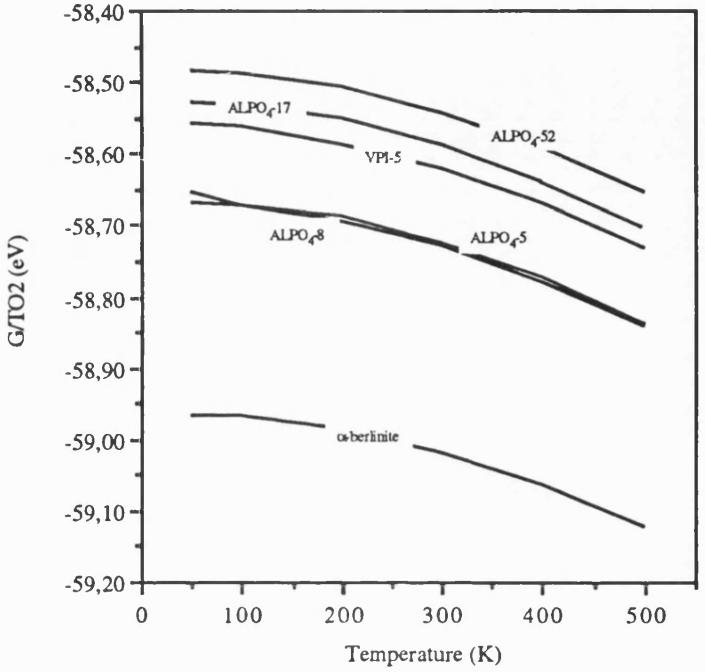

Figure 10.1: The Gibbs free energy/TO_2 of several $AlPO_4$-structures as a function of temperature.

As expected all the aluminophosphates considered show an increasing negative free energy with increasing temperature. The calculated values differ from each other, but the change of the Gibbs free energy with temperature is constant for all aluminophosphates and α-berlinite. Compared to α-berlinite all aluminophosphate structures have a much lower free energy (= less negative), which indicates that also aluminophosphates are metastable with respect to berlinite.

10.1.2. The free energy of aluminophosphates in terms of basic structural features

The stability of aluminophosphate structures can be expressed in terms of basic structural and topological features, e.g. CSQ, ring size or density, which was demonstrated in chapter 8.

The Gibbs free energy at different temperatures of aluminophosphate structures can also be correlated with these structural features.

In the static lattice simulation studies a correlation between framework density and stability was observed. This relationship is also consistent with increasing temperature. In Figure 10.2 the correlation between the Gibbs free energy at elevated temperatures of several aluminophosphate structures with their framework density is correlated. At all temperatures the Gibbs free energy decreases with increasing framework density.

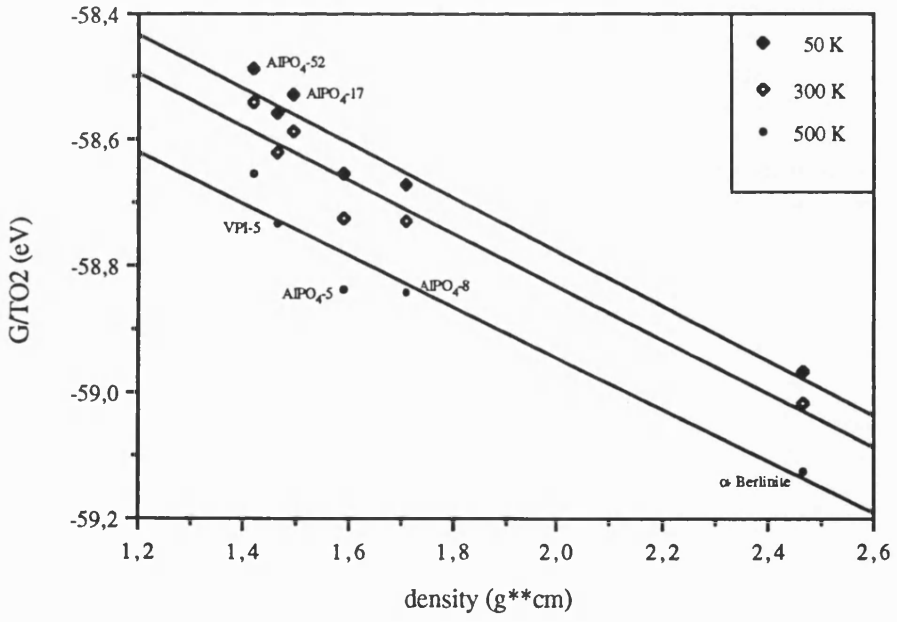

Figure 10.2: Correlation of the framework density with the Gibbs free energy at 50K, 300K and 500K.

A topological characteristic of framework structures, the CSQ, provides also an effective indication of the relative stability of aluminophosphate at 0 Kelvin (see chapter 8). The lower terms of the CSQ {Nk} show a good correlation with stability. Hence the CSQ of some aluminophosphate structures was correlated with Gibbs free energy at elevated temperatures in order to provide an additional tool to predict the relative free energy of aluminophosphate structures at different temperatures in terms of the CSQ.

In Figure 10.3 the variation of the Gibbs free energy at elevated temperatures and the CSQ of the 3rd, 4th and 5th shell is illustrated. Again all {Nk} show a good correlation with the Gibbs free energy of these aluminophosphate structures. However, the best correlation was found to be in the 3rd and 4th shell. With increasing negative free energy the coordination number increases, which corresponds to an increasing number of surrounding T-atoms and consequently to an increase of the ring size.

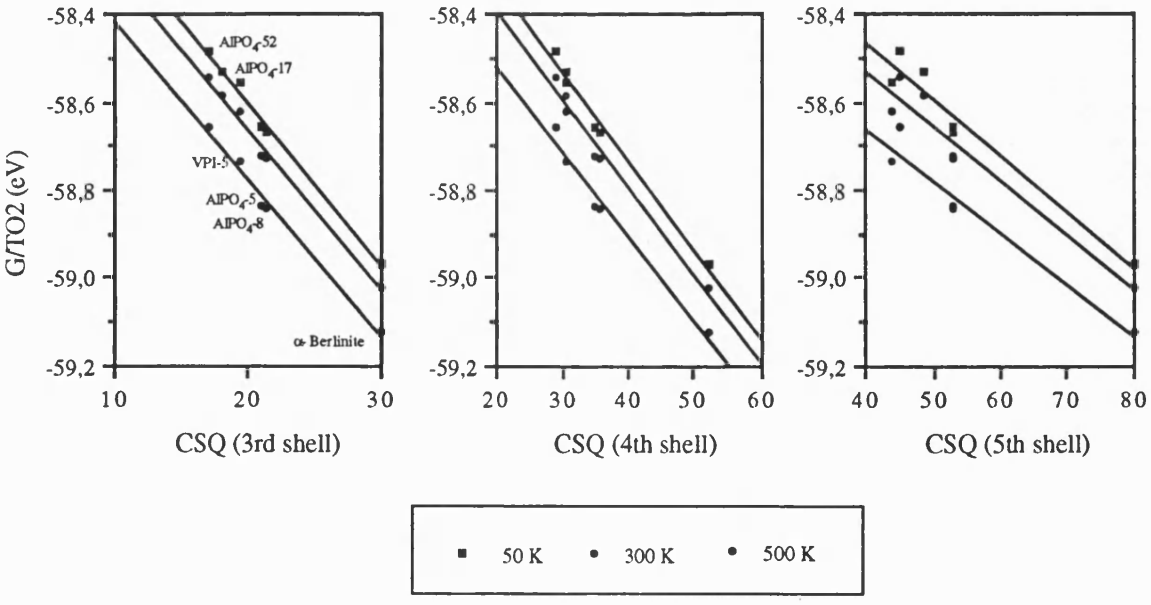

Figure 10.3: The Gibbs free energy at 50K, 300K and 500K of several $AlPO_4$-structures as a function of the CSQ.

The results show that the CSQ or density can also provide an effective indication of the free energy of aluminophosphate structures at elevated temperatures, and provide a predictive tool.

10.2. The structure and the thermal expansion behaviour of aluminophosphates at different temperatures

One measure of the temperature dependence of structures is the calculation of the thermal expansion coefficient. In chapter 9 the calculations of the thermal expansion coefficient of zeolites have shown surprisingly, that most of the zeolite structures show a contraction of their cell dimensions on heating. This is a major characteristic of zeolite structures as it has been not observed yet for any other framework structure, except for silicas. Therefore it is of great interest to calculate the thermal expansion behaviour of aluminophosphate as they are structurally related to zeolites.

In Figure 10.4. the thermal expansion coefficient at elevated temperatures of some aluminophosphate structures and α-berlinite is illustrated. The results show that α-berlinite, $AlPO_4$-8 and $AlPO_4$-5 have a positive thermal expansion, whereas $AlPO_4$-17 and $AlPO_4$-52 show a negative thermal expansion, which means a contraction of their cell dimensions on heating. Interestingly VPI-5, with its very large ring structures shows a contraction of the cell dimensions at lower temperatures and from 200K onwards an expansion.

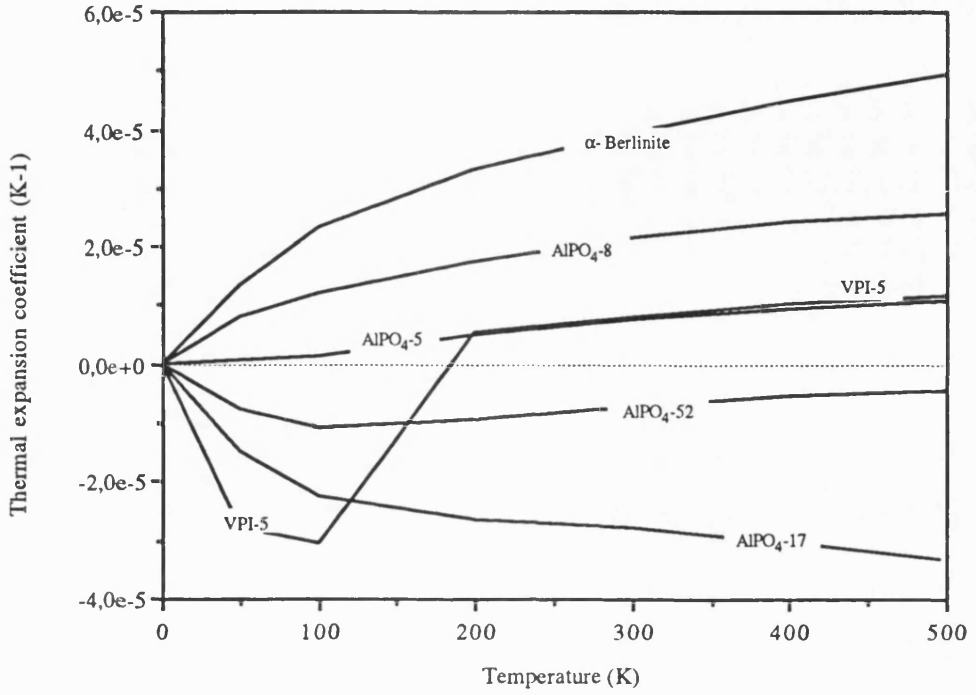

Figure 10.4: The predicted thermal expansion coefficient for several $AlPO_4$-structures.

In chapter 9 it was also demonstrated that the nature of the expansion or contraction of zeolites is anisotropic. In Table 10.1 the unit cell parameters of some aluminophosphate structures are listed to show that the structural changes of aluminophosphates are also anisotropic.

Temperature (K)	VPI - 5		$AlPO_4$ - 52		$AlPO_4$ - 8		
	a	*c*	*a*	*c*	*a*	*b*	*c*
50	19.0981	8.6618	14.0893	29.9871	34.1682	18.6027	8.4042
100	19.0858	8.6592	14.0521	29.9467	34.1708	18.0457	8.4065
200	18.9275	8.1912	14.0601	29.8548	34.1782	18.6099	8.4131
300	18.9313	8.4940	14.0670	29.7823	34.1878	18.6168	8.4217
400	18.9371	8.4984	14.0718	29.7331	34.1987	18.6248	8.4316
500	18.9438	8.5035	14.0758	29.6935	34.2105	18.6333	8.4424

Table 10.1: Unit cell parameters (Å) for VPI-5, $AlPO_4$-52 and $AlPO_4$-8 at several temperatures.

As in the zeolite studies the reasons for these results are not yet fully understood. An explanation of this behaviour may be also found by considering the alumino-phosphate structures itself.

Again, as in the zeolite studies, it is demonstrated that the most stable and dense structures ($AlPO_4$-8, $AlPO_4$-5 and VPI-5) are expanding with increasing temperature, whereas the less stable and dense structures ($AlPO_4$-17 and $AlPO_4$-52) show a contraction of their cell dimensions on heating. Additionally $AlPO_4$-8, $AlPO_4$-5 and VPI-5 have only a one-dimensional channel system, which may not allow a reduction of their cell dimensions. The other structures considered, have a three-dimensional channel system, which makes the framework more porous and therefore allows a structural 'expansion' towards the pores and channels. In Figure 10.5 the structure of an ABC-6 type (e.g. $AlPO_4$-17, $AlPO_4$-52), VPI-5 and $AlPO_4$-8 is shown along their a- or b-axes to illustrate the dense packed structures of VPI-5 and $AlPO_4$-8 compared

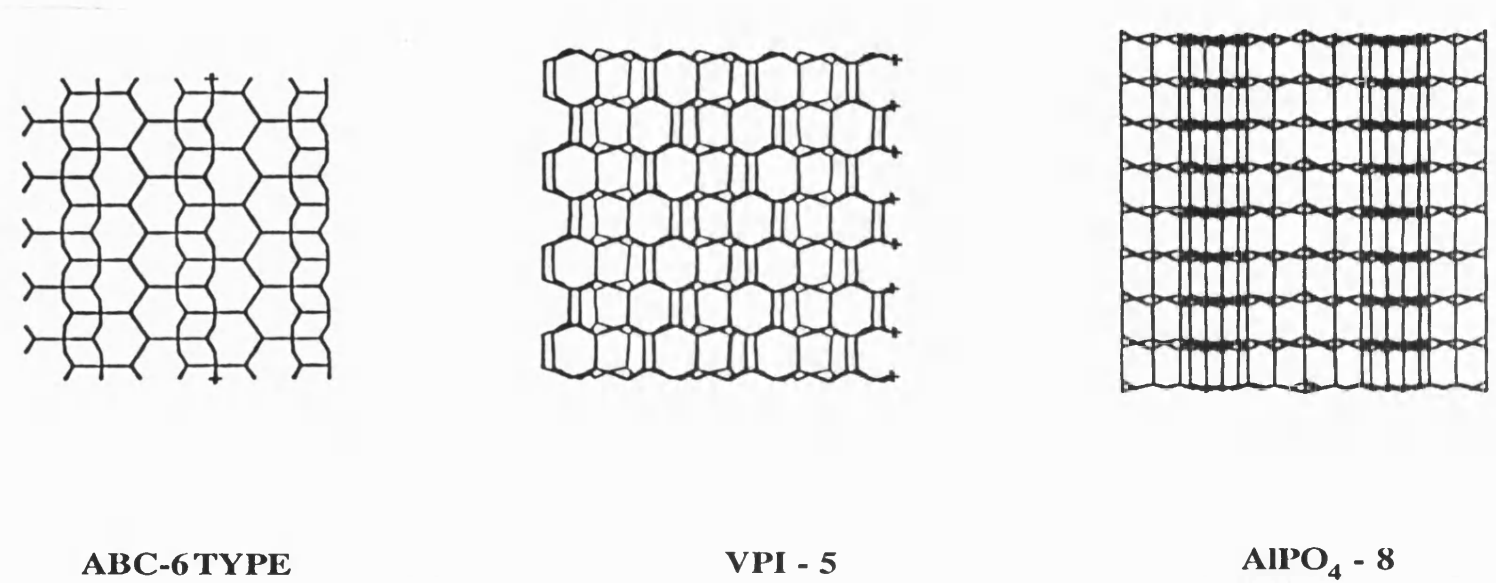

Figure 10.5: The structure of an ABC-6 type, VPI-5 and AlPO4-8 along their a- or b-axis.

to the more porous framework structures of $AlPO_4$-17 of $AlPO_4$-52. These observations are in conformity with the observations made for the expansion behaviour of zeolites.

An additional explanation of the different thermal expansion behaviour of aluminophosphates may be found by considering the crystal structures. In Figure 10.6 the structures of an ABC-6 type aluminophosphate, VPI-5 and $AlPO_4$-8 is shown along their c-axes or channel system. The ABC-6 type ($AlPO_4$-17 or $AlPO_4$-52) has one 4-ring and one 6-ring, VPI-5 has two 4-rings and one 6-ring and $AlPO_4$-8 has two 4-rings and two 6-rings alternately surrounding the channel. With increasing number of 4- and 6-rings surrounding the channel, the structure may become more 'stiff' and therefore does not allow any contraction towards the channels.

However, those aluminophosphate structures which are structural analogous of the zeolites (e.g. $AlPO_4$-17 is a structural analogous of erionite) show a contraction of the cell dimensions on heating. Aluminophosphate structures, which are characterised through their extra large channel systems show a positive thermal expansion behaviour.

The empirical correlation between the observation of negative thermal expansion and the existence of two- and three-dimensional channel systems, strongly suggests that the expansion behaviour is dependent on the nature of the channel system. Mechanistic studies, using computer graphic techniques are now planned to attempt

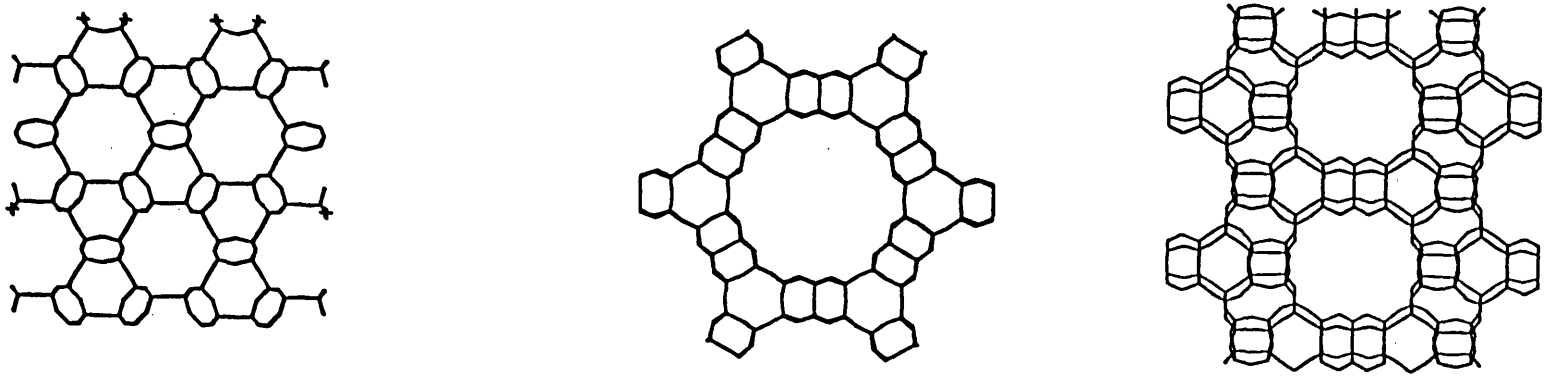

Figure 10.6: The structure of an ABC-6 type, VPI-5 and AlPO4-8 along their c-axis.

to elucidate the underlying reasons for the contraction on heating of aluminophosphates and zeolites with two- and three-dimensional channels. This work will focus on the difference in behaviour of the one-dimensional and the two- and three-dimensional systems; because as noted above, this difference could well hold the key to understand this fascinating behaviour.

10.3. The heat capacity, C_p, of aluminophosphates at different temperatures

As in the dynamic lattice simulation studies of zeolites the heat capacity, C_p, for several aluminophosphate structures was calculated at elevated temperatures, because it is an important thermochemical parameter in the studies of mineral behaviour in geochemical systems.

In Figure 10.7 the heat capacity of several aluminophosphates relative to α-berlinite ($\Delta C_p = C_{p\mathrm{AlPO4}} - C_{p\mathrm{Berlinite}}$) at different temperatures is shown. In general all aluminophosphates show an increasing heat capacity with increasing temperature. The heat capacity of all aluminophosphates considered, except of $AlPO_4$-17, show with increasing temperature the same trend and there are only small differences in their results. However, $AlPO_4$-17 shows compared to all other structures a much higher heat capacity at higher temperatures.

The heat capacity of the aluminophosphate structures is relative to berlinite much higher at lower temperatures but decreases with increasing temperature. This

observation was also made for zeolites; the heat capacity calculations of zeolites relative to quartz show the same trend with increasing temperature.

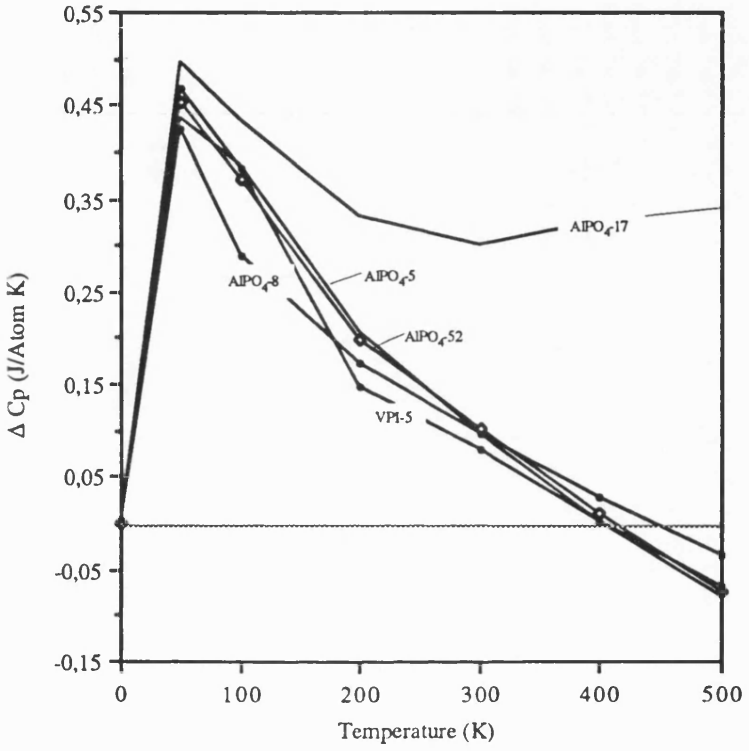

Figure 10.7: The heat capacity, C_p, relative to berlinite, of $AlPO_4$ structures, as a function of temperature ($\Delta C_p = C_{p\ AlPO4} - C_{pBerlinite}$).

In chapter 9 it was shown that the heat capacity of zeolites can be related with the stability; e.g. all siliceous zeolites show a decreasing heat capacity with decreasing stability. This observation is not consistent with the calculated heat capacity of aluminophosphates. The heat capacity of aluminophosphates at elevated temperatures cannot be related with the stability.

10.4. Summary

All aluminophosphates show with increasing temperature an increasing negative Gibbs free energy. The calculated values differ from each other but they all show the same trend with increasing temperature.

The relative free energy of aluminophosphates can also be expressed in terms of basic structural and topological features. The results show that the framework density, the framework structure and the CSQ provide an effective indication of the Gibbs free energy of aluminophosphates at elevated temperatures.

The calculation of the thermal expansion coefficients have shown that some aluminophosphate structures show a negative thermal expansion with increasing temperature. Aluminophosphate structures, characterised through a higher stability and density and a one-dimensional channel system show a positive thermal expansion, whereas the less stable and dense structures with a two- or three-dimensional channel system show a negative thermal expansion behaviour.

The results of the calculation of the heat capacity, C_p, at elevated temperatures demonstrate that all aluminophosphates show an increasing heat capacity with increasing temperature. The heat capacity of aluminophosphates cannot be related with the stability as shown in the simulation studies of zeolites.

APPENDIX I

Listing of the program STACK to calculate hypothetical ABC-6 zeolite structures (see chapter 7)

```
      PROGRAM STACK
      CHARACTER * 1 STACK, THIS, NEXT, BEFORE
      DIMENSION SIAX(6,1), SIAY(6,1), OAX(6,1), OAY(6,1)
      DIMENSION SIBX(6,1), SIBY(6,1), OBX(6,1), OBY(6,1)
      DIMENSION SICX(6,1), SICY(6,1), OCX(6,1), OCY(6,1)
      DIMENSION OXAA(6,1), OYAA(6,1), OXAB(6,1)
      DIMENSION OYAB(6,1), OXAC(6,1), OYAC(6,1)
      DIMENSION OXBC(6,1), OYBC(6,1), OXCA(6,1)
      DIMENSION OYCA(6,1), OXCB(6,1), OYCB(6,1)
      DIMENSION OXBA(6,1), OYBA(6,1), OXBB(6,1)
      DIMENSION OYBB(6,1), OXCC(6,1), OYCC(6,1)
      DIMENSION COORDS1 (6,100), COORDS2 (6,100), COORDS3 (6,100)
      DIMENSION STACK(15)
      REAL VECT,R,P


      WRITE(6,*) 'HOW MANY STACKING UNITS'
      READ(5,*) NSTAC
      WRITE(6,*) 'TYPE IN STACKING SEQUENCE'
      IF (NSTAC .GT. 15) THEN
      WRITE(6,*) 'TOO MANY STACKING SEQUENCES'
      STOP
      END IF

      READ(5,200) (STACK(J), J=1,NSTAC)
200   FORMAT(15A1)


      WRITE(6,*) 'TYPE IN LATTICE VECTOR'
      READ(5,*) VECT

      R=3.2/VECT
      P=VECT/(SQRT(3.0)*3.2)
      WRITE(6,*) 'R =  ',R
      WRITE(6,*) 'P =  ',P

C A-ring Si(x,y) coordinates
      SIAX(1,1)=R
      SIAX(2,1)=R/2
      SIAX(3,1)=-R/2
      SIAX(4,1)=-R
```

```
      SIAX(5,1)=-R/2
      SIAX(6,1)=R/2

      SIAY(1,1)=O
      SIAY(2,1)=-R*(SQRT(3.0)/2)
      SIAY(3,1)=-R*(SQRT(3.0)/2)
      SIAY(4,1)=0
      SIAY(5,1)=R*(SQRT(3.0)/2)
      SIAY(6,1)=R*(SQRT(3.0)/2)

C A-ring Ox(x,y) coordinates
      DO10  I=1,6
      OAX(I,1) = SIAY(I,1)
      OAY(I,1) = SIAX(I,1)
10    CONTINUE

C B-ring Si(x,y) coordinates
      DO20  I=1,6
      SIBX(I,1) = SIAX(I,1)
      SIBY(I,1) = SIAY(I,1) -(P*R)
20    CONTINUE

C B-ring Ox(x,y) coordinates
      DO 30  I=1,6
      OBX(I,1) = SIAY(I,1)
      OBY(I,1) = SIAX(I,1) - (P*R)
30    CONTINUE

C C-ring Si(x,y) coordinates
      DO 40  I=1,6
      SICX(I,1) = SIAX(I,1)
      SICY(I,1) = SIAY(I,1) + (P*R)
40    CONTINUE

C C-ring Ox(x,y) coordinates
      DO 50  I=1,6
      OCX(I,1) = SIAY(I,1)
      OCY(I,1) = SIAX(I,1) + (P*R)
50    CONTINUE

C Ox(x,y)-coordinates between A-A layer
      OXAA(1,1) = R+(0.134*R)
      OXAA(2,1) = (R+(0.134*R))/2
      OXAA(3,1) = (-(R+(0.134*R)))/2
      OXAA(4,1) = (-(R+(0.134*R)))
      OXAA(5,1) = (-(R+(0.134*R)))/2
      OXAA(6,1) = (R+(0.134*R))/2

      OYAA(1,1) = 0
      OYAA(2,1) = (-(R +(0.134*R)) * (SQRT(3.0))/2)
      OYAA(3,1) = (-(R +(0.134*R)) * (SQRT(3.0))/2)
      OYAA(4,1) = 0
      OYAA(5,1) = ((R + (0.134*R)) * (SQRT(3.0))/2)
      OYAA(6,1) = ((R + (0.134*R)) * (SQRT(3.0))/2)
```

```
C Ox(x,y) - coordinates between B-B layer
      DO 52     I=1,6
      OXBB(I,1) = OXAA(I,1)
      OYBB(I,1) = OYAA(I,1)-(P*R)
52    CONTINUE

C Ox(x,y) - coordinates betweem C-C layer
      DO 54     I=1,6
      OXCC(I,1) = OXAA(I,1)
      OYCC(I,1) = OYAA(I,1)+(P*R)
54    CONTINUE

C  Ox(x,y)-coordinates between A-B layer
      OXAB(1,1) = R/2
      OXAB(2,1) = -R/2
      OXAB(3,1) = (R/4)*(-1+SQRT(3.0)*P)
      OXAB(4,1) = (-R/4)*(-1+SQRT(3.0)*P)
      OXAB(5,1) = (R/4)*(1+SQRT(3.0)*P)
      OXAB(6,1) = (-R/4)*(1+SQRT(3.0)*P)

      OYAB(1,1) = (-R/2)*P
      OYAB(2,1) = (-R/2)*P
      OYAB(3,1) = (R/4)*(SQRT(3.0)+P)
      OYAB(4,1) = (R/4)*(SQRT(3.0)+P)
      OYAB(5,1) = (R/4)*(-SQRT(3.0)+P)
      OYAB(6,1) = (R/4)*(-SQRT(3.0)+P)

C  Ox (x,y) position between A-C layer
      OXAC(1,1) = R/2
      OXAC(2,1) = -R/2
      OXAC(3,1) = (R/4)*(-1-SQRT(3.0)*P)
      OXAC(4,1) = (R/4)*(1-SQRT(3.0)*P)
      OXAC(5,1) = (-R/4)*(-1-SQRT(3.0)*P)
      OXAC(6,1) = (-R/4)*(1-SQRT(3.0)*P)

      OYAC(1,1) = (R/2)*P
      OYAC(2,1) = (R/2)*P
      OYAC(3,1) = (R/4)*(SQRT(3.0)-P)
      OYAC(4,1) = (R/4)*(-SQRT(3.0)-P)
      OYAC(5,1) = (R/4)*(SQRT(3.0)-P)
      OYAC(6,1) = (R/4)*(-SQRT(3.0)-P)

C Ox(x,y) position between B - C layer
      DO 60     I=1,6
      OXBC(I,1) = OXAB(I,1)
      OYBC(I,1) = OYAB(I,1) - (P*R)
60    CONTINUE

C Ox(x,y) position between B - A layer
      DO 65     I=1,6
      OXBA(I,1) = OXAC(I,1)
      OYBA(I,1) = OYAC(I,1) - (P*R)
65    CONTINUE

C Ox(x,y) coordinates between C - A layer
```

```
      DO 70   I=1,6
      OXCA(I,1) = OXAB(I,1)
      OYCA(I,1) = OYAB(I,1)+ (P*R)
70    CONTINUE

C Ox(x,y) coordinates between C - B layer
      DO 80   I=1,6
      OXCB(I,1) = OXAC(I,1)
      OYCB(I,1) = OYAC(I,1) + (P*R)
80    CONTINUE


      DO 90       J=1,NSTAC
      THIS=STACK(J)
      NEXT=STACK(1)
      BEFORE=STACK(1)

       IF (J .NE. NSTAC) THEN
         NEXT = STACK(J+1)
         BEFORE=STACK(J-1)
       ELSE
         BEFORE=STACK(J-1)
       END IF

       IF (BEFORE .EQ. THIS) THEN
         ZADDSI = R
         ZADDOX = R
       ELSE
         ZADDSI = R*SQRT((2.0*P)*SQRT(3.0)-2-(P*P))
         ZADDOX = R*SQRT((2.0*P)*SQRT(3.0)-2-(P*P))
       END IF

       IF (J .EQ. 1) THEN
         ZCURRSI = 0
         ZCURROX1 = R/2
         ZCURROX2 =(R/2)*SQRT((2.0*P)*SQRT(3.0)-2-(P*P))
       ELSE
         ZCURRSI = ZCURRSI+ZADDSI
         ZCURROX1 = ZCURROX1+ZADDOX
         ZCURROX2 = ZCURROX2+ZADDOX
       END IF

       IF (THIS .EQ. 'A') THEN
          IF (NEXT .EQ. 'A') THEN
         DO 92   I=1,6
         COORDS1 (1,NBAS+I) = SIAX(I,1)
         COORDS1 (2,NBAS+I) = SIAY(I,1)
         COORDS1 (3,NBAS+I) = ZCURRSI
         COORDS2 (1,NBAS+I) = OAX(I,1)
         COORDS2 (2,NBAS+I) = OAY(I,1)
         COORDS2 (3,NBAS+I) = ZCURRSI
         COORDS3 (1,NBAS+I) = OXAA(I,1)
         COORDS3 (2,NBAS+I) = OYAA(I,1)
         COORDS3 (3,NBAS+I) = ZCURROX1
92       CONTINUE
```

```
          NBAS=NBAS+6
          END IF

          IF (NEXT .EQ. 'B') THEN
          DO 95   I=1,6
          COORDS1 (1,NBAS+I) = SIAX(I,1)
          COORDS1 (2,NBAS+I) = SIAY(I,1)
          COORDS1 (3,NBAS+I) = ZCURRSI
          COORDS2 (1,NBAS+I) = OAX(I,1)
          COORDS2 (2,NBAS+I) = OAY(I,1)
          COORDS2 (3,NBAS+I) = ZCURRSI
          COORDS3 (1,NBAS+I) = OXAB(I,1)
          COORDS3 (2,NBAS+I) = OYAB(I,1)
          COORDS3 (3,NBAS+I) = ZCURROX2
95        CONTINUE
          NBAS=NBAS+6
          END IF

          IF (NEXT .EQ. 'C') THEN
          DO 97    I=1,6
          COORDS1 (1,NBAS+I) = SIAX(I,1)
          COORDS1 (2,NBAS+I) = SIAY(I,1)
          COORDS1 (3,NBAS+I) = ZCURRSI
          COORDS2 (1,NBAS+I) = OAX(I,1)
          COORDS2 (2,NBAS+I) = OAY(I,1)
          COORDS2 (3,NBAS+I) = ZCURRSI
          COORDS3 (1,NBAS+I) = OXAC(I,1)
          COORDS3 (2,NBAS+I) = OYAC(I,1)
          COORDS3 (3,NBAS+I) = ZCURROX2
97        CONTINUE
          NBAS=NBAS+6
          END IF
        END IF

        IF (THIS .EQ. 'B') THEN
          IF (NEXT .EQ. 'B') THEN
          DO 99   I=1,6
          COORDS1 (1,NBAS+I) = SIBX(I,1)
          COORDS1 (2,NBAS+I) = SIBY(I,1)
          COORDS1 (3,NBAS+I) = ZCURRSI
          COORDS2 (1,NBAS+I) = OBX(I,1)
          COORDS2 (2,NBAS+I) = OBY(I,1)
          COORDS2 (3,NBAS+I) = ZCURRSI
          COORDS3 (1,NBAS+I) = OXBB(I,1)
          COORDS3 (2,NBAS+I) = OYBB(I,1)
          COORDS3 (3,NBAS+I) = ZCURROX1
99        CONTINUE
          NBAS = NBAS+6
          END IF

          IF (NEXT .EQ. 'A') THEN
          DO 102   I=1,6
          COORDS1 (1,NBAS+I) = SIBX(I,1)
          COORDS1 (2,NBAS+I) = SIBY(I,1)
          COORDS1 (3,NBAS+I) = ZCURRSI
```

```
          COORDS2 (1,NBAS+I) = OBX(I,1)
          COORDS2 (2,NBAS+I) = OBY(I,1)
          COORDS2 (3,NBAS+I) = ZCURRSI
          COORDS3 (1,NBAS+I) = OXBA(I,1)
          COORDS3 (2,NBAS+I) = OYBA(I,1)
          COORDS3 (3,NBAS+I) = ZCURROX2
102       CONTINUE
          NBAS = NBAS+6
          END IF

          IF (NEXT .EQ. 'C') THEN
          DO 105   I=1,6
          COORDS1 (1,NBAS+I) = SIBX(I,1)
          COORDS1 (2,NBAS+I) = SIBY(I,1)
          COORDS1 (3,NBAS+I) = ZCURRSI
          COORDS2 (1,NBAS+I) = OBX(I,1)
          COORDS2 (2,NBAS+I) = OBY(I,1)
          COORDS2 (3,NBAS+I) = ZCURRSI
          COORDS3 (1,NBAS+I) = OXBC(I,1)
          COORDS3 (2,NBAS+I) = OYBC(I,1)
          COORDS3 (3,NBAS+I) = ZCURROX2
105       CONTINUE
          NBAS=NBAS+6
          END IF
        END IF

        IF (THIS .EQ. 'C') THEN
          IF (NEXT .EQ. 'A') THEN
          DO 110   I=1,6
          COORDS1 (1,NBAS+I) = SICX(I,1)
          COORDS1 (2,NBAS+I) = SICY(I,1)
          COORDS1 (3,NBAS+I) = ZCURRSI
          COORDS2 (1,NBAS+I) = OCX(I,1)
          COORDS2 (2,NBAS+I) = OCY(I,1)
          COORDS2 (3,NBAS+I) = ZCURRSI
          COORDS3 (1,NBAS+I) = OXCA(I,1)
          COORDS3 (2,NBAS+I) = OYCA(I,1)
          COORDS3 (3,NBAS+I) = ZCURROX2
110       CONTINUE
          NBAS=NBAS+6
          END IF

          IF (NEXT .EQ. 'B') THEN
          DO 120   I=1,6
          COORDS1 (1,NBAS+I) = SICX(I,1)
          COORDS1 (2,NBAS+I) = SICY(I,1)
          COORDS1 (3,NBAS+I) = ZCURRSI
          COORDS2 (1,NBAS+I) = OCX(I,1)
          COORDS2 (2,NBAS+I) = OCY(I,1)
          COORDS2 (3,NBAS+I) = ZCURRSI
          COORDS3 (1,NBAS+I) = OXCB(I,1)
          COORDS3 (2,NBAS+I) = OYCB(I,1)
          COORDS3 (3,NBAS+I) = ZCURROX2
120       CONTINUE
          NBAS=NBAS+6
```

```
          END IF

          IF (NEXT .EQ. 'C') THEN
          DO 122   I=1,6
          COORDS1 (1,NBAS+I) = SICX(I,1)
          COORDS1 (2,NBAS+I) = SICY(I,1)
          COORDS1 (3,NBAS+I) = ZCURRSI
          COORDS2 (1,NBAS+I) = OCX(I,1)
          COORDS2 (2,NBAS+I) = OCY(I,1)
          COORDS2 (3,NBAS+I) = ZCURRSI
          COORDS3 (1,NBAS+I) = OXCC(I,1)
          COORDS3 (2,NBAS+I) = OYCC(I,1)
          COORDS3 (3,NBAS+I) = ZCURROX1
122       CONTINUE
          NBAS=NBAS+6
          END IF
        END IF
90      CONTINUE

        DO 160  I=1,NBAS
        WRITE (7,300) (COORDS1(K,I), K=1,3)
160     CONTINUE

        DO 170  I=1,NBAS
        WRITE (7,301) (COORDS2(K,I), K=1,3)
        WRITE (7,302) (COORDS3(K,I), K=1,3)
        WRITE (7,303) (COORDS2(K,I), K=1,3)
        WRITE (7,304) (COORDS3(K,I), K=1,3)
170     CONTINUE


300     FORMAT ('SI4+ CORE     ',3(F15.8,2X))
301     FORMAT ('OX2- CORE     ',3(F15.8,2X))
302     FORMAT ('OX2- CORE     ',3(F15.8,2X))
303     FORMAT ('OX2- SHEL     ',3(F15.8,2X))
304     FORMAT ('OX2- SHEL     ',3(F15.8,2X))
1000    STOP
        END
```

REFERENCES

Ackermann R. J., Sorell C.A., *Appl. Cryst.*, **7**, 461, 1974

Akporiaye D.E., Price G.D., *Zeolites*, **9**, 23, 1989

Akporiaye D.E., Price G.D., *Zeolites*, **9**, 321, 1989

Anastasoff J.V., Hart P.J., *Phys. Rev.*, **59**, 5, 1941

Angel R.J., G.D. Price, Yeomans J., *Acta Cryst.*, **B41**, 310, 1985

Argauer R.J., Landolt G.R., *US-Patent 3*, **70**, 886, 1972

Axe J.D., Shirane G., *Phys. Rev.*, **B1**, **342**, 197

Bacon G.E., *Neutron Diffraction*, 3rd ed. Oxford Univ. Press, 1975

Barrer R.M., Denny P.J., *J. Chem. Soc*, 971,1961a

Barrer R.M., *Hydrothermal Chemistry of Zeolites*, Academic Press, London, 1982

Barrer R.M., Kerr I.S., *Trans. Farad. Soc.*, **55**, 1915, 1959

Barrer R.M., Vaughan D.E.W., *Trans. Faraday. Soc.*, **63**, 2275, 1967

Barron T.H.K, Huang C.C., Pasternak A., *J. Phys.*, C, **9**, 3925, 1976;

Barthomeuf D., *J. Phys. Chem*, **88 (1)**, 42, 1984

Bates J.B., *J. Chem. Phys.*, **57**, 4042, 1972

Bates J.B., Quist A.S., *J. Chem. Phys.*, **56**, 1528, 1972

Baur W.H., *Acta Crystal.*, **B33**, 2615, 1977

Baur W.H., *Am. Mineral.*, **56**, 1572, 1971

Bechmann R., *Phys. Rev.*, **110**, 1060, 1958;

Bennett J.M., Cohen J.M., Artoli G., Pluth J.J., Smith J.V., *Inorg. Chem*, **24**, 188, 1985

Bennett J.M., Cohen J.P., Flanigen E.M., Pluth J.J., Smith J.V., *Intrazeolite Chemistry*, Stucky G.D. and Dwyer F.G. eds., Am. Chem. Soc., 109, 1983

Bennett J.M., Cohen J.P., Flanigen E.M., Pluth J.J., Smith J.V., *"Intrazeolite*

Chemistry", Stucky G.D., Dwyer F.G. eds, Am.Chem. Soc., 109, 1983

Bennett J.M., Dytrych W.J., Pluth J.J., Richardson J.W. Jr, Smith J.V., *Zeolites*, **6**, 349, 1986

Bennett J.M., Gard J.A., *Nature*, **214**, 1005, 1967

Bennett J.M., Kirchner R.M., Wilson S.T., *"Zeolites: Facts, Figures, Future"*, Jacobs P.A. and van Santen R.A. eds., Elsevier Science Publishers B.V., **49**, 731, 1989

Bibby D.M., Aldridge N.B., Milestond N.B., *J. Catal.*, **72**, 373, 1981

Boisen M.B., Downs R.T., Gibbs G.V., D'Arco Ph., *Am. Mineral.*, **75**, 748, 1990

Born M., Huang K., *Dynamical Theory of Crystal Lattices*, Clarendon Press, Oxford, 1954

Breck D.W., *Zeolite Molecular Sieves: Structure, Chemistry and Use*, Wiley and Sons, London, 1973

Brunner G.O., J. *Solid State Chem.*, **29**, 41, 1979

Brunner G.O., Laves F., *Wiss. Zeitschr.*, TU Dresden, **20**, 387, 1971

Catlow C.R.A., Dixon M., Mackrodt W.C, *"Computer Simulation of Solids"*, Catlow and Mackrodt eds, Springer Verlag, Berlin, 1982

Catlow C.R.A., Doherty M., Price G.D., Sanders M.J., Parker S.C., *Mat. Sci. Forum*, **7**, 163, 1986

Catlow C.R.A., Hayns M.R., *J. Phys*, C, **5**, L237, 1972

Catlow C.R.A., Mackrodt W.C., *Computer Simulation of Solids*, Springer Verlag, Berlin, 1982

Catlow C.R.A., Norgett M.J., *U.K.A.E.A. Report, A.E.R.E. M2936*, United Kingdom, Energy Authority, Harwell, 1976

Catlow C.R.A., *Proc. R. Soc.*, **A353**, 533, 1977

Catlow C.R.A., *Solid State Chemistry Techniques*, Cheetham A.K., Day P., eds, Oxford Science Publications, 231, 1988

Catlow C.R.A., Stonham A.M., *Solid State Phys.*, **16**, 4321, 1983

Catlow C.R.A., Thomas J.M., Parker S.C., Jefferson D.A., *Nature*, **295**, 658, 1982c

Chang Z.P., Barsch G.R., *IEEE Trans. on Sonics and Ulatrasoniscs,* **23(2)**, 127, 1976

Cheetham A.K., Day P. (eds), *Solide State Chemistry Techniques*, Oxford Univ. Press, Oxford 1987

Cheetham A.K., Eddy M.M., Thomas J.M., *JCS Chem. Commun.*, 1337, 1984

Cherukuri S.C., Pye L.D., Chakraborty I.N., Condrate R.A., Ferraro J.R., Cornilsen B.C., Martin K., *Spectrosc. Lett.*, (U.S.A.), **18**, 123, 1985

Cochran W., *"The dynamics of atoms in crystals"*, Edward Arnold, London, 1973

Couves J.W., Jones R.H., Parker S.C., Tschaufeser P., Catlow C.R.A., Thomas J.M., *Chem. Commun.*, 1992 (in press)

Csicsery S.M., *Zeolite Chemistry and Catalysis*, Rabo J. ed, ACS Monograph, Washington, 171, 680, 1976

Csicsery S.M., *Zeollites*, **4**, 202, 1984

Davidon W.C., *A.E.C. Report*, ANL - 5990, 1959

Davis M.E., Montes C., Graces J.M., Crowder C., *ACS Sym. Ser.*, **398**, 291, 1989

Davis M.E., Saldarriaga C., Montes C., Garces J., Crowder C., *Nature* , **33**, 698, 1988

Deer W.A., Howie R.A., Zussman J., *Rock-forming Minerals*, **4**, 354, Framework Silicates, Longman London, 1963

Dessau R.M., Kerr G.T., *Zeolites*, **4**, 315, 1984

Dessau R.M., Schlenker J.L., Higgins J.B., *Zeolites*, **10**, 522, 1990

Dessau R.M., Schlenker J.L., Higgins J.B., *Zeolites*, **10**, 522, 1990

Dick B.G., Overhauser A.W., *Phys. Rev.*, **112**, 91, 1958

Dolasse W.A., *Z. Kristallographie,* **121** 369, 1965

Dolasse W.A., *Z. Kristallographie*, **121**, 369, 1965

Donahoe R.J., Hemingway B.S., Liou J.G., *Am. Mineral.*, **75**, 188, 1990

Dorner B., Grimm H., Rzany H., *J. Phys*, C, **13**, 6607, 1980

Dovesi R., Pisoni C., Roetti c., Silvi B., *J. Chem. Phys.*, **86**, 6967, 1987

Downs R.T., Gibbs G.V., Boisen M.R. Jr., *Am. Mineral.*, **75**, 1253, 1990

Dyer A, *Chem. Ind.* (London), **7**, 241, 1984

Engelhardt G., Kunathd D., Samoson A., Tarmak M., Magi M., Lippmaa E., *Workshop on Adsorption of Hydrocarbons in Zeolites*, Berlin-Adlershof, 1979

Etchepare J., Merian M., *J. Chem. Phys.*, **68**, 336, 1978;

Etchepare J., Merian M., Kaplan P., *J. Chem. Phys.*, **68**, 1531, 1977

Etchepare J., Merian M., Smetankine L., *J. Chem. Phys.*, **60**, 1873, 1973

Ewald P.P., *Ann. Physik*, **64**, 253, 1921

Fillipini G., Gramacciolli C.M., Simonetta M., Suffritti G.B., *Acta Cryst.*, **A32**, 259, 1976

Fischer K., *N. Jahrb. Mineral.*, Monatshefte **1-13**, 1966

Fischer W., *Z. Kristallographie*, **138**, 129, 1973

Flanigen E.M., *Adv. Chem. Ser.*, **121**, 119, 1973

Flanigen E.M., Benett J.M., Grose R.W., Cohen J.P., Parron R. L. Kirchner R.M, Smith J.V., *Nature*, **217**, 512, 1978

Flanigen E.M., *Zeolite Chemistry & Catalysis*, ACS Monograph **171** , Rabo J. ed., ACS Washington, 1976

Flanigen E.M., Mumpton F.A., *"Mineralogy and Geology of natural Zeolites"*; Mumpton F.A. ed; Mineralogical Soc. of America; Reviews in Mineralogy , **4**, 165, 1981

Flanigen E.M., *Zeolites: Science and Technology*, Riberio ed, Nato Advanced Science Institutes, 1983

Fletcher R.J., Powell M.J.D., *Computer J.*, **6**, 16, 1963

Fyfe C.A., Thomas J.M., Klinowski J., Gobbi G.C., *Angew. Chem.*, **95**, 257, 1983

Gard J.A., Tait J.M., *Acta Crystallog.*, **B28**, 825, 1972

Gates B.C., Katzer J. R., Schuit G.C. A., *Chemistry of Catalytic Processes*, McGraw

Hill, 1979

Gervais F., Piriou B., *Phys. Rev.*, **B11**, 3944, 1975

Ghiroso M.S., Carmichael I.S.E., Moret L.K., *Contrib. Mineral. Petrol.*, **68**, 307, 1979

Glinnemann J., *PhD-Thesis*, University Aachen, 1987

Goiffon A., Bayle G., Astier R., Jumas J.C., Maurin M., Philippot E., *Rev. Chim. Miner.*, **20.**, 338, 1983

Gordon R.G., Kim Y.S., *J. Chem. Phys.*, **56**, 3122, 1972

Grimm H., Dorner B., *J. Phys. Chem. Solids,* **36**, 407, 1975

Grønvold F., Stølen S., Svendsen S.R., *Thermochem. Acta,* **139**, 225, 1989

Hatch D.M., Ghose S., *Phys. Chem. Minerals*, **17**, 554, 1991

Hazen R.M., Finger L.W., Hemley R.J., Mao H.K., *Solid State Commun.*, **72**, 507, 1989

Heaney P.J., Veblen D.R., *Am. Mineral.*, **76**, 1018, 1991

Hemingway B.S., *Am. Mineral.*, **72**, 273, 1987

Hemley R.J., Jephcoat A.P., Mao H.K., Ming L.C., Manghnani M.H., *Nature*, **334**, 52, 1988

Henderson C.M.B., Taylor D., *Phys.Chem.Min.*, **2**, 337, 1978

Hill R.J., Gibbs G.V., *Acta Crystal.*, **B35**, 25, 1979

Höchli U.T., Scott J.F., *Phys. Rev. Lett.*, **26**, 1627, 1971

Hua G.L., Welberry T.R., Withers R.L., *J. Phys. Chem. Solids.*, **50 (2)**, 207, 1989

Iishi K., *Am. Mineral.*, **63**, 1190, 1978

Jackson R.A., Catlow C.R.A., *Molec. Simul.*, **1**, 207, 1988

Janssen R., Dols P.P.M.A., Tijink G.A.H., Veeman W.S., *"Zeolites: Facts, Figures, Future"*, Jacobs P.A. and van Santen R.A. eds., Elsevier Science Publishers B.V., **49**, 609, 1989

Jay A.H., *Proc. Roy. Soc.*, **A142**, 237, 1933

Jayrayamann A., Wood D.L., Meines Sr.R.G., *Phys Rev.*, **B35**, 8316, 1987

Jirak Z., Vratislav S., Jajicek J., Bosacek V., *J. Catal.*, **49**, 112, 1977

Jorgensen J.D., *J. Appl. Phys.*, **49**, 5473, 1978

Kato K., Nukui A., *Acta Cryst.*, **B32**, 2480, 1977

Kendrick J., Mackrodt W.C., *Solid State Ionics*, **8**, 247, 1983

Kihara K., *Europ. J. Mineral.*, **2**, 63, 1990

Kleinmann D.A., Spitzer W.G., *Phys. Rev.*, **125**, 16, 1962

Kokotailo G.T., Sawruk S., Lawton S.L., *Amer. Mineral.*, **57**, 439, 1972

Kosten K., Arnold H., *Zeit. Kristallographie*, **152**, 119, 1980

Kramer G.J., Farragher N.P., van Beest B.W.H., van Santen R.A., *Phys. Rev.*, B., **43 (6)**, 5068, 1991

Kramer G.J., van Beest B.W.H., van Santer R.A., *Nature*, **351**, 636, 1991

Lasaga A.C., Gibbs G.V., *Phys. Chem. Miner.*, **14**, 107, 1987

Lasaga A.C., Gibbs G.V., *Phys. Chem. Miner.*, **16**, 28, 1988

Leadbetter A.J., Smith T.W., *Phil. Mag.*, **33 (1)**, 113, 1975

Leadbetter A.J., Wright A.F., *Phil. Mag.*, **33 (1)**, 105, 1976

Lechert H., *Zeolites: Science and Technology*, Ribeiro F. ed, NATO Adv.Sci. Inst., 1983

Leslie M., Daresbury Laboratory Internal Report, DL/SCI/TM36T, 1984

Levien L., Prewitt Ch.T., Weidner D.J., *Am. Mineral.*, **65**, 920, 1980

Lewis G.V., Catlow C.R.A., *J. Phys.*, **C18**, 1149, 1985

Lewis G.V., *PhD Thesis*, Univ. of London, 1983

Liebau F., *Structural Chemistry of Silicates: Structure, Bonding and Classification*, Springer Verlag, Berlin, 1985

Mackrodt W.C., Stewart R.F., *J. Phys.*, **C10**, 1432, 1977

Matsui M., Busing W.R., *Americ. Mineral.*, **69**, 1090, 1984

McCusker L.B., Baerlocher Ch., *Zeolites*, 1991

McSkimmin H.J., Andreatch P. Jr., Thurston R.N., *J.Appl.Phys.*, **36(5)**,1524, 1965

Megaw H.D., *"Crystal Structures - A working approach"*, 1973

Meier W.M., Möck H.J., *J. Solid State Chem.*, **27**, 349, 1979

Meier W.M., *"Molecular Sieves"*, Society of Chemical Industriy, London, 1968

Meier W.M., Olsen D.H., *"Atlas of Zeolite Structure Types"*, Butterworths, 1987

Milton R.M., *Molecular Sieves*, Soc. Chem. Ind., London, **199**, 1968

Nada R., Catlow C.R.A, Dovesi R., Pisani C., *Phys. Chem. Miner.*, **17**, 353, 1990

Newsam J.M., *Mat. Sci. Forum*, **27/28**, 385, 1987

Newsam J.M., *Solid State Chemistry Vol.2: Compounds*, Cheetham A.K. & Day P. eds, Oxford University Press, 1990

Newsam J.M., Treacy M.M., Koetsier W.T., Gryuter C.B., *Proc. R. Soc. Lond.*, **A420**, 375, 1988

Ng H.N., Calvo C., *Can. J. Phys.*, **54**, 638, 1976

Norgett M.J., Fletcher R.J., *J. Phys.*, **C3**, 163, 1970

O'Keefe M., Hyde B.G., *Acta Cryst.*, **B34**, 27, 1978

Parker S.C., Catlow C.R.A., Cormack A.W., *Acta Cryst.*, **B40**, 200, 1984

Parker S.C., Catlow C.R.A., Cormack A.W., *JCS Chem. Comm.*, 529, 1983

Parker S.C., *PhD Thesis*, University of London, 1982

Parker S.C., Price G.D., *Adv. Solid State Chem.*, **1**, 295, 1989

Peacor D.R., *Z. Kristallograpahie*, **138**, 274, 1973

Pluth J.J., Smith J.V, Bennett J.M., *Acta Cryst.*, **C42**, 283, 1986

Pluth J.J., Smith J.V., Bennett J.M., *Acta Cryst.*, **C42**, 283, 1986

Pluth J.J., Smith J.V., Faber J. Jr., *J. Appl. Phys.*, **57 (4)**, 1045, 1984

Prasad S., Balakrishnan I., *Inorg. Chem*, **29**, 4830, 1990

Price G.D, Parker S.C., *Physical Properties and Thermodynamic Behaviour of Minerals*, Salje E.K.H. ed, D. Reidl Publishing Company, 591, 1988

Price G.D., Parker S.C., Leslie M., *Miner. Mag.*, **51**, 157, 1987

Price G.D., Parker S.C., *Phys. Chem. Miner.*, **10**, 209, 1984

Price G.D., *Phys. Chem. Minerals*, **10**, 77, 1983

Price G.D., Yeomans J., *Acta Cryst.*, **B40**, 448, 1984

Richet P., Bottinga Y., Denielou L., Petit J.P., Tepui C., Geoch. *Cosmochem. Acta*, **46**, 2639, 1982

Rietveld H.M., *J. Appl. Crystallogr.*, **2**, 69, 1969

Rollman L.D., *Adv. Chem. Ser.*, **173**, 387 1979

Salje E., Werneke Ch., *High-pressure researches in geosciences*, Schreyer W. ed., Schweizerbart'sche Verlagsbuchhandlung, Stuttgart, 1982

Sanders M.J., Leslie M., Catlow C.R.A., *JCS Chem. Comm.*, 1271, 1984

Sanders M.J., *PhD Thesis*, Univ. of London, 1982

Schwarzenbach D., *Z. Kristallographie*, **123**, 161, 1966

Scott J.F., *Phys. Rev. Lett.*, **21**, 907, 1968

Scott J.F., *Phys. Rev.*, **B4.**, 1360, 1971

Scott J.F., Porto S.P.S., *Phys. Rev.*, **161**, 903, 1967

Sheppard R.A., Gude A.J., Desborough G.A., White J.S., *Amer. Mineral.*, **59**, 837, 1974

Sidek H.A.A., Saunders G.A., Wang H., Xu Bin, Han J., *Phys. Rev.*, **B36**, 7612, 1987

Silvi B., D'Arco Ph., Saunders V.R., Dovesi R., *Phys. Chem. Minerals*, **17**, 674, 1991

Smith J.V., *Amer. Mineral.*, **64**, 55, 1979

Smith J.V., Bennett J.M., *Amer. Mineral.*, **66**, 777, 1981

Smith J.V., *Chem. Rev*, **88**, 149, 1988

Smith J.V., *"Zeolites: Facts, Figures, Future"*, Jacobs P.A. and van Santen R.A. eds., Elsevier Science Publishers B.V., 49, 29, 1989

Sowa H., Macavei J., Schulz H., *Zeit. Kristallographie*, **192,** 119, 1990

Stixrude L., Bukowinski M.S.T., *Am. Mineral.*, **75**, 1159, 1990

Striefler M.E., Barsch G.R., *Phys. Rev.*, **B12**, 4553, 1975

Taylor D., *Mineral. Mag.*, **38**, 592, 1972

Taylor D., *Mineral. Mag.*, **38**, 629, 1972

Thomas J.M., Fyfe C.A., Ramdas S., Klinowski J., Gobbi G.C., *J. Phys. Chem.*, **86**, 3061, 1982

Thomas J.M., Klinowski J. Anderson M.W., *Chem. Lett.*, **10**, 1555, 1983

Thomas J.M., Ramdas S., Millward R.G., Klinowski J., Audier M., GonzalezCalbert J, Fyfe C.A., *J. Solid State Chem.*, **45**, 368, 1982b

Thomas J.M., *"Zeolites: Facts, Figures, Future"*, Jacobs P.A. and van Santen R.A. eds., Elsevier Science Publishers B.V., 49, 3, 1989

Thong N., Schwarzenbach D., *Acta Cryst.*, **A35**, 658, 1979

Toby B.H., Eddy M.M., Fyfe C.A., Kokotailo G.T., Stribl H., Cox D.E., *J. Mater. Res.*, **3**, 563, 1988

Tomlinson S.M., Jackson R.A., Catlow C.R.A., *JCS Chem. Comm.*, 813, 1990

Tosi M.P., *Solid State Phys.*, **16**, 1, 1964

Tsuneykui S., Tsukada H., Aoki H., Matsui Y., *Phys. Rev. Lett.*, **61**, 869, 1988

Tsuneyuki S., Tsukada M., Aoki H., Matsui Y., *Phys. Rev. Lett.*, **61**, 869, 1988

van Beest B.W.H., de Man A.J.M., Jackson R.A., Catlow C.R.A., van Santen R.A., *Zeolites: Facts, Ficgures, Future;* P.A. Jacobs, R.A. van Santen eds; Elsevier Science Publishers, Amsterdam, **49**, 763, 1989

van Beest B.W.H., Kramer G.J., van Santer R.A., *Phys. Rev. Lett.*, **64 (16)**, 1955, 1990

van Santen R.A., Vogel D.L., *Adv. Solid State Chem.*, **151**, 1988

van Tandeloo G., van Landuyt J., Amelinckx S., *Phys. Stat. Soc.*, **33**, 723, 1976

Venuto P.B., Habib E.T., *Fluid Catalytic Cracking*, Marcel Dekker, New York, 1979

Vogt E.T.C., Richardson J.W. Jr., *J. Solid State Chem.*, **87**, 469, 1990

Wall A., *PhD Thesis*, Univ. of London, 1987

Wall A., Price G.D., Parker S.C., *Mineral. Mag.*, **50**, 693, 1986

Wang Q., *First Year Report*, Bath University, 1990

Wang Q., Saunders G.A., Lambson E.F., Tschaufeser P., Parker S.C., James B.J., *Phy. Rev*, **49** (B), 1992

Wedepohl P.T., *Proc. Phys. Soc.*, **92**, 79, 1967

Weisz P.B., *Pure Appl. Chem.*, **52**, 2091, 1980

Wells A.F., *Am. Cryst. Assoc. Monog.*, **8**, 1979

Whan D., *Chemistry in Britain*, **17 (11)**, 532, 1981

White G.K., Roberts R.B., Collins J.G., *High Temp., High Press.*, **17**, 61, 1985

Wilson S.T., Lok B.M., Flanigen E.M., U.S. Patent 4,310,440; *European Patent* 43,562)

Wilson S.T., Lok B.M., Messina C.A., Cannan T.R., Flanigen E.M., *J. Am. Chem. Soc.*, **104**, 1146, 1982

Wilson S.T., Lok B.M., Messina C.A., Flangigen E.M., *Proc. 6th. Int. Conf. on Zeolites*, 97, Olson D., Bisio A. eds., Butterworths, Surrey, UK, 1984

Wright A.F., Leadbetter A.J., *Phil. Mag.*, **31**, 1391, 1975

Wright A.F., Lehmann M.S., *J. Solid State Chem.*, **36**, 371, 1981

Wyckoff R.W.G., *Am. J. Sci.*, **9**, 448, 1925

Wyckoff R.W.G., *Crystal Structures*, **Vol 1**, New York: Interscience, 1948

Wyckoff R.W.G., *Crystal Structures*, **Vol 3**, 31, Interscience Publishers, 1965

Young R.A., Report 2569, Air force office scientific research, Washington 25, 1962

Yu L., Pang W., Li L., *J. Solid State Chem*, **87**, 241, 1990

Ziman J.M., *The principles of the theory of solids*, CUP, Cambridge, 1964